

Lawrence Berkeley National Laboratory

Recent Work

Title

RADIATION EFFECTS and METALLOPROTEINS STUDIED BY X-RAY PHOTOELECTRON SPECTROSCOPY

Permalink

<https://escholarship.org/uc/item/7kd089md>

Author

Wurzbach, James Alan.

Publication Date

1975-07-01

0 0 1 0 4 5 5 5 7 3 0

UC-48
LBL-4677
c.1

RADIATION EFFECTS AND METALLOPROTEINS STUDIED BY
X-RAY PHOTOELECTRON SPECTROSCOPY

James Alan Wurzbach
(Ph. D. thesis)

RECEIVED
LAWRENCE
BERKELEY LABORATORY

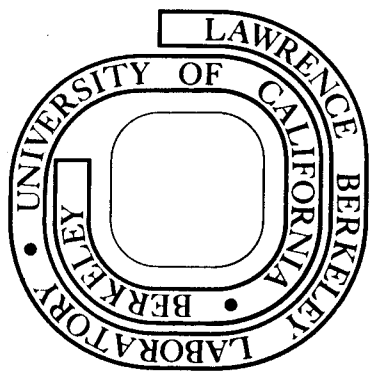
MAR 8 1978

July 1975

LIBRARY AND
DOCUMENTS SECTION

Prepared for the U. S. Department of Energy
under Contract W-7405-ENG-48

For Reference
Not to be taken from this room



LBL-4677
c.1

DISCLAIMER

This document was prepared as an account of work sponsored by the United States Government. While this document is believed to contain correct information, neither the United States Government nor any agency thereof, nor the Regents of the University of California, nor any of their employees, makes any warranty, express or implied, or assumes any legal responsibility for the accuracy, completeness, or usefulness of any information, apparatus, product, or process disclosed, or represents that its use would not infringe privately owned rights. Reference herein to any specific commercial product, process, or service by its trade name, trademark, manufacturer, or otherwise, does not necessarily constitute or imply its endorsement, recommendation, or favoring by the United States Government or any agency thereof, or the Regents of the University of California. The views and opinions of authors expressed herein do not necessarily state or reflect those of the United States Government or any agency thereof or the Regents of the University of California.

TABLE OF CONTENTS

	Page
Abstract	1
Acknowledgments	3
I. Introduction	5
References	10
II. Calculation of Intensity from the X-Ray Source of the Berkeley Iron-Free Spectrometer	13
Introduction	13
A. The Continuous X-Ray Spectrum	17
1. Energy Distribution	17
2. Spatial Distribution	23
3. Polarization	30
B. Characteristic X-Rays	32
1. Spatial Distribution	32
2. Energy Distribution	42
C. Mass Absorption Coefficients	46
D. Applications	51
1. Estimate of X-Ray Intensity	51
2. The Use of Magnesium and Aluminum Windows to Filter Bremsstrahlung	59
3. Estimate of Radiation Dose by Use of a LiF chip	63
References	64
III. Reliability of the SUNDER Fitting Program	68
IV. The Use of Carbon 1s and Nitrogen 1s signals as Reference Standards in XPS	91
A. Introduction	91
B. C 1s as an Internal Standard	99
C. Nitrogen 1s as an Internal Standard	132
References	156
V. XPS Study of Horse Heart Cytochrome c	160
A. Introduction	160
B. Experimental	163
C. Results and Discussion	180

	Page
1. Criticism of the HF Procedure for Iron Removal from Cytochrome C	180
2. The Suitability of Microperoxidase as a Model for Cytochrome C	184
3. The C 1s spectrum -- Internal Reference	188
4. N 1s Results	197
5. The Stability of Reference Signals and Optical Spectra .	204
6. Sulfur 2p Results	213
7. Iron 3p Results.	239
References	260
VI. XPS Study of the Binding of Rare Earth Ions to ATP	266
A. Introduction	266
B. Experimental	267
C. Results and Discussion	271
1. Powder Pattern	271
2. Sample Purity	272
3. Carbon 1s and Nitrogen 1s Results	275
4. Phosphorus 2p Results	289
D. Conclusions	296
References	299
VII. Conclusions	302

RADIATION EFFECTS AND METALLOPROTEINS STUDIED BY X-RAY
PHOTOELECTRON SPECTROSCOPY

James Alan Wurzbach

Lawrence Berkeley Laboratory
University of California
Berkeley, CA 94720

ABSTRACT

X-ray photoelectron spectroscopy (XPS) is used to study the bonding structure at the iron site of cytochrome c and the bonding of rare earth ions to the phosphate oxygens of ATP. Radiation effects are studied on several amino acid and simple peptide model systems.

The emission spectrum of the x-ray source is calculated from literature references. The distributions of photon energy as a function of photon frequency and as a function of take-off angle are obtained. From these distributions, the radiation dose absorbed by an organic sample is found to be 10^6 rads/sec.

The carbon 1s and nitrogen 1s spectra of amino acids and peptides are studied to characterize an internal reference standard for protein XPS spectra. The carbon 1s signal is found to be more suitable because its peak has more structure. During exposure to the x-ray tube, some of these signals change. Decarboxylation and deamination are observed; signal intensities diminish by 0 - 30 % during 10 hour experiments. Notwithstanding such variations, carbon 1s signals can be used as internal references in the study of proteins.

Samples of native cytochrome c prepared from solutions of pH 1.5, 3, 7, and 11 are studied. Control samples include porphyrin cytochrome c (PCC), the metal free analogue of the native protein, and microperoxidase (MP), a mixture of heme peptides derived from the peptic digestion of cytochrome c.

These samples show two sulfur 2p peaks. The first peak has a binding energy (BE) of 163 eV, which corresponds to the sulfur containing amino acids; the second peak is shifted to 167 eV. This large shift may be the result of iron-sulfur binding, or oxidation, or both. The nature of sulfur to iron binding cannot be assigned unambiguously.

Low spin ferricytochrome c and ferri-MP were found to have iron 3p BE's that are unusually low (51 eV) compared to other ferric compounds (54 - 58 eV) and even iron metal (53 eV). Iron 3p BE's reported in the literature for high spin ferric porphyrins are consistent with those of the standard ferric compounds. X-ray crystal structures of these compounds show that low spin heme iron lies in the porphyrin plane; while, high spin heme iron is displaced above the plane. Therefore, the unusually low iron 3p BE may be associated with low spin heme iron in the porphyrin plane.

The nitrogen 1s and phosphorus 2p spectra of ATP show no change except slight broadening when Nd^{3+} is substituted for Na^+ . Thus, there is no inconsistency with proposals that rare earth ions might be useful as substitutes for alkali metal ions and alkaline earth ions in proteins.

ACKNOWLEDGMENTS

I owe a debt of gratitude to Dr. Mel Klein and Professor Melvin Calvin for their guidance, creative ideas, and thoughtful advice throughout the completion of this dissertation.

I also thank Professor David Shirley for the education he has provided both in course work and in discussions of theory and interpretation of data. Professor John Clarke has been similarly helpful in his course and further discussions of solid state physics.

At the outset of this work, I had no formal or practical background in protein chemistry. Dr. L.E. Vickery has pointed out pertinent experiments and demonstrated essential techniques of protein preparation and handling. Dr. Jim Slama clarified several aspects of protein and porphyrin chemistry. Without such aid, no progress would have been possible.

Neither could this work have been completed without the skill of Charlie Butler, who maintained a temperamental piece of equipment in working order.

The help of Dr. Frank Grunthaner has been very useful, especially regarding sample preparation techniques and in providing extended experimental time on the HP 5950A spectrometer. I thank Professor Harry B. Gray for fruitful discussions and for reviewing the cytochrome section of this dissertation.

Many laboratory personnel have made important contributions to my education and work. These people include Joe Katz, Gene Miner, Dick Escobales, Claudette Lederer, Vic Elischer, and Emmet Burns.

I have learned much from my friends and associates here at Berkeley, particularly, Ray Glienna, Bob Miller, Steve Cooper, L.N. Kramer, Merle Millard, Salim Banna, Read McFeely, Bernice Mills, Sefik Suzer, Bill Davis, and Roger Pollak.

And when late hours, irregular results, and the experimenter found ourselves together in the Field Free Laboratory, Dr. Don Kulik would stumble upon us during his regular midnight visits to cool the spectrometer. I acknowledge Dr. Kulik's practical philosophy and his suggestions of what to do about irregular results.

I also acknowledge the support of the U.S. Energy Research and Development Administration.

I. INTRODUCTION

Photoelectron spectroscopy is a technique developed by Kai Siegbahn^{1,2} and coworkers for determining the binding energy (BE) of bound electrons in chemical systems.³ The technique has been given the name ESCA (Electron Spectroscopy for Chemical Analysis). Under appropriate experimental conditions, the method can be applied to gases,^{2,8} solids,¹ and in limited cases, liquids.⁴ In an ESCA experiment, a sample is exposed to photons of energy $h\nu$. Electrons are ejected from the sample by the photoelectric effect. In ESCA of solids, appreciable numbers of electrons escape from depths of 20 - 100 Å without scattering inelastically in the solid lattice.^{1,5,6} The kinetic energy (KE) distribution of the photoelectrons is measured by an electrostatic¹² or magnetic analyzer¹ under vacuum. The dominant terms in the BE⁷ are then given by Eq. (1).

$$BE = h\nu - KE \quad (1)$$

Thus, photoelectron spectroscopy can be used to profile the electron distribution among all the occupied levels that have a BE less than $h\nu$.

X-ray photoelectron spectroscopy (XPS) employs soft x-rays ($h\nu \sim 1000$ eV); ultraviolet photoelectron spectroscopy (UPS) uses hard UV photons ($h\nu \sim 20 - 40$ eV). Therefore, UPS measures only valence electrons⁸ while XPS can measure core electrons.⁹ Core orbital BE's in XPS are designated by the atom and orbital from which the photoelectron was ejected, for example, carbon 1s or C 1s. This dissertation deals exclusively with the XPS of solids.

XPS has been useful in mapping valence band structure in metals, semiconductors, and inorganic anions,¹⁰ as well as molecular orbitals in gases.² XPS is ideally suited for surface studies¹ because of the shallow escape depth of photoelectrons in solids.

XPS can probe the electronic structure of systems that are inaccessible to other techniques. These include: (i) compounds that have no convenient optical absorptions; (ii) ions having no EPR signal, like Cu^+ and low spin Fe^{++} ; (iii) light elements ($Z < 20$) that show little x-ray fluorescence. Absorption edges in x-ray absorption spectroscopy are commonly complicated by structure which is not a problem in XPS. The XPS spectrum also shows the x-ray induced Auger spectrum of the sample.

The BE in Eq. (1) depends on the ligands bound to the atom from which the photoelectron was ejected. For example, an atom surrounded by electronegative ligands will carry a slightly positive charge; the effect is to increase the BE of electrons photoejected from this atom. BE shifts motivated by changes in bonding arrangements are called chemical shifts.¹⁰ Because the chemical shift reflects the charge distribution at the parent atom, it can be related to several chemical properties. Chemical shifts have been correlated to Pauling electronegativities and atomic charges that have been calculated according to several different theories.¹¹ Group shifts have been suggested for various organic functional groups.¹¹ Applications of chemical shifts to a variety of chemical problems have been reviewed elsewhere.^{12,13}

XPS chemical shifts have been applied to structural problems in biology. The thrust of this work has been directed at determining the

chemical environment of metal binding sites in proteins,¹⁴⁻¹⁷ cell walls,¹⁸ and chlorophyll;^{14a} although, some non-metal work has been done on textiles.¹⁹ The basic experiment involves a measurement of the BE of the core electrons of the metal and its ligands. Inferences about the bonding geometry at the metal site are then drawn on the basis of comparison with BE's from a series of model compounds.

It was hoped that this thesis work could elucidate the structure of the copper sites in cytochrome oxidase.²⁰ With the support of Kramer's work¹⁴ on the XPS shifts of iron and sulfur, it was hoped that the atomic charges of iron, copper, and sulfur could be measured at various stages of the mitochondrial electron transport chain.

Preliminary measurements on a series of copper containing model complexes showed that several experimental advances would have to be achieved before a cytochrome oxidase project could be attempted.

- (1) The models demonstrated that the practical limit of detection in the Berkeley iron-free spectrometer was 1 part in 10^3 . The absolute limit was 1 part in 10^4 . The amount of copper in cytochrome oxidase (2 copper atoms, molecular weight 200,000) was, therefore, too small to produce a signal on which quantitative interpretations could be based. The apparatus required a smaller, simpler, metalloprotein.
- (2) The observed linewidths were large compared to the chemical shift of BE's. Spectrometer resolution yielded a Cu $2p_{3/2}$ peak with a full width at half maximum (FWHM) of 2-3 eV, but 80% of the known Cu $2p_{3/2}$ BE's fall within a 3 eV range between 933 and 936 eV.^{21,15}

- (3) All of the model complexes became discolored in the energy flux emitted by the x-ray tube. Several samples showed observable shifts due to dehydration in the vacuum or photoreduction²² in the x-rays. Radiation damage would be a major factor in any experiment of reasonable length.
- (4) To facilitate quantitative interpretations, a computer program named SUNDER was used to fit line-shapes to the observed peaks. SUNDER often calculated spurious fits because it was not designed for application to the wide, overlapping, low intensity signals that often characterized biological XPS spectra.
- (5) For solid samples, Eq. (1) must be corrected for sample charging, crystal potentials, and work functions; the magnitudes of these effects are generally not known. An internal reference signal to which all the other BE's could be standardized would have to be characterized.

The first two results listed above showed that cytochrome oxidase was too complicated to study with the given equipment. A simpler, more characterized system, cytochrome *c*,^{23,24} was selected for experiments. This work is discussed in Chapter V. It is demonstrated that XPS may be useful to show that iron is in or out of the porphyrin plane in heme proteins and complexes.

Following the cytochrome work, there is a discussion of an XPS study of the binding of rare earth ions to ATP.

Meaningful interpretations of these data were not possible until other technical problems (3-5 listed above) had been considered.

The intensity distribution from the x-ray source was not known; so, the radiation dose absorbed by the sample was not known. An estimate of the energy distribution from the x-ray source as a function of frequency could be derived from the literature. The results of this study are presented in the next chapter. The SUNDER fitting program's limitations are documented in Chapter III. In Chapter IV, the carbon 1s and nitrogen 1s signals are characterized as potential internal reference standards for biological studies. Also, the x-radiation, electrons, and heat from the x-ray tube had effects on amino acids and peptides that are shown in Chapter IV.

The information in these early chapters showed that the effectiveness of the carbon 1s internal reference had to be established for each class of samples studied. It was also necessary to establish the stability of each class of samples in the photon, electron, and infra-red fluxes from the x-ray tube. These considerations are included in the cytochrome and ATP studies, Chapters V and VI, respectively.

REFERENCES, CHAPTER I

1. K. Siegbahn, et al., ESCA - Atomic, Molecular, and Solid-State Structure Studied by Means of Electron Spectroscopy, Nova Acta Regiae Societatis Scientiarum Upsaliensis, Ser. IV, Vol. 20 (1967).
2. K. Siegbahn, et al., ESCA Applied to Free Molecules (North Holland, Amsterdam, 1969).
3. D.A. Shirley (Ed.), Electron Spectroscopy (North Holland, Amsterdam, 1972).
4. Hans Siegbahn and K. Siegbahn, Univ. Uppsala Inst. Phys. Rept. UUIP-823 (1973).
5. R. Steinhardt, J. Hudis, and M. Perlman, Ref. 3, p. 557.
6. M. Klasson, J. Hedman, R. Nilsson, C. Nordling, P. Melnik, Phys. Scr., 5, 93 (1972).
7. C.S. Fadley, Theoretical Aspects of X-Ray Photoelectron Spectroscopy, NATO Advanced Study Institute on Electron Emission Spectroscopy, Ghent University, Ghent, Belgium (Aug. 28 - Sept. 8, 1972).
8. D.W. Turner, C. Baker, A. Baker, C. Brundle, Molecular Photoelectron Spectroscopy (Wiley-Interscience, London, 1970).
9. For a comparison of XPS and UPS, see Ref. 3, p. 17.
10. D.A. Shirley in Advances in Chemical Physics, Vol. 23, Prigogine and Rice (Eds.), (Interscience, New York, 1973), pp. 85-159.
11. U. Gelius, et al., Phys. Scr., 2, 70 (1970).

12. W. Bremser, New Methods in Chemistry, Vol. 36 (Springer-Verlag, New York, 1973), pp. 1-37.
13. D. Hercules, Anal. Chem. 42, 20A (1970).
14. a) L.N. Kramer, Ph.D. dissertation, University of California, Berkeley, (1971), Lawrence Berkeley Laboratory Report #LBL-306.
b) L.N. Kramer, M.P. Klein in Electron Spectroscopy, D.A. Shirley (Ed.) (North Holland Publ. Co., Amsterdam, 1972), p. 733.
c) L.N. Kramer, M.P. Klein, Chem. Phys. Lett. 8 (2), 183 (1971).
15. F.J. Grunthaner, Ph.D. dissertation, California Institute of Technology (1974).
16. G. Jung, M. Ottnad, W. Bohnenkamp, W. Bremser, U. Weser, Biochim. Biophys. Acta 295, 77 (1973).
17. U. Weser, F. Donay, H. Rupp, FEBS Lett. 32 (1), 171 (1973).
18. J. Baddiley, I.C. Hancock, Nature 243, 43 (1973).
19. M. Millard in Electron Spectroscopy D.A. Shirley (Ed.) (North Holland Publ. Co., Amsterdam, 1972), p. 765.
20. R. Malkin and B. Malmstrom, Advan. Enzymol. 33, 177 (1970).
More recent reviews on cytochrome oxidase are:
 - (i) P. Nicholls and B. Chance in Molecular Mechanisms of Oxygen Activation, O. Hayaishi (Ed.) (Academic Press, New York, 1974), pp. 479ff.
 - (ii) B.F. Wilson in The Porphyrins, D. Dolphin (Ed.) (Academic Press, New York, 1975), in press.

21. D. Frost, A. Ishitani, C. McDowell, Mol. Phys. 24, 861 (1972).
22. Photoreduction of copper has recently been documented by B. Wallbank, C.E. Johnson, and I.G. Main, J. Electron Spectrosc. Relat. Phenom. 4, 263 (1974).
23. E. Margoliash and A. Schejter, Adv. Protein Chem. 21, 113 (1966).
24. H. Theorell and A. Akesson, J. Am. Chem. Soc. 63, 1812 (1941).

II. CALCULATION OF INTENSITY FROM THE X-RAY SOURCE OF THE BERKELEY IRON-FREE SPECTROMETER

Introduction

The x-ray source in the Berkeley iron-free spectrometer was designed and described by Fadley.¹ The tube was commonly operated at 12 kV and 20 mA. A modified version of this tube was able to operate at 12 kV and 30 mA. Aluminum and magnesium were the most commonly used targets. Fig. 1 shows a sketch of the geometry of the x-ray tube within the source housing.

Fadley gave no estimate of the output of this tube under operating conditions. Kramer² attempted to approximate the intensity by exposing a film badge to the x-ray flux under typical experimental conditions. He concluded that the dose absorbed by the film badge was $\sim 10^3$ rads/hr at maximum. The rad is defined as the absorption of 100 ergs of energy by one gram of tissue. In view of the damage observed to biological samples during typical experiments (see Chapter IV), it was necessary to obtain a more accurate estimate of the output from the x-ray tube and the dose absorbed by an organic sample. Kramer's estimate will have to be revised upward as a result of this work. Space limitations within the source housing of the Berkeley iron-free spectrometer would not permit convenient access of conventional detectors to the x-ray tube. A calculation of the energy and spatial distribution of x-rays from the tube based on literature values was considered adequate.

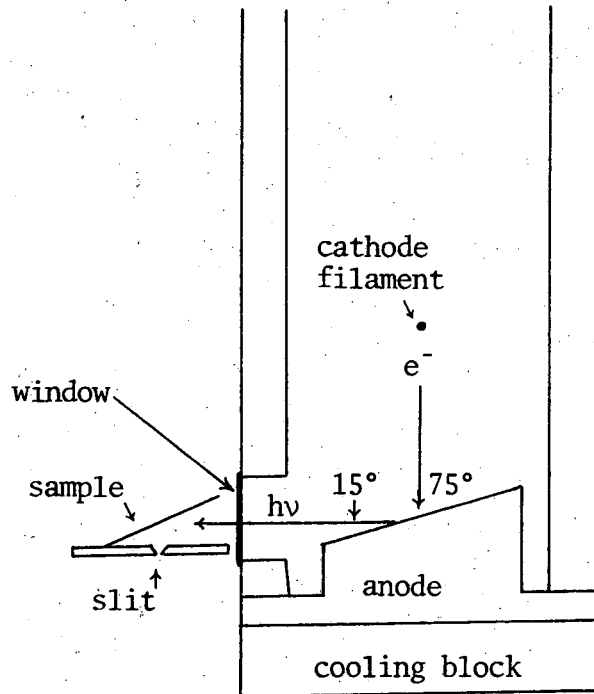


Figure 1. Schematic diagram of the x-ray tube on the Berkeley iron-free spectrometer. The radiating region of the anode is about 3.5 cm from the sample.

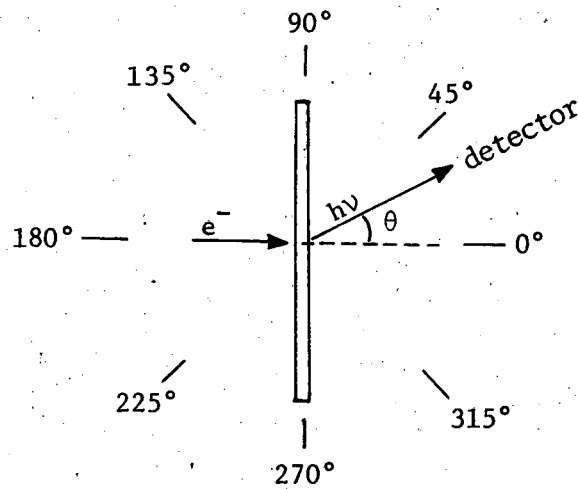


Figure 2. Schematic arrangement for measuring the spatial distribution of x-rays from a target thin enough to transmit the radiation.

X-ray production and absorption has been an active field of research since 1900. The experiments prior to 1935 have been adequately documented by Kulenkampff³ and Compton and Allison.⁴ Work through 1957 has been reviewed by Tomboulian⁵ and Stephenson.⁶ The bulk of this work was devoted to high accelerating potentials (20 - 50 keV). The targets used were often thin foils $10^2 - 10^3 \text{ \AA}$ thick with nanoampere filament currents. These conditions do not correspond to the operation of the x-ray source in the Berkeley spectrometer, but many of the principles developed in the early work still apply to XPS tubes. The theory of x-ray production and absorption has been discussed by Bethe and Salpeter.⁷ The results included in these reviews will be simply quoted here.

Since 1960 there has been an increasing amount of interest in the x-ray region directly relevant to XPS. Reports of new soft x-ray sources for XPS⁸ and other applications⁹ have not described recent soft x-ray research in detail. As this manuscript was being completed, Henke and Tester¹⁰ reported the development of an ultrasoft x-ray source for producing radiation in the $10 - 100 \text{ \AA}$ region ($\text{AlK}\alpha$ to $\text{BeK}\alpha$), and they described a flow proportional counter detector. They also report the spectral output from targets of aluminum, copper ($\text{CuL}\alpha$), oxygen (as Al_2O_3), and carbon operated at 6 - 10 kV and 20 - 30 mA. These conditions apply directly to XPS experiments.

Heinrich¹¹ has compiled an extensive bibliography of papers through the mid-sixties covering a wide variety of topics related to x-rays: production, detection, mass absorption coefficients, electron penetration,

applications, etc. For those interested in pursuing the topic, it is essential to consult Heinrich's listing.¹¹

Mass absorption coefficients have been tabulated over a wide spectral range.^{12,13} In this chapter, mass absorption coefficients according to Jönsson¹⁴ have been used. They are shown to be accurate for the micron path lengths encountered in this work, and they are conveniently derived from a graph.

An x-ray emission spectrum consists of sharp peaks characteristic of the anode material over a broad continuous background. The energy and spatial distributions and polarization of the continuous spectrum will be considered separately from the characteristic spectrum.

In the discussion that follows, a thick target will refer to an anode that is thick enough to stop the electrons incident upon it from the filament. This anode may still be thin enough to transmit the radiation produced in it. Extremely low filament currents must be used to keep from melting these targets in the absence of water cooling. The spatial distribution of x-rays from such a target is measured with respect to the forward direction as shown in Fig. 2. The spatial distribution of characteristic x-rays is measured with respect to the anode plane, which is perpendicular to the forward direction. The reader is cautioned to be aware of this 90° discrepancy between the spatial distributions of continuous and characteristic radiation.

A thin target refers to an anode that transmits all or part of the electrons from the filament. In the ideal thin target, a cathode electron

suffers only one deceleration opposite to the forward direction as it passes through the target. These targets have no practical significance; they were developed solely to test theories.

A. The Continuous X-Ray Spectrum

Energy Distribution

The most conspicuous feature of the energy distribution is the high frequency cut-off limit (Fig. 3) defined by Eq. (1).

$$E_0 = h\nu_0 = eV \quad (1)$$

e is electronic charge, V is the potential across the x-ray tube, ν_0 is the limiting cut-off frequency, E_0 is therefore, the high energy limit of photons in the continuous spectrum. Equation (1) seems obvious to students of quantum mechanics, but it was significant in the 1920's⁴ because classical electromagnetic theory completely failed to account for the high frequency limit.

In 1922, Kulenkampff³ observed the energy distribution emitted from several anodes at an angle of 90° from the direction of the incident electrons. He arrived at an empirical formula for the energy distribution which is given by Eq. (2).

$$\begin{aligned} I_\nu &= C[Z(\nu_0 - \nu) + Z^2b] & \nu \leq \nu_0 \\ &= 0 & \nu > \nu_0 \end{aligned} \quad (2)$$

ν_0 is the high frequency limit; C and b are constants, but $b \sim 0.0025$ and intensity is usually plotted versus photon energy in eV or keV.

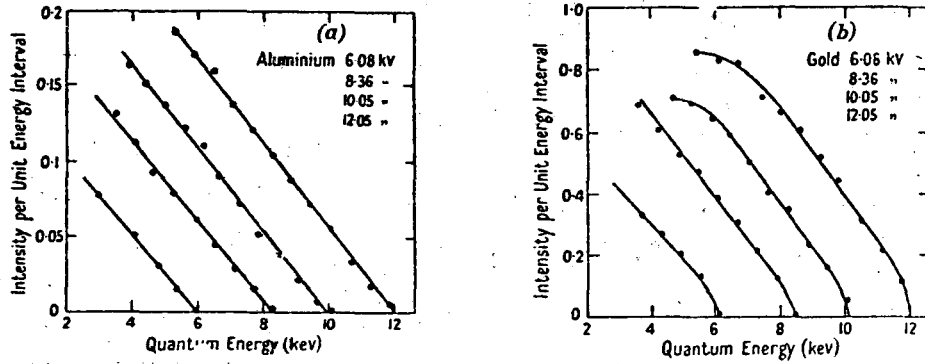


Figure 3. Intensity distribution of continuous x-ray spectrum from electron opaque targets of aluminum and gold. Intensity units are $\text{erg steradian}^{-1} \text{microcoulomb}^{-1} \text{keV}^{-1}$. Data taken in the forward direction. These data have been corrected so that they do not show the effect of target absorption.

Therefore, Eq. (2) is often approximated by Eq. (3).

$$I_E = C Z(E_0 - E) \quad E \leq E_0 \quad (3)$$

Dyson's experimental data¹⁵ experimental data illustrate these formulas as shown in Fig. 3. These data all show the high energy cut-off, E_0 , quite clearly. The distribution for aluminum (Fig. 3a) is linear to a high degree of approximation down to $0.5 E_0$. The gold data (Fig. 3b) show non-linearity near $0.5 E_0$; Kulenkampff³ observed that the intensity for aluminum was also non-linear below $0.4 E_0$, but the intensity was higher than that expected by Eq. (3). Dyson¹⁵ suggests the decrease of intensity at $0.5 E_0$ for heavy elements is due to inelastically back-scattered electrons. Figure 3b also shows non-linearity near E_0 that illustrates the effect of the second term in Eq. (2). This term depends on Z^2 , and it is much more important for gold ($Z = 79$) than aluminum ($Z = 13$). Equations (2) and (3) are seen to be valid down to $0.5 E_0$ where the observed intensities become non-linear. Little is known about the energy distribution below 3 keV except for the low voltage work described below.

The data in Fig. 3 were taken with a proportional counter (97.5% Ar, 2.5% CO₂) with a detection efficiency of 20% near photon energies of 12 keV and 100% near the K absorption edge of Ar (3.2 keV). These distributions were observed in the forward direction while Kulenkampff's formula (Eq. (2)) was determined from observations at 90°. The agreement between Eq. (2), (3), and Fig. 3 is related to the spatial distribution of continuous x-rays to be discussed in another section.

From Fig. 3 and Ref. 15, one can deduce a value of C for Eq. (3) which applies to Al, Cu, Au, and presumably many other elements, when intensity is measured in the forward direction.

$$C = \frac{2 \times 10^{-3} \text{ erg}}{\text{steradian microcoulomb (keV)}^2}$$

Green and Cosslett²⁴ found C to be 2.5×10^{-3} . This value of C in Eq. (3) yields an energy flux for I_E . Conversion to a photon flux is achieved through division by photon energy. Eq. (3) then becomes

$$I_{\text{photon}} = \frac{1 \times 10^6 \text{ photon}}{\text{steradian microcoulomb keV}} \frac{Z}{E} \frac{E_0 - E}{E} \quad E < E_0 \quad (4)$$

where E , the photon energy, is in keV. Equation (4) is plotted in Fig. 4 for $Z = 12$ and $E_0 = 12$ keV. The plot approaches infinity as E diminishes, but Eq. (4) is only applicable down to $0.4 E_0$ (4.5 keV in Fig. 4). I_{photon} must go to zero at $E = 0$, but the approach of I_{photon} to zero from $E = 0.4 E_0$ to $E = 0$ is not known. In Fig. 4, Eq. (4) has been arbitrarily extended below $0.4 E_0$; the errors involved in this extrapolation are unknown. Figure 2 may only be accurate to an order of magnitude near 1 keV.

Recent work¹⁶ using accelerating potentials of 20 - 50 keV on several anode materials showed that the energy distribution was defined more accurately by Eq. (5) than Eq. (3).

$$I \propto Z^n (E_0 - E)^{1.11} \quad 1.2 \leq n \leq 1.37 \quad (5)$$

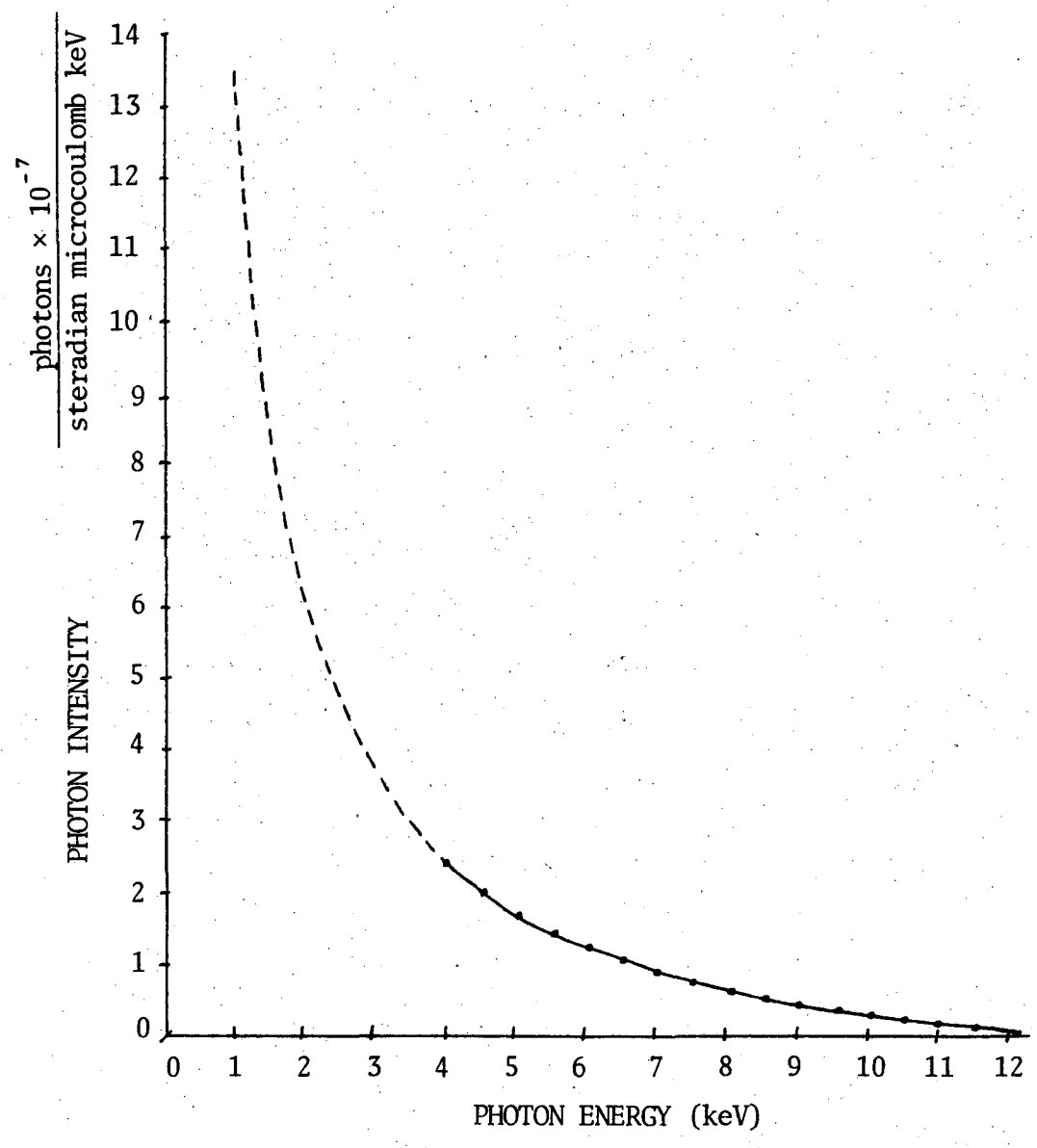


Figure 4. Distribution of continuous x-rays produced per microcoulomb in a magnesium target at an accelerating voltage of 12 kV. The effect of target absorption has not been taken into account.

The formula is valid from 50 keV to 11 keV and perhaps at lower photon energies. The validity of Eq. (5) is not known below 5 keV; although, mention was made of work done at 1.28 keV (9.671 Å).^{16a} The linearity of the results in Fig. 3 suggests that Eq. (3) is adequate for XPS experiments.

The efficiency of continuous x-ray production is defined in Eq. (6).

$$\text{Eff.} = \frac{\text{Total integrated continuous x-ray energy per unit time}}{\text{x-ray tube power}} = kV \quad (6)$$
$$k = 1.3 \times 10^{-9} \text{ volts}^{-1}$$

Efficiency has been used as the basis for comparing observed intensity distributions with one another or comparing theoretical formulas for intensity distributions with experiment. It can also be used in XPS as a quick estimate of the continuous x-ray energy produced in the anode.

Various values of k have been reported.^{4,6,15} The given value is consistent with Ref. 15. All values of k are derived by extrapolating Fig. 3 (or similar data) or Eq. (3) (or similar formulas) to zero quantum energy. For large accelerating potentials the extrapolation is reasonable because the integrated intensity at low energies, where problems occur, is small. At moderate potentials around 12 keV, where XPS sources operate, the non-linear region below $0.5 E_0$ and the unknown intensity below 3 keV represent an appreciable portion of the spectrum. In this case, the extrapolation is completely arbitrary.

The difficulties involved in the extrapolation to zero photon energy are listed in Ref. 6, Section 16 and Ref. 15, p. 934. To gain some insight into the validity of the extrapolation, some workers looked at the continuous spectrum with low accelerating potentials of 1 - 2 kV. Stephenson has described this work in Ref. 7.

Generally, the intensity distributions at low voltage began to approach the distribution for thin targets, which is quite reasonable since 1 - 2 keV electrons do not penetrate far into the anode. The approximate agreement between low voltage data and Fig. 1 suggests that the extension of Eq. (3) to low energy is reasonable.

Eq. (3) and Fig. 3 can be derived from thin target results. The intensity per unit energy interval from a thin target rises sharply at the high energy cut-off and is then constant to a high degree of approximation down to $0.5 E_0$, as shown by the data of Amrehn and Kulenkampff in Fig. 5. A thick target may be envisioned as successive laminations of thin targets. The energy of the electrons traversing the anode diminishes with each lamination. Therefore, the thick target intensity distribution can be obtained by integration of the thin target distribution multiplied by an appropriate electron energy loss function. The method of integration is illustrated in Fig. 6. A detailed example is given in Ref. 16.

Spatial Distribution

A schematic arrangement for measuring the spatial distribution of continuous x-radiation is shown in Fig. 2. The plane of the target lies

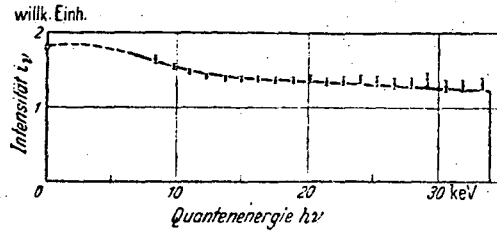
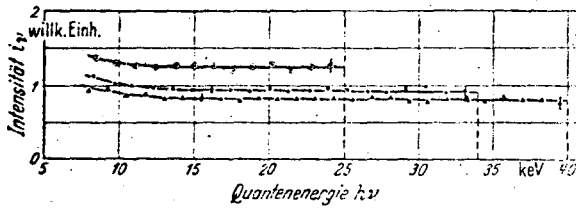


Figure 5. (a) Data by Amrehn and Kulenkampff. The continuous x-ray energy distribution from aluminum foil 255 - 325 Å thick at 34 kV. Solid line represents Sommerfeld's theory.



(b) Data by Amrehn and Kulenkampff. Continuous x-ray distributions from aluminum foil 225 - 325 Å thick at 25, 34, and 40 kV.

perpendicular to the paper along the $90^\circ - 270^\circ$ line. The incident electrons approach from the left along the $180^\circ - 0^\circ$ line. 0° is called the forward direction. All angles are measured with respect to the forward direction. If measurements are to be made in the forward hemisphere, the target must be thin enough to transmit the x-rays produced in it. Therefore, the cathode current must be small enough to prevent the target from melting without water cooling. (It will be seen that the polar diagram in Fig. 2 is rotated 90° with respect to similar diagrams showing the spatial distribution of characteristic x-rays.)

Honerjager's results¹⁹ from -5° to 200° are shown in Fig. 7 and 8. The targets are aluminum foils 6000 \AA , 350 \AA , and 100 \AA thick. They are supported on a thin celluloid backing. The accelerating potential was 34 kV, and the radiation was filtered through the equivalent of 4.5 mm of aluminum. Thus, these data represent only the high energy portion of the spectral distribution. The theoretical predictions of Sommerfeld⁷ have replaced Sherzer's theory shown in Figs. 7, 8. The salient features shown in Honerjager's data are: the two lobes of intensity that are symmetric across the $180^\circ - 0^\circ$ line, the maximum near 54° , the finite intensity in the forward direction for all the foils, and the zero intensity at 180° for the thinnest foils.

Coslett²⁰ and Dyson^{15,20} measured the spatial distribution of continuous x-rays from thick targets of aluminum, gold, copper, and beryllium. The targets were thick enough to stop the incident electrons but thin enough to transmit the resulting x-rays. The cathode electrons were focussed by

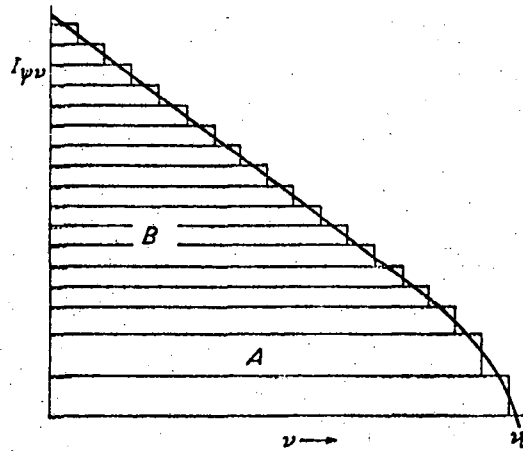


Figure 6. Formulation of a thick target spectrum from consecutive thin target spectra.

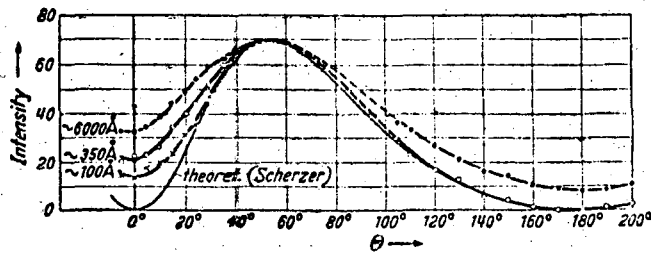


Figure 7. Data by Honerjager. Spatial distributions of hard continuous x-rays from thin aluminum targets (34 kV) shown with a theoretical prediction.

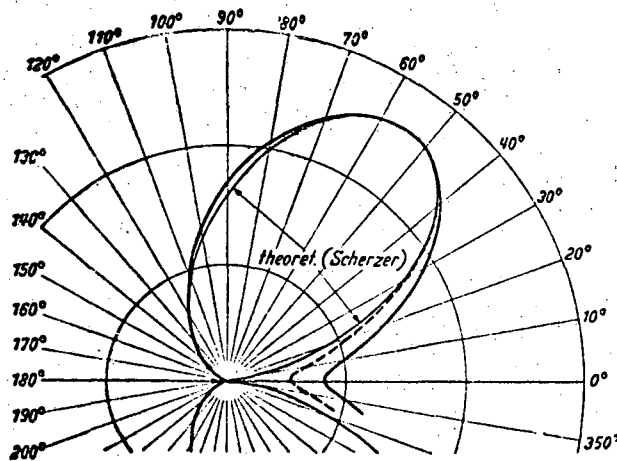


Figure 8. Same data as Figure 7 plotted on a polar diagram.

a magnetic lens to a 70 micron spot. The measurements were taken in the forward hemisphere from 0° to about 70° . The aluminum targets were commercial foils of thickness 0.78 mg/cm^2 (2.9 microns).

The distributions resulting from accelerating potentials of 10 and 12 kV are shown in Fig. 9. For these thick targets, the distinct, asymmetric lobes of Fig. 8 have broadened and merged into a roughly symmetric distribution. The intensity is isotropic within 60% at the higher energies and completely isotropic below $0.4 E_0$, at least in the forward direction.

The question of the angular distribution of soft x-rays (less than 10 keV) in the reverse hemisphere ($90^\circ - 270^\circ$) remains open. Experiment and calculations by Rao-Sahib and Wittry¹⁶ imply that continuous radiation is isotropic below $0.5 E_0$. As early as 1935, Compton and Allison expected the low energy radiation from a thick target to be isotropic (Ref. 4, p. 97); although there was no data to substantiate their claim.

The data still do not exist, but there are three facts on which to base a reasonable estimate. First, theory predicts that, for a thin target, the radiation becomes isotropic near the low energy end of the spectrum. This phenomenon is shown in Fig. 10 where Coslett and Dyson²⁰ calculated the thin film energy distribution at $V = 10 \text{ kV}$ for $Z = 16$ and 58. The curves represent observation angles of 0° , 90° and the average overall angles. It can be seen that near 2 keV, the three curves converge; the radiation becomes isotropic.

Second, Fig. 7 shows that a medium thickness film (6000 \AA) of aluminum has a spatial distribution that is asymmetric with a maximum near 60° , but

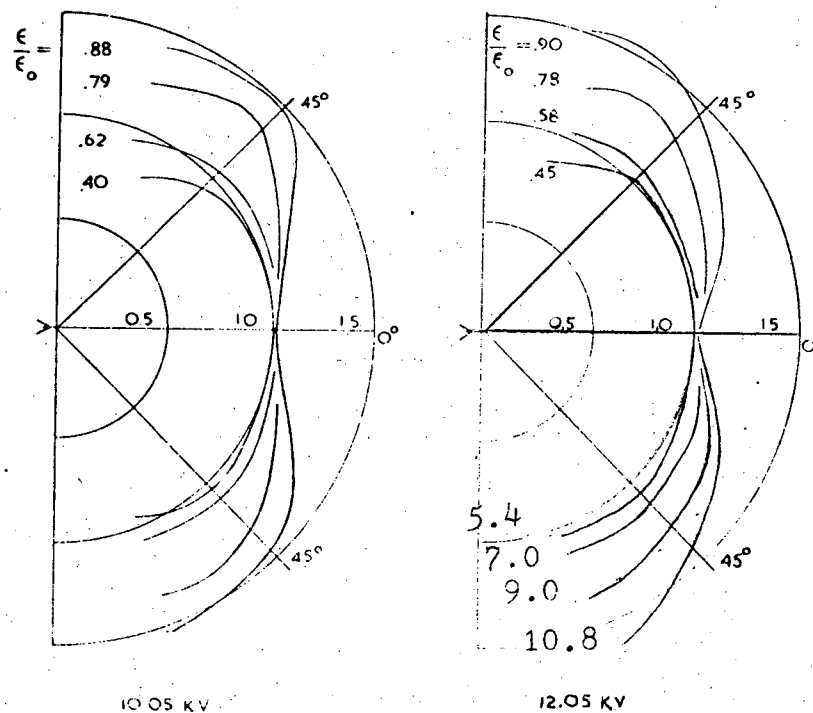


Figure 9. Data by Coslett and Dyson (Ref. 20). Angular distribution of continuous radiation from a thick (2.9 microns) aluminum target. Upper quadrant: as observed. Lower quadrant: corrected for target absorption.

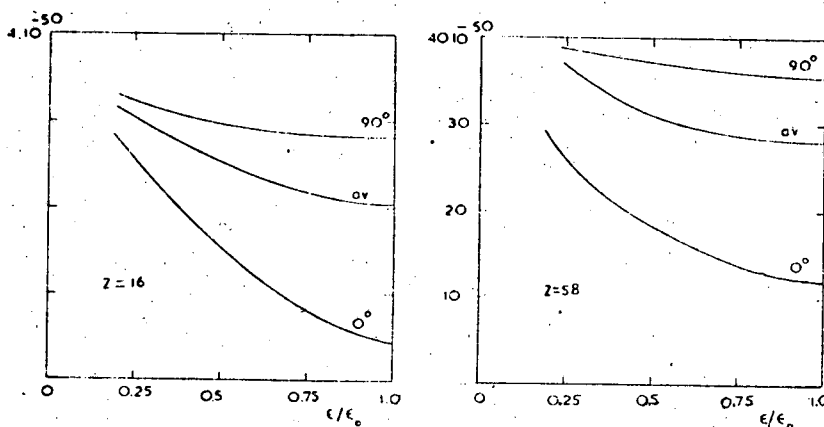


Figure 10. Energy distribution for thin targets calculated according to Kirkpatrick and Wiedmann (Ref. 18) at 0°, 90°, and averaged over all angles. Accelerating voltage = 10 kV. Units are erg steradian⁻¹ unit frequency interval⁻¹ electron⁻¹ (atom per cm²)⁻¹.

it also has an enhanced intensity at 0° and non-zero intensity at 180° . The 6000 Å film, therefore, gives a more isotropic distribution than the thin films.

Third, the thick targets in Fig. 9 show some asymmetry for the high energy photons, but the lower energy components are isotropic.

The three considerations given above imply that the spatial distribution becomes more isotropic: (i) as the target becomes thicker, and (ii) as the radiation becomes softer. These trends reflect the scattering of bombarding electrons within the anode. In an ideal thin target, the electrons suffer only one deceleration in a straight line along the forward direction. In a thick target, the electrons are deflected in many directions, and the symmetry of the thin target distribution averages out. Dyson¹⁵ has considered the scattering conditions in an aluminum target where $V = 10$ kV. He found that at a depth of 1200 Å, the electrons had experienced so many collisions that they were on the verge of diffusion, i.e., their directions were randomized. Trend (i) follows directly from scattering considerations. Trend (ii) can also be understood in terms of scattering because the softer radiation components are produced deeper in the target where diffusion has taken place.

Therefore, in a thick aluminum target operated at 12 kV, it is reasonable to assume that the radiation near E_0 will show some asymmetry in the forward direction; but the softer components below $0.5 E_0$ will be isotropic.

Polarization

The polarization of continuous x-rays has been discussed adequately elsewhere.^{4,6,18,21} A short statement will be presented here.

If an incident electron is decelerated in a straight line along the forward direction, classical electromagnetic theory provides that all the resulting x-rays will be plane polarized parallel to the forward direction. Quantum theories¹⁸ predict less than complete polarization, even at the high energy limit. Experimental work has concentrated on thin targets for comparison with theory, Kulenkampff's²¹ results on a 280 Å aluminum foil at 34 kV are shown in Fig. 11. The polarization ratio on the vertical scale is given by $p = (N_{\parallel} - N_{\perp}) / (N_{\parallel} + N_{\perp})$, where N refers to photon counts registered parallel and perpendicular to the forward direction. The data show good agreement with wave-mechanical theory. The theoretical variation of polarization with θ (see Fig. 2) is given in Ref. 18.

The only available thick target data are the earliest measurements. In a thick target, the directions of the incident electrons became randomized by collisions; therefore, polarization is expected to become smaller as target thickness increases. Dasannacharya⁴ confirmed this trend. Many workers⁴ found that even at the high energy limit, where polarization is maximum, the observed polarization was only 10 - 50% in thick targets.

In XPS tubes, it is probable that some polarization could be observed near E_0 , but not below $0.5 E_0$.

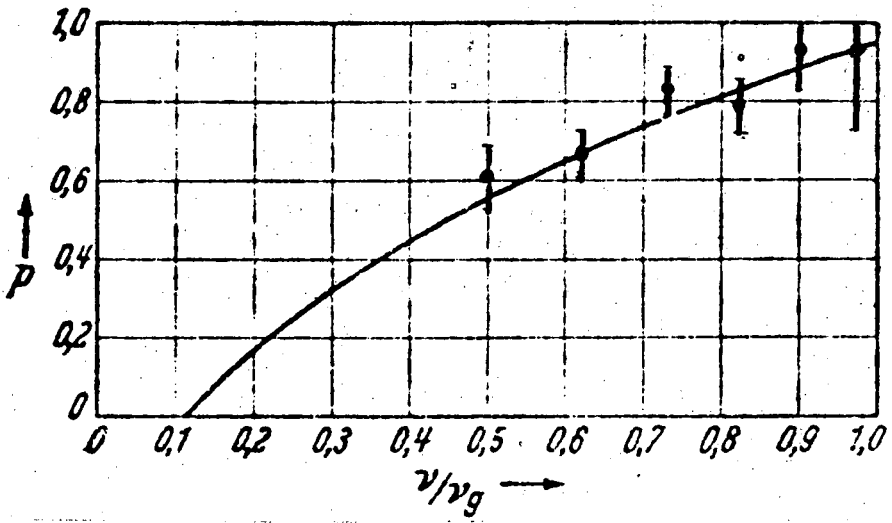


Figure 11. Data by Kulenkampff et al. Polarization of continuous x-rays from a 280 Å aluminum target at 34 kV. The solid curve represents Sommerfeld's wave mechanical theory.

B. Characteristic X-Rays

Spatial Distribution

Characteristic x-rays are produced when a cathode electron ejects an electron from an inner shell of one of the target atoms. The atom fills this inner hole with an electron from a higher orbital, and in some cases, ejects a photon. This process is known as direct production of characteristic radiation. The inner hole in the target atom can also be created by photoelectric absorption of continuous x-rays which results in the indirect production of characteristic radiation. Numerous experiments have been done to determine the amount of indirect radiation produced. The earliest experiments are described by Compton and Allison.⁴ Green (Ref. 23, Fig. 9; Ref. 24, Fig. 6) summarizes the results of these experiments, and gives an empirical expression for P_K , the ratio of direct K radiation to indirect K radiation, as a function of Z .

$$P_K Z^4 = 9.4 \times 10^6$$

This expression was fit to data for K emission through $Z = 79$. For an aluminum target ($Z = 13$), $P_K = 340$; therefore, direct production accounts for more than 99% of the characteristic K radiation. For copper ($Z = 29$), $P_K = 14$; direct production still accounts for 93% of the total. As a general rule, indirect production of K radiation is not significant for $Z < 30$. Indirect L radiation seems insignificant for $Z < 70$. Since almost all work in XPS is done with targets of $Z < 30$,

indirect production of characteristic radiation is not relevant to problems in XPS. Further information can be found in work by Green²⁴ and Hink.²⁵

It will be seen that the intensity of characteristic x-rays is a function of the take-off angle from the anode surface. This spatial distribution is, in turn, dependent on the depth at which the x-rays are produced. Therefore, the depth distribution of characteristic radiation has been studied extensively. Shimizu et al.²⁶ and Bishop²⁷ have made theoretical calculations of the radiation produced as a function of depth. Castaing and Descamps²⁸ used traces of Zn in a Cu anode at an accelerating voltage of 29 kV to measure the depth distribution experimentally. Schmitz et al.²⁹ made a similar measurement using a Cu wedge on a Ni target and accelerating voltages of 30, 25.5, and 28 kV. The results of these calculations and experiments are plotted together in Schmitz's article. The theoretical and experimental distributions agree quite well; they all rise quickly to a peak at about 0.5 μ (Cu target, 30 kV) and then drop off quickly to zero. Schmitz reports values of z_{95} , the depth at which 95% of the characteristic radiation has been excited. For $\text{CuK}\alpha$ from a Cu target and accelerating voltage of 30, 25, 5, and 20 kV, z_{95} equals 1.55, 1.30, and 0.90 μ , respectively. The value of z_{95} appears to be relatively independent of the current from the cathode to the anode. (See Table I, Ref. 31).

One can reduce the depth distribution to its simplest form by considering all of the radiation to be produced at some average depth. Hanson and Salem³⁰ called this depth the effective depth; they calculated values

for the effective depth of $\text{CuK}\alpha$ production in a Cu target as a function of accelerating voltage from 10 kV to 30 kV. At 30 kV (Cu target) they report an effective depth of 0.88μ . This value seems somewhat large when compared to the distribution shown in Schmitz's article. The effective depth was found to have a linear dependence on the accelerating voltage.

Using a model similar to the effective depth, Green²⁴ considered all the characteristic radiation to be produced at a point at a depth \bar{z} below the surface of the anode. He measured the mean depth of production of $\text{CuK}\alpha$ in a Cu target at accelerating voltage from 12 to 50 kV. At 30 kV (Cu target) he found the mean depth to be about 0.62μ . (See Fig. 7, Ref. 27.) This value was found to be in good agreement with a mean depth calculated from the depth distribution measured by Castaing and Descamps. Green also found that the mean depth was a linear function of the accelerating voltage, and it is proportional to $(E_0 - E_K)$, where E_0 is the accelerating voltage and E_K is the energy of the K-shell of the target atom.

The mean depth of characteristic production would also be expected to vary with the atomic number, Z , of the target, i.e., one should be able to write (Eq. (10), Ref. 24):

$$\rho \bar{z} = G(Z) (E_0 - E_K)$$

where $G(Z)$ is some function of Z . However, Green observed that $G(Z)$ is nearly constant over a range of Z from 6 to at least 30 for the same E_0 and $E_0 \gg E_K$, $\rho \bar{z}$ is approximately proportional to $E_0 - E_K$ and independent of Z . To account for this observation, Green suggests two opposing

processes that cancel each other. First, electrons strike the target and travel essentially undeviated to a depth where scattering events have randomized the electron paths. Green calls this depth z_{diff} , the depth where complete diffusion occurs. No value of z_{diff} was given; so, no comparison is possible with Dyson's diffusion depth of 1200 - 2400 Å (10 keV in Al) described in the spatial distribution of continuous radiation. Once the electrons reach z_{diff} they complete their paths through the target by a second process, a random walk, until they come to rest. For targets of high Z , the depth z_{diff} is small compared to low Z targets, but the total length of the random walk is longer. These two effects almost cancel each other, and the mean depth of x-ray production is, therefore, nearly independent of Z . There is some experimental evidence that is consistent with this model. For more details, one should consult Green's article.²⁴

Since $\rho \bar{z}$ depends mostly on $E_0 - E_K$, the data for Cu can be applied to aluminum and other elements. From Green's Cu data, $G(Z)$ can be estimated at $(2.0 \pm 0.8) \times 10^{-5} \text{ cm}^2/\text{g keV}$. The correspondence mean depth of $K\alpha$ production in aluminum at 12 keV is 0.8 ± 0.3 microns. The success of the concept of a mean depth is attributed to the strong peak in the measured distributions of $K\alpha$ production depths.²⁹

The intensity of characteristic radiation has been measured as a function of take-off angle θ from the target surface.^{23,24} The spatial distribution is described (using the same notation as Green) in terms of $N K\alpha(\theta)/4\pi$, the number of $K\alpha$ photons observed per steradian per electron an angle θ to the target surface. $N K\alpha/4\pi$ refers to the photons generated

per steradian per electron. Characteristic radiation is generated isotropically within the target, so $N K\alpha/4\pi$ has no dependence on θ . These photons, however, are attenuated as they travel to the surface of the target where they can be observed. This attenuation is a function of the depth at which the photons were generated and the angle θ at which they are observed, $N K\alpha(\theta)/4\pi$ is, therefore, given by (Eq. (1), Ref. 24)

$$\frac{N K\alpha(\theta)}{4\pi} = \frac{1}{4\pi} \int_0^{\infty} \frac{dN K\alpha}{dz} \exp\left(-\frac{\mu_{K\alpha}}{\rho} \rho z \csc\theta\right) dz \quad (7)$$

where z is the depth in the target and $\mu_{K\alpha}$ is the absorption coefficient for the $K\alpha$ radiation, and ρ is the density of the target material. Using the simple model discussed above where all the radiation is generated at a point within the target at a depth \bar{z} below the surface, Eq. (7) reduces to

$$\frac{N K\alpha(\theta)}{4\pi} = \frac{N K\alpha}{4\pi} \exp\left(-\frac{\mu_{K\alpha}}{\rho} \rho \bar{z} \csc\theta\right) . \quad (8)$$

Of the photons generated within the target, only a certain fraction of them, $f(\chi)$, are observed at the surface. $f(\chi)$ is the ratio of observed to generated radiation.

$$f(\chi) = \frac{N K\alpha(\theta)}{N K\alpha} = \exp(-\chi \rho \bar{z}) \quad (9)$$

where

$$\chi = \frac{\mu_{K\alpha}}{\rho} \csc\theta .$$

$f(\chi)$ must be a function of the accelerating voltage because it depends on \bar{z} . Green^{23,24} has made experimental measurements of $f(\chi)$ for $K\alpha$ radiation targets of carbon, aluminum, titanium, iron, copper, germanium, molybdenum, and for $L\alpha$ radiation in neodymium, tantalum, and for the $M\alpha$ of gold. The results are plotted as $f(\chi)$ and $-\ln f(\chi)$ for various accelerating voltages as a function of $\csc\theta$.²³ The target may be a mixture of elements, e.g., 3% Al in 97% Mg. To determine the spatial distribution of $AlK\alpha$ from this target, one needs $f(\chi)$ plotted against χ to account for the absorption of Al x-rays in the Mg anode. For these applications, $f(\chi)$ and $-\ln f(\chi)$ are also plotted vs. χ . Elsewhere,²⁴ $f(\chi)$ is plotted for several take-off angles as a function of accelerating voltage. Since \bar{z} was found to be nearly independent of Z , the atomic number of the target atom, it was possible to plot universal curves of $f(\chi)$ vs. χ which apply to $5 \leq Z \leq 30$ for several accelerating voltages.^{23,24} From these universal plots, one can derive the spatial distribution of characteristic radiation from almost any light element in a target of pure or mixed composition.

Using Green's data (Fig. 10, Ref. 24), polar graphs have been made of $f(\chi)$ vs. take-off angle θ for $AlK\alpha$ radiation from a pure Al target. See Fig. 12. The distributions are given for accelerating voltages of 6 kV and 12 kV. In both cases, the electron beam was normal to the target surface, i.e., $\gamma = 90^\circ$ as shown in Fig. 14. The plots show that $f(\chi)$ at 6 kV is greater than corresponding values of $f(\chi)$ at 12 kV. This does not mean that an electron accelerated to 6 keV excites more radiation

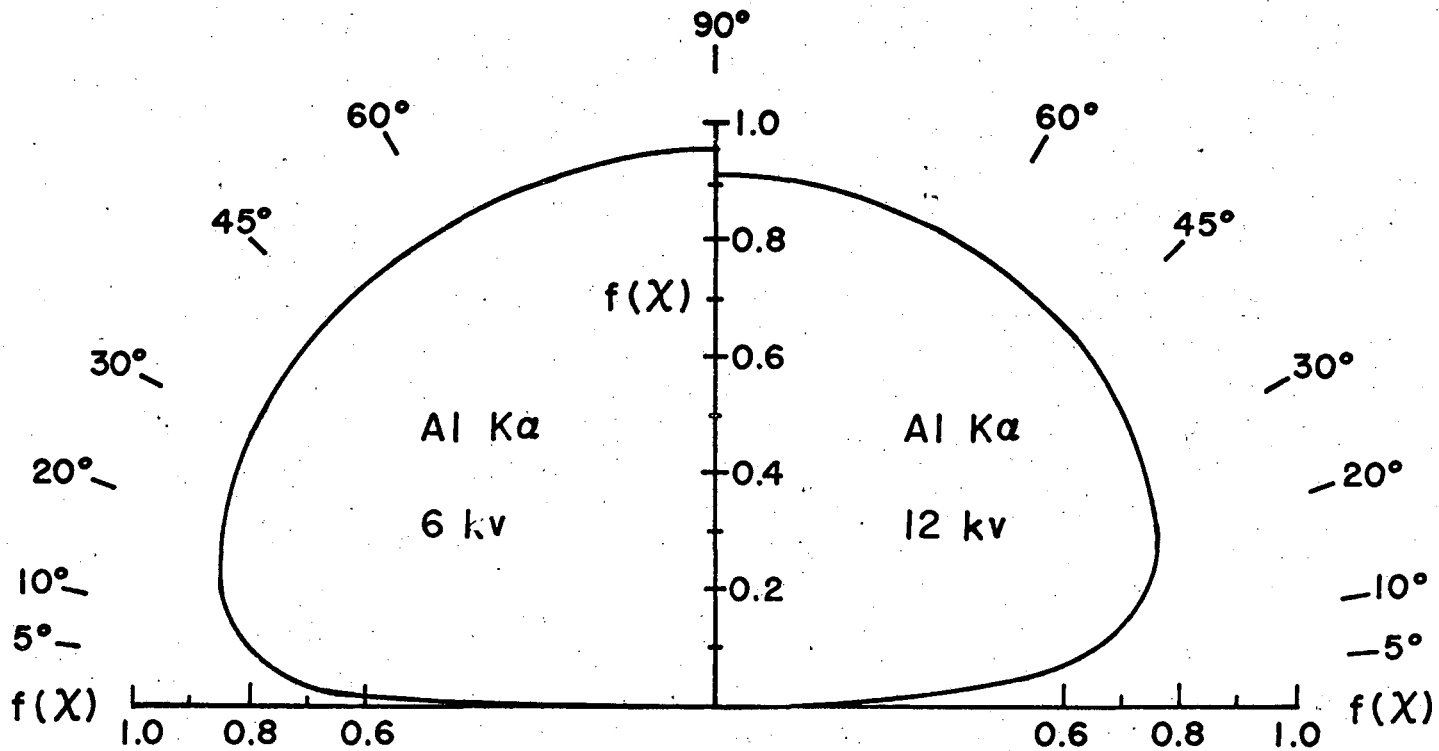


Figure 12. Spatial distribution of characteristic aluminum radiation from a pure aluminum target. Data taken from plots by Green (Ref. 24). For both cases, incident electrons strike the target normal to the surface.

XBL753-5134

than a 12 keV electron because the graphs show $f(\chi)$ vs. θ and not absolute intensity. Recall that $f(\chi)$ is the fraction of generated photons that are actually observed. It will be seen later that a 12 keV electron generates greater intensity than a 6 keV electron, but since the 12 keV electron penetrates deeper into the target, a greater fraction of the photons it generated will be absorbed by the target material, and consequently, $f(\chi)$ at 12 kV is less than $f(\chi)$ at 6 kV. Maximum intensity is found at $\theta = 90^\circ$. At this angle, the photons travel the least distance through the target to reach the surface. Attenuation by target absorption is, therefore, a minimum. It is also observed that $f(\chi)$ is always less than unity, even at the maximum intensity. Photons generated at any finite depth in the target will suffer some attenuation on the way to the surface even at $\theta = 90^\circ$, but $f(\chi)$ for K radiation approaches unity as the accelerating potential E approaches E_K , the energy of the K shell. When $E = E_K$, there is virtually no penetration into the target, and target absorption is effectively zero. In this case, the spatial distribution would be spherical.

At 6 kV, the distribution is nearly spherical from 90° to 20° . Within this range, one observes between 90% to 96% of the photons generated at a given angle. Most commercial tubes employ a take-off angle of about 10° . At $\theta = 10^\circ$ on the 6 kV curve, $f(\chi) = 0.86$; there is relatively little target absorption even at this shallow angle. The 12 kV curve is more distorted. It is approximately spherical from $90^\circ - 50^\circ$; at $\theta = 10^\circ$, $f(\chi) = 0.69$.

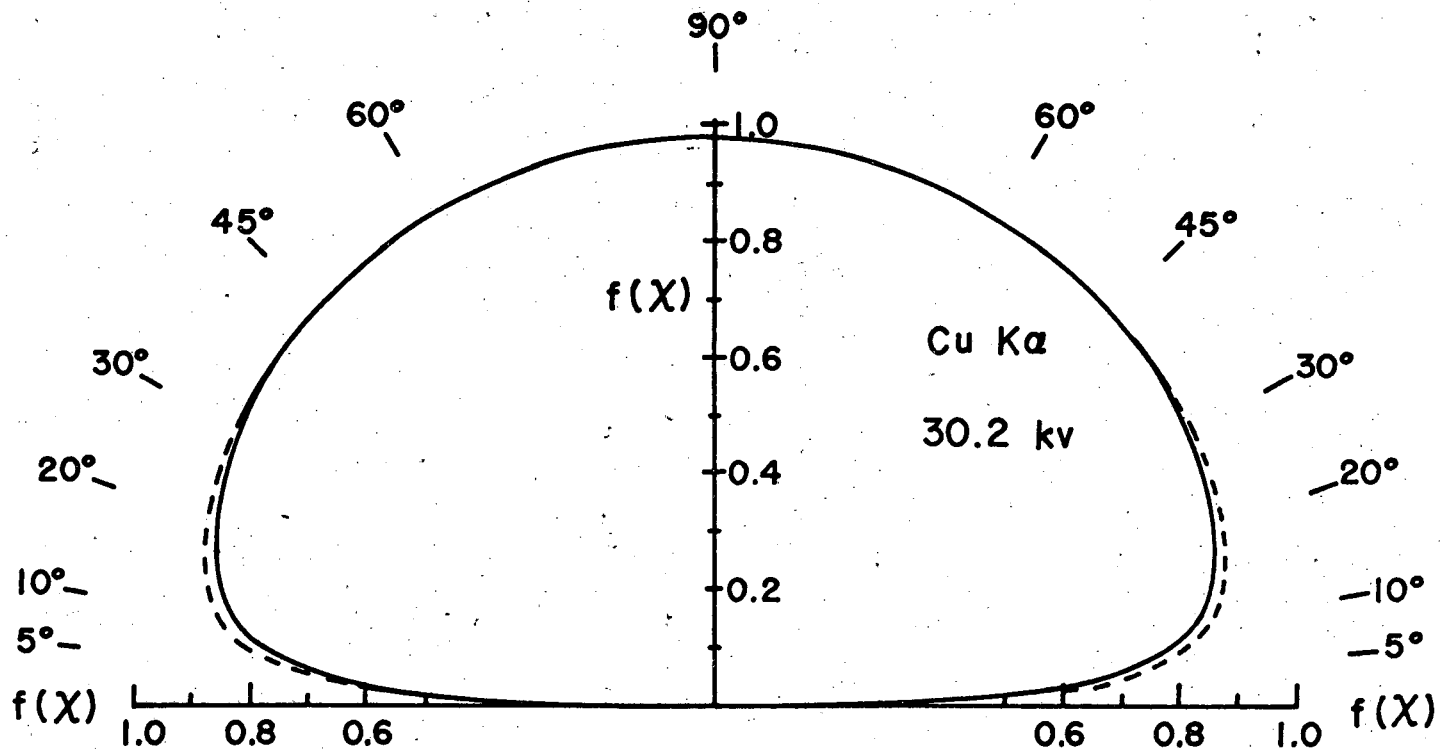


Figure 13. Spatial distribution of characteristic copper radiation from a pure copper target with the incident electron beam at $\gamma = 45^\circ$ (dashed curve) and $\gamma = 90^\circ$ (solid curve). Data taken from plots by Green (Ref. 24). Accelerating potential is 30.2 kV. The angle γ is defined in Fig. 14.

XBL753-5/35

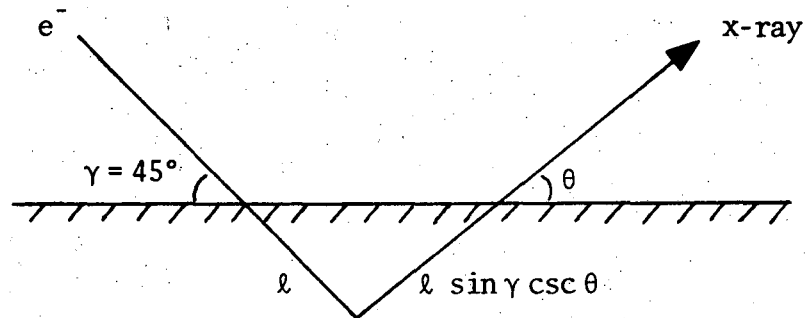


Figure 14. An electron beam makes an angle of $\gamma = 45^\circ$ with the target surface. Electrons incident at $\gamma = 90^\circ$ would travel the same distance through the target, but the direction would be straight down.

The effect of γ , the angle made by the incident electrons on the target is suggested in Fig. 13. These data were also taken from Green's plots (Fig. 18, Ref. 24). In Fig. 13 the spatial distribution of $\text{CuK}\alpha$ radiation is shown for an electron beam accelerated to 30.2 kV and striking the target at angles of $\gamma = 90^\circ$ and $\gamma = 45^\circ$. There is not much difference between the two curves. $f(\chi)_{45}$ exceeds $f(\chi)_{90}$ by about 10% at $\theta = 3^\circ$; this is the greatest deviation. It is significant that $f(\chi)_{45}$ is always greater than or equal to $f(\chi)_{90}$. Apparently, the electrons at $\gamma = 45^\circ$ travel the same distance, ℓ , through the target material as those incident at 90° , but due to their oblique entrance angle, the 45° electrons remain closer to the surface. (See Fig. 14).

It must be noted that as γ becomes smaller, increasing numbers of incident electrons are expected to reflect off of, or backscatter from, the target surface. It is unlikely that the reducing γ will dramatically increase characteristic production. Green had plotted $f(\chi)$ vs. $\text{csc}\theta$ when the incident electron beam was normal to the target. It was suggested that the $f(\chi)$ curves would lie along the same curve if they were plotted against $\sin\gamma\text{csc}\theta$ (see Fig. 17). No such simple relation was found. There are data in Shirai's paper³¹ which generally agree with Green's results.

Energy Distribution

The intensity of characteristic x-rays generated per electron has been studied by several workers since 1947. This work has covered the

$K\alpha$ radiation from Be, B, C, and many other light elements up to Ag. Green and Cosslett²² give references to these measurements and summarize the results. Compton and Allison⁴ give references to the early work, done before 1935; this work showed that the photon intensity of characteristic radiation was proportional to $\left(\frac{E_0 - E_X}{E_X}\right)^n$, where E_X is the energy of the X shell in the target atom. In terms of the variable $U_0 = E_0/E_X$, $I \propto (U_0 - 1)^n$. Compton and Allison quote a value of $n = 1.65$ as the most reliable.

Green and Cosslett²² have reported characteristic production efficiency as $N/4\pi$, which is the number of characteristic quanta generated per steradian per electron. These authors plotted $\log(N/4\pi)$ vs $\log(U_0 - 1)$ from $U_0 \cong 0.01$ up to $U_0 = 35$ for several targets from $Z = 6$ to 79. The resulting graphs were all straight lines with a slope of 1.63. For a few elements, e.g., Al, some non-linearity was observed for $U_0 > 10$, or less. These plots confirm that intensity is proportional to $(U_0 - 1)^n$ with $n = 1.63$; so, one may write

$$\frac{N}{4\pi} = \frac{M}{4\pi} (U_0 - 1)^{1.63} \quad (10)$$

where M is the constant of proportionality. The value of the exponent $n = 1.63$ is consistent with $n = 1.65$ quoted by Compton and Allison. More recent work summarized in Ref. 22 yielded values of $n = 0.94$, 1.38, and 1.60. The lower values of n were made for $U_0 > 10$ where non-linearity in $\log(N/4\pi)$ vs. $\log(U_0 - 1)$ reduces the slope; $n = 1.60$

was found for $1.9 < U_0 < 6$ which is within the region where Eq. (10) is valid.

Equation (10) can be rewritten as

$$\frac{N}{4\pi} = \frac{N'}{4\pi} (E_0 - E_X)^{1.63} \quad (11)$$

where $N' = M/(E_X^{1.63})$; E_0 and E_X are in keV. Values of N' , E_K , and M are given in Table I for several light elements. The entries for N' were taken from a plot of N' vs. Z (Fig. 8, Ref. 22). Values of $M/4\pi$ for Al and Cu were taken from column six of the table in Ref. 22. (There is an apparent error in Ref. 22; column six of the table should be labeled $\mathcal{N}/4\pi$ instead of just \mathcal{N}). $M/4\pi$ for carbon was taken from a plot of $\log N/4\pi$ vs. $\log(U_0 - 1)$ (Fig. 4, Ref. 22); $\log(N/4\pi) = \log(M/4\pi)$ when $\log(U_0 - 1) = 0$. To be sure that all the entries were self-consistent, a value for N' was calculated from $M/4\pi$ and E_K according to Eq. (11). N' (calc.) agrees to one significant figure with the corresponding values of N' taken from Fig. 8 in Ref. 22. This agreement shows that the entries are consistent with one another and indicates that the graph of N' vs. Z can be read with an accuracy of only one significant figure.

The graph of N' vs. Z , from which the values of N' were taken, was made with data from solid targets of pure elements. A value of N' for $Z = 10$ was taken from this graph and included in Table I even though a "solid" target of pure neon is obviously hypothetical. The other solid targets have about 6×10^{22} atoms per cm^3 . The neon gas pressure corresponding to this density is about 2500 atmospheres at 25°C , another

Table I. Values of N' and $M/4\pi$ for calculating characteristic x-ray production efficiency.

Z	1 N'	2 E_K (keV)	3 $M/4\pi$	4 N' (calc.)
6	2.0×10^{-4}	0.284	2.8×10^{-6}	2.7×10^{-4}
10	1.4×10^{-4} *	0.867		
11	1.2×10^{-4}	1.072		
12	1.1×10^{-4}	1.305		
13	9.5×10^{-5}	1.560	1.4×10^{-5}	8.5×10^{-5}
29	2.2×10^{-5}	8.979	6.4×10^{-5}	2.3×10^{-5}

1. Obtained by inspection from graph in Fig. 8, Ref. 22, to be used in Eq. (11), $N/4\pi = (N'/4\pi)(E_0 - E_X)^{1.63}$. These entries are only accurate to one significant figure. See footnote 4.
 2. Taken from Appendix 1 of K. Siegbahn, et al., ESCA -- Atomic, Molecular, and Solid State Structure Studied by Means of Electron Spectroscopy (Almqvist and Wiksells AB, Stockholm, Sweden, 1967).
 3. Obtained by inspection from Fig. 4, Ref. 22 or taken from the Table in Ref. 22. To be used in Eq. (10), $N/4\pi = M/4\pi(U_0 - 1)^{1.63}$. Column six of the table in Ref. 22 should be labeled $M/4\pi$.
 4. Values of N' calculated according to $N' = 4\pi/E_K^{1.63}(M/4\pi)$. The values agree to one significant figure with the values in the first column. This result indicates that the entries in the table are self-consistent and that one's ability to read values of N' from the graph in Fig. 8 of Ref. 22 is limited to one significant figure.
- * This is a hypothetical value for neon. See text.

hypothetical quantity. Although the meaning of N' for neon is somewhat questionable, it may be useful if it is scaled down according to the number of neon atoms per cm^3 in a practical application.

C. Mass Absorption Coefficients

The theory of x-ray absorption has been described in detail by Bethe and Salpeter.⁷ In addition to Ref. 12 and 13, Heinrich lists several sources of mass absorption coefficients. The mass absorption coefficients used in this chapter are those described by Sandstrom.³¹

X-rays are absorbed according to the usual exponential law,

$$I = I_0 \exp(-\mu d) = \sigma + \tau \quad (12)$$

where μ , the total mass absorption coefficient, can be separated into two components, σ and τ . σ represents x-ray absorption due to scattering; σ is only significant at short wavelengths. To a good approximation,

$$\frac{\sigma}{\rho} = 0.20 \text{ cm}^2/\text{g} \quad (13)$$

where ρ is the density of the absorbing material.

τ represents x-ray absorption due to the photoelectric effect. Jönsson³¹ developed empirical expressions for τ that are convenient to use and sufficiently accurate for the applications described later.

$$\begin{aligned}
 \frac{\tau}{\rho} &= \frac{Z}{A} (\tau_e L)_K && K < E \\
 &= \frac{Z}{A} (\tau_e L)_K \frac{L_I}{K} && L_I < E < K \\
 &= \frac{Z}{A} (\tau_e L)_K \frac{M_I}{K} && M_I < E < L_{III}
 \end{aligned}
 \tag{14}$$

where Z is atomic number, A is atomic weight, L is Avogadro's number, K , L_I , M_I are energies of atomic levels, and $(\tau_e L)_K$ is expressed as a function of $Z\lambda$. λ is the wavelength of radiation being absorbed.

To test the accuracy of Jönsson's coefficients, a comparison was made with coefficients measured experimentally by Andrews.³¹ Plots were constructed of % transmission through a one micron thickness of aluminum using the coefficients of Andrews and Jönsson. The results are shown in Fig. 16. The agreement between the two sets of coefficients is generally good over the energy region measured. During the construction of Fig. 16, it could be seen that the coefficients derived from Jönsson's plot (Fig. 15) underestimated Andrews' coefficients, and appreciable differences would have been observed in Fig. 16 if a thickness of several microns were used. Thus, the mass absorption coefficients from Eq. (14) and Fig. 15 are only accurate for short path lengths of absorption. The applications described in this chapter employ path lengths of a few microns or less.

Absorption through various thicknesses of beryllium and aluminum are shown in Fig. 17 (Fig. 6 from Ref. 31).

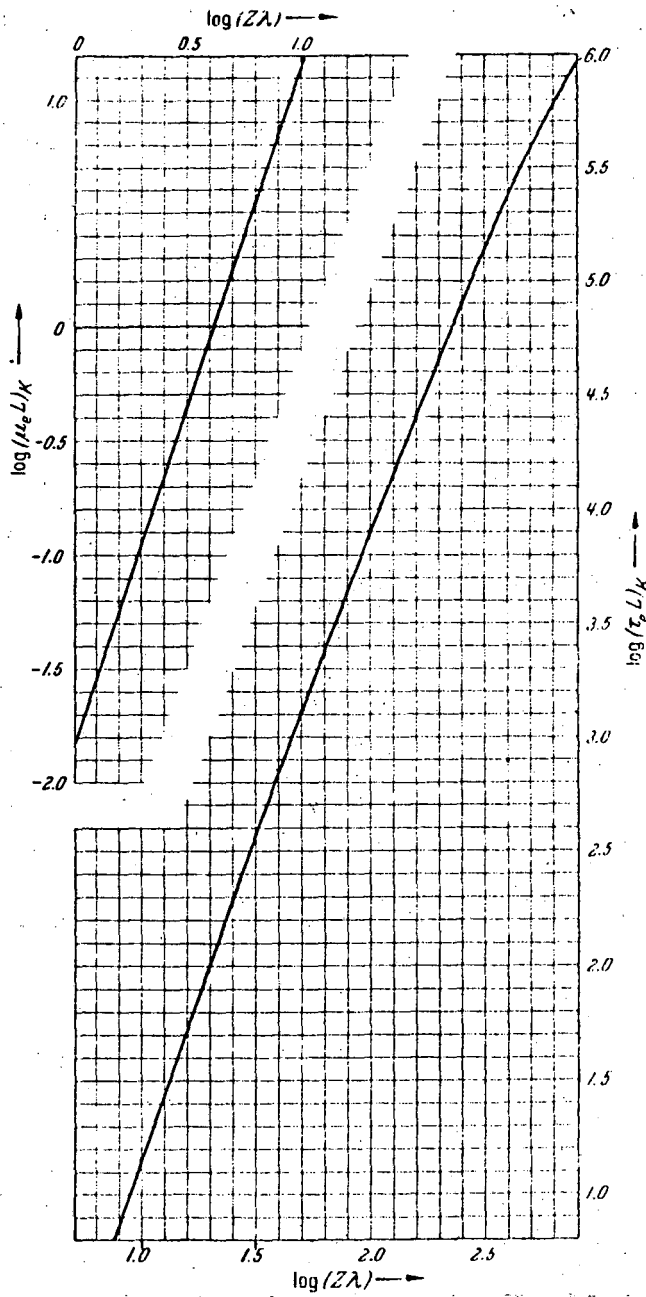


Figure 15. Jönsson's graph for the empirical derivation of mass absorption coefficients.

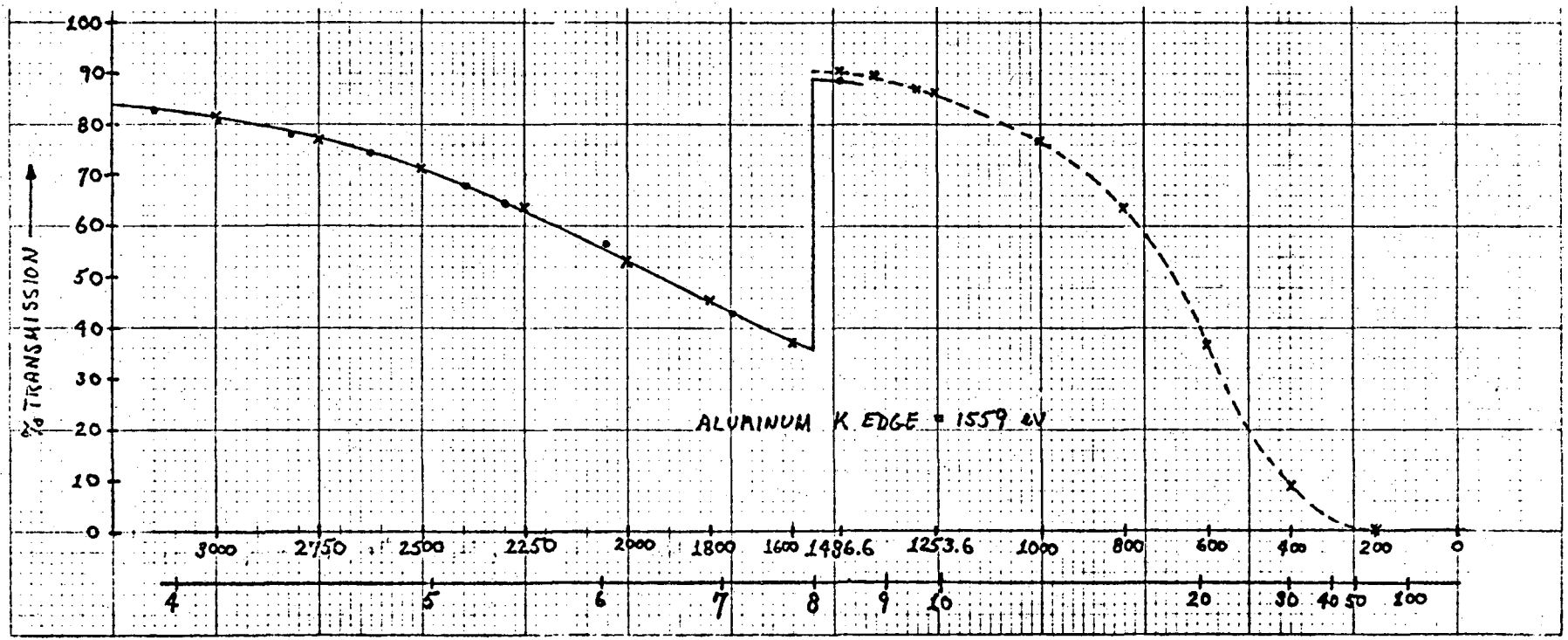


Figure 16. Comparison of values of per cent transmission through 0.001 cm (1 micron) of aluminum calculated with absorption coefficients that were:

- measured by Andrews
- × derived from Jönsson's graph.

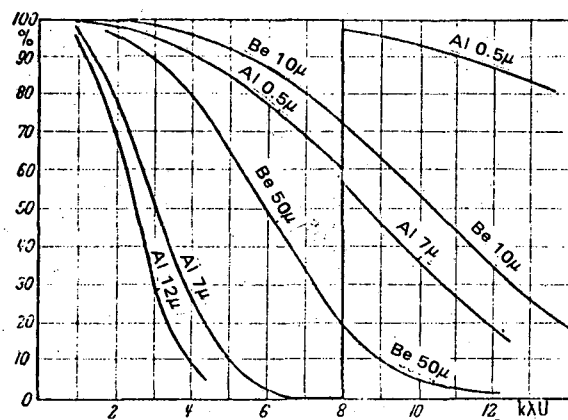


Figure 17. Transmission through beryllium and aluminum. (Taken from Ref. 31.)

D. ApplicationsEstimate of X-Ray Intensity

The material in the preceding sections can now be applied to an approximate calculation of the radiation emitted by the x-ray tube of the Berkeley iron-free spectrometer. The geometry of the tube is shown schematically in Fig. 1. The face of the anode is cut at a 15° angle; so γ , the angle of electron incidence, is 75° ; and θ , the x-ray take-off angle is 15° . The radiating region of the anode is separated from the sample by about 3.5 cm. The anode is an alloy of 97% Mg and 3% Al. The tube was usually operated at 12 kV and 30 mA.

The number of $\text{MgK}\alpha$ photons per steradian per electron can be calculated from the value of N' in Table I and Eq. (11).

$$\frac{N}{4\pi} = \frac{1.1 \times 10^{-4}}{4\pi} (12 - 1.305)^{1.63} = \frac{4.2 \times 10^{-4} \text{ photons}}{\text{ster. electron}}$$

The fraction of photons that reach the surface of the anode at a 15° take-off angle is given by $f(\chi)$. The absorption coefficient for the transmission of $\text{MgK}\alpha$ photons ($\lambda = 9.869 \text{ \AA}$) through Mg ($Z = 12$) can be taken from Jönsson's graph in Fig. 15 and Eq. (14); it is $314 \text{ cm}^2/\text{g}$. $\text{csc } 15^\circ = 3.86$; so, $\chi = \mu/\rho \text{ csc } 15^\circ = 1200 \text{ cm}^2/\text{g}$. $f(\chi)$ can now be taken from Green's plot in Fig. 10, Ref. 24; it is 0.8. So the number of MgK photons per electron observed at the anode is given by Eq. (9).

$$\frac{N(15^\circ)}{4\pi} = (0.8)(4.2 \times 10^{-4}) = \frac{3 \times 10^{-4} \text{ photons}}{\text{ster. electron}}$$

At 30 mA of current, this figure becomes

$$\frac{N(15^\circ)}{4\pi} = 6 \times 10^{13} \frac{\text{MgK}\alpha \text{ photons}}{\text{ster. sec.}}$$

A similar set of calculations indicate that the 3% aluminum component in the target should emit 2×10^{11} AlK α photons per steradian per electron, about 0.3% of the Mg flux. 90% of the AlK α photons produced are lost by target absorption in the magnesium anode.

The continuous x-ray distribution can be calculated from Eqs. (3), (4). Two values of C are given with Eq. (3) for different take-off angles; they differ by only 25%. Figure 9 shows that intensity changes by 60% at most due to take-off angle, this difference is insignificant for the estimations being made here. Either value of C given with Eq. (3) can be used to estimate the continuous photon distribution observed for a take-off angle of 15° (or, 105° according to Fig. 2). Using Dyson's value of C, 12 kV accelerating potential, and 30 mA of current, one finds

$$I = \frac{4 \times 10^{11} \text{ photons}}{\text{ster. sec keV}} \frac{12 - E}{E}$$

The shape of this distribution has already been shown in Fig. 4.

To correct this distribution for target absorption through a Mg anode, the depth distribution of continuous radiation must be known. The calculation of target absorption is greatly simplified if one assumes a mean depth of continuous production. Green and Cosslett²² suggest

that the mean depth is 0.25 times the Thomson-Whiddington range. A mean depth of 0.18 mg/cm^2 at 12 kV was obtained from Fig. 7, Ref. 24. Absorption coefficients were found from Jönsson's graph (Fig. 15). The continuous distributions with and without target absorption at 15° are shown in Fig. 18. For purposes of comparison to curve B, the $\text{MgK}\alpha$ intensity with target absorption has been converted to units of photon density, and this value is indicated on the figure. The conversion was trivial because $\text{MgK}\alpha$ radiation has a width of about 1 eV at 1254 eV; so the photon intensity calculated above was simply multiplied by 10^3 to convert to units consistent with the ordinate of Fig. 22.

It can be seen that the characteristic $\text{MgK}\alpha$ radiation is 10^4 more intense than the continuous radiation at similar energies. However, the integrated intensity of curve A (without target absorption) is 3.2×10^{13} keV/ster, sec while the characteristic intensity (without target absorption) is 10.5×10^{13} . Therefore, the ratio of characteristic energy produced to continuous energy produced is 3.2. After target absorption, the ratio is about the same.

Curve B shows that the target filters out a substantial portion of the softer components of the spectrum.

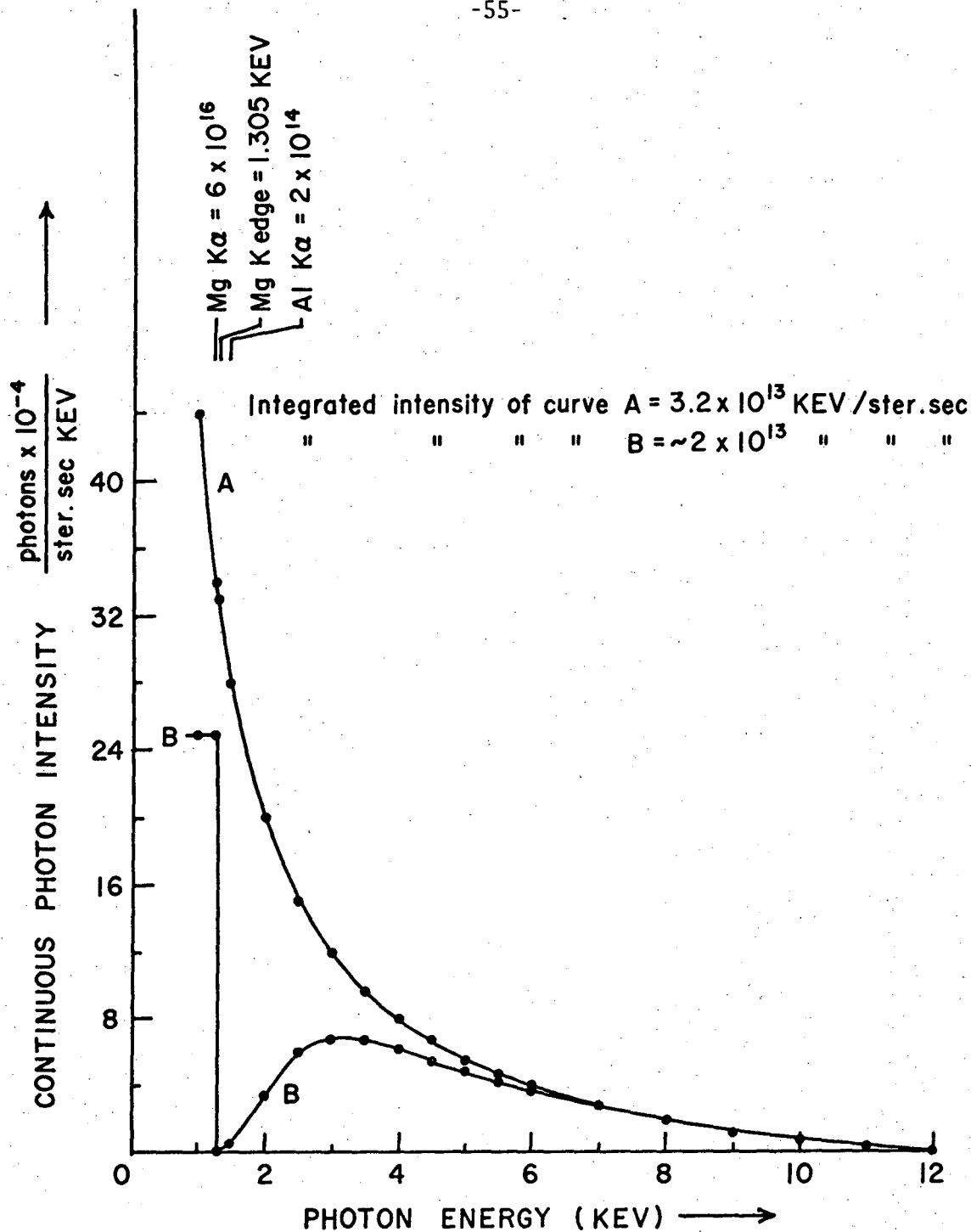
As shown in Fig. 1, the radiation passes through a beryllium window 0.5 mils (12.5 microns) thick before it falls on the sample plate 3.5 cm from the x-ray source. The attenuation through the window is given approximately by the ten micron Be curve in Fig. 17.

The distribution must then be scaled by $1/(3.5)^2$ to obtain the intensity falling on a 1 cm^2 sample area 3.5 cm from the source. This correction assumes a point source of x-rays; the point approximation is 97% accurate compared to the actual geometry. When the distribution in Fig. 18 is corrected for these two effects, the result is the distribution of photons that fall on the sample surface.

It is estimated^{32,33} that XPS measures only the first 15 - 50 Å of a solid sample. Assuming 50 Å to be the measured depth, an estimate can be made of the radiation absorbed in the measured region of the sample. If the sample is assumed to be organic, absorption coefficients through carbon for the photon range 0 - 12 keV can be estimated from Jönsson's graph in Fig. 15. The fraction of photons absorbed follows directly assuming unit density and a 50 Å path length. The distribution of photons impinging on the sample, derived from Fig. 18, can be multiplied by these fractions to determine the distribution of photons absorbed in the measured depth of the sample. This distribution and the absorption coefficients through carbon are shown in Fig. 19.

The integrated intensities over three energy intervals of continuous radiation as well as the total integrated intensity for all continuous radiation are given in Table II. The table also shows the intensity of magnesium and aluminum characteristic radiation absorbed in the first 50 Å of the target.

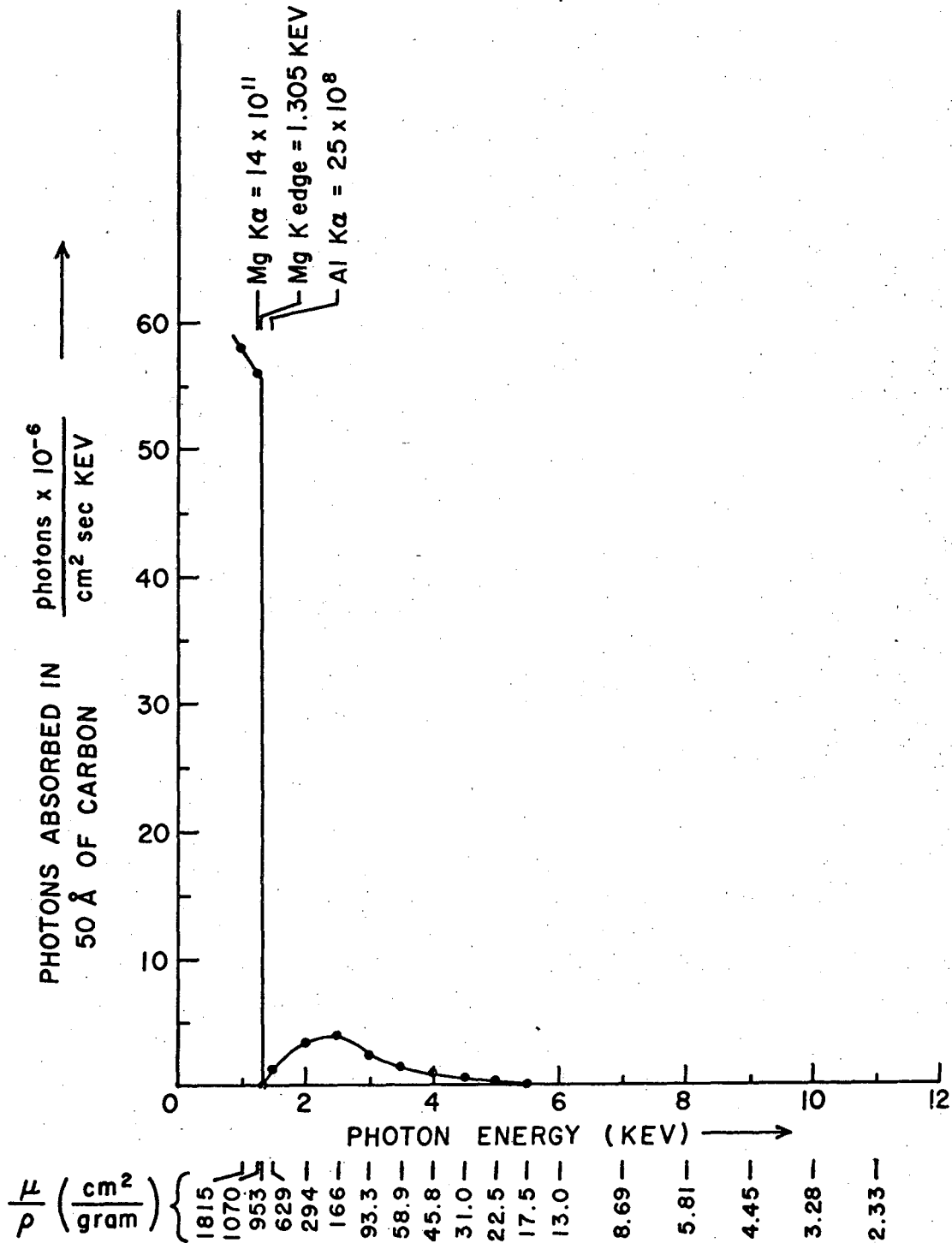
The immediate observation from Table II is that the magnesium $K\alpha$ intensity accounts for 95% of the energy absorbed in the sample. The



XBL753-5136

Figure 18. Continuous photon intensity from a magnesium target (97% Mg, 3% Al), 12 kV, 30 mA. (A) Without target absorption. (B) With target absorption, assuming mean depth of 0.18 mg/cm^2 and 15° (105°) take-off angle.

Characteristic intensities are given at the top of the figure *with* target absorption.



XBL753-5137

Figure 19. Distribution of photons absorbed in 50 Å of an organic sample that has been irradiated by the x-ray source of the Berkeley iron-free spectrometer. The mass absorption coefficients below the graph are those of carbon at the energies indicated.

Table II. Integrated intensities from various portions of the distribution of photons absorbed in 50 Å of an organic sample irradiated by the x-ray source in the Berkeley iron-free spectrometer.

Energy Region	$\frac{\text{keV}}{\text{cm}^2 \text{ sec}}$	$\frac{\text{erg}}{\text{cm}^2 \text{ sec}}$	$\frac{\text{Rads}}{\text{sec}} = \frac{100 \text{ erg}}{\text{gram sec}}$	Per Cent of Total Dose
Integrated continuous intensity from 0 → 1.3 keV	7×10^7	0.1	2×10^5	3 %
Integrated continuous intensity from 1.3 → 5 keV	2×10^7	0.03	6×10^4	1 %
Integrated continuous intensity from 5 → 12 keV	0.4×10^7	0.006	1×10^4	0.2 %
Total integrated continuous intensity 0 → 12 keV	1×10^8	0.16	3×10^5	5 %
Magnesium K α intensity 1.254 keV	2×10^9	3	6×10^6	95 %
Aluminum K α intensity 1.487 keV	0.4×10^7	0.006	1×10^4	0.2 %

calculated MgK α energy flux corresponds to the absorption of 1×10^9 photons/cm² sec in the first 50 Å of the sample. In the same volume, there are about 2×10^{16} atoms. Even after a ten hour experiment, only 1% of the sample atoms have absorbed MgK α photons. It would seem that radiation damage would not be a problem in such a system. However, the MgK α flux converts to units of 6×10^6 rads/sec, where a rad is defined as the absorption of 100 ergs of photon energy in one gram of tissue. At this dose rate, 5 - 20 % of the organic sample will decompose in $10^1 - 10^2$ seconds; 50 - 100 % of the sample can decompose in $10^2 - 10^3$ seconds.³⁴ The discrepancy between the small number of atoms that absorbed photons and the decomposition of the sample can be explained if one suggests that the secondary electrons excited by the ionizing x-rays do the bulk of the damage.

The continuous radiation represents only about 5% of the energy absorbed, whereas, it represented about 25% of the energy produced by the cathode electrons. The target filtered out some of the soft components that would have been absorbed in the sample. The higher energy components were simply not absorbed. Photons in the 5 - 12 keV range contribute only 0.2% of the absorbed energy. The great majority of continuous radiation absorbed in the sample comes from the soft x-ray region below the magnesium K edge where the anode did not filter effectively.

The absorption profile of the high energy components of the continuous radiation becomes more complicated in the case of organo-metallic

compounds and metallo-proteins. The metal atoms in such samples will absorb very strongly in regions where pure organic compounds are transparent.

The Use of Magnesium and Aluminum Windows to Filter Bremsstrahlung

At one point in the research, it was believed that the bremsstrahlung, particularly the high energy bremsstrahlung, were causing unacceptable radiation damage to the sample and increased background counts in the data. The 0.5 mil (12.5 micron) beryllium window commonly used on the x-ray tube was ineffective in filtering out the objectionable photons (see Fig. 17). A given anode material has a K absorption edge at a slightly higher energy than its K emission peak; therefore, the anode material is nearly transparent in the region of the K emission peak, and nearly opaque in the energy regions above and below the emission peak (see Fig. 16).

It was hoped that this absorption pattern could be used to improve the data by using a Mg window with a Mg anode. Mg windows were made by vapor deposition with thicknesses of 1.5, 3, 6, and 9 microns.³⁵ Mg does not deposit in a mechanically sound, pinhole-free film; so, each Mg film was deposited on a one micron thickness of Al, which had more desirable structural properties. The transmission of these filters is shown in Fig. 20. The thickest filter is opaque, or nearly so, through 3 keV while transmitting about the same amount of characteristic Mg

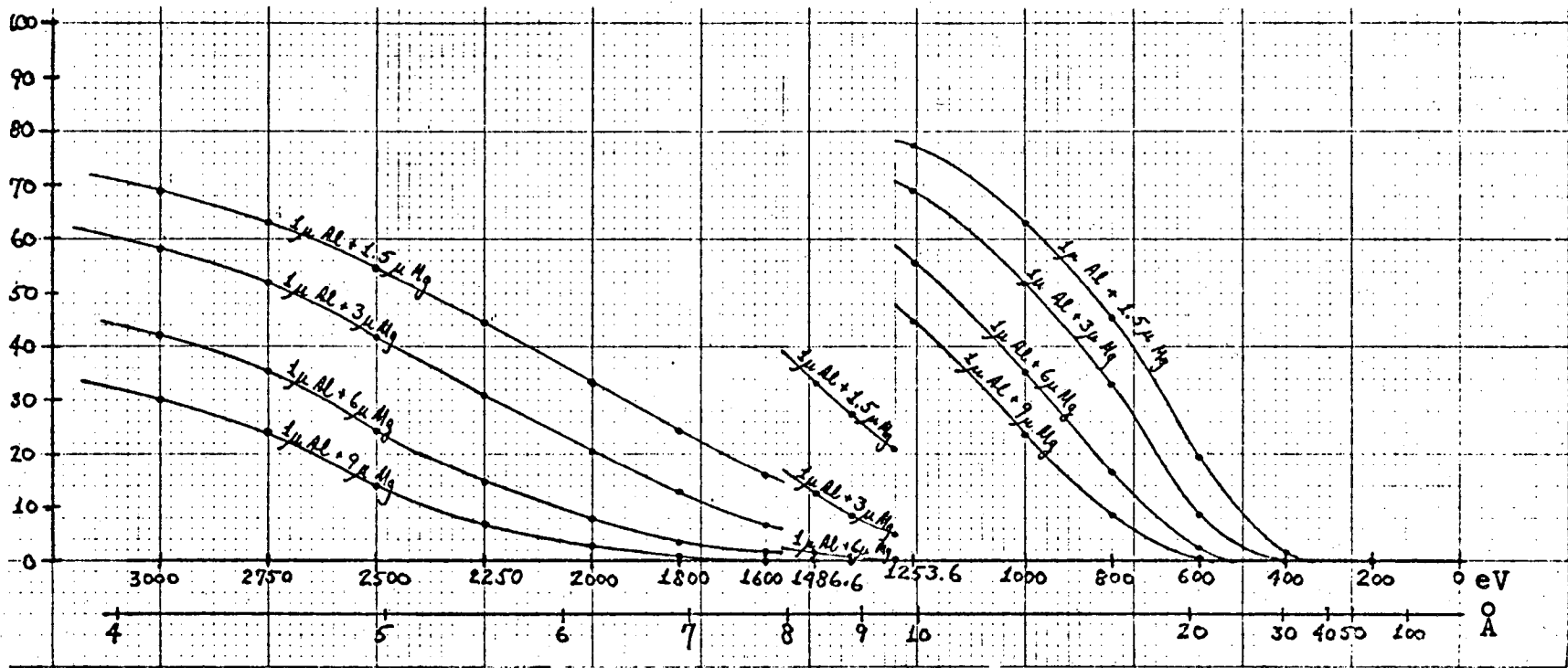


Figure 20. Transmission profiles of Mg/Al filter windows of various thicknesses. The mass absorption coefficients used to prepare these profiles were derived from Fig. 15.

radiation as a 0.5 mil Be window. The thinner Mg/Al foils filter less bremsstrahlung, but transmit more characteristic radiation than the 0.5 mil Be. At least half of the windows had pinholes; the thicker windows tended to have more pinholes than the thinner ones.

The filter windows were tested on samples of gold foil and pellets of tyrosine. The x-ray tube voltage was started at 3 kV and increased to 5, 7.5, 10, and finally to 12 kV. The cathode current was usually 20 mA, but sometimes 10 and 1 mA currents were used as controls. All windows survived the runs at low power up to 7.5 kV and 20 mA. At higher power, some of the windows melted in the heat of the x-ray tube. High energy electrons from the filament and scattered from the anode seemed to be the main sources of heat. Surprisingly, the thinner windows tended to survive the heat more often than the thick windows, but at best, the chances of any window surviving the heat were 50 - 75 %. In some runs, a thick window was placed over a thinner one. The thin window would protect the thicker one from the heat while the thicker window provided for extra filtering. The two layers could be arranged so that the pinholes in the separate windows would not coincide. As a measure of the heat involved, a brass washer that separated the two layers always stuck to the aluminum frames on which the windows were mounted. There was no adhesive on the brass; presumably, it was crudely welded to the window frames.

The signal to background ratios obtained through the filter windows were equal to the 0.5 mil Be window, but the transmitted intensity was

half that of the Be. In many cases, the filter windows increased the background and decreased the net signal over the background. The absorption in the filters is due to photoelectric processes. The absorption of the Mg/Al windows out beyond 3 keV means that there will be more bremsstrahlung photoelectrons entering the sample chamber and analyzer from the Mg/Al windows than from the Be. Therefore, the increased background is easily understood. The reason for the decrease in the net signal is not explained. The transmission of characteristic radiation, which gives rise to the signal over the background, should be greater than or equal to the standard Be window. It is possible that absorption coefficients derived from Fig. 18 for the region below the K absorption edge are inaccurate for the thicknesses of the Mg/Al windows used here. The actual absorption would seem to be greater than the calculated absorption.

The failure of the filter windows to improve the data can be understood from Fig. 18 and 19. Because of the shallow take-off angle built into the geometry of the x-ray tube, the anode itself absorbs most of the bremsstrahlung in the region between the K edge and 3 - 4 keV. The higher energy components of the continuous spectrum pass through both the anode and the filters, but the organic sample does not absorb them. So the anode was already an efficient filter in the energy region relevant to low Z samples.

Estimate of Radiation Dose by Use of a LiF Chip

A small chip of LiF $3 \times 3 \times 1$ mm provides a convenient measure of radiation dose.³⁶ The energy absorbed by the exposed chip is easily measured as light given off in a thermoluminescence meter. LiF chips were exposed for 3 and 10 seconds to the x-ray tube at a power of 12 kV and 20 mA. The thermoluminescence meter gave the maximum reading of 10^3 rads because the chips saturate at that dose. Therefore, a lower limit of $10^2 - 10^3$ rads/sec was set on the output of the x-ray tube. The calculated dose absorbed by an organic sample is 10^6 rad/sec according to the principles developed in this chapter. All other existing detectors would also saturate at the high dose rate of the Berkeley spectrometer.

REFERENCES, CHAPTER II.

1. C. Fadley, Ph.D. dissertation, University of California, Berkeley, Lawrence Berkeley Laboratory Report UCRL-19535, 1970.
2. L.N. Kramer, Ph.D. dissertation, University of California, Berkeley, 1971, Lawrence Berkeley Laboratory Report #LBL-306, p. 27.
3. H. Kulenkampff, Annalen der Physik, 69 (Series 4), 548 (1922).
4. A.H. Compton and S.K. Allison, X-Rays in Theory and Experiment (D. Van Nostrand, New York, 1935), Chap. 2.
5. D.H. Tomboulion, "The Experimental Methods of Soft X-Ray Spectroscopy and the Valence Band Spectra of the Light Elements," in Handbuch der Physik, Vol. XXX, S. Flügge (Ed.), (Springer-Verlag, Berlin, 1957).
6. S. Town Stephenson, "The Continuous X-Ray Spectrum," in Handbuch der Physik, Vol. XXX, S. Flügge (Ed.) (Springer-Verlag, Berlin, 1957).
7. H. Bethe and E. Salpeter, Quantum Mechanics of One and Two Electron Atoms (Academic Press, New York, 1957), section IV.
8. A. McLachlan, R. Leckey, J. Jenkins, J. Liesegang Rev. Sci. Instrum. 44, 873 (1973).
9. J.L. Gaines, "A Generator for Producing Monoenergetic, High Intensity, Soft X-Rays," Lawrence Laboratory Report UCRL-73588, Dec. 1, 1971.

10. B.L. Henke and M.A. Tester, in Advances in X-Ray Analysis, Vol. 18, Pickles, Barrett, Newkirk, Ruud (Eds.) (Plenum Press, New York, 1975), pp. 76 ff.
11. T. McKinley, K. Heinrich, D. Wittry (Eds.), The Electron Microprobe, Proceedings of Symposium of the Electrochemical Society, Washington, D.C., Oct. 1964 (John Wiley & Sons, New York, 1966), p. 841 ff, p. 999 ff.
12. A.J. Bearden, J. Appl. Phys. 37, 1681 (1966).
13. X-Ray Attenuation Coefficients from 10 kV to 100 meV, U.S. Dept. of Commerce, NBS Circular #583 (1957).
14. Ref. 31, pp. 87 - 88.
15. N.A. Dyson, "The Continuous X-Ray Spectrum from Electron-Opaque Targets," Proc. Phys. Soc. (London), 73, 924 (1959).
16. T.S. Rao-Sahib and D.B. Wittry, "The X-Ray Continuum from Thick Targets," in Proceedings of the Sixth International Conference on X-Ray Optics and X-Ray Microanalysis, Osaka, Japan, Sept. 5 - 10, 1971, p. 131.
- 16a. T.S. Rao-Sahib, D.B. Wittry, Proc. 5th National Conference on Electron Probe Analysis, New York, July, 1970.
This reference was not available at the Berkeley or San Francisco libraries of the University of California, nor at the main library of the Lawrence Berkeley Laboratory. Presumably, it may be obtained from Dr. L. Vassamillet, Carnegie-Mellon Univ., 4400 - 5th Avenue, Pittsburgh, PA 15213.

17. H. Amrehn and H. Kulenhampff, Z. Physik 140, 452 (1955).
18. P. Kirkpatrick, L. Wiedmann, Phys. Rev. 67, 321 (1945).
19. R. Honerjäger, Ann. der Phys. 38, 33 (1940).
20. V.E. Coslett and N.A. Dyson, "Measurements of the Spectral and Angular Distribution of X-Rays from Thin Targets," X-Ray Microscopy and Microradiography, V. Coslett, A. Engström, H. Pattee (Eds.), (Academic Press, New York, 1957), p. 405.
21. H. Kulenhampff, S. Liesgang, M. Scheer, Z. Physik, 137, 435 (1954).
22. M. Green, V. Coslett, Brit. J. Appl. Phys. (J. Phys. D), Ser. 2, Vol. 1, 425 (1968).
23. M. Green, "Target Absorption Correction in X-Ray Microanalysis," X-Ray Optics and X-Ray Microanalysis (Academic Press, New York, 1963).
24. M. Green, Proc. Phys. Soc. 83, 435 (1964).
25. W. Hink, "Floureszenstrahlung von Massiv und Membrantargets," X-Ray Optics and Microanalysis (Hermann, Paris, 1966), p. 143.
26. R. Shimizu, K. Murata, G. Shinoda, "Depth Distribution of Characteristic X-Rays in Microanalyzer Target," X-Ray Optics and Microanalysis (Hermann, Paris, 1966), p. 127.
27. H. Bishop, "Calculations of Electron Penetration and X-Ray Production," X-Ray Optics and Microanalysis (Hermann, Paris, 1966), p. 112.
28. R. Castaing, J. Descamps, J. Phys. Radium 16, 304 (1955).

29. U. Schmitz, P. Ryder, W. Pitsch, Vth International Congress on X-Ray Optics and Microanalysis, Tubingen, 1968, G. Mollenstedt and K. Gaukler (Eds.) (Springer-Verlag, Berlin, 1969), p. 104.
30. H. Hanson and S. Salem, Phys. Rev. 124, 16 (1971).
31. A. Sandström, "Experimental Methods of X-Ray Spectroscopy," Handbuch der Physik, S. Flugge (Ed.), XXX (Springer-Verlag, Berlin, 1957), p. 85 ff.
32. R. Steinhardt, J. Hudis, M. Perlman, Electron Spectroscopy, D.A. Shirley (Ed.) (North-Holland, Amsterdam, 1972), p. 557.
33. M. Klasson, et al., Physica Scripta 5, 93 (1972).
34. B. Tolbert, Atomlight (publication by New England Nuclear Corporation).
35. These foils were crafted by Gordon Steers in the Vacuum Coatings Shop at the Lawrence Berkeley Laboratory, University of California, Berkeley, 94720.
36. Ralph Thomas, Health Physics Division, Lawrence Berkeley Laboratory, Private Communication.

III. RELIABILITY OF THE SUNDER FITTING PROGRAM

A computer program named SUNDER was developed by Claudette Ruge Lederer and C.S. Fadley¹ for the purpose of fitting lineshapes to photoelectron spectra. The details of the program have been described elsewhere.¹ Fadley first used the program on strong, well resolved peaks from high purity samples, and SUNDER proved to be a useful tool for providing quantitative interpretations of his data. Since XPS has expanded to a wide variety of new applications, SUNDER has been asked to fit weak, overlapping signals from atoms of low concentration in some mixture. The question of SUNDER's accuracy in these applications has not been investigated.

What follows is a set of criteria that can be used to judge the quality of experimental data and SUNDER's ability to fit it realistically. These criteria are the result of experience accumulated by applying SUNDER to various sets of data. The criteria are to be regarded as guidelines rather than infallible rules. As more experience with the program becomes available, it may be necessary to revise these standards.

SUNDER can fit four different lineshapes to XPS data. Only Lorentzian lineshapes with a smoothly added "constant" tail will be considered here. For each lineshape, SUNDER calculates a position, full width at half-maximum (FWHM), an area, and a tail parameter that represents the ratio

¹. C.S. Fadley, Ph.D. dissertation, University of California, Berkeley, 1970, Lawrence Berkeley Laboratory Report UCRL-19535.

of tail height to peak height. SUNDER also calculates a straight line background which introduces two more parameters, a slope and an intercept. The choice of a Lorentzian lineshape, the method of joining the tail to the main peak, and the linear background are all based on purely empirical considerations, i.e., this combination gave the most reasonable fit to several test peaks. Fadley¹ has already discussed some of the limitations of this approach.

It will be seen that SUNDER calculates a reliable, or at least self-consistent, lineshape when:

- (1) the signal to noise ratio is greater than ten;
- (2) there are enough points on both sides of the peak to characterize the background and tail;
- (3) the calculated tail parameter is less than 0.1, preferably below 0.05;
- (4) the number of fitted lines is less than or equal to the number of observed peaks and shoulders.

The calculated position of a single lineshape fitted under a single peak is remarkably insensitive to noisy data; the FWHM is somewhat more sensitive, but the area and tail may be completely unreliable. When all four of the above standards are not satisfied, SUNDER can still be useful to tell whether or not a given model is consistent with the observed data. The data can be fit with lineshapes whose ratios and/or positions have

been fixed according to some physical model. SUNDER may converge on this fit, but that does not mean the model is correct; it only means the model is consistent with the data.

In the discussion that follows, "peak" will refer to experimentally observed data; whereas, "line" will refer to a calculated lineshape that is fit to the peak.

A. Statistics

To say that data have been taken with good statistics is to say that enough counts have been collected to give a high signal to noise ratio. Just how large this ratio must be in order for SUNDER to calculate a reliable fit has never been determined. Therefore, an experiment was run to find the minimum acceptable value for the signal to noise ratio. The gold $4p_{3/2}$ peak and the gold $4f$ doublet were counted over multiple scans. Each scan was about 12 minutes long, and the data from each scan were accumulated with all the previous scans. SUNDER was used to calculate a position, FWHM, and an area for the accumulated data at the end of each scan. The results are shown in Table I. SUNDER calculates a least squares standard deviation for each fitted parameter; these are also shown in Table I.

A practical definition for the signal to noise ratio can be given as follows. Each peak stands on a background; let B equal the number of counts in the background. Let S be the counts in the signal over, but not including, the background. At the crest of a peak, the total

Table I. Lineshape parameters calculated by SUNDER from data accumulated over multiple scans of the gold 4f and gold 4p3/2 regions of gold foil (MgK α). The tabulated error limits are the least square standard deviations calculated by SUNDER. Actual experimental errors may be larger, especially in the case of positions.

	Total Number of Scans							
	1	2	3	4	5	6	7	8
Gold 4p3/2 Position (KE)	703.3 ± 0.3	703.2 ± 0.1	703.1 ± 0.1	703.1 ± 0.1	703.1 ± 0.1	703.1 ± 0.1	703.0 ± 0.1	703.0 ± 0.1
Gold 4p3/2 FWHM	4.94 ±0.88	5.11 ±0.43	4.98 ±0.36	5.27 ±0.35	5.48 ±0.34	5.62 ±0.29	5.66 ±0.27	5.58 ±0.25
Gold 4p3/2 Area	3221 ± 885	6837 ± 955	9786 ±1147	13240 ±1505	16968 ±1851	21256 ±2031	24650 ±2221	28420 ±2354
Gold 4p3/2 S/N Ratio	3.0	4.8	5.8	6.4	6.8	7.9	8.4	9.3
Area Au 4f Area Au 4p3/2	12.75 ±3.51	11.93 ±1.68	12.54 ±1.47	12.35 ±1.42	11.89 ±1.31	11.18 ±1.08	11.22 ±1.03	11.05 ±0.93

00404500767

number of counts is $S + B$. The standard deviation of that total count is $\sqrt{S + B}$. Let noise be denoted by N and be defined as twice the standard deviation; therefore, $N = 2\sqrt{S + B}$. In these terms, the signal to noise ratio becomes $S/N = S/2\sqrt{S + B}$. These definitions are summarized in Fig. 1.

The information in Table I shows that the calculated line position is relatively insensitive to the quality of the statistics. The gold $4p_{3/2}$ position varies only by 0.3 eV from $S/N = 3$ to $S/N = 9$. This variation is larger than the calculated least square error which is about 0.1 in most scans. However, the actual experimental error includes many other factors such as small variations in the magnetic field of the spectrometer. A more realistic standard deviation that accounts for all experimental factors is about 0.2 - 0.3 eV. The variation of the gold $4p_{3/2}$ line position is, therefore, quite consistent with past experience. Apparently, a single line can be fit to noisy data, and the calculated line position can be considered quite reliable.

Table I indicates that the FWHM is more sensitive to statistics. Calculated values of gold $4p_{3/2}$ FWHM converge to a value of 5.6 eV. This limit is reached when $S/N = 8$. When $S/N < 8$, SUNDER seems to underestimate the FWHM.

The dependence of the gold $4p_{3/2}$ area on the S/N ratio can be determined from the ratio of the gold $4f$ doublet to the gold $4p_{3/2}$ peak. SUNDER cannot fit an accurate area to the gold $4p_{3/2}$ peak in any individual scan because the data are too noisy ($S/N \sim 3$). However, the gold $4f$ is strong ($S/N \sim 40$ in one scan), and its area could be calculated

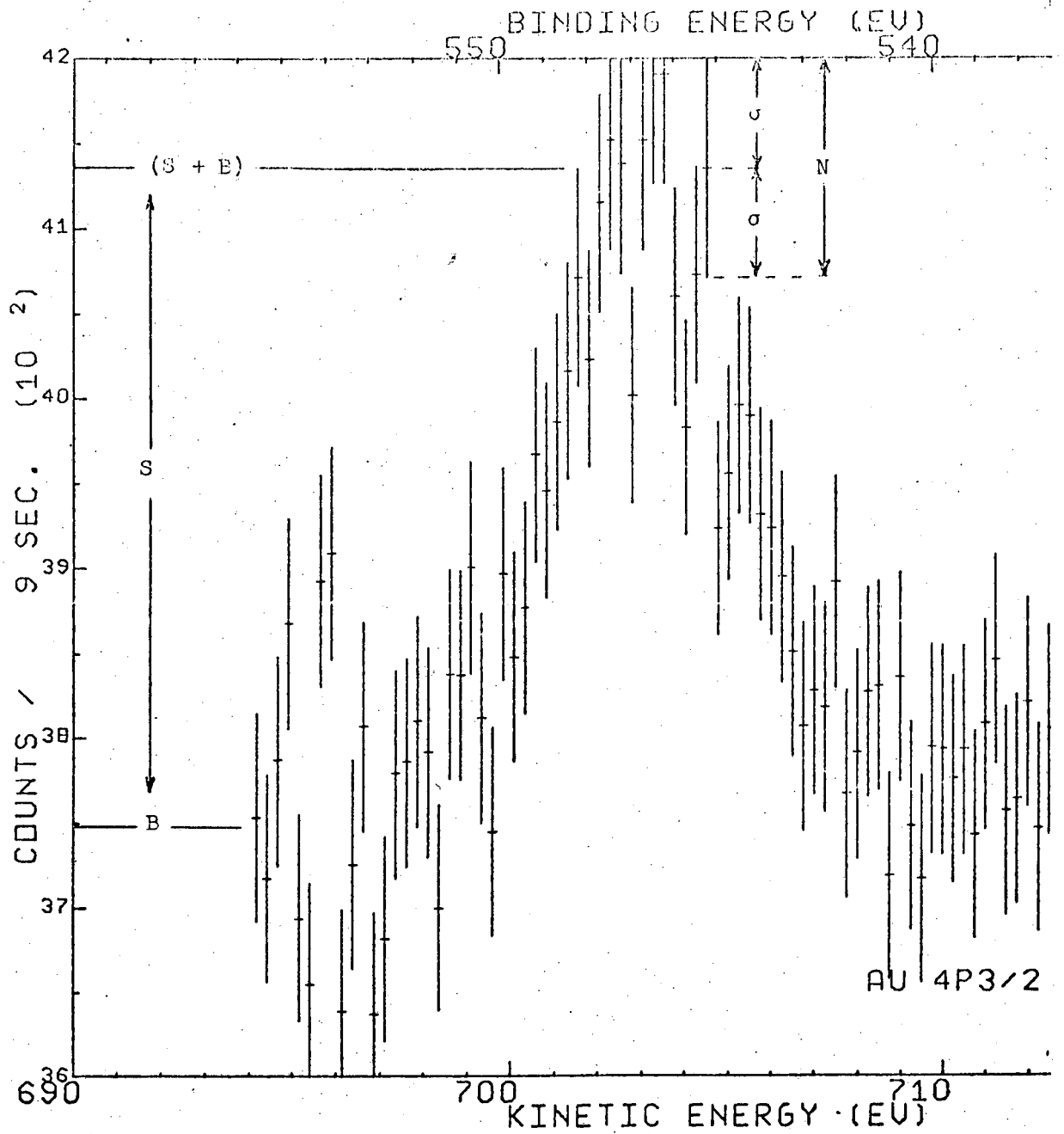


Figure 1. The gold 4p_{3/2} region of gold foil (MgK α). The definitions of counts in the background, B, counts in the signal over the background, S, and noise, N, are shown pictorially. The energy scales are nominal.

with consistent accuracy from scan to scan. Therefore, any error in the area ratio of $4f$ to $4p_{3/2}$ will be due to uncertainty in the $4p_{3/2}$ area. It is presumed that as the $4p_{3/2}$ data accumulate and S/N improves, SUNDER will be able to calculate a consistent value for its area also. At that point, the ratio of $4f$ to $4p_{3/2}$ will become constant with respect to S/N. The appropriate data have been plotted in Fig. 2. Except for the first two points, which show large error bars, the ratios define a descending trend toward a constant value of 11.1. This value is reached at S/N = 8 . Two more scans raise S/N to 9.3 with no appreciable effect on the $4f:4p_{3/2}$ ratio.

Certain conclusions can be drawn from Table I and Fig. 2. Single lineshape positions can be calculated with consistent accuracy for S/N = 3 and perhaps below 3. FWHM and area are not consistent until S/N = 8 . For $5 < S/N < 8$, the FWHM is about 0.8 - 0.9 its consistent value, but the calculated area is completely unreliable.

Since a signal to noise ratio of 8 indicates adequate statistics, one can use the definitions of S, B, and N to estimate the number of scans that will be necessary to get good statistics. If n is the number of scans, and s and b represent the signal and background counts in a single scan, then the condition for adequate statistics becomes

$$\frac{S}{N} = \frac{ns}{2n(s + b)} = 8$$

or

$$n = \frac{256(s + b)}{s^2}$$

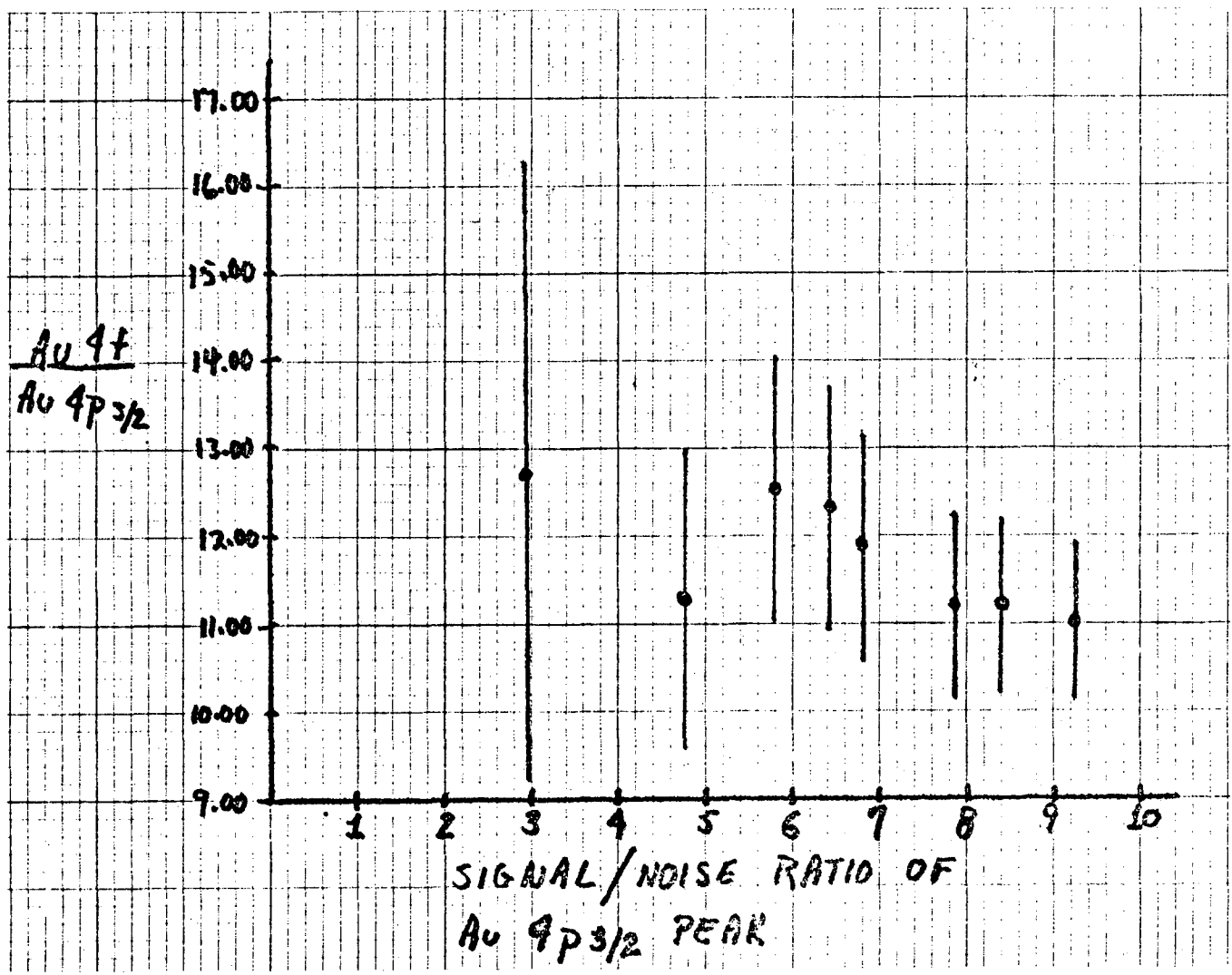


Figure 2. Ratio between the total area of the Au4f doublet and the area of the Au 4p_{3/2} peak versus the signal to noise ratio of the Au 4p_{3/2} peak.

From the first scan, one can estimate s and b . For a weak signal, $s/b \sim 0.1$ and $b \sim 1000$; therefore, $n = 28$.

The implicit approximations that $S = ns$ and $B = nb$ may be invalid due to radiation damage and deterioration of the surfaces of the sample and x-ray anode. These topics will be discussed at length later. In the present example, the gold was not subject to radiation damage; a fit of the first and last gold 4f scan showed that the counting efficiency dropped by only 10% over the course of the four hour experiment.

B. Effect of the Background

All of the calculated lineshapes stand on a background which SUNDER approximates as a straight line. A wide scan over a range of 1000 eV reveals that the background looks like a broad hump. The straight line approximation is, therefore, only valid over short intervals of energy. This lack of precision in the calculated background has little effect on the calculated position and FWHM. The tail parameter and area, particularly area ratios of two lines under one peak, may be completely unreliable (0 - 100% error).

Enough data points must be taken on both sides of a peak to enable SUNDER to calculate a reasonable background and tail. On the high binding energy side of a peak, there must be at least ten data points. Fadley suggests a few FWHM as an upper limit on the number of points taken here. Otherwise, one risks taking an energy interval so large that the linear background approximation is not accurate. On the low

binding energy side, it is best to take data out beyond the $K\alpha_{3,4}$ satellite peaks. Sometimes it is not feasible to take so many points because the extended counting time makes radiation damage a severe problem. In such cases, the data must be taken at least as far as one FWHM.

These ideas are illustrated in Figures 3 and 4. 3a and 3b show two fits of the same data, the phosphorus 2p region of the sodium salt of adenosine 5' monophosphate (AMP). In 3a, SUNDER was free to fit the most reasonable linear background. In spite of the large number of points taken on both sides of the peak, SUNDER converged on an obviously spurious background. It lies above the data points on the high binding energy side of the peak. In 3b, the spurious background has been corrected by fixing the background slope at zero, i.e., flat. The line positions and widths are scarcely affected, but the relative line intensities have been reversed. It is likely that 3a has too many points on the high binding energy side of the peak. In agreement with Fadley's suggestion of fitting this region within a few FWHM of the peak position, the first 30 channels of 3a should be deleted.

A similar situation is shown in Fig. 4. These points show the oxygen 1s region of a complex of neodymium and adenosine 5' triphosphate (ATP). In this case, there is a deficiency of points on the low binding energy side. When SUNDER was free to calculate the most reasonable background, the result, shown in Fig. 4a, was again spurious. The same data were fit in Fig. 4b with the background constrained to be flat. In contrast to Fig. 3, there was no appreciable effect on the relative intensities.

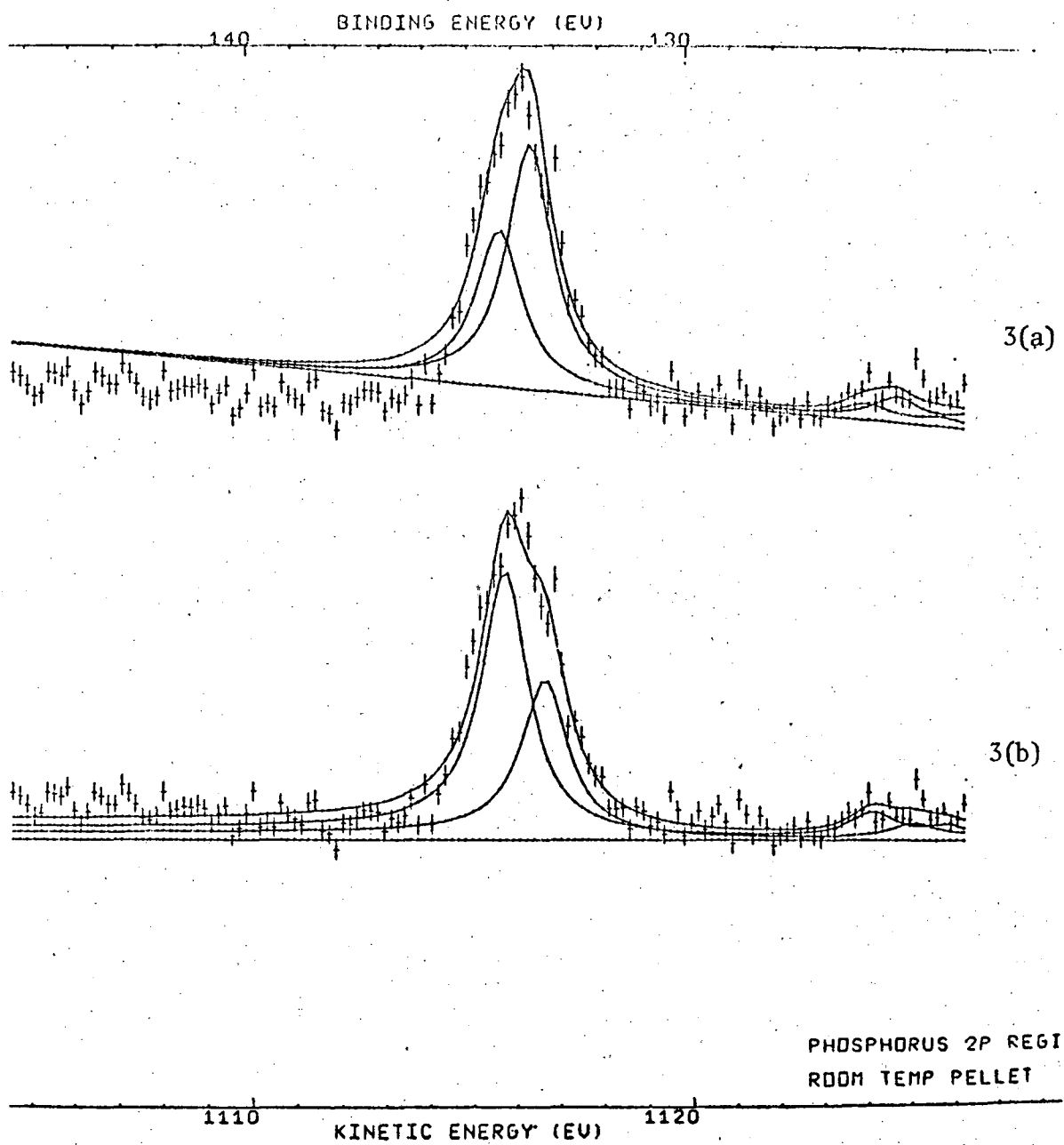


Figure 3. (a) Phosphorus 2p region ($MgK\alpha$) of the sodium salt of adenosine-5'-monophosphate. Background slope was left free to vary. SUNDER converged on an unrealistic slope.

(b) Same data with background slope fixed at zero. This slight correction reversed the area ratio.

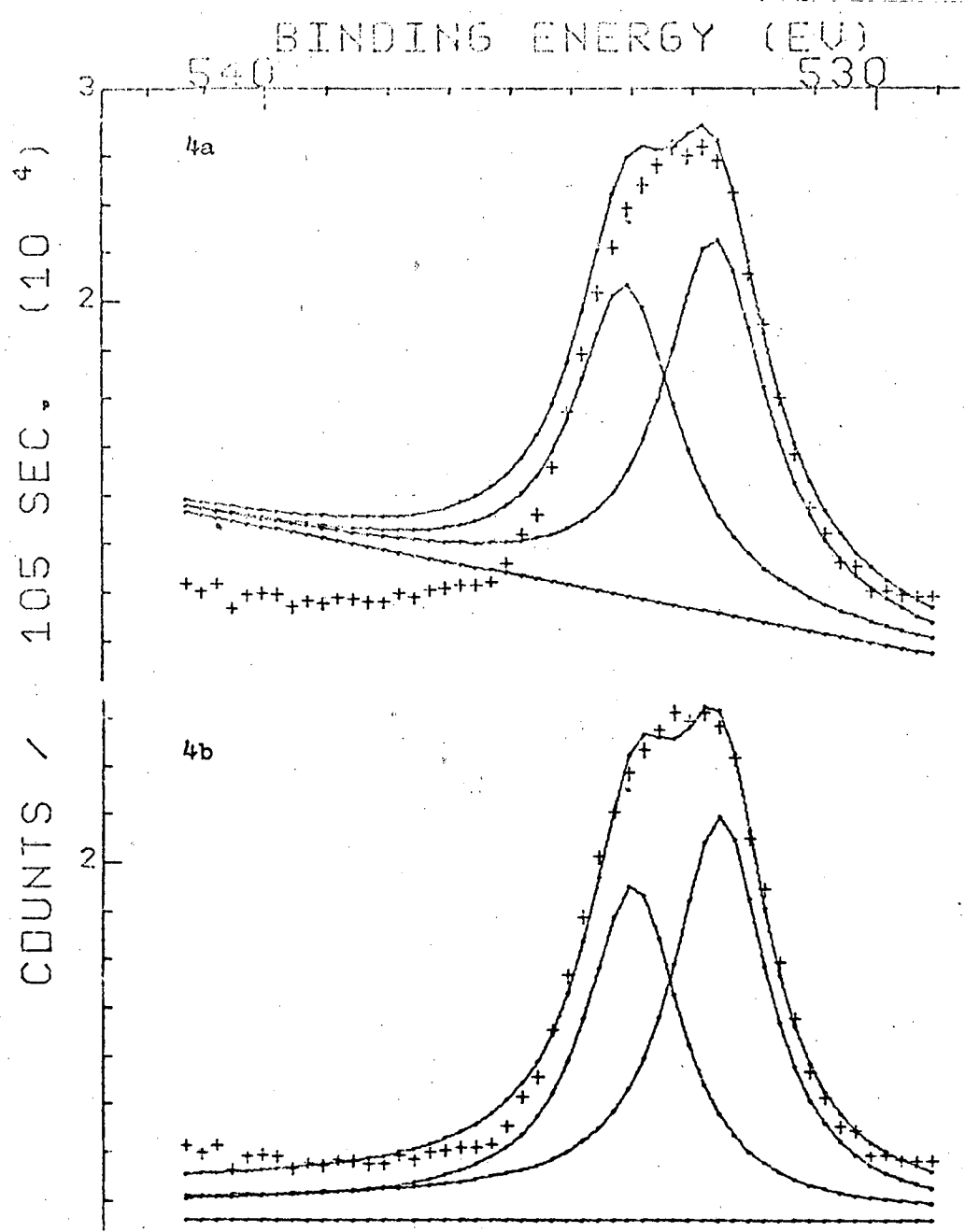


Figure 4. Two fits of the same data showing the oxygen 1s region of a complex of neodymium and adenosine-5'-triphosphate. In (4a), the data were fit with the slope free to vary. In (4b), the slope was fixed flat. There was no effect on the area ratio.

The spurious slope in Fig. 3a is not steep; it is only about -12 ± 4 counts/eV. The adjustment to a flat slope in 3b was rather minor, but it produced a complete inversion of relative intensities. In Fig. 4, the adjustment of the slope was much more severe, going from -244 counts/eV to zero; but there was no change in the relative intensities. These results lead to the conclusion that there is considerable instability in SUNDER's area ratios when the background is inaccurate. However, there is no way to tell that the background is spurious except in obvious cases like Figures 3a and 4a.

The uncertainty can be minimized by taking a wide scan extending 20 to 50 eV on each side of the peak. The wide scan will define an overall background that can be compared to the calculated background for consistency. The problem will persist as long as the signal to background ratio S/B remains low. (S/B is not to be confused with S/N, the signal to noise ratio.)

C. Effect of the Tail Parameter

XPS peaks usually have a relatively flat tail that extends tens of eV out to high binding energy. The tail is due to the inelastic scattering of photoejected electrons that are traversing the sample material. The tail parameter, which is defined as the ratio of tail height to peak height, is supposed to account for these scattered electrons in the calculated spectrum.

The data points on the high binding energy side of a peak are fit with both the background and tail. These parameters are obviously not independent. Unless the background or tail are fixed at a certain value, the computer is free to select any combination of these parameters that will converge for a given set of data. There is no way to insure that SUNDER has calculated the correct combination. This extra degree of freedom in the program introduces some uncertainty in the calculation of areas and area ratios. Calculated line positions and FWHM seem to be affected only slightly by changes in the tail.

Fig. 5 shows the carbon 1s spectrum of paraoxybenzoic acid. In 5a, the computer was free to calculate the best least squares value for the tail parameter. As a result, the tail from the dominant line, due to aliphatic and aromatic carbon, overwhelmed the small carboxyl line. To resolve the carboxyl line, the data were fit eight times with the tail parameter fixed at a slightly different value each time. The fit with a tail parameter of 0.035 seemed most reasonable; it is shown in Fig. 5b. This fit, however, does not necessarily correspond to the combination of background and tail that is physically correct.

Fig. 5 illustrates an extreme example where the tail of a strong line actually eliminated a weak line. This example is faulty because of the poor statistics on the weak line. When a peak which has been measured with adequate statistics is standing on the tail of another peak of comparable size, the effect on the area ratio is not known. Sometimes, other evidence has been available to check the area ratios. In cases

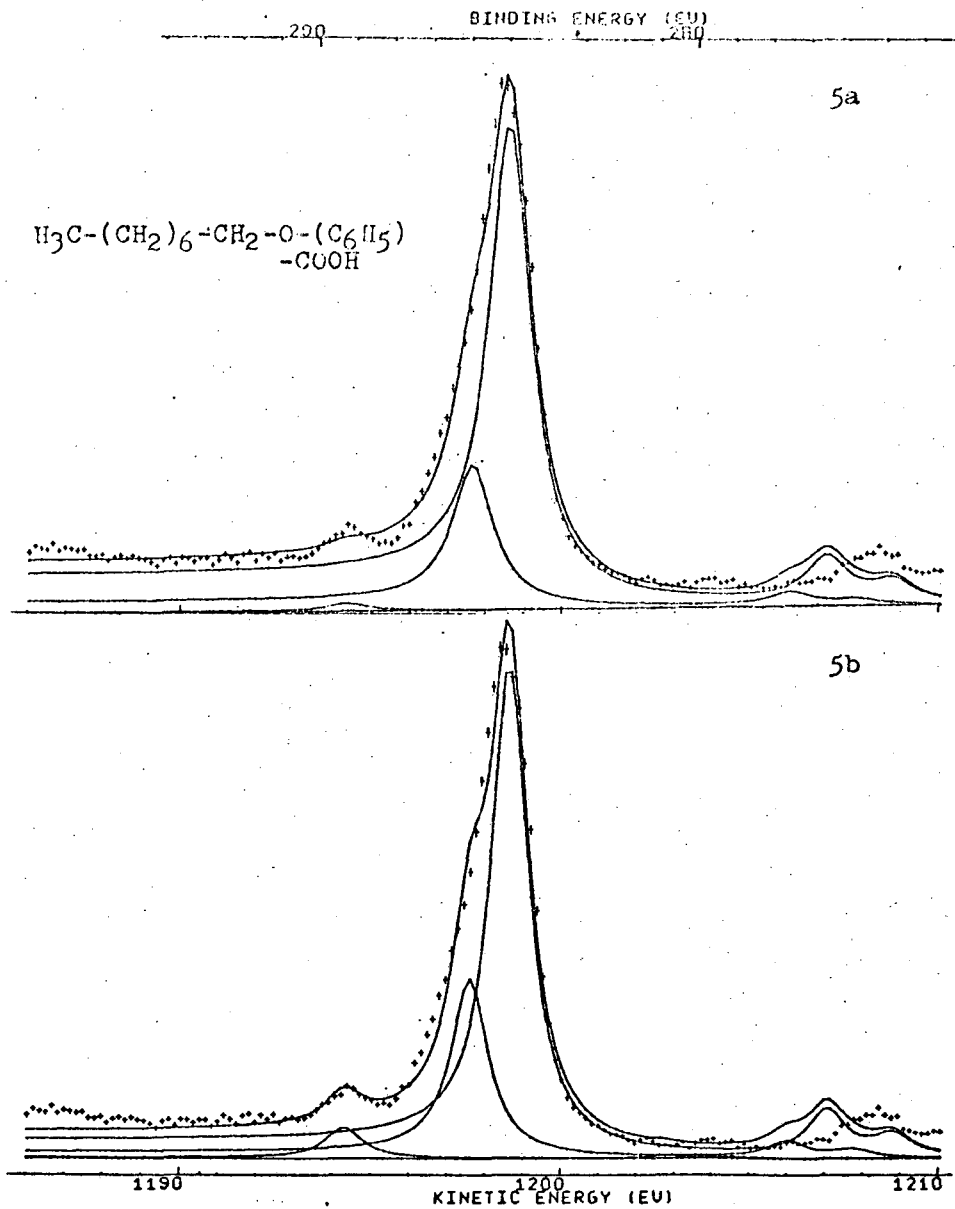


Figure 5. Two fits of the same data showing the carbon 1s region of paraoctyloxybenzoic acid. In (5a), the small carboxyl line has been lost in the tail of the dominant aliphatic and aromatic line. In (5b), the carboxyl line has been resolved by fixing all tail parameters to 0.035 as described in the text.

where the ratios were found to be reliable, that tail parameter was usually less than 0.10. This result suggests that as a general rule, one should not expect to get reliable area ratios unless the tail parameter is less than 0.10.

SUNDER contains an imperfection in the process of calculating tails for a collection of two or more closely spaced lines. One of the lines will be assigned a large tail parameter and the rest will be given vanishingly small ones. It is necessary for the programmer to constrain SUNDER to give all the lines in the spectrum the same tail parameter. As Fadley¹ has already suggested, this procedure is reasonable for lines of similar position and FWHM.

D. Two Lines Under Single Peak

By far, the most common use of the SUNDER program has been the interpretation of complicated spectra by fitting two or more lines under a single peak. One desires a set of standards that the data should satisfy to permit a reliable SUNDER fit of several lines under one peak. These criteria would be some hopelessly cumbersome combination of S/N ratios, data points per eV, curvature of data at shoulders, etc. The question of SUNDER's ability to fix complex spectra is addressed most easily by examples.

The case of fitting two lines under a single peak with a definite shoulder will be considered in some detail. The meaning of a "definite" shoulder will become clearer later on. Figure 6 shows the Eu 4d and

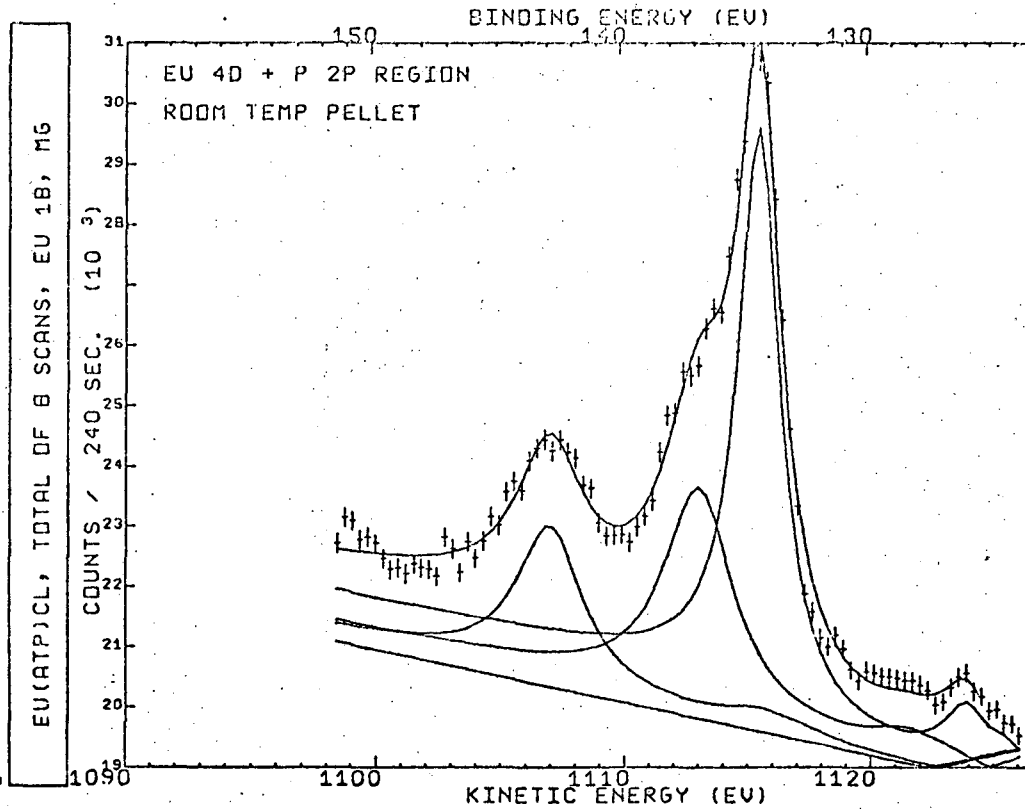


Figure 6. The europium 4d and phosphorus 2p region of a complex of europium and adenosine-5'-triphosphate. The Eu 4d_{3/2} line is well resolved, but the Eu 4d_{5/2} line overlaps the P 2p doublet. SUNDER successfully calculated an area, FWHM, and position for the 5/2 line that were consistent with the 3/2 line and other data. The calculated position and FWHM of the P 2p doublet were found to be consistent with P 2p signal from a similar complex made with neodymium.

No constraints were put on the fit except that the tail parameters were made equal.

P 2p region of a complex of europium and ATP, Eu(ATP)Cl . The Eu 4d $_{5/2}$ overlaps the P 2p signal to form a peak with a definite shoulder. All the lines were constrained to have the same tail parameter; otherwise, SUNDER was free to make the best least squares fit. The well resolved Eu 4d $_{3/2}$ line can be used as a check on the fit of the obscured 4d $_{5/2}$ line.

The 5/2 and 3/2 lines are expected to have the same FWHM; in Fig. 6, SUNDER has in fact assigned them the same FWHM within the errors of the calculation. The 5/2:3/2 ratio should be 3:2 according to multiplicities; the observed ratio is $(3.04 \pm 0.56):2$. The 3/2 - 5/2 separation can be used to check the position of the 5/2 line. Fadley¹ measured this separation for Eu_2O_3 , another formally tripositive europium compound. Fadley's value was 5.7 eV; 6.0 ± 0.2 eV was measured in Fig. 6. The two separations are in close, though not exact, agreement. Thus, SUNDER was successfully able to calculate a position, FWHM, and area for the unresolved Eu 4d $_{5/2}$ line that were accurate at least within the calculated errors. Presumably, the error in the separation and the large propagated error in the area could be reduced by further counting.

The P 2p signal in the Eu(ATP)Cl was isolated by looking at the spectrum of another complex of ATP with a different rare earth element, neodymium. Given the similarity of chemistry of the rare earths, the bonding of the phosphate to the metal is expected to be similar for both Eu(ATP)Cl and Nd(ATP)Cl . In the Nd(ATP)Cl , however, the Nd 4d spectrum is shifted to lower binding energy; therefore, the P 2p signal is no

longer complicated by the metal's 4d signal. This P 2p peak should have the same binding energy and FWHM as the P 2p peak in the Eu(ATP)Cl data.

The areas of the two P 2p signals cannot be compared because they come from different samples. The signal from any sample depends on the surface density of the material to be measured. The surface density, in turn, depends on variables like sample texture, crystal structure, and moisture content, and how tightly the sample pellet is pressed. These conditions are difficult to reproduce for different compounds. It is also difficult to reproduce the cleanliness of the x-ray anode and window, both of which affect the signal. Therefore, the comparison of peak areas from the same element in different samples is difficult; the same comparison between different compounds is unreasonable. These problems can be avoided by the use of a suitable internal standard, but none exists here.

The Nd 4d and P 2p region of Nd(ATP)Cl is shown in Fig. 7. The P 2p binding energies and FWHM are seen to be the same within the calculated error in both the Nd and Eu compounds. Thus, SUNDER was also able to calculate the P 2p signal with a reasonable degree of accuracy.

It should be noted that the other three standards for acceptable data had to be satisfied before SUNDER could successfully fit the Eu(ATP)Cl spectrum. For example, the data in Fig. 6 represent the accumulated total of eight scans; the S/N ratio is 12 for the Eu 4d_{5/2} peak and about 30 for the P 2p peak. When the data from just one scan were fit, the S/N ratio for Eu 4d_{5/2} was only 4.7, which is well below the minimum of 8; and SUNDER failed to make a successful fit.

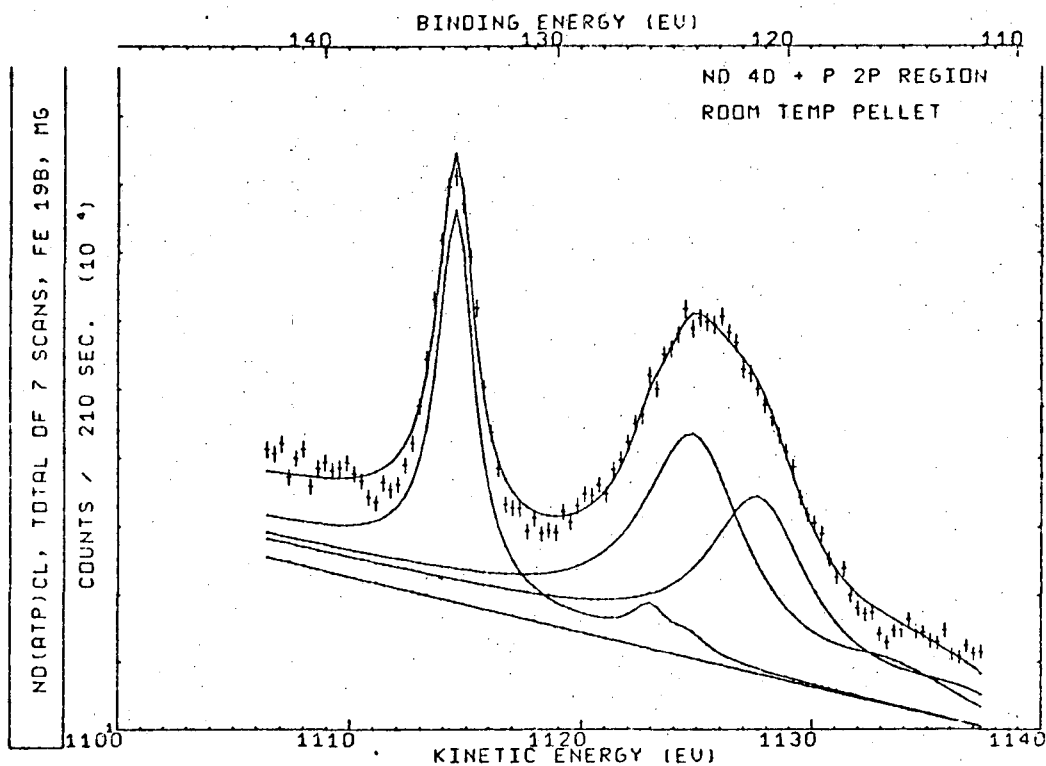


Figure 7. The neodymium 4d and phosphorus 2p region of the neodymium analogue of the complex in Fig. 6. The P 2p doublet is no longer obscured by the metal 4d signal. The P 2p binding energy and FWHM are the same as those calculated in Fig. 6, within the experimental error. The two lines under the Nd 4d peak represent the 3/2 and 5/2 components. They should have a ratio of 2:3; the observed ratio is approximately the reverse of 2:3. SUNDER is unable to fit broad peaks with no shoulders unless the programmer aids the fit by fixing certain parameters, such as area ratios or FWHM. In this fit, all three lines had the same tail parameter, and the two Nd 4d lines had the same FWHM.

The meaning of a "definite" shoulder is subjective. From Fig. 6 it could be said that a curve drawn through the data points should have a slope of 45° or less in the region of the unresolved peak. Slight asymmetries in the data are excluded as shoulders.

If SUNDER is to make a meaningful calculation, the number of lines fitted to the data cannot exceed the number of peaks and shoulders as defined above. If this rule is violated, the fit has significance only as a test of whether or not the given fit is consistent with the data. Consider Fig. 8 which shows the carbon 1s region from a complex of Cu^{2+} and glycine, the simplest amino acid. There should be three components to the spectrum: a carboxyl carbon and the alpha amino carbon from glycine, and an aliphatic carbon signal from organic vapor impurities that condense on the sample surface. Bearing two oxygens, the carboxyl carbon signal should be found at high binding energy (BE), but the relative positions of the amino and impurity carbon signals are not known. The data show a resolved peak toward high BE and a larger peak with a slight asymmetry that cannot be called a shoulder. So Fig. 8 shows fits of three lines to two peaks with no shoulders. Comparison of 8a and 8b, which are two fits of the same data, show that SUNDER can be made to converge on fits that have the relative positions of the amino and impurity carbon lines reversed. To obtain these contradictory fits, it was necessary to constrain the carboxyl and amino carbon lines to have the same FWHM and area. Without this aid, there was too much instability in SUNDER to permit a reasonable fit. This kind of instability has already been observed in Fig. 3 where two lines were fit under a single peak with no shoulders.

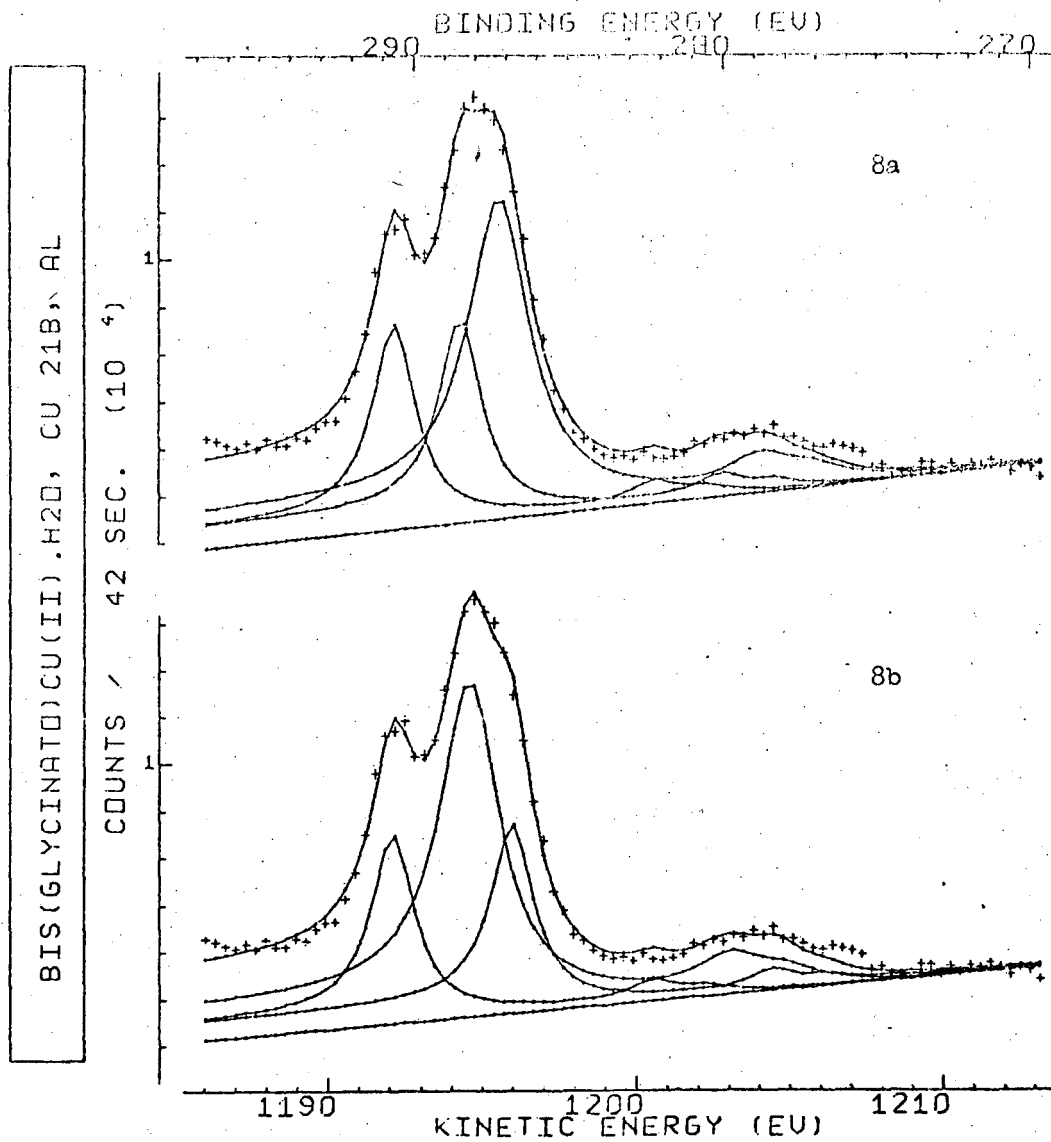


Figure 8. Two fits of the carbon 1s region of a complex of copper and glycine, $\text{Cu}^{++}(\text{gly})_2 \cdot \text{H}_2\text{O}$. SUNDER converged on contradictory fits. In both fits, the two smaller lines were constrained to have the same area and FWHM. SUNDER cannot distinguish which line assignment is correct.

The data in Fig. 8 satisfy the other three requirements that should enable a reliable fit: the statistics are adequate, the proper number of points have been taken on both sides of the peak structure, and the tail parameters are small. Without a definite shoulder, SUNDER simply does not have enough information to make a fit that distinguishes which, if either, of the two carbon line combinations is correct. One can only conclude that both of the proposed models are consistent with the data.

IV. THE USE OF CARBON 1s AND NITROGEN 1s SIGNALS AS REFERENCE STANDARDS IN XPS

A. Introduction

The binding energy of a photoejected electron can be defined as the positive energy required to remove the electron from a given orbital out to infinity with zero kinetic energy. For atoms and molecules in free space, this definition implies that binding energy is referred to zero at the vacuum level.

In XPS measurements of solids, it is convenient to measure binding energy with respect to zero at the Fermi level. When a conducting sample and a metallic spectrometer are electrically connected, they are in equilibrium, which means that the Fermi levels are equal. The respective work functions, and therefore the vacuum levels, need not be equal. So when a photoejected electron leaves the sample and enters the spectrometer, it is accelerated by a contact potential equal to the difference between the sample and spectrometer work functions. These considerations are summarized in Eq. (1), the familiar energy conservation relation

$$h\nu = KE + BE^F + \phi_{sp} \quad (1)$$

where: $h\nu$ = energy of the x-ray photon

KE = kinetic energy of the photoejected electron

BE^F = binding energy of photoejected electron referred to the Fermi level

ϕ_{sp} = work function of the spectrometer.

There is also a term corresponding to recoil energy which is derived from momentum conservation. It has not been included because it is insignificant except for H, He, and Li. More detailed reasoning leading to Eq. (1) has already been published.^{1,2}

For insulating samples, the situation is similar, but more complicated. These samples develop a surface charge in the x-rays. Irradiation causes a flux of photoelectrons, Auger, secondary, and Compton scattered electrons leaving the sample. The resulting positive charge can be at least partially neutralized by electrons impinging on the sample from the x-ray window; bulk and surface conductivity induced in the insulator by the ionizing x-rays can also neutralize the surface charge.

Ebel and Ebel³ have investigated these charging contributions on gold coated glass plates and uncoated Teflon. At constant x-ray tube current, they found that the surface charge potential increased non-linearly from -3 to +3 volts as the x-ray tube voltage was raised from 2 to 6 kV. When the voltage was constant at 5 kV and current was varied, the surface potential rose from 0 to +2 volts. They were also able to measure bulk and surface currents of 0.1 to 1 nanoamps. Apparently, at low x-ray voltage, the electrons from the window exceed the electron flux out of the sample, which results in a negative surface potential. The reverse is true at higher x-ray voltages. The charging causes spurious binding energy measurements; so, a term, V_C , reflecting the surface charge potential must be added to Eq. (1).

Assuming that the insulating sample is electrically connected to the spectrometer, the respective Fermi levels will be equal, as shown in Fig. 1. A photoelectron leaving the sample will have kinetic energy KE' , but as it approaches the spectrometer, it will be accelerated by a contact potential, ϕ_c , so that the kinetic energy actually measured in the spectrometer is KE . The magnitude of ϕ_c is given by the difference between the sample and spectrometer work functions.

Although the concepts developed here are identical to the case of a conducting sample, there are important differences. The Fermi level of an insulator is not uniquely defined. It lies at some point between the valence and conduction bands. Furthermore, an unperturbed macroscopic insulator is not necessarily in electrical contact, i.e., equilibrium, with the spectrometer. The Fermi levels need not be equal. If the sample is thin enough (a few microns) for the x-rays to penetrate, then radiation-induced bulk and surface conductivity³ can provide at least partial electrical contact.

The radiation induced conductivities³ can be interpreted in terms of holes in the valence band or partial filling of the conduction band. The holes would be caused by photoionization of the valence levels and valence electrons that drop to lower energies to fill holes in core states. The flux of electrons impinging on the sample from the x-ray window could fill some of the conduction levels. Qualitatively, the steady state population of the conduction band is expected to be low. These electrons will drop to the valence band to fill holes, and they might be drawn away into the conduction band of the grounded metallic spectrometer.

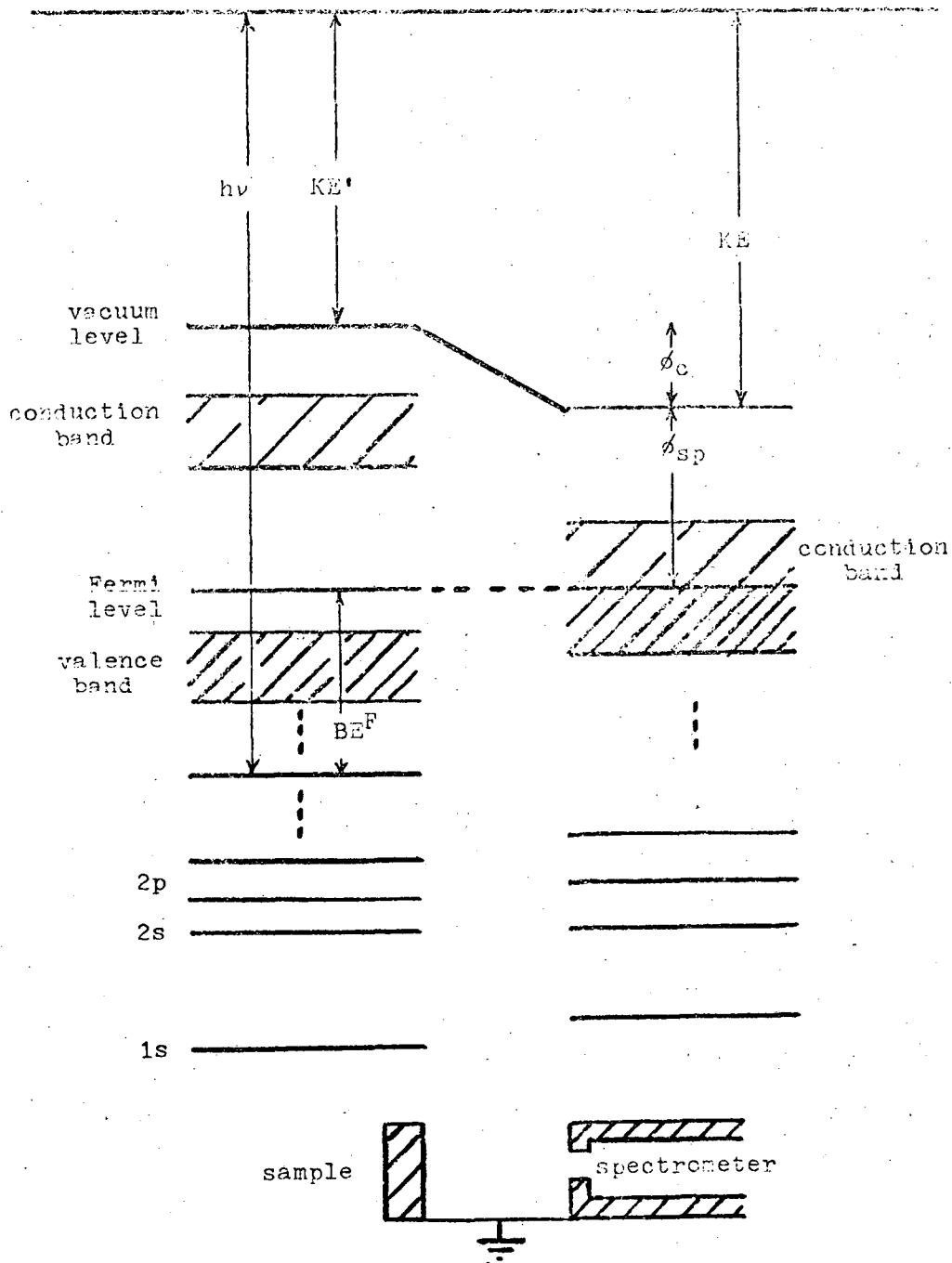


Figure 1. Energy level diagram for the photoejection of a core electron from an insulating sample. The sample is presumed to be thin enough to be in equilibrium with the spectrometer during irradiation.

Assuming electrical equilibrium between the irradiated sample and the spectrometer, the energy balance is given by Eq. (1) plus V_C .

$$h\nu = BE^F + KE + \phi_{sp} + V_C \quad (2)$$

The discussion given above shows that BE^F is experimentally convenient, but theoretically ambiguous. Binding energy referred to the vacuum level, BE^V , has more physical significance, and it is the result given by most theoretical calculations. From Fig. 1, BE^V is given by Eq. (3).

$$h\nu = BE^V + KE - \phi_c + \phi_{sp} - V_C \quad (3)$$

The vacuum level suffers as an experimental reference level because it is hard to measure directly in an XPS experiment. Neither is it easily determined indirectly, because ϕ_c and V_C are generally not known, and ϕ_c , in particular, is also difficult to measure.

It is possible to overcome these uncertainties if a reference binding energy can be assigned to a standard signal. All of the sample binding energies could then be measured with respect to the standard according to Eq. (4).

$$BE_{sample}^V = BE_{std}^V + KE_{std} - KE_{sample} - \phi_{c\ std} + \phi_{c\ sample} + V_{C\ std} - V_{C\ sample} \quad (4)$$

The choice of the standard signal must be carefully made so that the contact potentials and charging effects cancel in Eq. (4). It is generally difficult to find standards that satisfy this requirement.

Several standards have been proposed to solve the reference problem. In any spectrometer that contains rubber o-rings and is evacuated by oil diffusion pumps, hydrocarbon vapors from the rings and pump condense in a thin film on the surface of a sample. Siegbahn¹ first proposed using the carbon 1s signal from this contaminant film as a reference. Others^{4,5,6} have suggested the vapor deposition of gold or palladium onto the sample surface, the so-called gold "decoration" technique. Various heterogeneous mixtures of primary standards with the sample material have also been put forward. Graphite,⁷ Pb_3O_4 ⁸ and MoO_3 ⁹ have been proposed as reasonable standards for general XPS work. Gold dust has been cautiously suggested as a potential standard under carefully controlled circumstances.¹⁰ KNO_3 has been used to reference an extensive series of nitrogen compounds; $Na_4P_2O_7$ ¹¹ was used for phosphorus compounds.¹²

Each of these referencing systems have been criticized in the literature. The C 1s signal from the condensed vapor contaminants has been a widely used reference, and it has been the most severely criticized. One cannot be sure of the origin of the impurity, and it may not be the predominant form of carbon, especially in organic samples. Dianis and Lester¹⁰ suggest that every surface has some catalytic activity that may be reflected in a shift of the contaminant C 1s signal from sample to sample. Their suspicion was shown to be true in the experiments of Nordling⁷ who observed that the contaminant C 1s shifted to higher binding energy on the surface of samples that contained highly electronegative elements. Similar shifts have been seen by Ogilvie¹³ in metal

oxide catalysts supported on alumina and by Nefedov¹⁴ in a series of sodium halides. It has been indicated^{14,15,3} that the contaminant C 1s reference is successful in reflecting the surface charge on the sample, and that, therefore, it should be an adequate reference for a homologous series of compounds.^{14,15} The other critics of this reference have not been specific on this point.

The gold "decoration" technique has also been found to be inadequate. Betteridge¹⁶ found that during deposition, the gold may react with the sample causing shifts or broadening of the gold peaks. Shifts to higher binding energy were observed with KCN, and NaCl; shifts to low binding energy were found with Na₂S₂O₃ and copper phthalocyanin. Over a temperature range of -50° to 200°C, peaks due to metallic gold were seen at the higher temperatures. The gold on copper phthalocyanin displayed anomalous effects. Urch¹⁷ also observed anomalous behavior with this reference. The splitting between the peaks of an insulated layer of gold "decoration" and a simultaneously irradiated grounded gold mesh appeared to vary as function of the depth of the vacuum deposited gold. Dianis¹⁰ found that vacuum deposited gold responded to an applied dc bias, but claimed to see small changes in the FWHM of the gold peaks.

Nefedov¹⁴ saw spikes in the C 1s signal from graphite powder mixed with his samples. The spikes are presumably due to differences in potential between graphite particles in variable contact with sample particles. Dianis¹⁰ suggests that MoO₃ mixed with the sample is an unacceptable reference because it did not reflect an applied dc bias on the sample holder. He suggests that mixing any other insulating powder, such as Pb₃O₄, KNO₃, or Na₄P₂O₇, with the sample might also fail to reflect

an applied charge accurately. Gold dust mixed with samples on the Berkeley iron-free spectrometer gave variable results which eliminated it as a possible reference.¹⁸

The variable results obtained with the standards described above can be attributed to the fact that they are all external references. The reference peaks did not originate from the sample; instead, they came from some foreign material that was mixed with the sample or deposited on top of it. These foreign materials have conductivities and work functions distinct from those of the sample. In general, therefore, Eq. (4) cannot be satisfied by an external reference. The disparity in surface charge potentials between samples and external references has been well documented in the studies cited above. The question of contact potential differences was not considered. The best one can hope for is that the ϕ_c and V_c differences in Eq. (4) will cancel when the chemical shift is calculated.

The present study was directed toward a series of biological compounds. It was recognized that all of these samples contained carbon and nitrogen in the same functional groups. It was hoped that the C 1s or N 1s or both signals might be useful as internal reference standards. The principal assumption is that a C 1s or N 1s signal in a given functional group is the same from one biological compound to the next. Interesting metal and sulfur spectra could be referred to the C 1s or N 1s signal with high accuracy because the reference and measured signal come from the same material. They are both influenced by the same charging and contact potentials. Thus, Eq. (4) reduces to:

$$BE_{\text{sample}}^V = BE_{\text{std}}^V + KE_{\text{std}} - KE_{\text{sample}} \quad (5)$$

in which the kinetic energies are measured and BE_{std}^V is assigned a fixed value.

B. C 1s As An Internal Standard

There are difficulties in using the C 1s as an internal standard. The contaminant layer of condensed organic vapors mentioned above is also present in the Berkeley iron-free spectrometer. The spectrometer resolution is generally insufficient to distinguish the contaminant signal from the sample spectrum. It is also difficult to assign a fixed value to BE_{std}^V because the C 1s signal shows a chemical shift of 9 eV between $-\text{CH}_3$ and $-\text{CF}_3$.^{1,19} It is necessary to determine a chemical shift scale for the various functional groups common to most biological samples.

Experiments were undertaken to determine the characteristics of the contaminant carbon layer. To determine how long it takes for the layer to form, a gold foil was cleaned in acetone and ethanol, then etched in warm (100°C) dilute (0.1 M) aqua regia for two hours. This treatment is known to form chloroauric acids, $\text{HAuCl}_4 \cdot x\text{H}_2\text{O}$.²⁰ These compounds decompose to the metal upon heating;²⁰ so, the gold foil was left at 600°C for 9-1/2 hours. The drastic cleansing methods were intended to remove all carbon due to sources outside the spectrometer. Since the foil was handled in air, it is not to be considered clean in the strictest sense. Other experiments were designed to clean the gold completely;

they did not succeed, and they are summarized below. In a practical sense, the foil was cleaner than any other samples run in the spectrometer, and it was mounted and run like the other samples. Therefore, it represents an approximation to what can be expected for a regular sample.

The foil was placed in the spectrometer and exposed to a rough vacuum for 15 minutes. Then the C 1s region was measured with AlK α x-rays. The results are shown in Fig. 2. Two distinct peaks were observed, that were separated by 4 eV; the main peak was at lower binding energy. The main peak grew to a steady height in about two hours, apparently at the expense of the smaller peak which diminished to zero. The origin of the smaller, high binding energy peak is not known. It may have been adsorbed CO₂ from the atmosphere which came off of the gold in the vacuum and radiation flux. This behavior would be consistent with the observations on peptides to be described later. It is unlikely that the source of the smaller peak was simply buried under the accumulating contaminant layer; no sample was ever observed in which the contaminant layer completely obliterated the signal. The contaminant C 1s FWHM was 1.56 ± 0.14 eV.

Two efforts were made to clean the gold foil until it was completely free of carbon while it was in the spectrometer. These experiments involved a high temperature source holder designed by Fadley,²¹ who reported that it was possible to remove the carbon layer with this apparatus by passing hydrogen gas over the heated sample. One run was made with oxygen gas, another with hydrogen. High temperature was reached

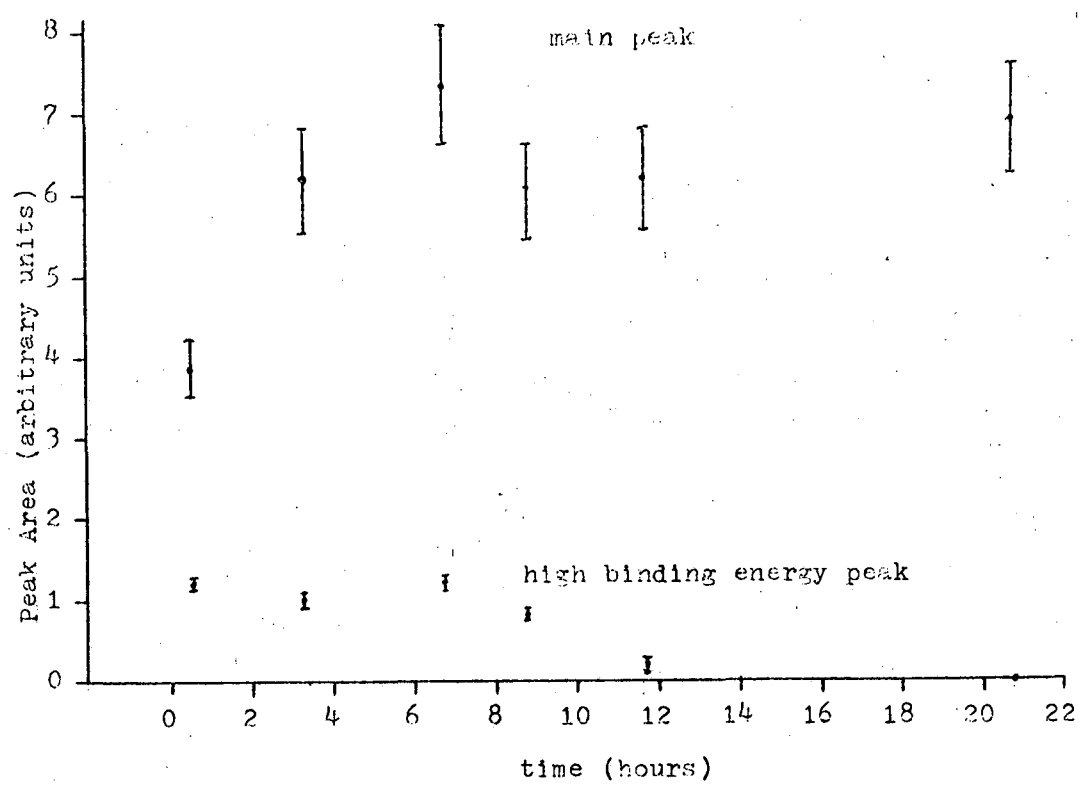


Figure 2. Growth of the contaminant C 1s signal on a reasonably clean gold foil. The origin of the high binding energy peak that decays to zero is not known. The main peak, which is associated with the contaminant layer, had a FWHM of 1.56 ± 0.14 eV.

once, and there were several mechanical failures. The carbon signal never completely disappeared.

Oxalic and oxamic acid were run to observe the contaminant peak on organic samples. Pellets of each material were pressed with a force of nine tons on a 1/2" diameter die. The data are shown in Fig. 3. The sample peaks are chemically shifted away from the contaminant peak by 5.4 eV in oxalic acid and 4.7 and 3.8 eV in oxamic acid. The interpretation of these separations is not straightforward because the contaminant signal has been known to shift to higher binding energies on the surface of samples containing highly electronegative elements.^{7,13,14} The oxalic acid signal does not necessarily reflect the position of a carboxyl carbon because each -COOH group in oxalic acid is likely to perturb the other. The data show that the contaminant C 1s peak has a FWHM of 1.65 ± 0.07 eV. The data show that the contaminant peak can account for up to 50% of the C 1s signal in a given sample.

In order to assign reasonable values for BE_{std}^V in Eq. (5), it was necessary to set up a chemical shift scale for the biologically relevant functional groups that cause distinguishable shifts in C 1s signals. The compounds used in this study are shown with their structures in Table I. The samples were obtained from commercial sources and were used without further purification. All samples were measured in the solid state at room temperature. The glycyglycylglycine (tri-gly) samples were lyophilized from solutions of the pH shown with their structures. The protonation of these peptides and the individual amino acids was based on their pK values²² and their pH in solution. The

data are shown in Fig. 4. The binding energies of biologically significant functional groups are given in Table II.

Several studies of the C 1s chemical shift in organic compounds have already appeared in the literature.^{1,19,23-29} The work by Gelius and co-workers^{19,26} and Lindberg²³ was the most extensive; they cite references to C 1s shifts in the gas phase. Gelius related the C 1s shifts to a charge parameter, q , derived from CNDO calculations.

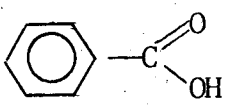
$$\Delta E = kq_A + V_A + c \quad (6)$$

ΔE is the C 1s shift, and kq_A is the potential at the core level of atom A due to the charge on atom A. V_A is the molecular potential at A due to the charges on all the other atoms in the molecule; c is a constant related to the reference level.

These studies are not directly applicable to biological molecules. Gelius' correlations of C 1s shifts with q_A were not successful with ionic compounds unless V_A was included. Many of the amino acids and peptides in this study exist in their zwitterion form, and V_A cannot be calculated because crystal structures are unknown. This is particularly true of the tri-gly samples lyophilized from extreme pH values; it is not likely that these samples correspond to the published crystal structures.^{30,31} Where possible, comparison is made with the shifts Gelius observed.

In the present study, spectrometer resolution was not adequate to distinguish the various functional groups. It was necessary to use the SUNDER fitting program to aid in the interpretation of the spectra.

Table I. Compounds used in the preparation of a C 1s binding energy scale.

No.	Compound	Structure
1.	Oxalic acid:	$\begin{array}{c} \text{O} \quad \text{O} \\ \parallel \quad \parallel \\ \text{HO}-\text{C}-\text{C}-\text{OH} \end{array}$
2.	Oxamic acid:	$\begin{array}{c} \text{O} \quad \text{O} \\ \parallel \quad \parallel \\ \text{HO}-\text{C}-\text{C}-\text{NH}_2 \end{array}$
3.	Glycylglycylglycine, pH 1-2:	$\begin{array}{c} \text{O} \quad \text{O} \quad \text{O} \\ \parallel \quad \parallel \quad \parallel \\ \text{H}_3\text{N}-\text{CH}_2-\text{C}-\text{N}-\text{CH}_2-\text{C}-\text{N}-\text{CH}_2-\text{C}-\text{OH} \\ \quad \\ \text{H} \quad \text{H} \end{array}$
4.	Glycylglycylglycine, pH 5-6:	$\begin{array}{c} \text{O} \quad \text{O} \quad \text{O} \\ \parallel \quad \parallel \quad \parallel \\ \text{H}_3\text{N}-\text{CH}_2-\text{C}-\text{N}-\text{CH}_2-\text{C}-\text{N}-\text{CH}_2-\text{C}-\text{O}^- \\ \quad \\ \text{H} \quad \text{H} \end{array}$
5.	Glycylglycylglycine, pH 9.6:	$\begin{array}{c} \text{O} \quad \text{O} \quad \text{O} \\ \parallel \quad \parallel \quad \parallel \\ \text{H}_2\text{N}-\text{CH}_2-\text{C}-\text{N}-\text{CH}_2-\text{C}-\text{N}-\text{CH}_2-\text{C}-\text{O}^- \\ \quad \\ \text{H} \quad \text{H} \end{array}$
6.	5-Hydroxyvaleramide:	$\text{HO}-\text{CH}_2-\text{CH}_2-\text{CH}_2-\text{CH}_2-\overset{\text{O}}{\parallel}{\text{C}}-\text{NH}_2$
7.	1-Asparagine:	$\begin{array}{c} \text{O} \quad \text{O} \\ \parallel \quad \parallel \\ \text{H}_2\text{N}-\text{C}-\text{CH}_2-\text{CH}-\text{C}-\text{O}^- \\ \\ \text{NH}_3 \\ + \end{array}$
8.	Benzoic acid:	
9.	Paraoctyloxybenzoic acid:	$\text{H}_3\text{C}-(\text{CH}_2)_6-\text{CH}_2-\text{O}-\text{C}_6\text{H}_4-\overset{\text{O}}{\parallel}{\text{C}}-\text{OH}$
10.	1-Tyrosine:	$\begin{array}{c} \text{O} \\ \parallel \\ \text{HO}-\text{C}_6\text{H}_4-\text{CH}_2-\text{CH}-\text{C}-\text{O}^- \\ \\ \text{NH}_3 \\ + \end{array}$
11.	dl-Lysine monohydrochloride:	$\begin{array}{c} \text{O} \\ \parallel \\ \text{Cl}^- \quad \text{H}_3\text{N}^+-\text{CH}_2-\text{CH}_2-\text{CH}_2-\text{CH}_2-\text{CH}-\text{C}-\text{O}^- \\ \\ \text{NH}_2 \end{array}$
12.	Serine:	$\begin{array}{c} \text{O} \\ \parallel \\ \text{HO}-\text{CH}_2-\text{CH}-\text{C}-\text{O}^- \\ \\ \text{NH}_3 \\ + \end{array}$

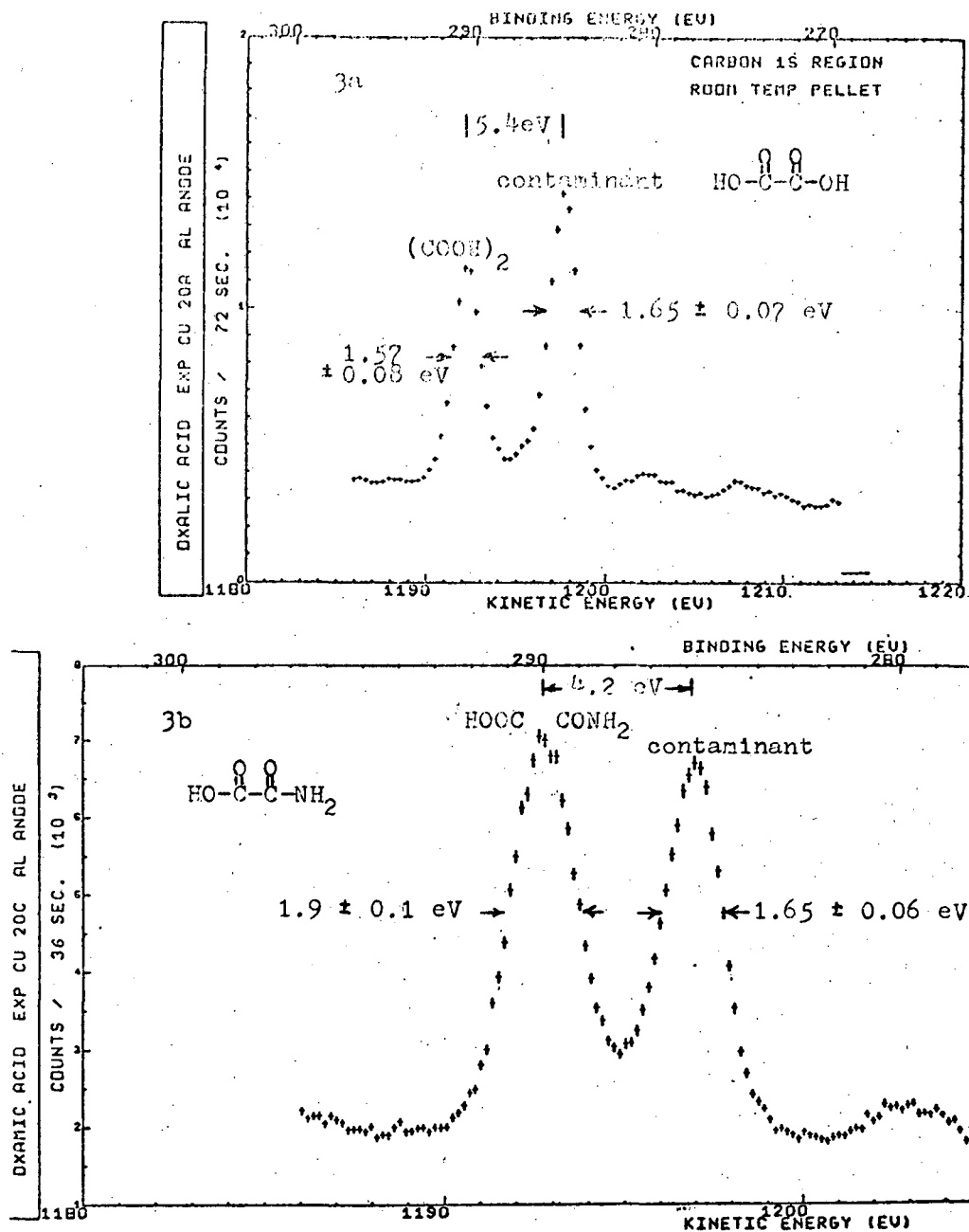
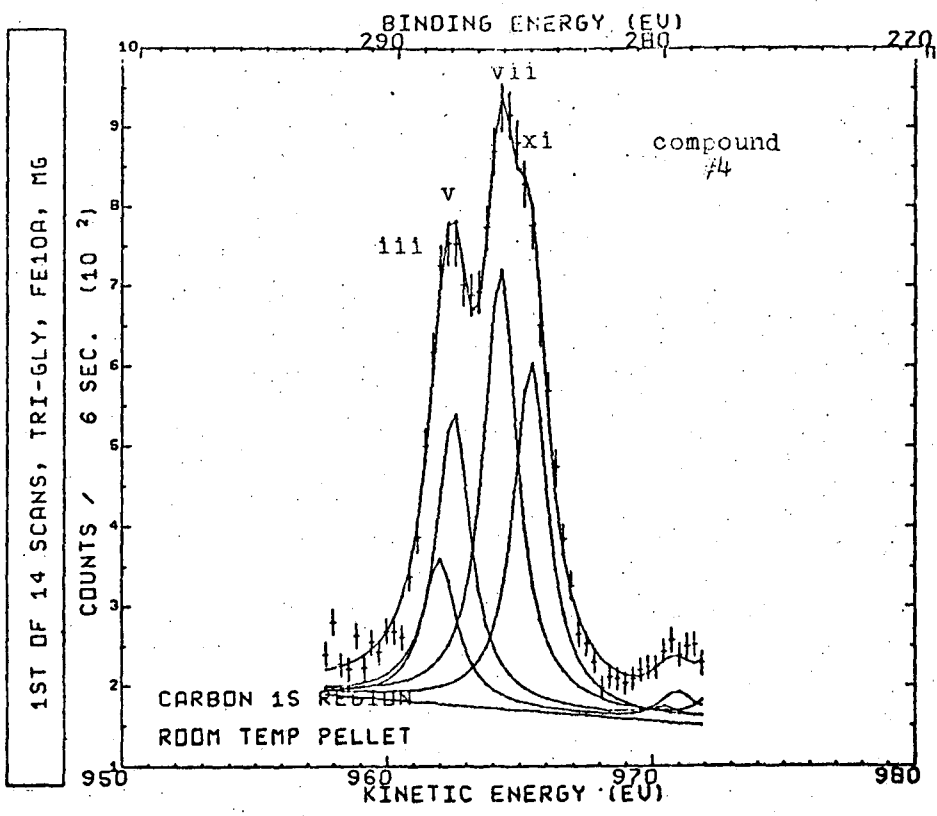
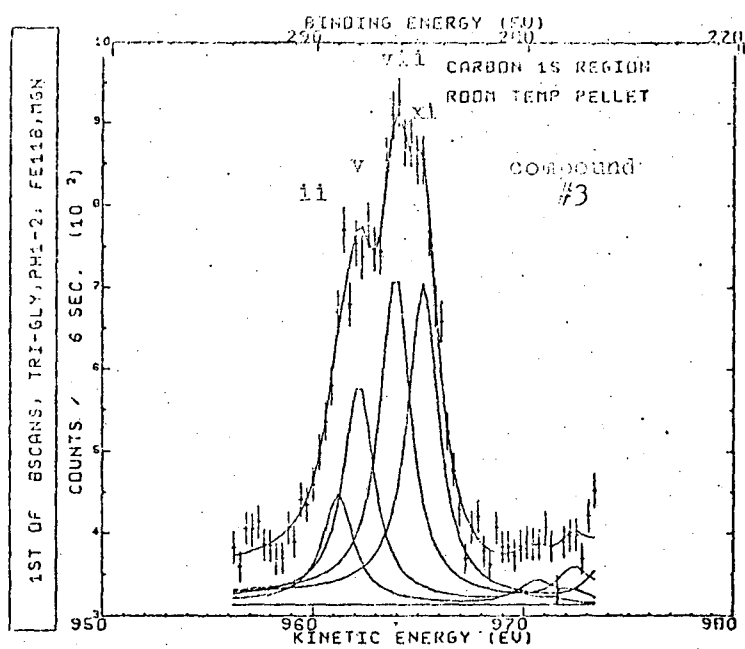
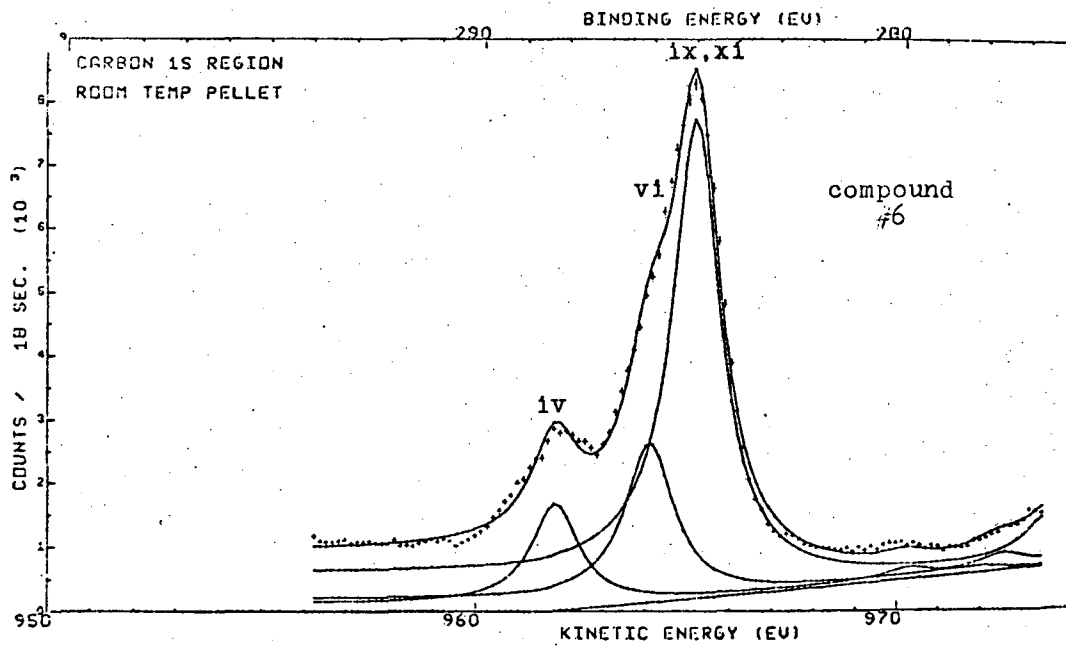
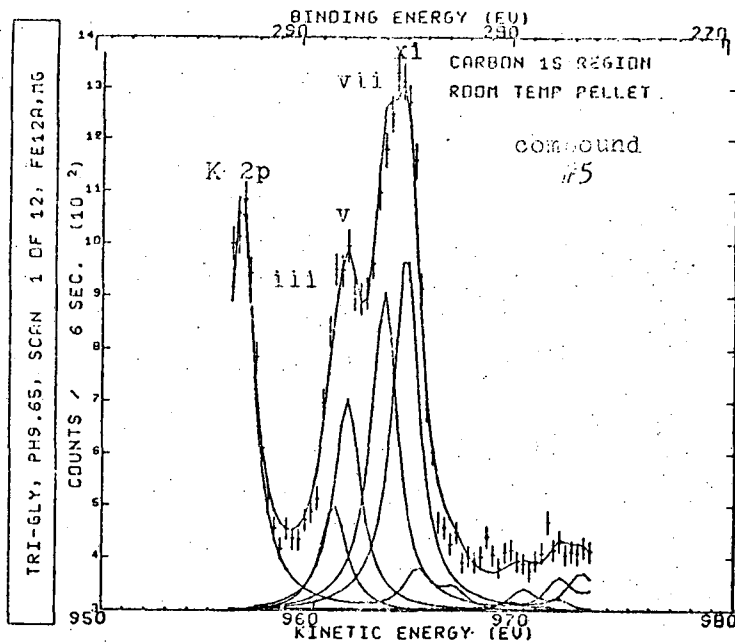
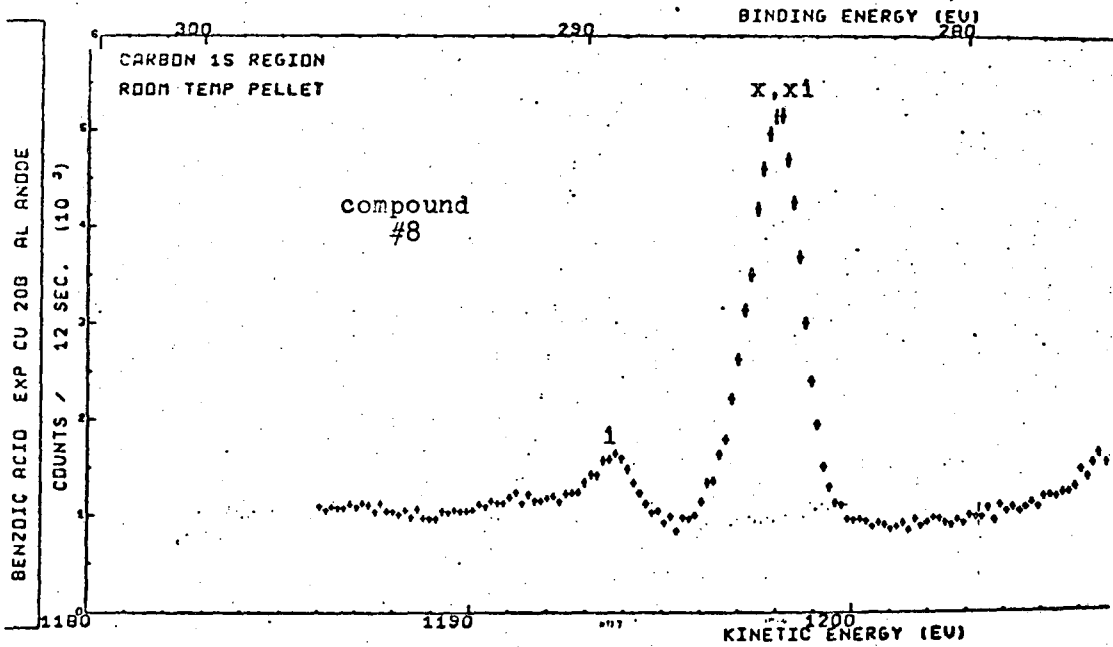
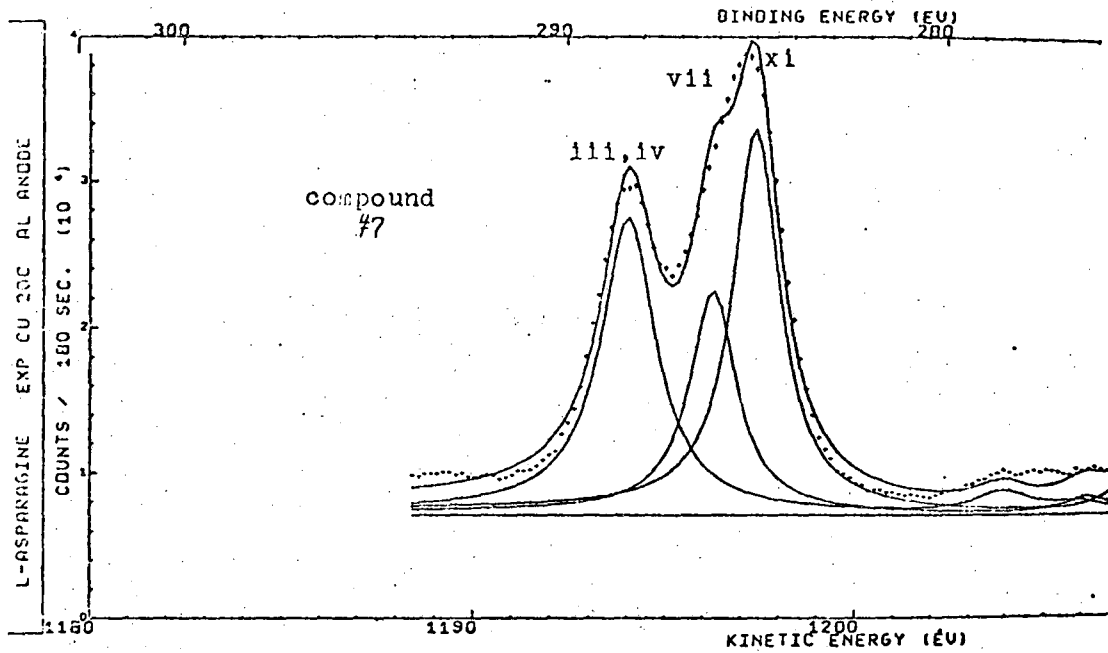


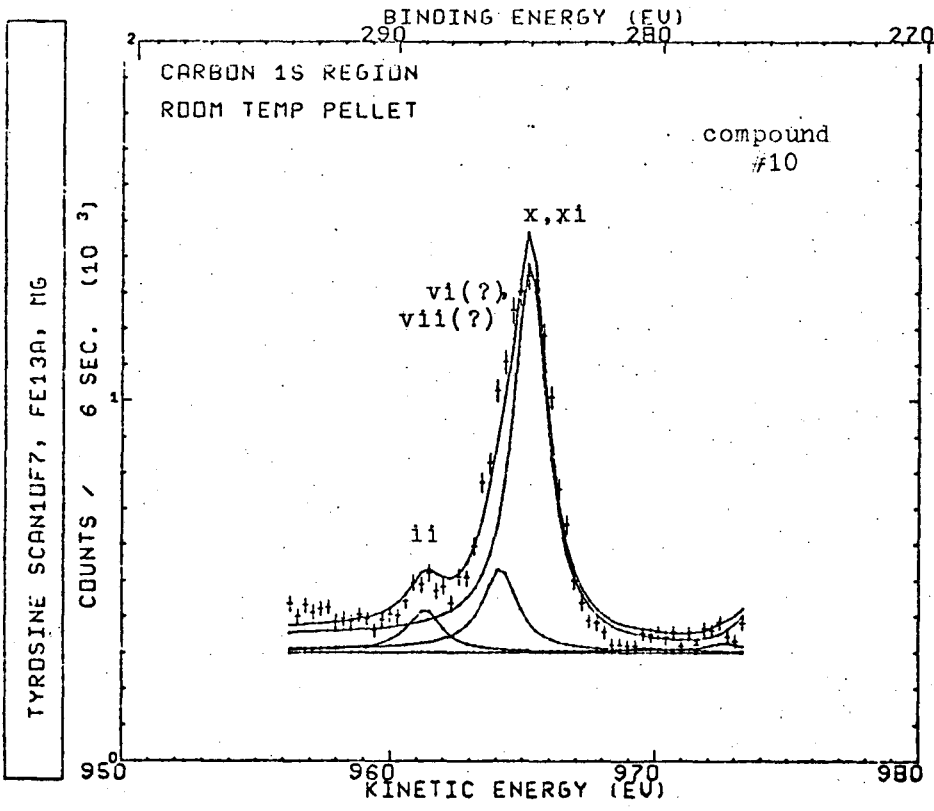
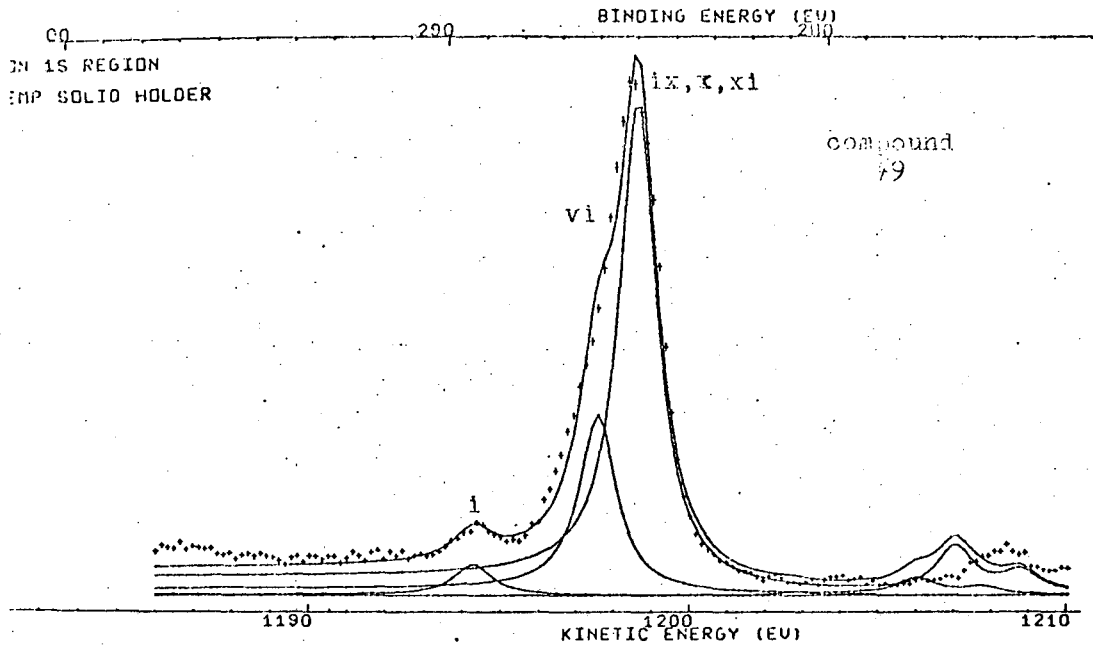
Figure 3. (a) C 1s spectrum of oxalic acid ($AlK\alpha$).
 (b) C 1s spectrum of oxamic acid ($AlK\alpha$). The wide peak at high binding energy was decomposed into two lines corresponding to COOH and $CONH_2$ (FWHM = 1.3 ± 0.1 eV).

Figure 4. C 1s spectra of compounds used in the C 1s binding energy scale. The spectra are identified according to the compound numbers listed in Table I. The line assignments are given above the respective lines in lower case Roman numerals according to the functional group listing in Table II. Most of the background slopes have been fixed flat. In all spectra except #7, the FWHM of all lines in a given fit were constrained to be the same. The calculated FWHM's fell in a range of 1.5 ± 0.2 eV. The spectra of compounds #1 and #2 were shown in Fig. 3.









-111-

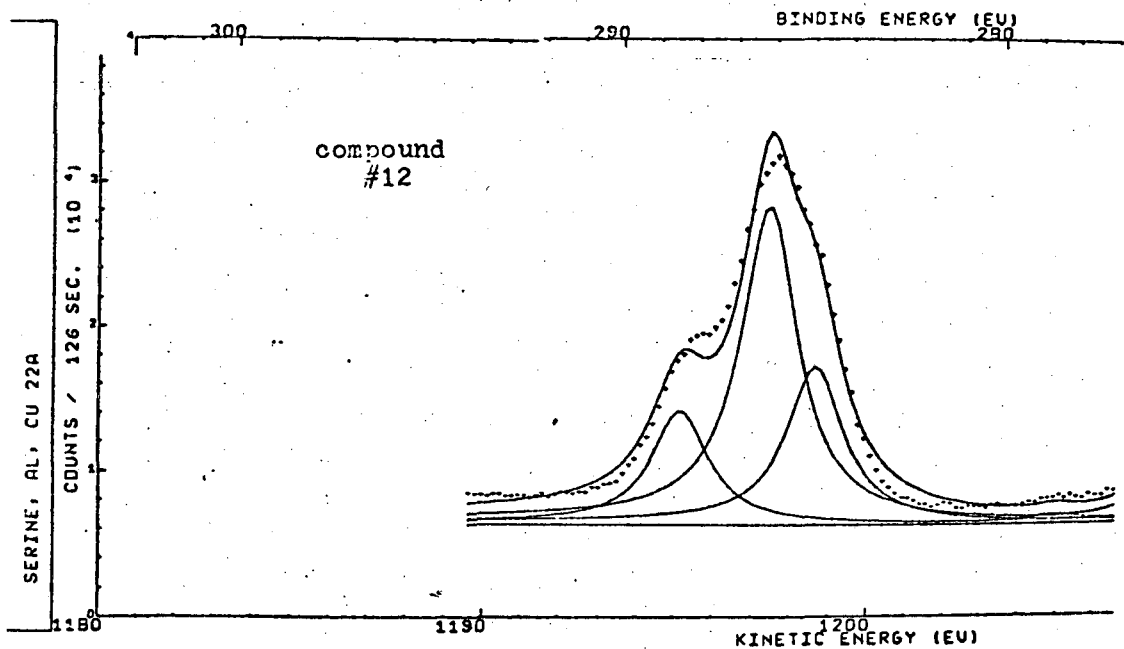
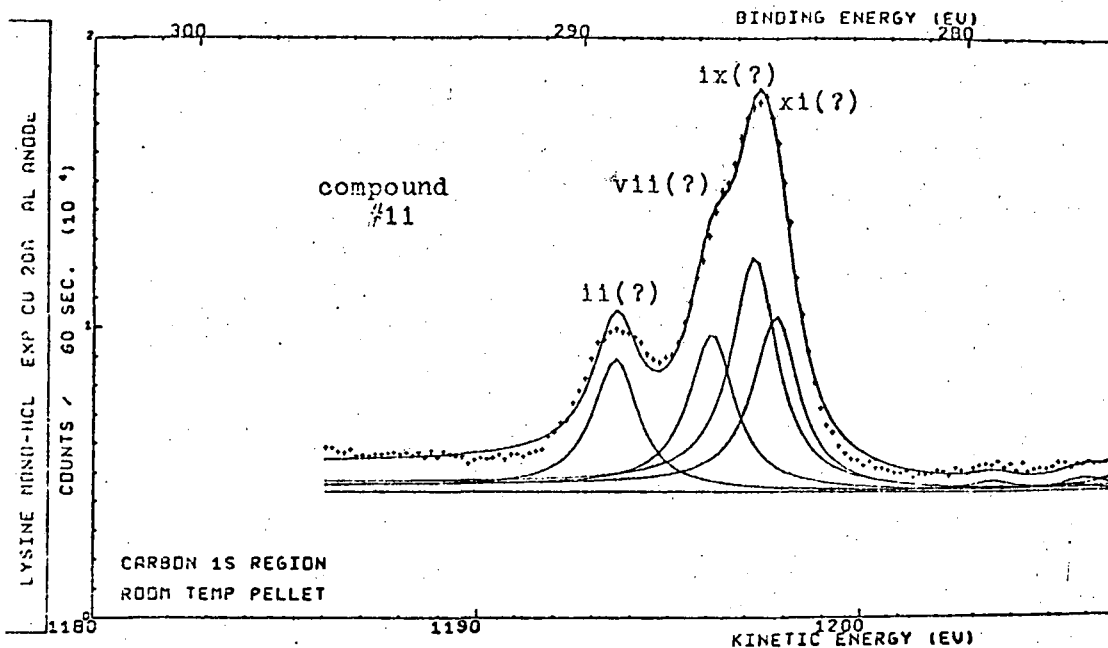


Table II. Carbon 1s binding energies for biological compounds. Aliphatic, aromatic, and contaminant carbon have been assigned a binding energy of 285.0 eV by definition. The other carbon 1s binding energies were derived by their separation from the aliphatic/aromatic/contaminant line. Therefore, the errors in the binding energies are the same as the errors in the separation given in the third column.

No.	Group	Structure	Separation from Aliphatic/Aromatic/Contaminant Line (eV)	Binding Energy (eV)	Observed in Compound No.
i.	Carboxyl	R-COOH	4.2 ± 0.2	289.2	8, 9
ii.	Amino acid carboxyl	$\begin{array}{c} \text{H} \\ \\ \text{R}-\text{C}^*-\text{COOH} \\ \\ \text{NH}_3^+ \end{array}$	4.0 ± 0.1	289.0	3, 10
iii.	Amino acid carboxylate	$\begin{array}{c} \text{H} \\ \\ \text{R}-\text{C}^*-\text{COO}^- \\ \\ \text{NH}_2 \end{array}$	3.4 ± 0.1	288.4	4, 5, 7
iv.	Unsubstituted amide	$\begin{array}{c} \text{O} \\ \\ \text{R}-\text{C}-\text{NH}_2 \end{array}$	3.3 ± 0.1	288.3	6, 7
v.	Peptide amide	$\begin{array}{c} \text{O} \\ \\ \text{R}-\text{C}-\text{N}-\text{R}' \\ \\ \text{H} \end{array}$	2.9 ± 0.2	287.9	3, 4, 5
vi.	Hydroxyl & ether	$\begin{array}{c} \text{R}-\text{CH}_2-\text{OH} \\ \text{R}-\text{CH}_2-\text{O}-\text{R}' \end{array}$	1.1 ± 0.2	286.1	6, 9(?), 10(?)
vii.	Peptide α carbon	$\begin{array}{c} \text{O} \\ \\ \text{---N---CH}^*-\text{C---N---} \\ \quad \quad \\ \text{H} \quad \text{R} \quad \text{H} \end{array}$	1.1 ± 0.1	286.1	3, 4, 5, 7, 10(?)
viii.	Carbon α to COOH	$\begin{array}{c} \text{R}-\text{CH}_2^*-\text{COOH} \end{array}$	0.0 to 1	~285.5	---
ix.	Aliphatic	-(CH ₂) _n -	0.0 (defn.)	285.0	5, 19, 11(?)
x.	Aromatic	-(CH) _n -	0.0 (defn.)	285.0	8, 9, 10
xi.	Contaminant hydrocarbon film	?	0.0 (defn.)	285.0	ALL

Inspection of Fig. 4 shows that the raw data are quite broad. From the previous chapter, it is known that SUNDER cannot make a reasonable fit of multiple lines under a peak without structure unless the programmer puts constraints on some of the lineshape parameters.

To assist SUNDER, the data were fit with a line representing each functional group plus an aliphatic contaminant line. Often, the area ratios were fixed to correspond to the known molecular structure. This technique was used when fitting the first of several scans because radiation damage was minimum. As a check for radiation damage, the last of several scans was also fit. Since damage was suspected, it was not reasonable to fix the area ratios according to the undamaged molecular structure. In these cases, the line separations obtained from the fit of the first scan were fixed into the fit of the last scan. Data accumulated over several scans were the most difficult to fit because they contained radiation damage incurred during the later scans, and there was no basis for fixing line separations.

These techniques permit SUNDER to converge on these sets of data. Of course, several combinations of lines were made to fit each set of data; although, most of these fits could not be interpreted in terms of a reasonable molecular structure. The fits shown in Fig. 4 are by no means unique. It can only be said that the binding energies derived from each fit are reasonably consistent with the other fits, and with other binding energy scales,¹⁹ and with the molecular structure. A definitive scale requires a higher resolution instrument.

Lindberg²³ found that the binding energy of methyl and aliphatic C 1s signals to be 285.0 and 285.4 eV respectively. Gelius¹⁹ referred

the binding energies of the compounds in his series to the hydrocarbon contaminant film's C 1s at 285.0 eV. For the purposes of this study, it is assumed that the spectrometer and SUNDER fitting program cannot distinguish the C 1s signals from methyl, aliphatic, aromatic, and contaminant hydrocarbon sources. The C 1s binding energy of all these species is given the value of 285.0 eV.

For these experiments, tri-gly (Sigma Chemical Co., lot #31C-2760) was lyophilized from a solution of pH 0.92 (HCl) for compound #3, taken directly from the bottle (a carefully prepared solution had a pH of 5.6) for #4, and lyophilized from pH 9.6 (KOH) for #5. Tri-gly would not lyophilize from pH 13 or 11. The sample in this experiment dried almost completely; it had the texture of dry paste. The others were dry powders. Samples 3, 4, and 5 were pressed into pellets in a steel die at 2000 psi, 500 psi, and thumb pressure, respectively. They were mounted on gold coated sample plates; no gold showed in the spectra.

Fig. 4 shows only the first scan from each experiment. SUNDER was instructed to fit each spectrum with three lines in a ratio of 1:2:3 corresponding to amino acid carboxyl(ate), peptide amide, and peptide α carbons. The ratios were derived by inspection of the structures in Table I. A fourth line was fit with its area free to vary, corresponding to the contaminant carbon signal. All separations between lines were left free.

Fig. 4 shows that these fits were very successful in reproducing the experimental data. The separation of each line from the contaminant signal (4.03, 3.05, 1.32 eV in #3; 3.45, 2.92, 1.15 eV in #4; 3.41, 2.76,

1.04 eV in #5) seems to decrease as the pH is increased. Protonation seems to shift all of the functional groups, even the neutral amide and α carbons, to a higher binding energy.

The amino acid carboxyl(ate) carbon is seen in #4 and #5 to be 3.4 ± 0.1 eV from the contaminant line. Gelius observed a separation of 3.1 eV for the carboxylate carbon of sodium glycinate. The agreement is acceptable. It is interesting that Gelius observed the carboxylate of sodium acetate to be 4.0 eV from the contaminant C 1s, an increase of 0.9 eV in comparison to the glycinate. Similarly, the amino acid carboxyl line of sample #3, pH 1-2, was observed 4.0 eV from the contaminant line. The carboxyl lines of the benzoic acid samples, #8 and #9, were found at slightly higher binding energy, and Gelius observed a 4.5 eV shift of COOH from the contaminant signal on frozen acetic acid. The amino acid carboxyl group has a lower binding energy than R-CO₂H. Apparently, the -NH-CH₂-CO₂H structure lends stability to the COO(H) carbon. SCF calculations on glycine and glycylglycine³² indicate that COO⁻ carries a 0.4 atomic charge, but no comparison was made with acetate.

5-hydroxyvaleramide (Aldrich, lot #060261), sample #6, was taken directly from the bottle and pressed into a 1/2" diam. pellet at 4000 lb. The spectrum in Fig. 4 shows the first scan out of a series of five. The FWHM of the main line is 1.36 ± 0.1 eV. It would be difficult and dubious to separate the main line into aliphatic and contaminant contributions. Thus, the assumption that these signals have the same binding energy is justified. The line separations and area ratios are all free to vary. The ratio between the amide and hydroxyl lines, marked iv and

vi, respectively, in Fig. 4, should be equal. Within the limits of SUNDER's accuracy, they might be. One could also postulate decarboxylation in the radiation flux even in the first scan.

Sample #7, *l*-asparagine was pressed into a 1/2" diam. pellet with 9 tons of force. Figure 4 shows the C 1s spectrum accumulated over six scans. There is a region of 3-4 channels near the crest of the larger peak that SUNDER could not fit without completely artificial parameter fixing. The figure shows the most reasonable fit. All separations are free. The FWHM of the highest binding energy line was free to differ from the other two; it was calculated to be 1.76 ± 0.08 eV, and the other two were 1.49 ± 0.05 eV. The former corresponds to amide and carboxylate carbons that are slightly separated. The smallest line fell on the same position as the peptide α carbon of the tri-gly, pH 5-6. From the asparagine structure in Table I, it is reasonable to assign this line to the amino acid α carbon. The largest line is complicated by the presence of the CH₂ group. This CH₂ carbon should be shifted slightly from the aliphatic position by the adjacent amide group. The largest line, therefore, represents contaminant carbon plus a shifted CH₂ group.

Benzoic acid, sample #8, and paraoxybenzoic acid, #9, illustrate the difficulty of locating the carbon α to COO(H), but without the -NH₂ group characteristic of the amino acids. Both samples were pressed into 1/2" diam. pellets at 9 tons. The benzoic acid spectrum from a single scan shows a large peak due to aromatic carbon. (There may not be a contaminant contribution here because the benzoic acid sublimed in the vacuum during the experiment.) Bus²⁴ observed the 1s of carbon α to

COO(H) at 285.6 eV, i.e., 0.6 eV from the hydrocarbon contaminant line. Gelius¹⁹ observed α carbon 1s at 0.0 to 0.3 eV from the contaminant line. Presumably, therefore, an α carbon line might lie from 285.0 to 285.6 eV in the present study. It certainly cannot be located reliably with the samples and techniques used here. However, the aromatic and carboxyl peaks are distinctly visible; they are separated by 4.2 ± 0.2 eV.

The paraoctyloxybenzoic acid spectrum is more complicated. It is the sum of six scans. The molecular structure shows that there are at least four chemically different kinds of carbon: carboxyl, hydroxyl and etheryl, α to COOH, aliphatic, aromatic, and contaminant carbon. SUNDER cannot fit all these contributions to spectrum #9 in Fig. 4. The carboxyl peak is weak but discernible. The last four contributions can be assigned to the main line. The hydroxyl and etheryl carbons can be assigned to the intermediate line, which is in the same location as the hydroxyl carbon of #6. This consistency is encouraging, but a definite conclusion cannot be made because the quality of the fit is only fair. All separations and area ratios were free.

Tyrosine was pressed into a pellet at 1000 psi and mounted on a gold coated sample plate. There was no gold in the spectrum. The same problems encountered in #9 are observed here. The intermediate line at 286.1 eV should represent a peptide α carbon and a hydroxyl carbon. Repeated fits continued to put a line in this position within ± 0.2 eV. The peptide α carbon was observed here in #6. The assignment of the line is, therefore, consistent with the other data, but because of the marginal statistics, the fit does not stand by itself as evidence. The

data show the first of seven scans; the ratio of the carboxyl line to the intermediate line was fixed at 1:2; all separations were free.

The lysine spectrum is the only one that seems to agree with the assignment of different binding energies to aliphatic and hydrocarbon contaminant carbon. The two lines at low binding energy could conceivably be assigned to aliphatic and contaminant carbon. They are separated by 0.6 eV. The other two lines correspond to peptide α and carboxyl carbon. However, the area ratios in this fit cannot be reasonably interpreted in terms of lysine's molecular structure. In particular, the locations of $-\text{CH}_2-\text{NH}_2$ and $-\text{CH}_2-\text{NH}_3^+\text{Cl}^-$ carbons are not accounted for in this interpretation of the fit. To obtain spectrum #11 it was necessary to fix the position of the largest line. The difficulty in making an acceptable fit can probably be attributed to instability in the sample from various sources:

1. Radiation damage (the spectrum is the sum of five scans);
2. Loss of HCl in the vacuum;
3. The monohydrochloride should be found on the ϵ amino group according to the pK values of lysine,²² but the actual sample is probably an equilibrium mixture of protonated ϵ and α amino groups.

The serine (1/2" diam. pellet pressed at 6000 lb) spectrum does not agree with the data in this work or that of Gelius. Qualitatively, the lines shown in spectrum #12 would be assigned to carboxylate, hydroxyl

plus peptide α , and contaminant carbon. The separations were fixed according to this model based on the separations observed in the other spectra. The poor quality of the fit shows that this model is not consistent with the serine data. The assignment of this spectrum remains undetermined.

All the samples in this study were irradiated with Mg or $AlK\alpha$ x-rays through a 0.0005" beryllium window. The x-ray tube was operated at 12 kV and 20 mA. From the first chapter (Table III) it was learned that an organic sample exposed to the same tube operated at 12 kV and 30 mA absorbed radiation at the rate of $10^6 - 10^7$ rad/sec. 95% of this dose was due to the characteristic $K\alpha$ radiation of the anode. The samples are expected to react to such a high dose level. Furthermore, the x-ray tube shared a vacuum in common with the sample vacuum. It was possible for decomposition products from the sample to foul the anode surface being bombarded by cathode electrons. The effects of radiation on the compounds in this study are given in Table III and in Figures 5, 6, and 7.

Figure 5 shows the pH 1-2 tri-gly sample. Eight scans of the C 1s region were taken. The first scan is shown in Fig. 5a; it has already been seen in Fig. 4; the assignment of the lines in this fit was discussed there. The area ratios of the first three lines were fixed at 1:2:3 according to the molecular structure. The area of the fourth (contaminant) line was left free. All the separations were left free.

Fig. 5b shows the seventh scan in the series. Radiation damage was suspected; so, it was not sensible to fix the area ratios according to the undamaged molecular structure. Therefore, to aid SUNDER, four

Table III. Effects of soft x-rays (about 1 keV) on the compounds in the carbon 1s binding energy study.

No.	Texture, Color Before Exposure	Hours of X-Ray Exposure (12 kV, 20 mA)	Color After Exposure	Condition of X-Ray Anode
1.	White powder	2-1/2	White powder, no visible effect	Discolored due to #8
2.	"	2	"	"
3.	"	11	Lemon yellow	No effect
4.	"	11	Lemon yellow	Black smudge where e ⁻ struck anode
5.	White, dry paste	22	Yellow	No effect
6.	White powder	8	Light lemon yellow (Pellet 1 mm thick was even slightly yellow on backside due to high energy bremsstrahlung)	—
7.	"	9	Light green, turned brown upon exposure (hours to days) to air	Discolored due to #8
8.	"	1	Sublimed in vacuum	Severely discolored, bluish brown except where e ⁻ struck anode
9.	"	6	Slightly off white	Slightly discolored
10.	"	10	—	—
11.	"	1-1/2	Light green	Discolored due to #8
12.	"	7-1/2	Light green, turned brown upon exposure (hours to days) to air	No effect

-121-

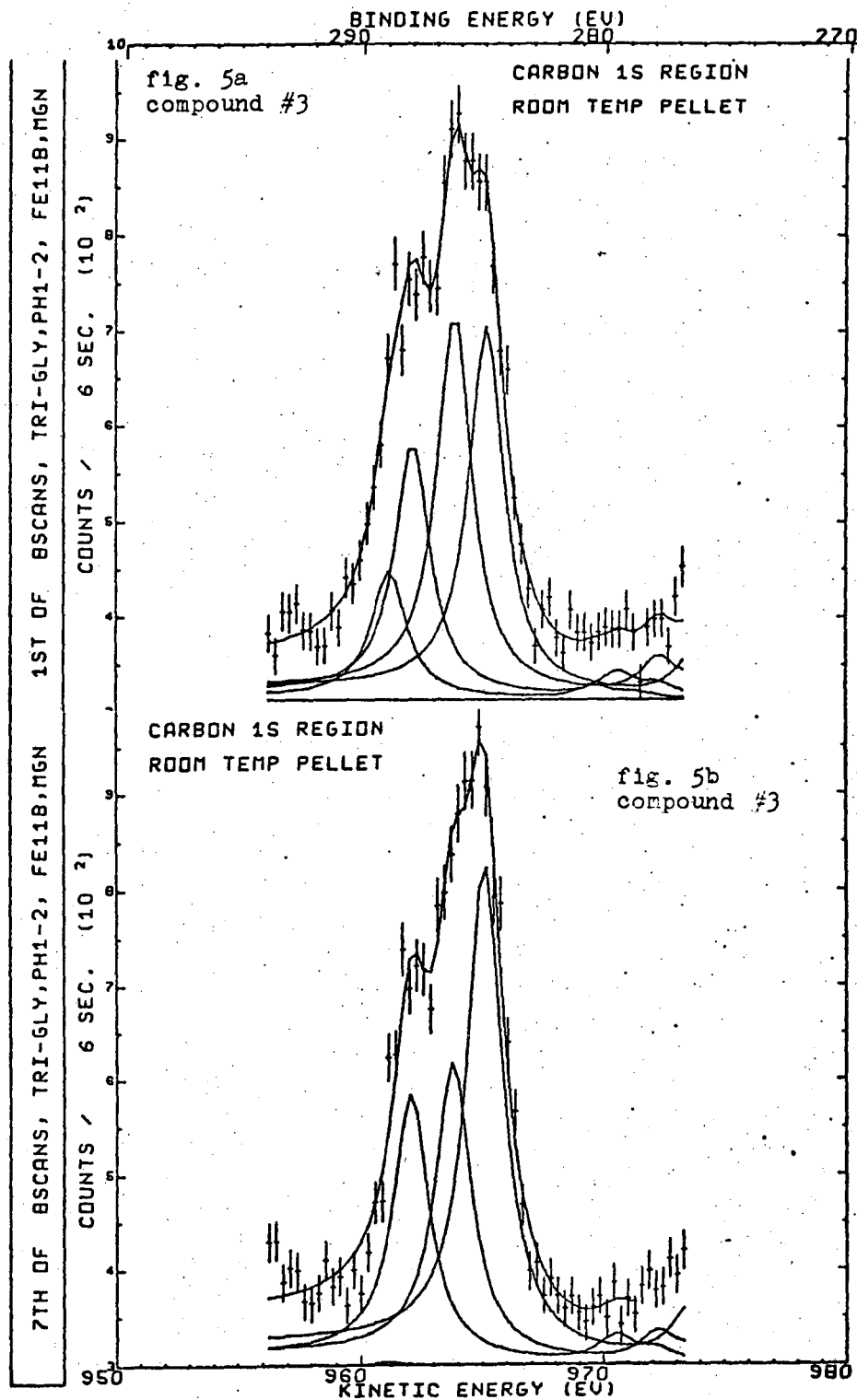
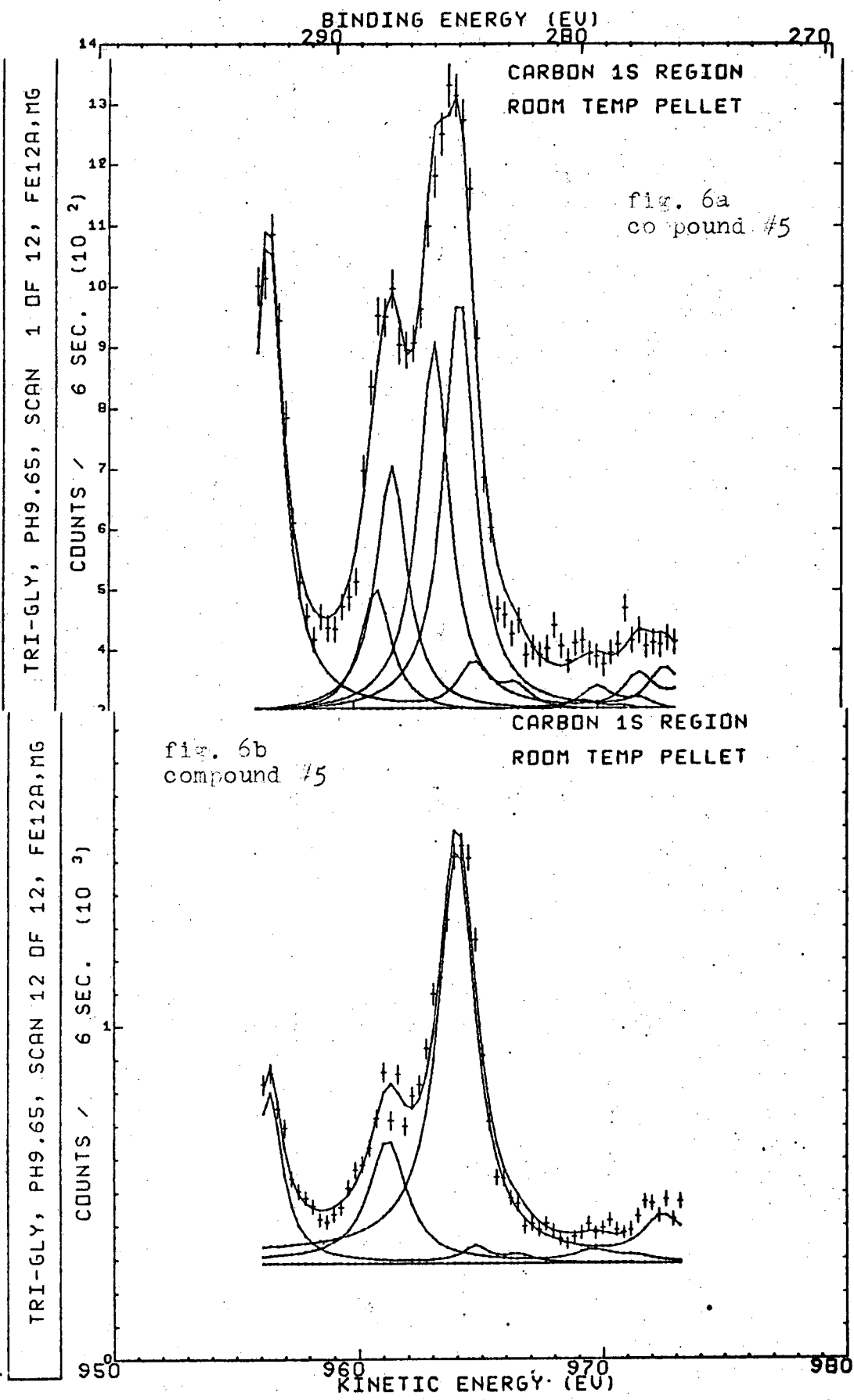


Figure 5. Data showing the first (5a) and seventh (5b) scans from a series of eight scans on the C 1s region of pH 1-2 tri-gly, compound #3. Three area ratios in (5a) were fixed at 1:2:3 according to the molecular structure in Table I. The line separations in (5b) were fixed to match those calculated in (5a). Decarboxylation is evident in the seventh scan (5b).

Figure 6. Data showing the first (6a) and last (6b) scans from a series of 12 scans on the C 1s region of pH 9.6 tri-gly, compound #5. The last scan (6b) could only be approximated with two lines under the C 1s data. The potassium 2p and carboxylate/peptide amide lines appear to have diminished relative to the peptide α /contaminant line. (Note the change of scale between 6a and 6b.) 6c shows a plot of the carboxylate/peptide amide line area and the peptide α /contaminant line area versus time. The carboxylate signal has dropped by 50% while the contaminant signal has remained constant. Fig. 6d and 6e show similar plots for the carbon 1s lines of N-acetyl tryptophanamide (see Table IV) and tri-gly, pH 1-2.



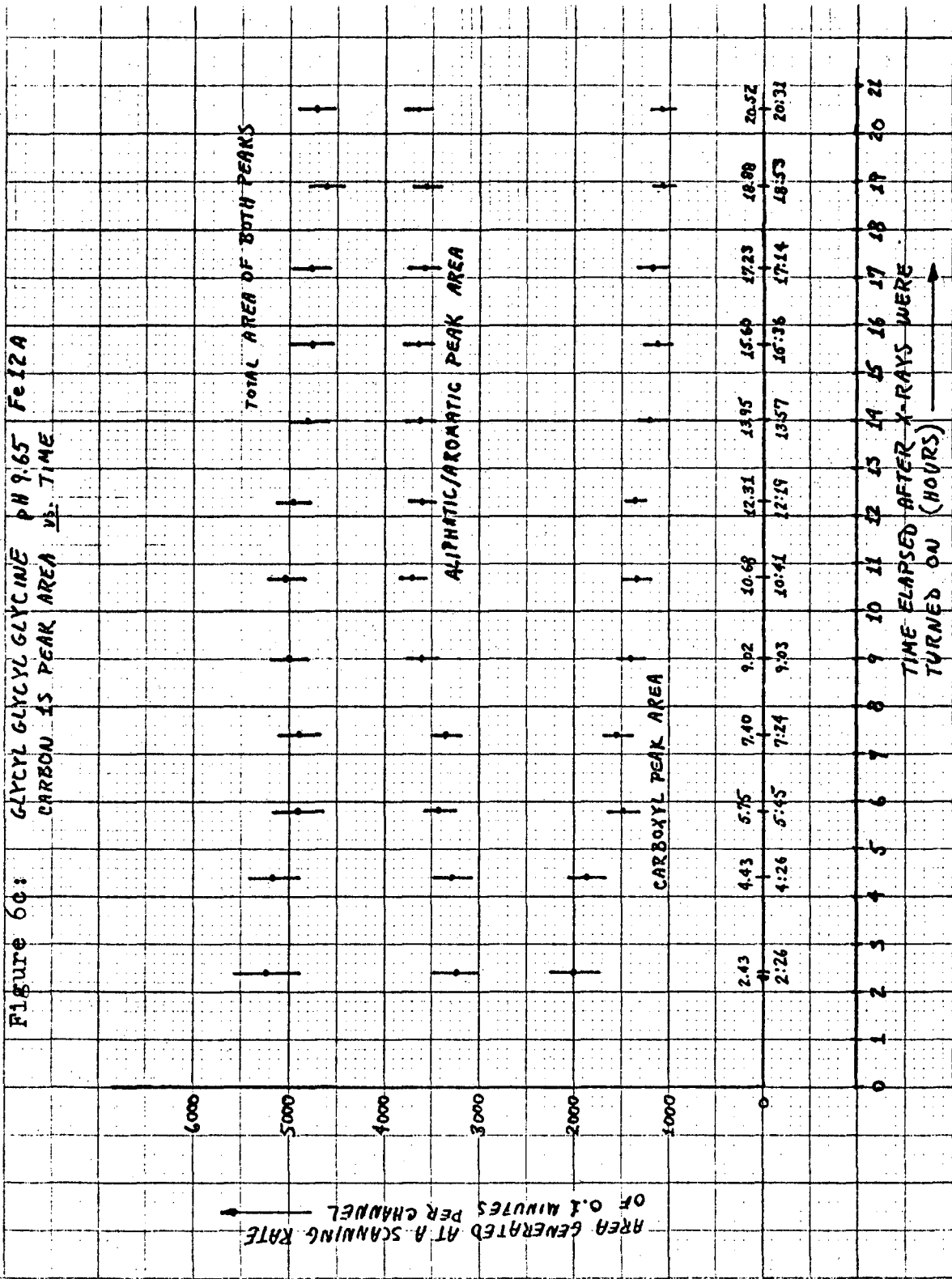


Fig. 6d

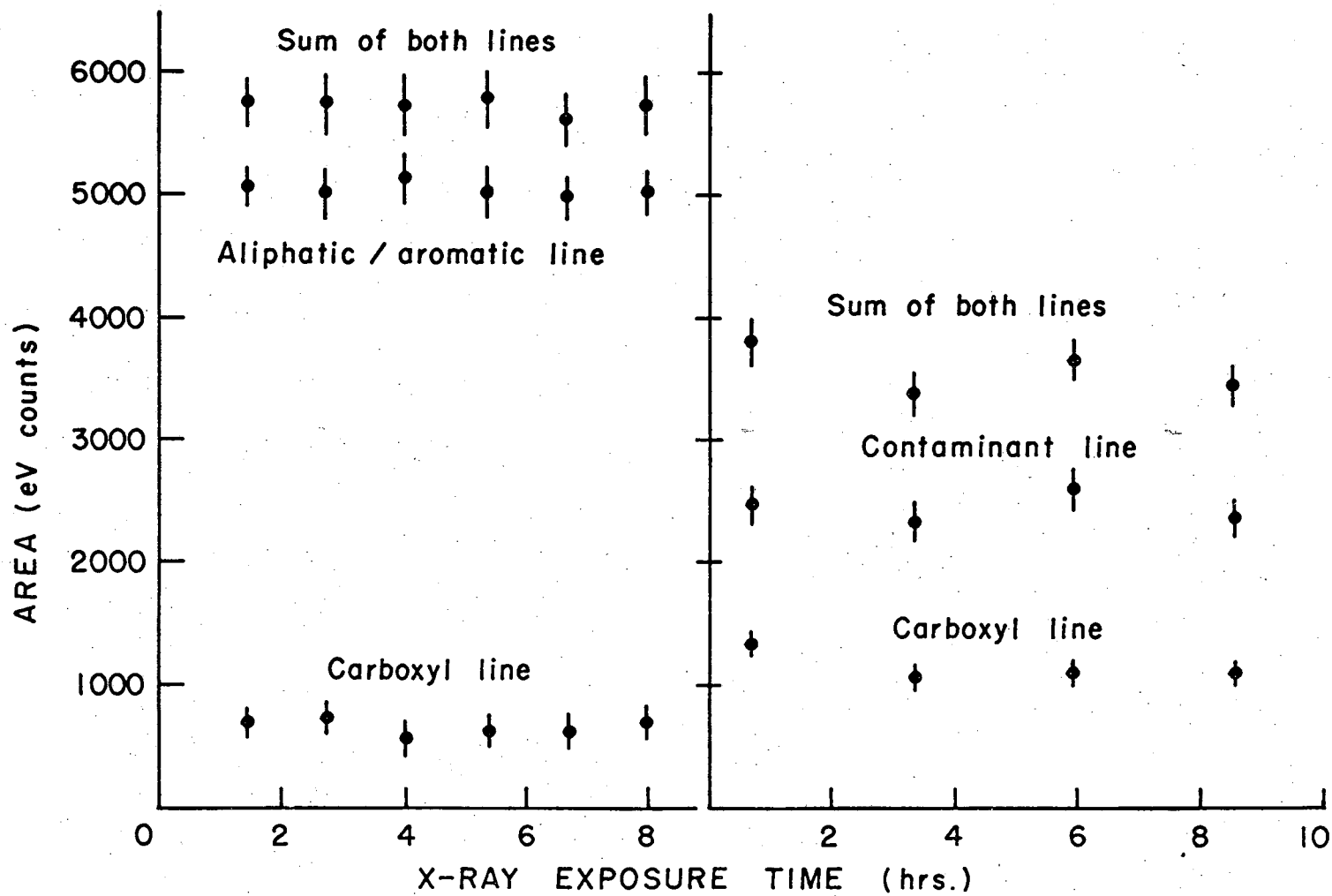


Fig. 6e

00004500794

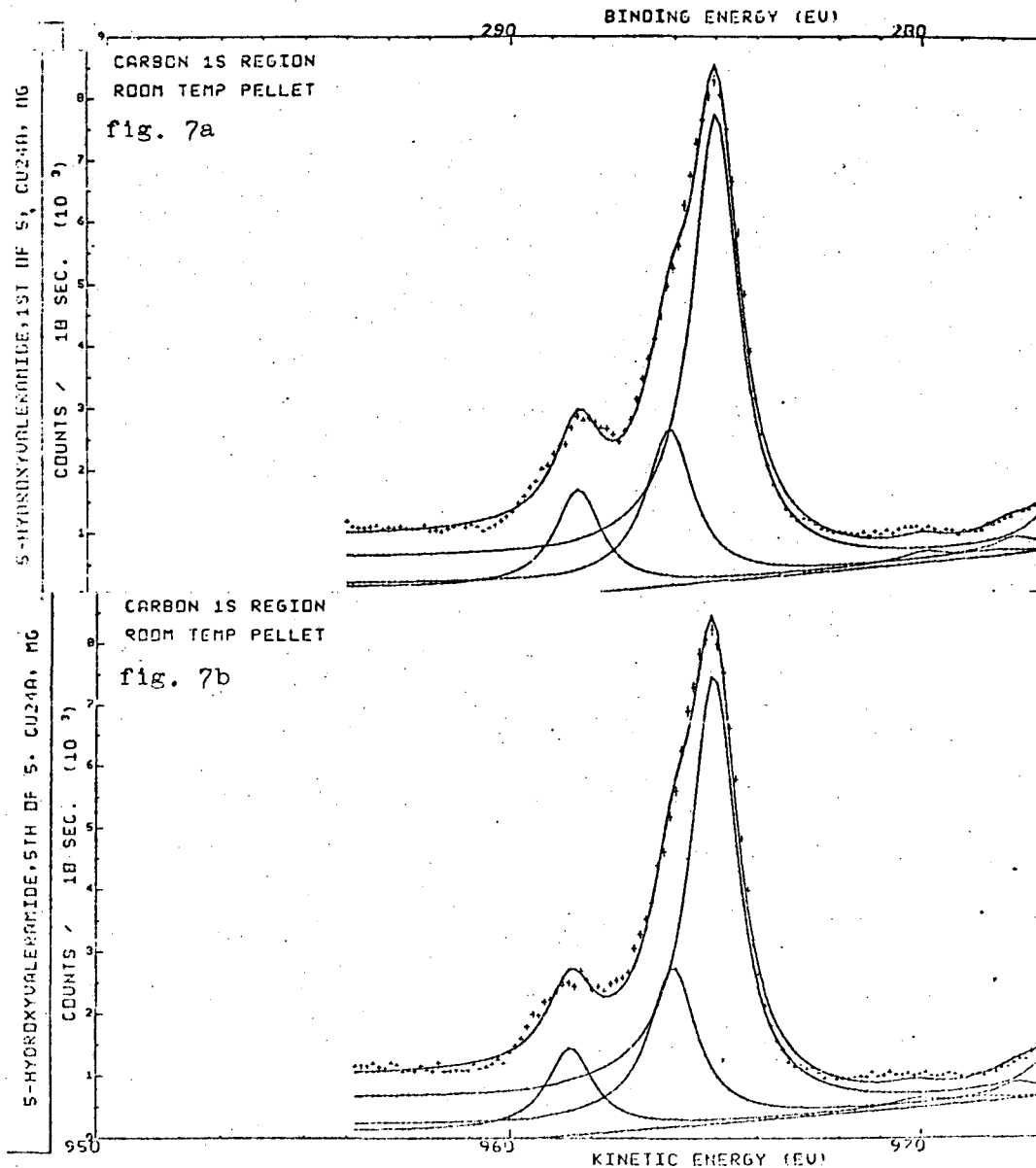


Figure 7. Data showing the first (7a) and last (7b) scans from a series of five scans on 5-hydroxyvaleramide, compound #6. All separations, area ratios, and background slopes were free to vary in these fits. The data are very stable in the x-ray flux.

-127-

lines were fit to the data in 5b with their separations fixed according to the fit observed in 5a. All area ratios were left free. Like 5a, the fit in 5b was very successful in reproducing the data, but the carboxyl line in 5b is apparently absent. In fact, a vestigial carboxyl line is barely discernible at 961 eV on the kinetic energy scale. The FWHM's of the individual lines in 5a and 5b are 1.7 and 1.8 eV, respectively; the carboxyl line was not lost by broadening. Furthermore, SUNDER could not fit a carboxyl line to these data by any reasonable parameter fixing technique. If the data from 5b are superimposed over 5a, the spectrum in 5b is clearly deficient in the carboxyl region. The tri-gly has definitely suffered decarboxylation in the x-rays. The contaminant line has also increased relative to the two remaining tri-gly lines.

Twelve scans over 22 hours were taken on the pH 9.6 tri-gly sample shown in Fig. 6. The first scan, Fig. 6a, has already been shown and discussed in Fig. 4. It was fit with three area ratios fixed at 1:2:3 and all separations free. The carboxylate line is clearly visible in the fit, but it is not well separated from the peptide amide line. Fig. 6b shows the last scan which has been approximated by two lines under the C 1s signal. These data had been fitted with four lines that had their separations fixed to match those in 6a, but the scatter of points in the carboxylate region did not permit a reasonable interpretation of this fit. It can be seen that the carboxylate/peptide amide line has been diminished relative to the peptide α /contaminant line. However, the potassium 2p line, which was presumed to be unaffected by radiation, had also diminished relative to the peptide α /contaminant line, but it is constant relative

to the carboxylate/peptide amide line. Either the potassium and carboxylate lines have diminished together while the contaminant was constant, or the potassium and carboxylate were stable while the contaminant layer grew on the surface during 22 hours in the vacuum.

All twelve C 1s scans were fit as two line approximations. The individual line areas and the total C 1s area were plotted *versus* x-ray exposure in Fig. 6c. The carboxylate/peptide amide line area fell by about 50% while the peptide α /contaminant line grew only slightly. The total C 1s area is roughly constant. Apparently, the potassium and carboxylate lines fell together, presumably representing the loss of a photolysis product in the form of a carboxylate salt. This interpretation must be tentative because salts have low vapor pressures. It is also possible that the x-ray anode became fouled and reduced the counts on all the lines while the contaminant layer grew on the surface. Thus, the potassium and carboxylate signals could be attenuated while the contaminant signal remained approximately constant. No firm conclusion can be drawn from these data alone.

The data from the first and last of five scans over the C 1s region of 5-hydroxyvaleramide are shown in Fig. 7a and 7b, respectively. Neither area ratios, separations, nor background slope were fixed in these fits. (Fixing the background slope to be flat made no significant difference.) It can be seen that this sample suffered almost no radiation damage after eight hours in the x-rays. The unsubstituted amide carbon line at binding energy 288.3 eV has been reduced by about 20%. The nitrogen line of this sample was not at all diminished; nitrogen lines are discussed

below. An amide carbon appears to be considerably more stable in the x-rays than the carboxyl carbon.

Radiation effects that are obvious to the naked eye are summarized in Table III. Certain generalizations are evident. All of the nitrogen containing samples, except #2, oxamic acid, changed color during irradiation. Oxamic acid's anomalous behavior may be due to the volatility of many of its possible decomposition products, e.g., CO_2 , formamide, ammonia, etc. The peptides turned from white to yellow. So did 5-hydroxyvaleramide, #6, which suggests that it is the amide function in the peptides that causes the yellow color. (The 1 mm thick pellet of 5-hydroxyvaleramide was even faintly yellow on the backside. 1 keV x-rays cannot penetrate 1 mm of organic material. The color must be due to the high energy bremsstrahlung shown in Fig. 22 of Chapter 1.) The amino acids turned from white to a light green. If the samples were permitted to come in contact with the atmosphere for a period of hours or longer, they would turn from green to a burnt brown. Lysine, #11, did not show this second color change because it was protected from the air. The samples that contained no nitrogen, #1 and #9, did not change color significantly from their original white.

The interpretations of the spectra shown above are consistent with the known radiation chemistry of amino acids. The published work was done in energies both above (meV range)³³⁻³⁷ and below (ultra-violet range)³⁸ the soft x-ray region. The results are still applicable to XPS because all radiation produces most of its chemical changes by secondary electrons.³⁹ Qualitatively, radiation effects are the same in all energy regions.

The evolution of CO_2 (and NH_3) from the irradiation of dry, solid glycine has been well documented.³³ Gottschall and Tolbert³⁴ studied dry glycine in vacuum with ^{137}Cs gamma rays (0.663 meV). After a dose of 160×10^6 rads (equal to two minutes exposure in the Berkeley iron-free spectrometer) 1 - 1-1/2 % of the glycine had decarboxylated to release CO_2 . Many other products were observed at less than 10% of the CO_2 quantities. These included: H_2CO , CH_4 , H_2O , α keto acids, and carboxylic acids. Effects similar to glycine are observed with other aliphatic amino acids such as alanine,^{33,34,37} isovaline,³⁷ and lysine.³⁷ Deamination will be discussed later in connection with nitrogen 1s lines.

The various products observed from these amino acids can be explained by a system of chemical reactions involving free radical intermediates.³⁴ These reactions must include radical degradations as well as direct radiation effects because the dose was 10^8 rads; whereas, most amino acids saturate with free radicals at 10^6 rads.³⁴ There are also reactions in the solid phase with electrons in the lattice, and it is suggested that there are radical reactions to regenerate the amino acids.³⁴

Aromatic amino acids often form $(\text{C}_6\text{H}_5)\cdot\text{CH}_2$, benzyl radicals.³⁷ Tyrosine loses -OH in dry irradiation³⁷ and gains -OH in aqueous irradiation.³³ It has been reported that tyrosine suffers little decarboxylation to tyramine.³³

A series of alkali metal glycinate salts showed increasing sensitivity to radiation as one descended the periodic table from Na^+ to Rb^+ .³⁴ A correlation is suggested between the metal's electronegativity and radiation stability; a similar correlation between electron density

at the oxygen atom and radiation stability has already been treated.³⁵ However, such correlations only involve a factor of two in stability, and a factor of two is insignificant for the extended exposures at the high dose rate of the Berkeley spectrometer.

In summary, a self-consistent scale of C 1s binding energies for biologically significant functional groups has been developed. Spectrometer resolution was usually inadequate to distinguish the important functional groups; so, it was necessary to use the SUNDER fitting program to interpret the data. SUNDER could not converge on the data unless the programmer aided it by fixing certain parameters. The scale, therefore, suffers in that it may have some artificial prejudice from the programmer built into it.

Actually, the possibility of prejudice is not a problem because the most logical references for protein work are the carboxyl(ate) and peptide α -carbon lines. Both of these lines are resolved as separate peaks or distinct shoulders from the rest of the carbon data. It was learned in Chapter Two that SUNDER can fit such data with reliable accuracy.

The scale provides for internal referencing of biological spectra, which avoids problems of crystal potentials and charging. By contrast, the most commonly used external reference for this kind of work is the hydrocarbon contaminant line. Although it is subject to charging and work function differences, it is generally adequate for a homologous series of proteins and peptides. Finding the contaminant line in the C 1s spectrum also involves all of the artificial techniques used in constructing the internal binding energy scale.

Radiation damage and vacuum effects seem to be an unavoidable problem in these experiments at this time. The carboxyl(ate) line diminishes in the radiation flux; although, it survives long enough to locate its position in the first few scans. The build-up of the contaminant signal can obscure the C 1s spectra of extended runs. Unsubstituted amides are stable in the radiation, or perhaps they are so unstable that they are damaged before the first C 1s scan is completed. In the latter case, the decomposition products appear to be stable in these spectra. There are color changes which might be attributed to the bonding of the nitrogen in each sample, but the observations are not sufficiently extensive to permit a firm conclusion.

Improvements on the weaknesses in the internal binding energy scale await more sensitive apparatus. The present scale is the best that can be done with the present equipment and the SUNDER program.

C. Nitrogen 1s as an Internal Reference

Nitrogen in proteins is generally found in the same functional groups. The majority of the nitrogen is usually found in the amide linkages that form the chain structure of the molecule. Almost all the rest is in the form of free amino groups, unsubstituted amides, and heterocyclic ring systems. These groups are found on the side chains of lysine and arginine, asparagine and glutamine, and tryptophan, histidine, and proline, respectively.

Since the peptide amide linkage is common to all proteins and is not obscured by vacuum contaminants, the peptide amide nitrogen 1s signal was investigated as a possible alternative to carbon 1s as an internal reference for biological compounds. Experiments were performed to see if the peptide nitrogen 1s could be distinguished from the other biologically significant forms of nitrogen, and to examine the stability of the nitrogen 1s signal in the radiation flux.

The compounds that were used in this study are shown in Table IV. Those materials that were also used in the carbon 1s study have been given the same compound number as in Table I. Binding energies and FWHM's are given in Table V. The data are shown in Figure 8.

The FWHM's seem to group around a value of 1.7 ± 0.1 eV except for three samples (#6, 14, 15) that have a FWHM of 1.4 ± 0.1 eV. Of these three samples, #6 and #14 show that the FWHM expands from 1.4 eV to 1.7 eV as the experiment progresses through several scans. The FWHM of #15 expands to 1.5 eV over six scans. The FWHM of #10 varies from 1.4 to 1.9 eV over six scans; #13 shows a variation from 1.5 to 1.9 eV over 15 scans. I conclude that, in the Berkeley iron-free spectrometer, the minimum 1s FWHM for an unperturbed nitrogen atom in a pure sample is 1.4 eV. Protonation and exposure to radiation can broaden the FWHM to 1.7 ± 0.2 eV.

The ability of XPS to distinguish a peptide amide nitrogen from a free α -amino group is shown in the sequence of tri-gly spectra shown in Fig. 8. The preparation of the samples was given with Fig. 4. In the pH 1-2 sample, the amino group is expected to be protonated, and its N 1s

Table IV. Compounds used in nitrogen 1s binding energy study.

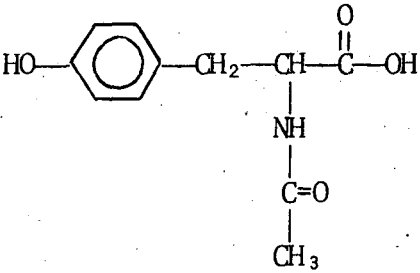
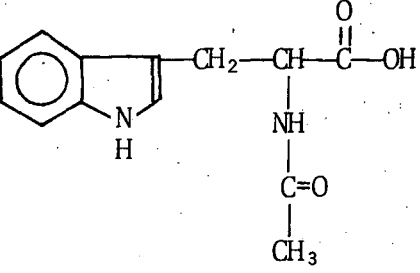
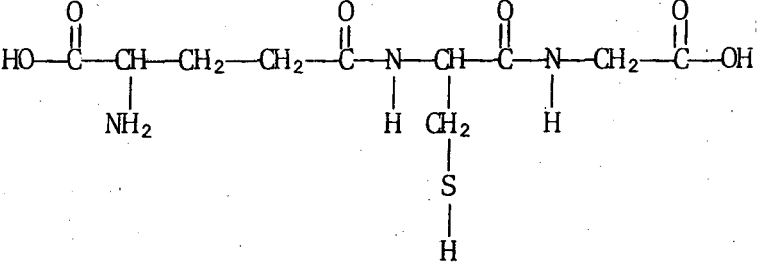
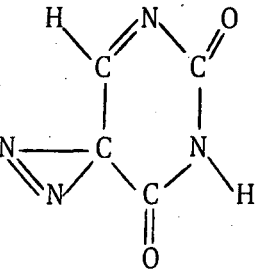
No.	Name	Structure
3.	Tri-gly, pH 1-2:	See Table I
4.	Tri-gly, pH 5-6:	"
5.	Tri-gly, pH 9.6:	"
6.	5-Hydroxyvaleramide:	"
10.	L-Tyrosine:	"
13.	N-Acetyl tyrosineamide:	
14.	N-Acetyl tryptophanamide:	
15.	Reduced glutathione:	
16.	5-Diazouracil:	

Table V. Binding energies of nitrogen 1s lines.

No.	Scans	Carbon 1s Reference Line	C 1s Binding Energy (eV)	Nitrogen 1s Binding Energy (eV \pm 0.2)	Nitrogen 1s FWHM (eV)	Separation (eV)
3.	1st scan out of 8	peptide amide	287.9	401.6 399.9	1.7 \pm 0.1 "	0.0 1.7
4.	1st scan out of 14	peptide amide	287.9	401.2 400.0	1.7 \pm 0.1 "	0.0 1.2
5.	2nd scan out of 12	peptide amide	287.9	407.4 400.2	2.4 \pm 0.55 1.7 \pm 0.1	0.0 7.2
6.	1st scan out of 4	unsubst. amide	288.3	399.8	1.4 \pm 0.1	—
6.	4th scan out of 4	"	"	399.8	1.7 \pm 0.1	—
10.	total of 6 scans	aliph./ contam.	285.0	402.0	1.6 \pm 0.1	—
13.	1st scan out of 15	arom./ contam.	285.0	400.0	1.7 \pm 0.1	
14.	1st scan out of 6	arom./ contam.	285.0	400.2	1.4 \pm 0.1	—
15.	1st scan out of 15	peptide α	286.1	401.1 399.9	1.4 \pm 0.1 "	0.0 1.2
15.	total of 15 scans	"	"	401.0 \pm 0.3 399.9 \pm 0.2	1.7 \pm 0.2 "	0.0 1.1

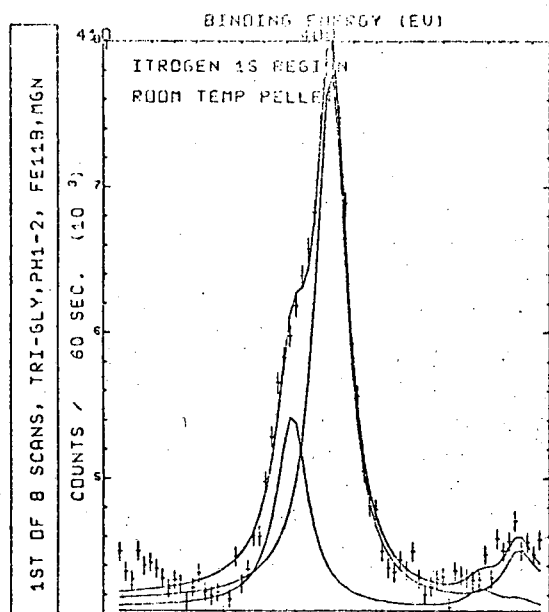


Figure 8. (a) Nitrogen 1s region of tri-gly, pH 1-2 (MgK α). Note the rise in the data at high binding energy.

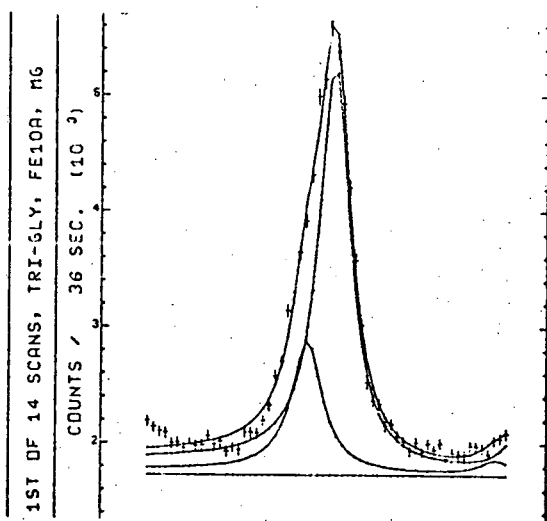


Figure 8. (b) Nitrogen 1s region of tri-gly, pH 5-6 (MgK α). The rise at high binding energy is slightly more prominent than in 8a.

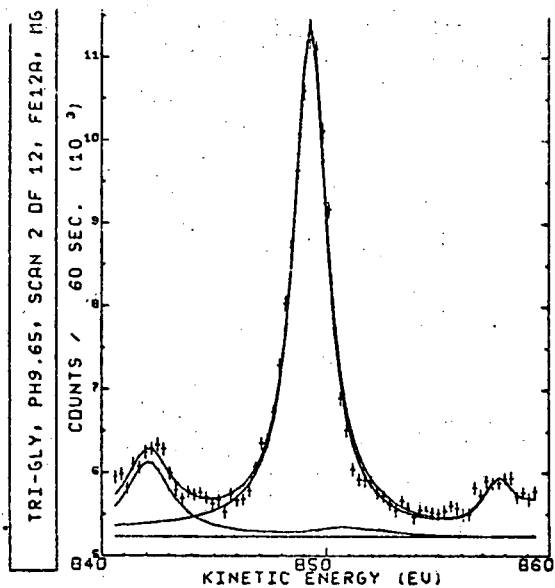
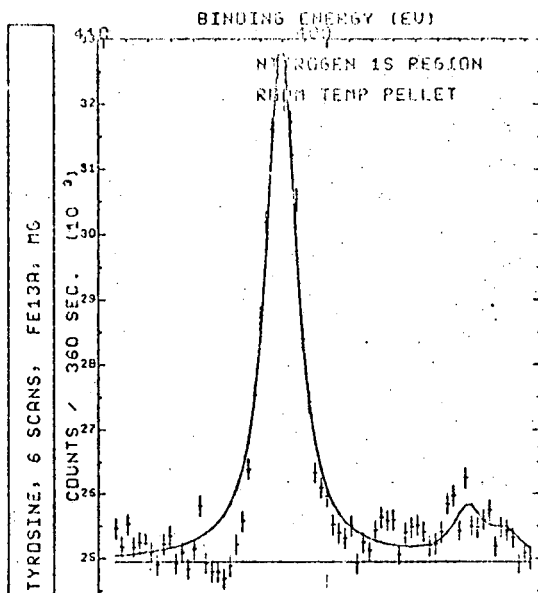


Figure 8. (c) Nitrogen 1s region of tri-gly, pH 9.6 (MgK α). The high binding energy peak is clearly visible.



-137-

Figure 8. (d) Nitrogen 1s region of tyrosine. SUNDER had difficulty fitting the dip in the data at 405 eV.

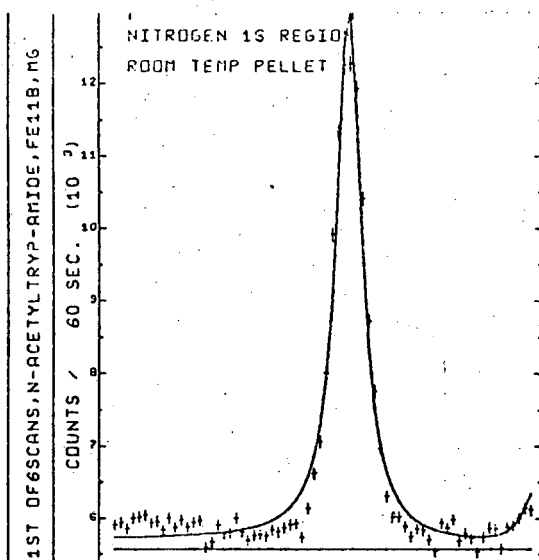


Figure 8. (e) Nitrogen 1s region of N-acetyl tryptophanamide. Pyrrole and amide nitrogen coincide under one peak, $\text{FWHM} = 1.4 \pm 0.1 \text{ eV}$ ($\text{MgK}\alpha$).

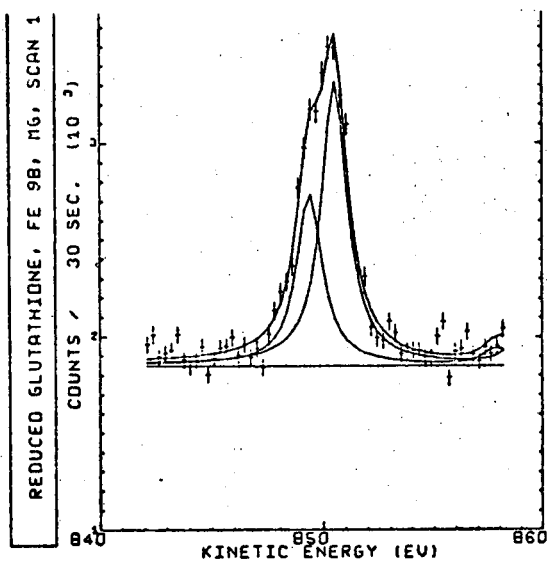


Figure 8. (f) Nitrogen 1s region of reduced glutathione ($\text{MgK}\alpha$).

signal is expected to be shifted to higher binding energy. There should be a 2:1 ratio of peptide amide nitrogen to amino nitrogen. The data show a shoulder on the high binding energy side of the main peak. SUNDER calculated a ratio of $(2.8 \pm 0.2):1$ for the two lines, and a separation of 1.7 ± 0.1 eV. (These numbers should be reliable according to the standards developed in Chapter Two because the S/N ratios are 8 and 21, the background reasonable, the tail is small, and the shoulder is distinct.) The assignment of the smaller, high binding energy line to amino nitrogen is consistent with what was expected, consistent with the work of Kramer,⁴⁰ and confirmed by the tyrosine N 1s data below. The calculated 3:1 ratio of amide to amino nitrogen shows that the amino line has been diminished, presumably by deamination of the x-ray flux.

In the pH 5-6 tri-gly sample, a shoulder is still visible on the main peak, but the separation between the two lines has been reduced to 1.2 ± 0.14 eV. In the pH 9.6 tri-gly sample, the amino group should not be protonated. The data show that at this high pH, the amide and amino nitrogens are indistinguishable; there is a single line of normal FWHM, 1.7 ± 0.1 eV, at binding energy of 400.2 ± 0.2 eV, which is identical to the amide N 1s position. Thus, the ability of the apparatus to distinguish the amide and amino nitrogens depends on the extent of protonation on the molecular level, i.e., the "pH" of the solid sample. This problem means that there will be some uncertainty in the analysis of N 1s signals, but it also points out the possibility of determining, at least qualitatively, the "pH" of the solid protein samples.

The data on 5-hydroxyvaleramide show that an unsubstituted amide nitrogen has essentially the same binding energy as the peptide amide nitrogen. The data on tyrosine, sample #10, and the corresponding amide, sample #13 (Sigma, lot #50C-1030), confirmed the assignment of amide and amino nitrogen lines in the tri-gly samples. N-acetyl tryptophanamide, sample #14 (Sigma, lot #90C-2630), contains an amide nitrogen and another nitrogen in the side chain that is analogous to a pyrrole nitrogen. The data show that these two forms are completely indistinguishable. This N 1s signal has the minimum FWHM of 1.4 ± 0.1 eV, and its position corresponds to the amide binding energy.

The results from this series of compounds indicates that there are only two binding energies relevant to nitrogen in protein samples. 400.0 ± 0.2 eV is the 1s binding energy corresponding to nitrogen in the form of: an unprotonated amino group, a side chain pyrrole, and a peptide amide linkage. This binding energy can also be applied to nitrogen in an unsubstituted amide group; although, 399.8 ± 0.2 eV might be a slightly more accurate value. A nitrogen atom in a protonated amino group has a binding energy of 401.9 ± 0.2 eV. Unfortunately, the binding energy for this group converges to the amide N 1s binding energy as protonation decreases.

There is a peak in the spectrum of pH 9.6 tri-gly (Fig. 8c) at a BE of 407.4 eV. This value is significantly higher than any other N 1s BE observed in this series. Although several sources can be suggested for the origin of this peak, it remains unexplained. The properties of the high binding energy (HBE) nitrogen 1s peak are: (a) It appears clearly in Fig. 8c. (b) It may be present in Figs. 8a, 8b, and 8d where

a rising trend is observed near 407 eV. These are compounds #3, 4, and 10 which contain free amino groups. (c) There is no evidence of any HBE peak in the spectra of the amide compounds #6, 13, and 14, e.g., Fig. 8e. (d) It is not observed in the spectrum of reduced glutathione (Fig. 8f), but the data do not extend to the HBE region.

It is possible that the HBE peak originates from molecules of ammonia gas that are formed by radiation damage and trapped in the sample lattice or diffusing through it. This "gas" theory is motivated by the fact that amino groups are known to be released as ammonia in ionizing radiation. (See discussion of radiation damage below.) Properties a - d show that evidence for the HBE peak appears only in the samples with free amino groups. It is also known that, due to extra-atomic relaxation effects,⁴¹ vacuum referenced core BE's in gaseous molecules are 3 - 8 eV higher than the corresponding vacuum referenced BE's in condensed phases; the HBE peak is 7 eV from the main peak. Finally, workers who study the irradiation of solid amino acids in vacuum report that quantitative analysis of gaseous photolysis products (NH₃, CO₂, etc.) is severely hindered by "trapping" or "caging" of these products within the sample lattice. Thus, the HBE peak may be a "gas" peak; quotation marks emphasize that the peak reflects gases trapped in the sample rather than a free gas in the sample chamber. (The sample chamber vacuum was 10⁻⁵ torr at all times.)

To test the "gas" theory, 5-diazouracil monohydrate (Aldrich, lot #022217, structure shown in Table IV) was run on a high temperature solid sample holder.²¹ Diazo compounds are unstable with respect to the loss

of N_2 upon heating:⁴² 5-diazouracil decomposes at 213°C. The experiments were aimed at generating N_2 gas in the interior of the sample by heating while monitoring the HBE region in the XPS spectrum. It was hoped that the HBE peak could be made to appear on demand by turning the heat on and off.

The 5-diazouracil was pressed into a 20 mil Pb foil that had been roughened with sandpaper. The foil was then bolted directly onto the sample heater with a thermocouple under one of the bolts. At 100°C, the pressure in the vacuum tank rose abruptly for several seconds, presumably because the water of hydration was coming off the sample. This result implied that good thermal contact had been achieved.

Six experiments were run with variable results. In the final run, a broad signal was observed in the HBE region, but it was still visible after the sample had cooled overnight. These experiments failed in that the HBE peak could not be made to appear on demand. The "gas" theory was neither proven nor disproven because the N_2 came off in a brief pulse of a few seconds rather than slowly over a few minutes. Since it took 6 seconds to obtain a single data point, a HBE peak could disappear before a fast spectrum could be taken.

There are several other possible explanations for the HBE peak.

(i) It could be due to nitrogen gases formed by radiation damage and adsorbed on the sample surface. (ii) The peak represents nitrogen that has been oxidized by electron or radiation damage. (iii) The peak is a satellite caused by two electron excitation or some other discrete energy loss.

The radiation stability of the various forms of biological nitrogen under XPS conditions is shown in Figs. 9 - 15. In each experiment, the samples were irradiated with a Mg anode in an x-ray tube operated at 12 kV and 20 mA. The resulting dose (see Chapter I) is 10^6 rads/sec for an organic sample. Repeated scans were made of the N 1s region. Each scan was fitted by the SUNDER program. The lineshape areas for the individual scans (not the accumulated data) are plotted against x-ray exposure time in Figs. 9 - 15.

The area of the N 1s line from the amino group of tyrosine, sample #10, fell 50% in 8 hours, as shown in Fig. 9. A saturated solution of tyrosine had a pH of 7.0; the amino group was assumed to be protonated. Converting the amino group of tyrosine to an acetyl amide, sample #13, imparted a limited amount of stability to the nitrogen signal, as shown in Fig. 10; but the line area still fell by 30% in 8 hours. The N-acetyl-tryptophanamide, sample #14 shown in Fig. 11, had a stable N 1s signal. It showed a generally descending trend over 8 hours, but the calculated area fell by only 10%. Recall, however, that the tryptophanamide has two nitrogen atoms whose 1s signals coincide. Suppose the pyrrole nitrogen is stable while the amide nitrogen suffers the same damage as the tyrosineamide, i.e., a 30% reduction. The total nitrogen signal in the tryptophanamide would drop by 15%, which is roughly the observed damage.

The results in Figs. 9 - 11 are significant because the N-acetyl amide linkages in samples #13 and #14, Fig. 10 and 11, resemble the peptide amide linkage. The most qualitative interpretation of Figs. 9 - 11 is that amino nitrogen signals are less stable than those of (peptide)

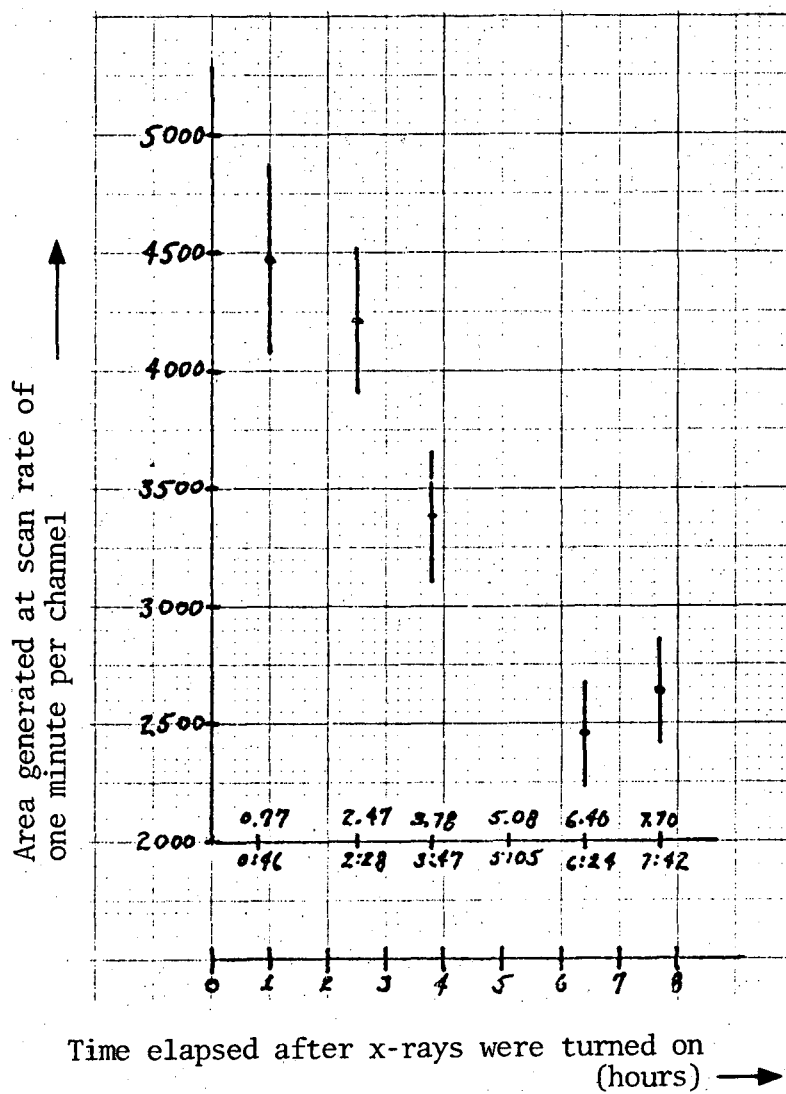
Area of nitrogen 1s peak vs. time

Figure 9. 1-Tyrosine, variation of nitrogen 1s peak area calculated by SUNDER vs. x-ray exposure time.

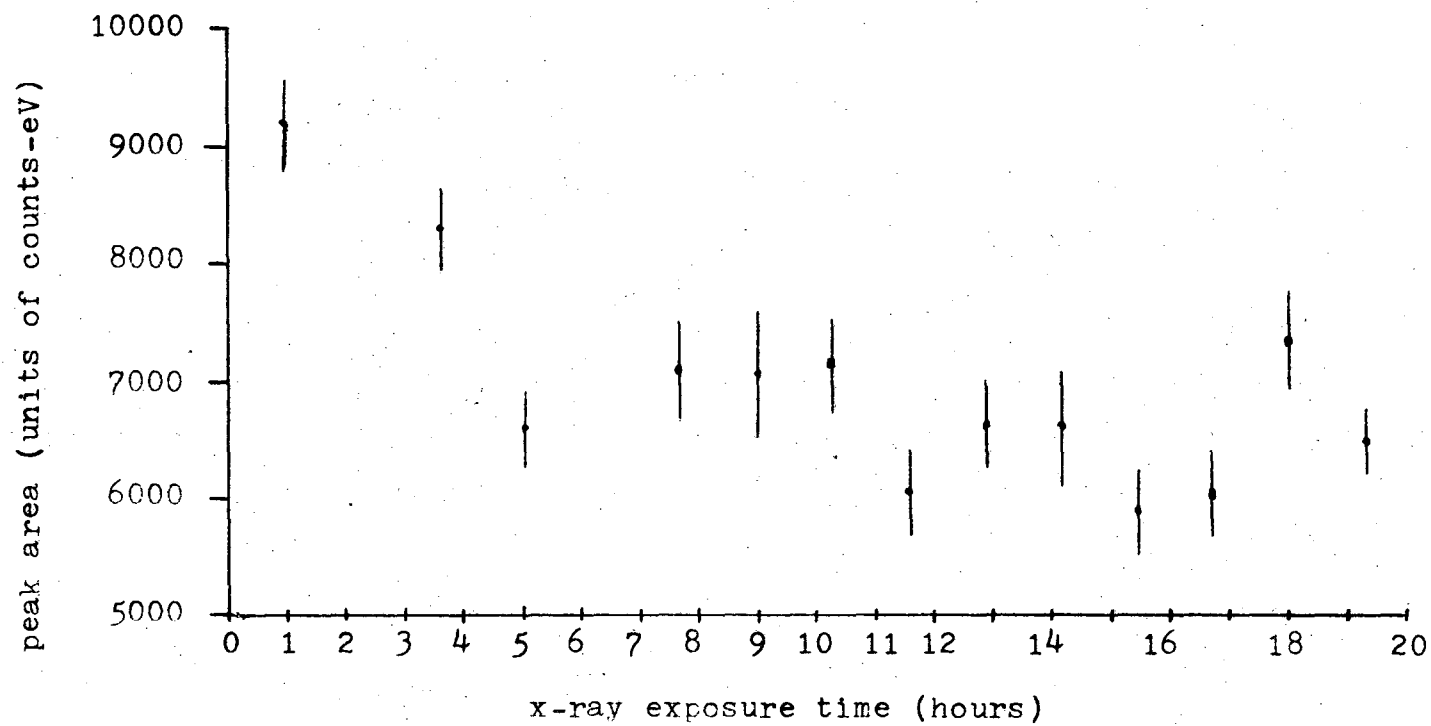


Figure 10. N-acetyl tyrosineamide, sample #13. Variation of nitrogen 1s peak area calculated by SUNDER vs. x-ray exposure time.

-145-

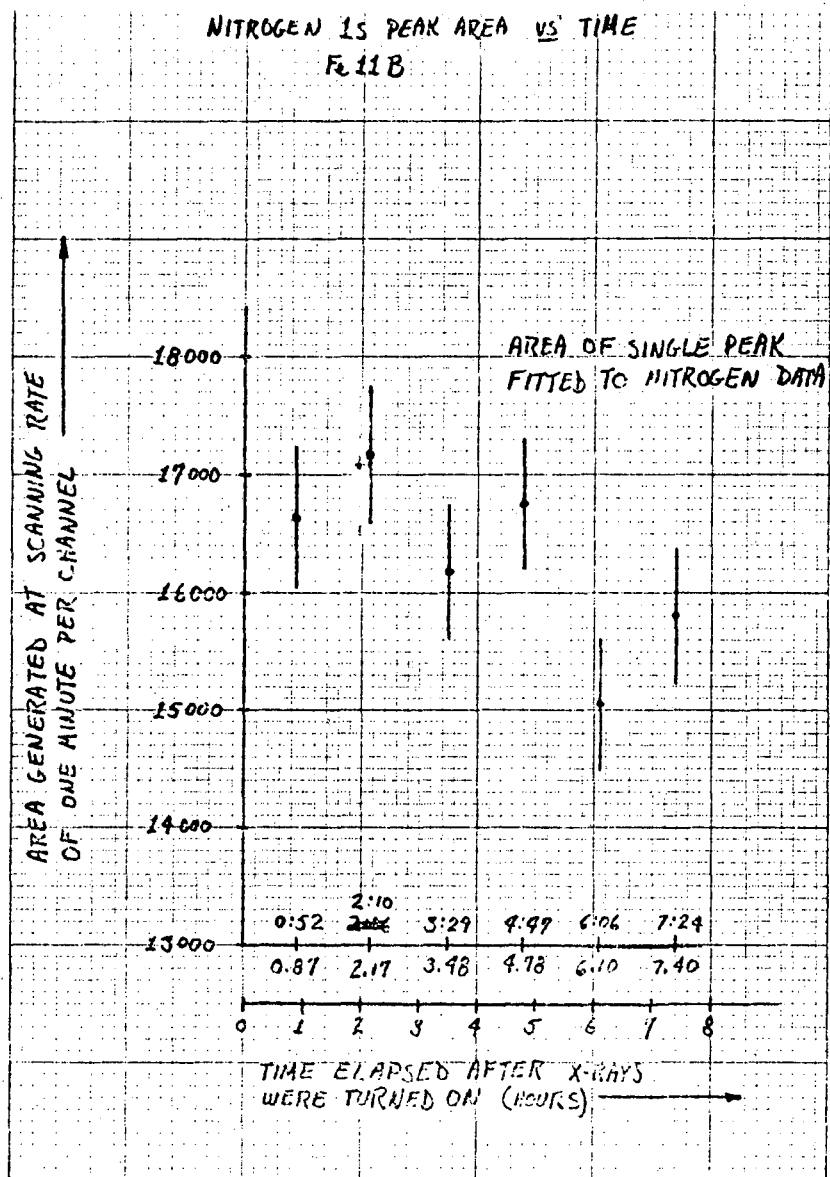


Figure 11. N-acetyl tryptophanamide, sample #14. Variation of nitrogen 1s peak area calculated by SUNDER vs. x-ray exposure time.

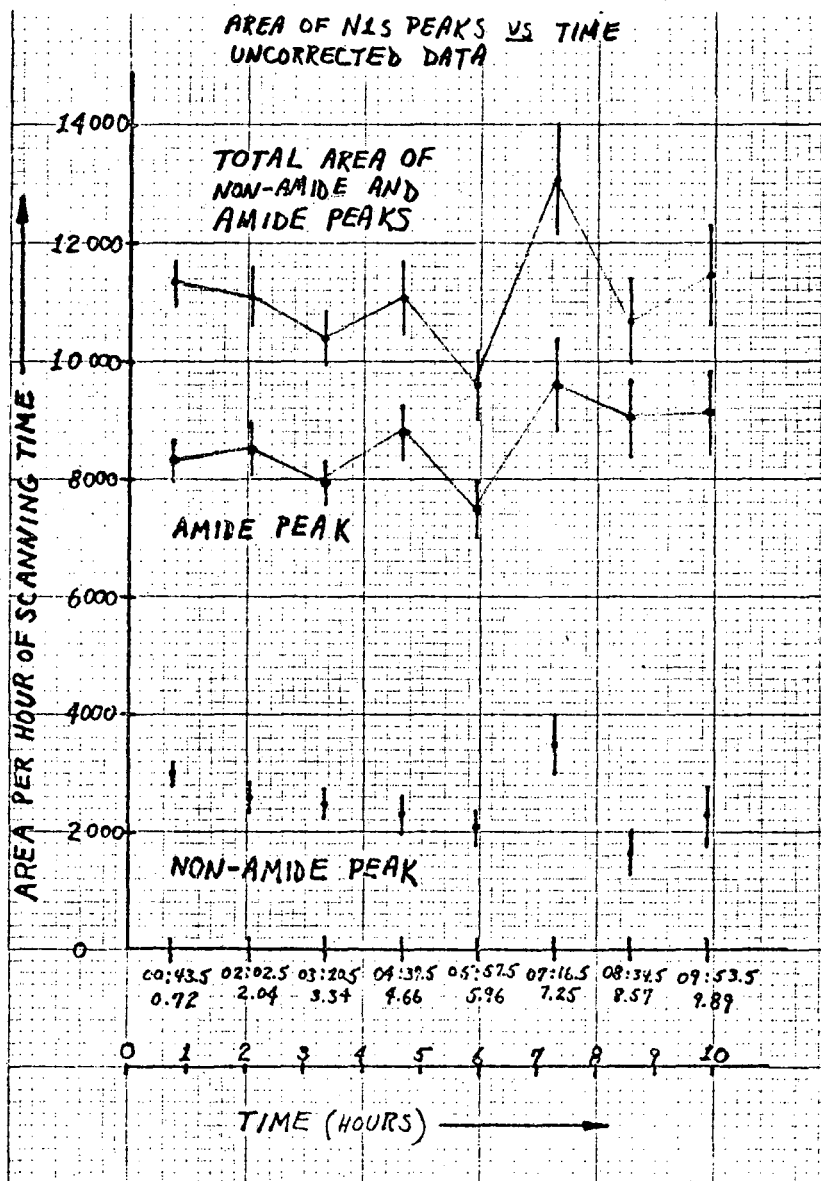


Figure 12. Tri-gly, pH 1-2. Variation of nitrogen 1s line areas calculated by SUNDER vs. x-ray exposure time. The total nitrogen signal is approximately constant over a ten hour experiment.

-147-

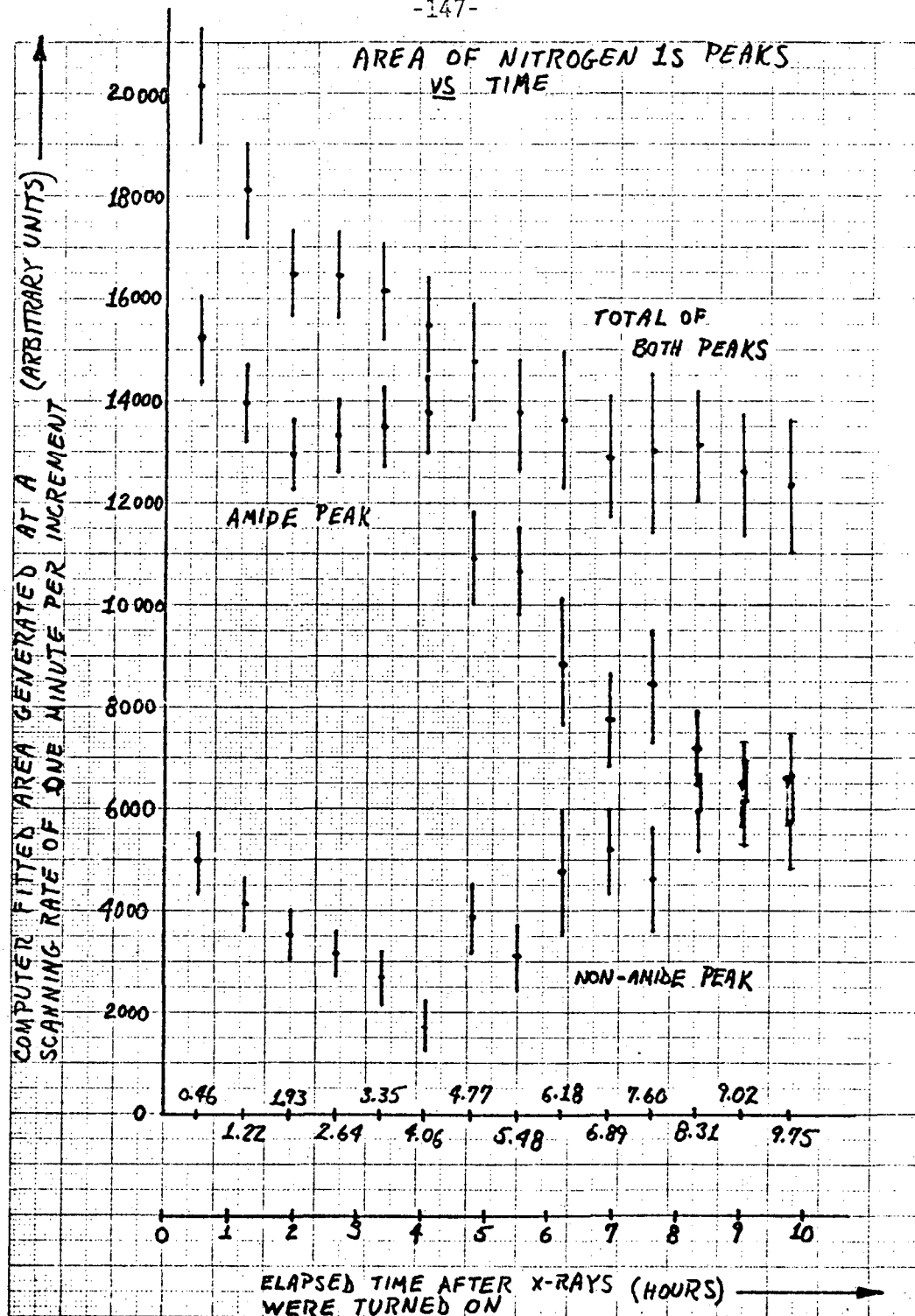


Figure 13. Tri-gly, pH 5-6. Variation of nitrogen 1s line area calculated by SUNDER vs. x-ray exposure time. The loss of total nitrogen signal is real, but the convergence of the amino and amide line areas is probably artificial.

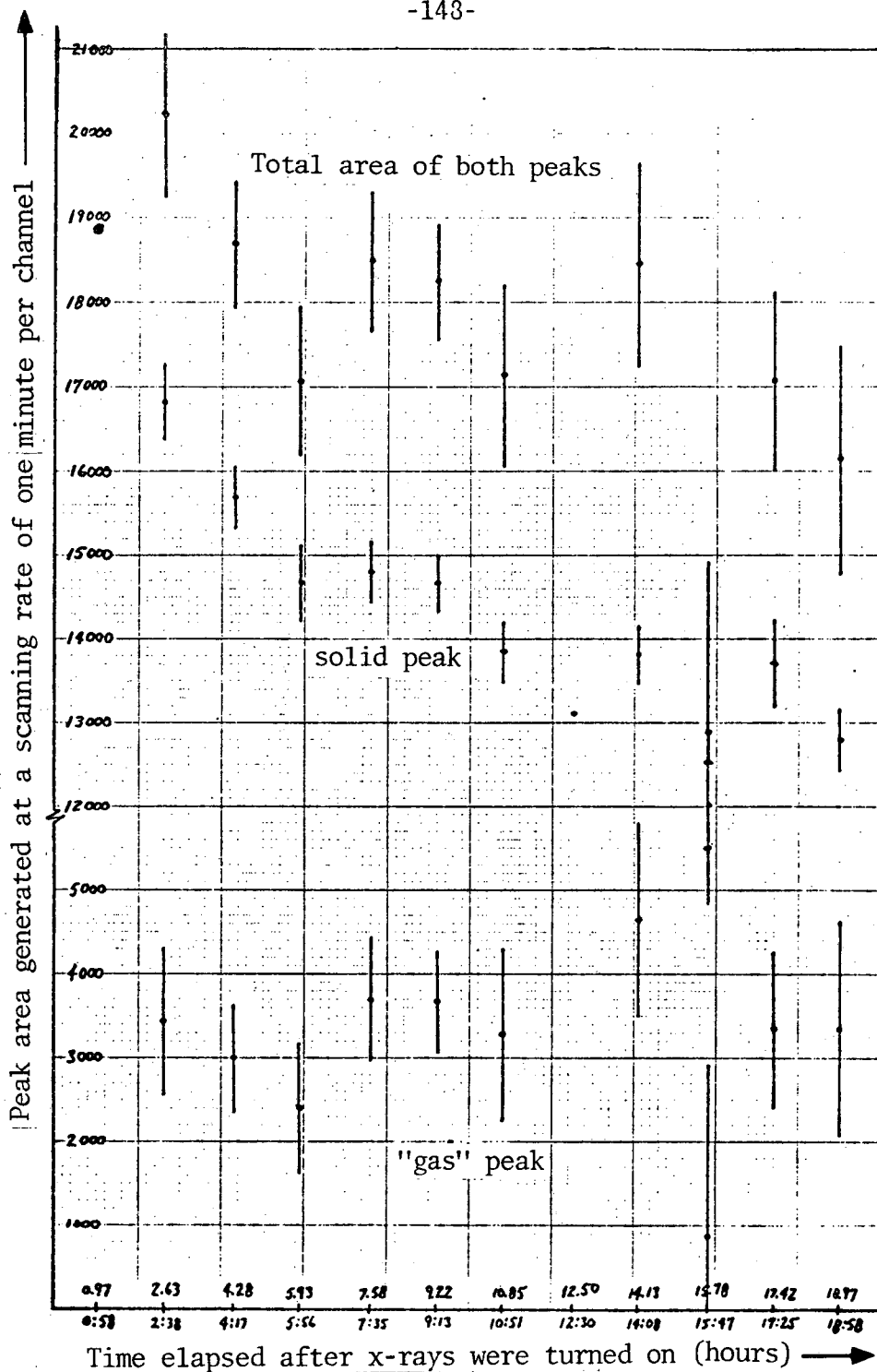


Figure 14. Tri-gly, pH 9.6. Variation of nitrogen 1s peak areas calculated by SUNDER vs. x-ray exposure time. SUNDER could not fit an area to the "gas" peak in the first scan, but its area is about 2000 units.

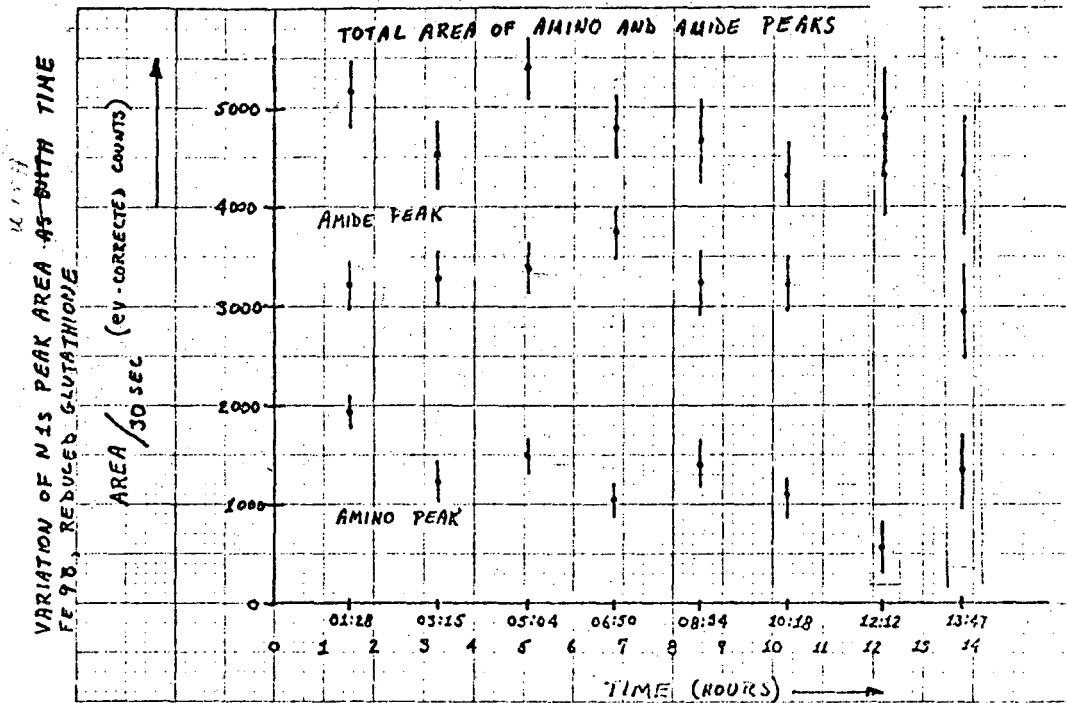


Figure 15. Variation of nitrogen 1s line areas calculated by SUNDER vs. x-ray exposure time. The sample is reduced glutathione, which is reported to protect biological systems against radiation effects.

amide nitrogen. There is indirect evidence that nitrogen in an aromatic ring system is substantially more stable than either of the other two forms.

The N 1s signal of pH 1-2 tri-gly was decomposed by SUNDER into two lines representing amino and amide nitrogen. The calculated area of each line, and the sum of both line areas, are shown in Fig. 12. The amino line, represented as "non-amide" in Fig. 12, fell by about 30% over the course of the experiment. The amide line grows a corresponding amount so that the total area of both lines is approximately constant.

The SUNDER program can account for some of this unexpected behavior. The S/N ratio of the N 1s data points is well over 20. SUNDER will fit an accurate area under these points, but the combination of line areas that it chooses may be spurious. The individual line areas can be taken to be accurate if the S/N ratio for each line is at least 8 (see Chapter II). In the first scan, S/N for the amino line was 8, but in succeeding scans it dropped below 8. SUNDER's reliability became marginal. Any spuriously calculated deficiency or excess in the amino line area would be cancelled by an opposite error in the amide line, such that the total area would fill the data. Thus, the slight ascent in the amide area is probably an artificial cancellation of a spuriously calculated reduction of the amino area.

The pH 5-6 tri-gly data in Fig. 13 shows substantially different behavior. The total area of the amino and amide lines drops by about 40% in 10 hours. The amino line shows a descending trend through the first half of the experiment: then it abruptly increases to converge

with the rapidly descending amide line. The amino/amide behavior in the second half of the plot is most probably a spurious result of the SUNDER fits. The amino shoulder on the pH 5-6 tri-gly data (Fig. 8) is not distinct; SUNDER (see Chapter II) cannot be expected to calculate an accurate area ratio for these data. The smoothly descending trend of the amino line in the first half of Fig. 13 suggests that SUNDER had some success in calculating the areas in this time interval. In the second half of the experiment, the amino line had been diminished to a point where SUNDER could no longer make an accurate fit. SUNDER began to fit the lines closer together with a narrower FWHM, and gave them approximately the same area. As in Fig. 12, the total area is accurate and the plot of total area against time has physical significance. The convergence of the amino and amide line areas in the second half of the experiments, however, is probably artificial.

Fig. 14 shows the pH 9.6 tri-gly data, in which the N 1s "gas" peak was clearly observable. The "gas" peak was relatively constant throughout the experiment. The solid peak represents both the unprotonated amino and amide signals, which coincide as shown in Fig. 8. The combined signals drop by 30% after 18 hours. The total area of both peaks was plotted on the assumption that the trapped "gas" (or surface oxidized nitrogen) originated from the "solid" nitrogen. Since the "gas" peak is approximately constant, there is little significance in the total area plot.

The tri-gly series indicates that the pH 1-2 sample was significantly more stable than the other two samples. This result may be due

to the extra protonation or the presence of chloride ions throughout the sample. The other tri-gly samples showed degradation consistent with Figs. 9 - 12.

Having observed the damage done to amino acids and peptides, reduced glutathione⁴³ was measured because of its ability to protect biological substances from radiation effects.⁴⁴ The data points are shown in Fig. 8; the areas of the N 1s lines vs. time are shown in Fig. 15. The amino line showed a generally descending trend, losing perhaps 30 - 50% of its area during the experiment. The amide line was approximately constant. The N 1s signals are, therefore, not quite as stable as the pH 1-2 tri-gly results in Fig. 12.

Gamma radiation studies on solid glycine and alanine³⁴ indicate that both CO₂ and NH₃ are released as gaseous products from amino acids. The G values (molecules of product per 100 eV of absorbed energy), however, are small. G(CO₂) = 0.2, G(NH₃) = 0.01. Much more of each product are released when the samples are dissolved; G(CO₂) = 1, G(NH₃) = 4, G(RNH₂) = 1. It is apparent that gaseous or unstable products are being trapped in the sample.³⁴ The G values derived from the wet analysis indicate that about 4 molecules of NH₃ or related unstable precursors are formed for every 100 eV of absorbed radiation. At the dose rate of the Berkeley iron-free spectrometer, this figure translates into one deamination per thousand amino acid molecules per second. A linear extrapolation suggests that in 10³ seconds, every amino acid molecule in the sample has been deaminated.

Similar results were observed for N-acetyl amides of amino acids and simple peptides gamma irradiated in the polycrystalline state, glassy state, and concentrated solutions.⁴⁵ Irradiated samples were dissolved in water. Gases liberated upon dissolution were pumped off; the remaining solution was gently hydrolyzed. The peptide degradation was measured as the amount of NH_3 liberated by dissolution and hydrolysis. $G(\text{NH}_3)$ varied from 1 to 3, i.e., about 3 peptide linkages were broken per 100 eV absorbed, or 0.1% of the sample in the Berkeley spectrometer. The hydrolysis of the dissolved sample indicated that 80% of the peptides broken yielded other amide products. UV studies³⁸ indicate that peptide fracture may or may not lead to changes in the ORD spectra of proteins.

The studies summarized above seem to suggest that in 10^3 seconds (20 min) all amino groups and peptide linkages in the sample will be deaminated or broken. Yet, the amino signals in Figs. 9 - 15 seem to level off after 50% loss. The peptide nitrogen signals decrease by 30%, and some are quite stable. The data in Figs. 9 - 15 are in apparent disagreement with the results from gamma irradiation.

Actually, there is only limited room for comparison of the experimental results. The linear extrapolation of the gamma ray G values to a "100% destruction time" of 10^3 seconds in the Berkeley spectrometer is not at all valid. An obvious correction to the linear extrapolation would be to recognize that the number of amino groups and/or peptide links become smaller as radiation damage proceeds; so, in a constant radiation flux, the rate of damage should decrease exponentially according to first

order kinetics. The resulting half-life of the sample is still of order 10^3 seconds. A "90% destruction time" is about an hour. First order kinetics does not explain the disparity between gamma ray and XPS results.

The main reason why both the linear and exponential extrapolations fail is that the XPS system might be saturating with radiation. Saturation with free radicals at 10^6 rads has already been reported for amino acids,³⁴ and recombination of free radicals to restore the parent amino acids has also been suggested at 10^8 rads.³⁴ One hour in the Berkeley spectrometer corresponds to 10^9 rads. Saturation and recombination are likely possibilities for explaining the apparent stability of peptide samples in the Berkeley spectrometer.

The increased stability of peptide linkages over amino groups might be explained by the fact that 80% of the peptide radiolysis products are other amides. These forms of nitrogen have the same binding energy; so, peptide links may be cleaved with a relatively small loss of signal.

Gross changes in the samples that were visible to the naked eye have already been shown in Table III for samples #3 - 10. Samples #13, 14, 15 turned from white powders to light green (20 hours exposure), light lavender (8 hours), and light yellow (14-1/2 hours). The color changes are similar to Table III.

In summary, the N 1s signal can also be used as an internal reference. The structure of the N 1s signal is generally simpler than that of carbon because many of the biological forms of nitrogen have the same 1s binding energy. The shape of the N 1s signal, however, is strongly

dependent on the pH at which the samples are prepared because of protonation on the amino groups. Referencing must, therefore, be restricted to the amide N 1s signal. The amide N 1s signal is reasonably stable in the x-rays; its intensity drops by 0 - 30% in a 10 hour experiment. The N 1s signals seem to be somewhat less stable in the x-rays than the corresponding C 1s signals (see Figs. 6 and 7).

REFERENCES, CHAPTER IV

1. Kai Siegbahn, et al., ESCA, Atomic, Molecular, and Solid State Structure Studied by Means of Electron Spectroscopy, Nova Acta Regiae Societatis Scientiarum Upsaliensis, Ser. IV, Vol. 20, (1967).
2. C.S. Fadley, Theoretical Aspects of X-Ray Photoelectron Spectroscopy, NATO Advanced Study Institute on Electron Emission Spectroscopy, Ghent (1972).
3. M.F. Ebel and H. Ebel, J. Electron Spectrosc. & Relat. Phenomena 3, 169 (1974).
4. D.J. Hnatowich, J. Hudis, M. Perlman, and R. Ragani, J. Appl. Phys. 42, 4883 (1971).
5. J.M. Thomas, et al., Trans. Faraday Soc. 67, 1875 (1971).
6. D. Chadwick, Chem. Phys. Lett. 21, 291 (1973).
7. R. Nordling, et al., Inorg. Chem. 9, 2469 (1970).
8. W.J. Stec, et al., Inorg. Chem. 11, 219 (1972).
9. W.E. Swartz, P.H. Watts, J.C. Watts, J.W. Brasch, and E.R. Lippincott, Analyt. Chem. 44, 2001 (1972).
10. W.P. Dianis, Analyt. Chem. 45 (8), 1416 (1973).
11. J. Jack and D. Hercules, Analyt. Chem. 43, 729 (1971).

12. W. Swartz and D. Hercules, *Analyt. Chem.* 43, 1066 (1971).
13. J.L. Ogilvie and A. Wolberg, *Appl. Spectr.* 26, 401 (1972).
14. Nefedov, *Zh. Anal. Kh.* 27, 2049 (1972).
15. L.N. Kramer, private communication.
16. D. Betteridge, J.C. Carver, and D.M. Hercules, *J. Electron Spectrosc. & Relat. Phenomena* 2, 327 (1973).
17. D.S. Urch, *J. Electron Spectrosc. & Relat. Phenomena* 5, 791 (1974).
18. Roger Pollak, private communication.
19. U. Gelius, *et al.*, *Physics Scripta* 2, 70 (1970).
20. B.E. Douglas, D.M. McDaniel, Concepts and Models of Inorganic Chemistry (Blaisdell, Waltham, Mass., 1965), p. 313.
21. C.S. Fadley, Ph.D. Dissertation, University of California, Berkeley, 1970, Lawrence Berkeley Laboratory Report UCRL-19535.
22. Greenstein and Winitz, Chemistry of Amino Acids, Vol. 1 (John Wiley & Sons, NY, 1961), p. 486 ff.
23. B.L. Lindberg, *et al.*, *Physica Scripta* 1, 286 (1970).
24. J. Bus, *R. Trav. Chim. Pays-Bas* 91, 251 (1972).
25. D.T. Clark, *Chem. & Phys. of Lipids* 13, 439 (1972).
26. U. Gelius, *et al.*, *Physica Scripta* 3, 237 (1972).

27. H. Kuroda, *J. Syn. Org. J.* 30 (11), 942 (1972).
28. J. Nelson and A. Frost, *Chem. Phys. Lett.* 13, 610 (1972).
29. M.E. Schwartz and J.D. Switalok, *J. Am. Chem. Soc.* 94, 6899 (1972).
30. E. Hughes and H. Yakel, *Second International Congress of Crystallography, Stockholm, Abstracts of Papers*, p. 90(90), 1951.
31. H. Yakel and E. Hughes, *Acta Cryst.* 5, 847 (1952).
32. J. Ryom and J.L. Whitten, *J. Am. Chem. Soc.* 94 (7), 2396 (1972).
33. A. Swallow, *Radiation Chemistry of Organic Compounds* (Pergamon Press, NY, 1960), pp. 200 ff.
34. W. Gottschall and B. Tolbert, in *Radiation Chemistry*, Vol. 1, *Advances in Chemistry Series #81*, E.J. Hart (Ed.), (American Chemical Society, Washington D.C., 1968), pp. 374 ff.
35. W. Gottschall and B. Tolbert, *J. Phys. Chem.* 72, 922 (1968).
36. R. Braams, in *Radiation Research*, G. Silini (Ed.), *Proc. 3rd Internat. Cong. Rad. Res., Cortina d'Ampezzo, Italy, June-July, 1966* (John Wiley, NY, 1967), p. 371.
37. L.S. Myers, Jr., in *Radiation Chemistry of Macromolecules*, Vol. 2, M. Dole (Ed.), (Academic Press, NY, 1972), pp. 346 ff.
38. W.D. Wilson and J.F. Foster, *Biophysical J.* 12, 609 (1972).
39. U. Fano, in *Symposium on Radiobiology*, J.J. Nickerson (Ed.) (John Wiley & Sons, NY, 1952), pp. 13 - 34.

40. L.N. Kramer, Ph.D. Dissertation, University of California, Berkeley, 1971, Lawrence Berkeley Laboratory Report LBL-306.
41. D.A. Shirley, Chem. Phys. Lett. 16 (2), 220 (1972).
42. J.D. Roberts, M.C. Caserio, Basic Principles of Organic Chemistry (W.A. Benjamin, NY, 1965), pp. 691 - 696.
43. W.B. Wright, Acta Cryst. 11, 632 (1958).
44. Z.M. Bacq, Chemical Protection Against Ionizing Radiation (Charles C. Thomas-Publisher, Springfield, IL, 1965).
45. W.M. Garrison, M.E. Jayko, M.A. Rogers, H. Sokol, and W. Bennett-Corniera, Radiation Chemistry, Vol. 1, Advances in Chemistry Series #81 (Amer. Chem. Soc., Washington, D.C., 1968), p. 384.

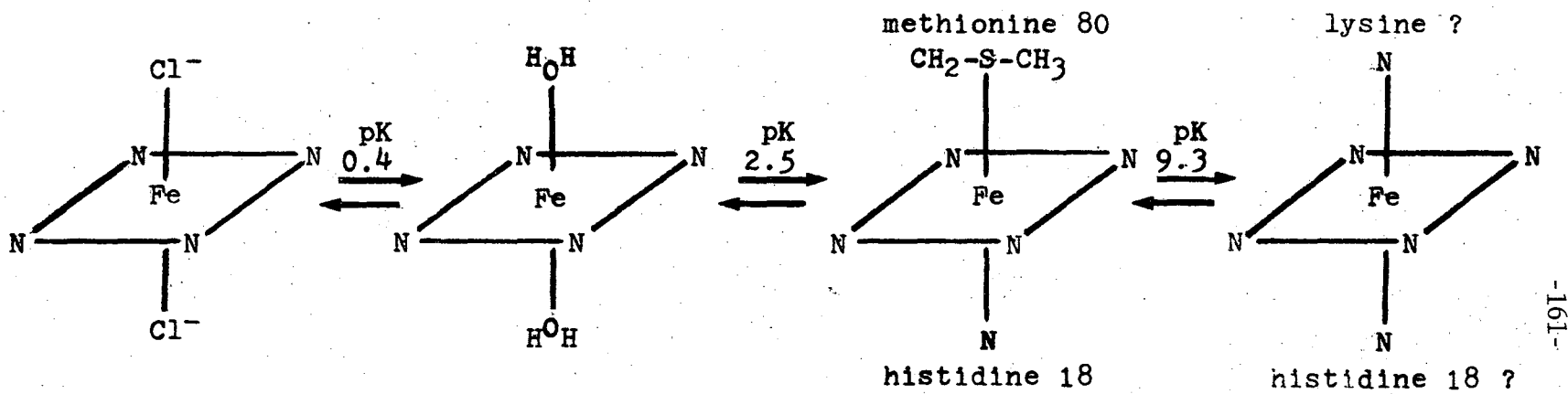
V. XPS STUDY OF HORSE HEART CYTOCHROME c

A. Introduction

Preliminary experiments on inorganic copper compounds and copper amino acid complexes indicated that the limit of detection for metals in XPS samples was about 1 part per 10^3 in the Berkeley iron-free spectrometer. Kramer's work¹ showed that the chemical shifts for Mg and Fe range over 5 eV from the pure metals to their halide salts; the FWHM of observed signals commonly ranged from 1.5 to 3 eV. The chemical shift range was small compared to the linewidths, and typical metal concentrations in proteins (1 metal atom per $10^4 - 10^5$ molecular weight) approach or exceed the limits of detection in the spectrometer. Therefore, the applicability of XPS to biological systems was in doubt, and it was necessary to test the technique on a well characterized system.

Horse heart cytochrome c was chosen as the test system because it is one of the smallest metalloproteins. (The non-heme iron proteins were examined previously by Kramer.¹) Cytochrome c has a molecular weight of 12,400 and contains one heme iron. This composition corresponds to 0.43% Fe by weight, which is slightly above the practical limit of detection. The protein is available in reasonably pure form in large quantities from commercial sources. It has been the object of intense study;^{2,4,12,16-18} the crystal structure of ferricytochrome c is known.³

In ferricytochrome c, there is a series of ligand changes at the iron^{2,4} as shown in Fig. 1. The equatorial positions are bound to the



-161-

Figure 1. Ligand changes at the iron atom of ferricytochrome c as a function of pH. The pK values are those for horse cytochrome c.

00004500812

pyrrole nitrogens of the porphyrin ring, but at low pH, the 5 and 6 axial positions are occupied by Cl^- (assuming pH adjusted with HCl) or H_2O . At neutral pH, the sulfur atom of methionine 80,^{16,17} and the imidazole nitrogen of histidine 18, move into the 5 and 6 positions. At higher pH, the coordination is not known, but it is believed to involve nitrogen atoms at the 5 and 6 axial locations. Thus, ferricytochrome c is ideally suited to test XPS. Samples can be prepared from various pH's and the sulfur and iron spectra can be examined for the appropriate shifts corresponding to pH induced ligand changes.

In support of this study, the sulfur amino acids were investigated in their native and oxidized forms. Porphyrin cytochrome c (PCC), the iron-free analogue of the native protein, was prepared and measured. Finally, mesoporphyrin and microperoxidase, a heme peptide derived from horse heart cytochrome c by digestion with pepsin, were also measured.

These experiments have potential biological significance because the cytochrome c/cytochrome oxidase system is the last step before oxygen in the respiratory electron transport chain.^{5a,b} It is also known that cytochrome c loses its ability to function in the respiratory chain if the sulfur of methionine 80 is carboxymethylated to block its binding to the iron,^{5c} while no effect results from altering methionine 65. As a probe of the bonding of iron to methionine 80, XPS might provide information about the role of cytochrome c in the respiratory chain.

B. Experimental

Two spectrometers were used in this study. Most of the experiments were performed on the Berkeley iron-free spectrometer. Microperoxidase and neutral ferricytochrome c were run on a Hewlett-Packard 5950A spectrometer at the Jet Propulsion Laboratory.⁶

All the samples were run as pellets of pure material or thin films dried onto quartz or gold plates. All the pellets were made of pure material in a 1/2" diameter die. The first protein pellets were pressed at 4 tons per square inch, but it was soon learned that 1/2 to 1 ton was adequate, and that even thumb pressure could make a mechanically strong sample. The pellets were mounted on an aluminum plate under an aluminum frame with no adhesive agent. Occasionally, the pellets were mounted directly onto an aluminum plate with double-sided tape. The pellet always covered the tape completely.

The pressure required to make pellets did no apparent harm to the protein. There was no detectable difference between the XPS spectra from a pellet of pH 6.6 ferricytochrome c and a similar sample prepared in the form of a film as described below.

Two-thirds of the samples were prepared as films, some on gold platens for the Hewlett Packard 5950A spectrometer, and the others on quartz plates for the Berkeley iron-free spectrometer. Protein solutions (1 mg/ml) were deposited on quartz plates cleaned with deionized water and glass bottled absolute ethanol. The pressure over the plates was reduced to several mm Hg and the water was left to evaporate for

one to several hours. The resulting films were about a micron thick as determined by optical spectra, assuming a uniform film and using the extinction coefficients from solution measurements. The molecular arrangement within such a film probably resembles a glass. The quartz plates allowed visible/UV optical spectra of the samples to be taken before and after irradiation.

There are several problems involved in obtaining thin, uniform films. A "hard" vacuum, e.g., a mechanical forepump, causes the solutions to evaporate too quickly. The solutions freeze and the samples lyophilize. Thick (several microns) films develop cracks reminiscent of a dry lake bed that are clearly visible under a stereo microscope. Slightly more than the minimum amount of solution (1 mg/ml) required to wet the desired sample area given an acceptable film. Even a thin film is cross-hatched with hairline cracks, but the sample plate cannot be seen through these cracks because they are too narrow. Layering more solution over a dry film to cover the hairline cracks is unnecessary and counterproductive. Such a multi-layer film is thick, has larger cracks, and collects airborne dust.

Salts left over from buffers or pH adjustments separate from solution during the drying of the films. The salts collect in the center of the sample plate while the protein is displaced to the outer edges of the plate, where it forms a thick, cracked crust. Samples prepared from solutions of extreme pH values had to be run as pellets for this reason.

There was no detectable difference between the XPS spectra from a pellet and a film of pH 6.6 ferricytochrome c.

Blank runs made on the quartz and aluminum sample plates showed the usual carbon contaminant line, but no nitrogen line. There was a barely detectable signal in the Fe 3p region, and a significant peak 10 eV below the S 2p region. These signals will be discussed later.

The sulfur amino acids were obtained from Calbiochem (A grade). Cysteine sulfinic acid and cysteic acid were also Calbiochem (A grade). Methionine sulfoxide and methionine sulfone were obtained from K & K Laboratories. The partially oxidized samples, cysteine sulfinic acid (Lot #40075) and methionine sulfoxide, gave S 2p spectra indicative of an impure mixture of oxidized forms. The oxidized amino acids were used directly from the bottle with no further purification. They were prepared as films except for the sulfoxide, which was run as a pellet (250 psi).

Microperoxidase (Sigma Chemical Co., Lot #113C-7160) is the name given to a mixture of heme peptides, mostly heme undecapeptide, obtained from horse heart cytochrome c by digestion with pepsin.⁷ Column chromatography on similar material resulted in three distinct bands.⁸ The preliminary interpretation was that these bands correspond to different peptide chain lengths attached to the heme. The amino acid analysis⁹ was done by a technique similar to Spackman's;¹⁰ the results are shown in Table I. The microperoxidase was hydrolyzed according to a standard procedure.¹¹ 0.5 - 1 mg of material in a test tube was dissolved in 2 ml 6 M HCl. The solution was bubbled with nitrogen for 45 min to remove

Table I. Results of amino acid analyses on microperoxidase (deoxygenated), horse heart cytochrome c (one analysis with dissolved air and one deoxygenated), and porphyrin cytochrome c (one analysis with dissolved air and one deoxygenated). Observed residues in microperoxidase calculated from the ratio with valine. Observed residues in all the cytochrome samples calculated from the ratio with leucine.

	Microperoxidase		Cytochrome c			Porphyrin Cytochrome c		Methionine plus Methionine Sulfone Mixture (Micromoles)	
	(Deoxygenated)		Theo.	Obs.	(Deoxy.) Obs.	Obs.	(Deoxy.) Obs.	Theo.	Obs.
Theo.	Obs.								
Tryptophan ^a			1						
Lysine	1	1.2	19	19.0	19.0	19.0	19.0		
Histidine	1	0.94	3	2.7	1.0	2.1	2.3		
Arginine			2	1.7	0.57	1.7	0.5		
Cysteic acid				trace	0.09	trace	trace	—	0.019
Methionine sulfoxide				0.4	0.09	1.7	1.3	—	0.23
Aspartic acid/ asparagine		0.08	8	8.2	8.0	8.3	8.1	—	0.01
Methionine sulfone						trace		0.32	0.38
Threonine	1	0.75	10	3.0	5.8	2.7	5.9	—	0.01
Serine		trace				trace	trace	—	0.01
Glutamic acid/ glutamine	3	3.2	12	12.0	12.0	12.0	13.0	—	0.02
Proline			4	3.5	3.6	3.4	2.9	—	trace
Glycine		0.13	12	13.0	12.0	12.0	14.0	—	0.02
Alanine	1	1.1	6	6.2	5.9	6.1	6.2	—	0.01
1/2 Cystine	2	1.7	2	0.55	0.74	0.78	0.99	—	trace
Valine	2	2.0 ^b	3	3.1	2.9	3.1	3.4	—	0.01
Methionine		trace	2	1.4	1.7		0.17	0.30	0.002
Allo-isoleucine				0.83	0.34	0.98	0.33		
Isoleucine		0.007	6	5.0	5.3	5.0	6.0	—	0.002
Leucine		0.006	6	6.0 ^b	6.0 ^b	6.0 ^b	6.0 ^b	—	0.006
Tyrosine			4	3.7	3.5	3.5	3.1		
Phenylalanine			4	3.9	3.7	4.0	4.1		

^aTryptophan was not detected by this method.

^bBy definition, the number of observed residues are established by ratio to these amino acids.

dissolved air and then frozen in liquid nitrogen. The tube was evacuated, sealed, and heated to $110^{\circ} \pm 8^{\circ}\text{C}$ for 22 hours. A black precipitate, probably iron heme, and inorganic salts, appeared in the solution after heating and was removed by centrifugation. The solutions were evaporated to dryness. The analyst⁹ dissolved the dry samples in 1.00 ml of pH 5.26 citric acid buffer (Beckman). A 400 λ aliquot was run on a Beckman 120 automatic amino acid analyzer containing a Beckman AA27 column for basic residues (lysine, histidine, ammonia, arginine) and a Beckman AA15 column for acidic and neutral residues. Citric acid buffers (Beckman) of pH 3.28 and 4.25 were used to separate the acidic and neutral residues.

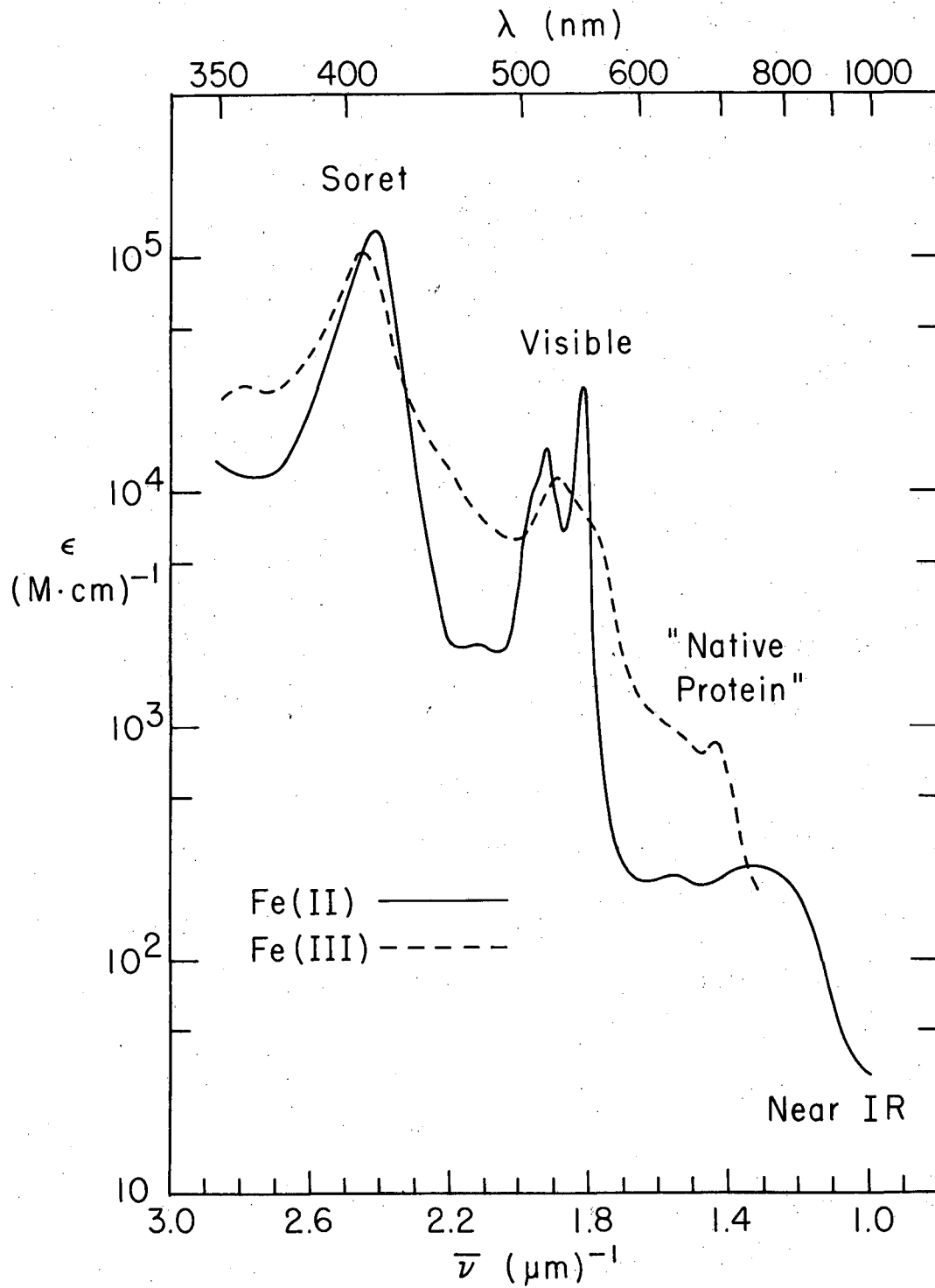
The microperoxidase results in Table I were obtained by taking ratios with respect to valine. The slight excess of lysine is consistent with the presence of a contaminant heme peptide with 21 residues including lysine 22. The 1/2 cystine result is low because these residues are attached by thioether linkages to the heme; the absent 1/2 cystine was probably included in the black precipitate which was discarded from the hydrolyzate. Histidine could have remained bound to the heme and discarded, which would explain the low histidine result. Generally, however, the microperoxidase results in Table I are consistent with the undecapeptide structure.⁷

Microperoxidase was taken directly from the bottle, dissolved in distilled water (the resulting solution had a pH of 7.1), and dried in a film as described above on a gold platen for use in the Hewlett 5950A spectrometer. Buffer salts left over from the pepsin degradation

collected in the center of the plate and resulted in a poor film. More microperoxidase was desalted over Sephadex G-10. The solution resistance decreased from 3×10^4 ohms to 1.6×10^4 ohms; the pH dropped from 7.1 to 5.9. The desalted microperoxidase yielded excellent films on quartz plates.

Horse heart cytochrome c was obtained from Sigma Chemical Co. (type VI). The purity of the commercial products was checked by elemental and amino acid analysis as described below. The optical absorption spectrum can be used to determine the oxidation state of iron and properties of certain ligands around the iron. The visible spectrum of oxidized and reduced horse cytochrome c from 1000 to 350 nm¹² is shown in Fig. 2. The 600 - 250 nm region, constructed from extinction coefficients by Margoliash and Frohwirt,¹³ is given on p. 125 of Ref. 2.

The ferrous spectrum is characterized by two bands in the visible region and a strong Soret absorption. All of these absorptions have been interpreted¹⁴ as $\pi-\pi^*$ transitions from filled A_{2u} and A_{1u} orbitals in the porphyrin ring to unoccupied E_g orbitals. The visible absorptions are split into two bands, α (longer wavelength) and β , by excitation to different vibrational levels in the E_g orbitals. The α band represents the 0-0 transition; β represents 0-1. The Soret band is also split by vibrational coupling, but the magnitude of the splitting is less than that of α to β . The same features are observable in the ferric spectrum, but the bands are broadened, possibly by charge transfer from ligand to iron during the electronic transitions.¹⁵ The α and



XBL7110-5408

Figure 2. Optical spectrum of cytochrome c (Ref. 12).

β bands in the ferrous spectrum, which are much sharper than those in the ferric spectrum, provide a convenient check on the amount of reduced form in a given cytochrome sample.

There is an additional peak in the ferric spectrum at 695 nm, which is specific to axial ligands of imidazole nitrogen from histidine 18 and sulfur from methionine 80.^{16,17} The absorption is interpreted as a charge transfer transition polarized perpendicular to the porphyrin plane,¹⁸ but it is not known whether the charge is transferred from ligand to iron or porphyrin to iron. The available evidence¹² is consistent with transfer from porphyrin to iron.

Horse heart cytochrome c was prepared several different ways for various experiments:

- (1) Crystals were taken directly from the bottle (lot #21C-7600) without dialysis or purification and pressed into pellets (4 tons) for preliminary experiments.
- (2) Dialyzed protein (lot #21C-7600) was dissolved in glass distilled water, adjusted to pH 2 with HCl, and left to stand a few minutes. The protein oxidizes spontaneously under aerobic conditions at this pH.^{2,4} The pH was returned to neutral with KOH. An optical spectrum was taken on a small aliquot without and with dithionite to check for reduced protein. The products were always 97 - 100% ferricytochrome. This material was either lyophilized or raised to pH 11 and lyophilized. Both forms were pressed into pellets (500 psi).

-171-

- (3) Dialysis tubing was cleaned in 5% NaHCO_3 . Protein (lot #82-C7700) was dialyzed in clean tubing against deionized water in a cold room for 24 - 36 hours (2 - 3 changes), then lyophilized. When the resulting pink, fluffy material was dissolved (5 - 10 mg/ml), the solution was pH 8. The pH was adjusted to 3 or 7 with HCl or 11 with NaOH. These solutions were dried onto quartz plates; the resulting films were thick and cross-hatched with cracks. Salts resulting from pH adjustment tended to move some protein to the outer edge of the plate, but plenty of cytochrome remained in the center of the plate. The visible and ultraviolet spectra of these samples were taken before and after irradiation.
- (4) Same as (3) except that the lyophilized protein was dissolved as 1 mg/ml, which resulted in a pH of 7. This solution was made directly into a film on a quartz plate without the addition of other reagents. A pH 11 solution was prepared by adding NaOH; then it was dried as a film on quartz. These films were thinner than (3) and were broken by barely detectable hairline cracks. Optical spectra were taken before and after irradiation.

Amino acid analyses of dialyzed, lyophilized cytochrome c (lot #82C-7780) are shown in Table I. The number of observed residues was derived by assuming the leucine analysis was correct and taking ratios with respect to leucine. In the first analysis, methionine is observed to be 30% low. Methionine sulfoxides account for the most of the missing residues. Methionine sulfoxides appear in analyses with pure methionine

controls;¹⁰ apparently, the analysis technique oxidizes the methionine. Dissolved atmospheric oxygen was considered a likely source of the problem. A second analysis was performed in which the protein solutions were bubbled with nitrogen to displace dissolved oxygen before freezing and hydrolysis. The deoxygenated sample shows a significant reduction of sulfoxides. Both of the samples are low in 1/2 cystine, which was probably bound to the black precipitate in the hydrolyzate. Threonine is low in both samples; there is no explanation, but deoxygenation appears to improve the analysis. Histidine and arginine are both low in the deoxygenated analysis. They may have complexed to the iron in the precipitate with their nitrogens. Similar behavior would be expected of lysine, but the lysine analysis appears to be accurate. The other residues are observed within 10% of the expected values, which is a typical error in amino acid analysis.

The elemental analysis⁹ of horse heart cytochrome c (Sigma, Type VI, lot #82C-7700, dialyzed, lyophilized) is shown in Table II. Theoretical weight percentages are based on a dry molecular weight of 12,365, assuming the lysine groups are not protonated, as derived from the published² amino acid composition. The commercial material was advertised as being free of $(\text{NH}_4)_2\text{SO}_4$; however, this claim is difficult to check because the theoretical weight percent of sulfur is only 1.04%. One additional tightly bound sulfate per protein molecule raises the percent to 1.28; two extra sulfates imply 1.52% sulfur. To distinguish these small changes, 30 mg samples of cytochrome c were required. The

Table II. Elemental analysis (Ref. 9) of horse heart cytochrome c (Sigma, Type VI, Lot #82C-7700, dialyzed, lyophilized). Weight percentages based on dry molecular weight of 12365 (no protonation of lysine) as derived from the amino acid composition in Ref. 2, pp. 174 ff.

	Theoretical Weight %	Trial			Average	Trial IV
		I	II	III		
C	54.39	48.82	48.67	48.78	48.76 ± 0.06	48.92 ± 0.05
H	7.16	7.26	7.35	7.28	7.30 ± 0.04	7.15 ± 0.05
N	16.77	14.42	14.48	14.52	14.47 ± 0.04	14.72 ± 0.05
S	1.04	0.91	0.93		0.92 ± 0.05	

Ratio	Theoretical	Obs. (Avg. I, II, III)	Obs. (IV)
$\frac{C}{N}$	3.24	3.37 ± 0.01	3.32 ± 0.01
$\frac{C}{S}$	52.3	53.00 ± 2.8	
$\frac{N}{S}$	16.1	15.70 ± 0.85	

carbon/hydrogen and nitrogen analyses in trials I, II, and III required 4 mg each. As a check on these figures, a fourth trial was run⁹ by an independent technique which yields a C, H, N analysis on only 1 mg of protein. All of the observed weight percentages were found to be reproducible.

All of the results are low except for hydrogen because the protein contains adsorbed water. The C/N ratio suggests that there is an excess of carbon, a deficiency of nitrogen, or both. Adsorbed CO₂ would account for some excess carbon; the dialyzed lyophilized cytochrome was fluffy and had a large surface-to-weight ratio. The C/N ratio is within 4% of the theoretical value; the difference is not significant. The C/S and N/S ratios agree with the expected values within experimental error. One extra sulfate per protein molecule would have given a C/S ratio of about 42, which would have been easily detectable within the experimental errors. The maximum sulfate impurity consistent with the observed N/S ratio is one SO₄⁼ per three cytochrome molecules.

The combined results indicate that the protein used in these experiments is pure with respect to amino acid and elemental composition. It was not deemed necessary to purify the protein on molecular sieve or ion exchange columns because the samples were to be measured in a condensed phase, often in the presence of protons or salts resulting from pH adjustments. The horse heart cytochrome c as prepared here is considered pure for XPS experiments.

As a control on the amino acid analysis of cytochrome c, a mixture of methionine sulfone and methionine was subjected to hydrolysis conditions

and analyzed like the protein samples. The sulfone was prepared by performic acid oxidation of methionine according to Moore.¹⁹ Excess performic acid was destroyed by the addition of HBr. The solution was dried on a rotary evaporator; more methionine was added, and the mixture was acid hydrolyzed like the protein samples. The amino acid analysis given in Table I shows almost no native methionine; it was apparently destroyed by traces of performic acid remaining after the HBR treatment. The large number of impurities in the analysis are the oxidation products of methionine; the major product (70%) is methionine sulfoxide. The analysis was not a useful control as originally planned, but it serves to suggest the approximate proportions of methionine oxidation products under amino acid hydrolysis conditions in the presence of an oxidizing agent.

Three attempts were made to produce prophyrin cytochrome c, PCC, the iron-free analogue of the native protein. The first attempt was based on the method of Nielands.²⁰ 160 mg of cytochrome c (Sigma, Type II) were dissolved in 10 ml of "pure" formic acid with 100 mg oxalic acid and 150 mg of a platinum catalyst. The procedure called for Mohr's catalyst; Adam's catalyst (platinum oxide) was used instead. Nitrogen gas was passed through the solution for 2 hours, and 100 mg of o-phenanthroline were added. The anhydrous solvent, formic acid, was supposed to denature the protein to expose the heme so that the porphyrin ring could be protonated. The liberated iron was supposed to complex with the phenanthroline. I failed to make this method work.

Contaminant water from "pure" (88%) formic acid might have been kept the protein "closed". Attempts to dry the acid with boric

anhydride²¹ were unsuccessful. A modification of Nieland's procedure using 99% trifluoroacetic acid also failed.

The second attempt followed the procedure of Jones and Jones.²² The technique is similar to Nieland's; cytochrome c was dissolved in a pyridine/acetic acid solution. The reducing agent was FeSO_4 , the products were separated on Sephadex G-25. I was also unsuccessful in reproducing the results of Jones and Jones.

The iron was finally removed successfully by the HF method of Robinson.^{23,24,25} I used the HF line in the laboratory of Prof. H. Rapoport; it is essentially the same as the one described by Robinson.

Several batches were prepared; in a typical run, 204 mg of cytochrome c (Sigma, Type VI, lot #82C-7700) were placed in a Kel-F reaction vessel with a stirring bar. The system was pumped down to 0.07 mm Hg and the reaction vessel was cooled with liquid nitrogen. About 5 ml of HF were distilled into the reaction vessel from a reservoir of HF containing CoF_3 . The reaction mixture immediately turned bright purple. The distillation was completed in about 2 min. After two more minutes, the reaction vessel was opened to the vacuum and the liquid nitrogen was replaced with an ice bath. Within 10 min, most of the HF had evaporated. It took 25 min to warm the vessel completely. The reaction vessel was removed from the line and placed in a dessicator with NaOH pellets under reduced pressure to remove traces of HF. The material was dissolved in about 5 ml of deionized water and lyophilized. 199 mg (no correction made for adsorbed water, etc.) of product were obtained. At every step after the addition of HF, it was necessary to minimize exposure of the product to light in order to prevent photo-damage.²⁶

The product was then treated according to Fisher et al.²⁶ 97 mg were dissolved in 6 M guanidine hydrochloride, 0.05 M ammonium acetate/ acetic acid, pH 5.0, and stirred for two hours. The solution was loaded onto a column (2.2 × 200 cm) of Sephadex G-50 (fine) that had been equilibrated with 0.05 M ammonium acetate/ acetic acid, pH 5.0, buffer. The column was eluted with the same buffer. The elution profile is shown in Fig. 3. Fractions 7 - 11 were dialyzed, lyophilized, and frozen. The single peak elution profile contrasts with the results of Fisher,²⁶ who interpreted the additional peak as denatured protein.

The visible spectrum of fraction #10 is shown in Fig. 4, the four visible bands are evidence of a metal-free porphyrin.^{14c} The positions agree to less than 2 nm with those observed by Robinson²⁴ and by Jones and Jones.²² Dickinson and Chien²⁷ and Fisher et al.²⁶ did not report their PCC optical spectra. Presuming some iron to remain in the system, a few granules of dithionite were added to the sample of fraction #10, and the optical spectrum was rescanned for changes near the α band of reduced cytochrome c at 550 nm. The entire spectrum lost intensity, but generally preserved its shape.

Iron analysis by x-ray fluorescence²⁸ on lyophilized PCC indicated 10 - 50 ppm of iron, i.e., 99% of the iron was removed. Copper and zinc were present in concentrations two or three times greater than iron.

The amino acid analyses of similar samples of PCC are given in Table I. The first PCC sample contained dissolved air; nitrogen gas

Porphyrin cytochrome c, 4th batch (1st half)
Vol. III, p. 26

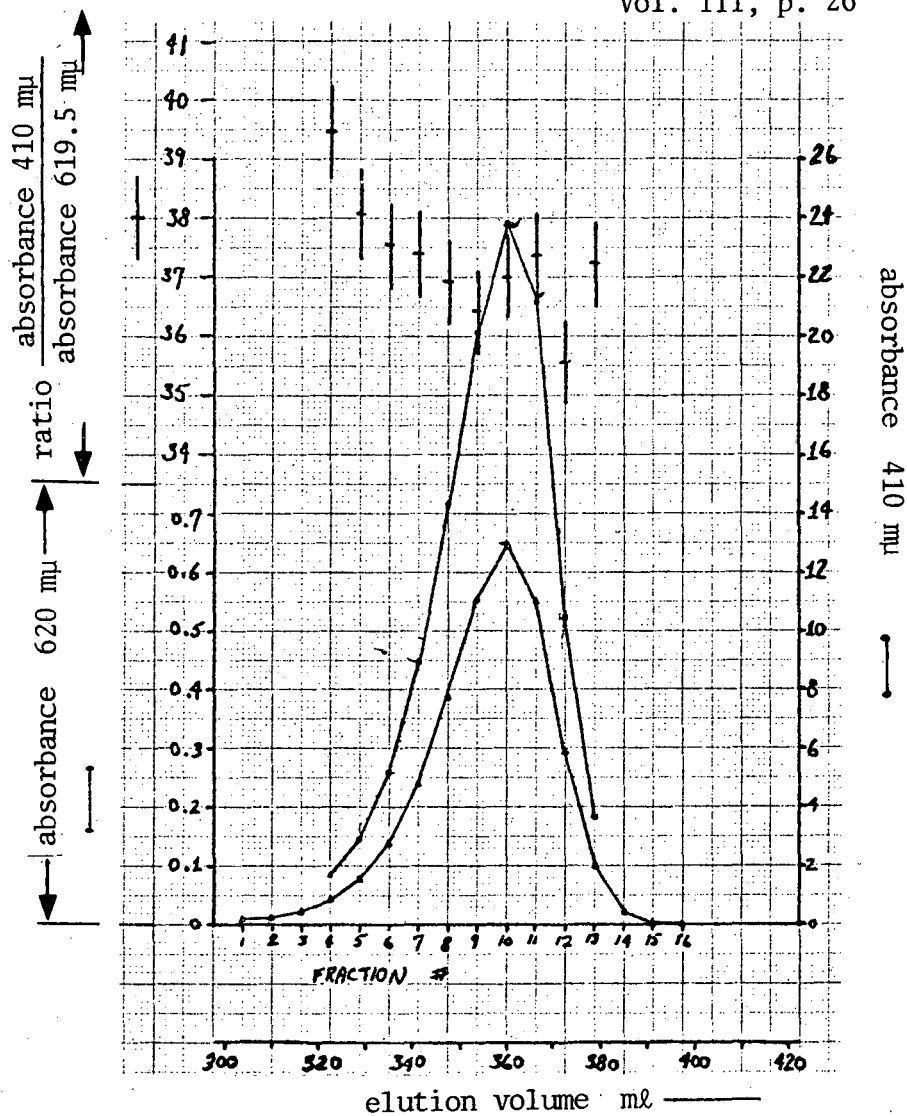
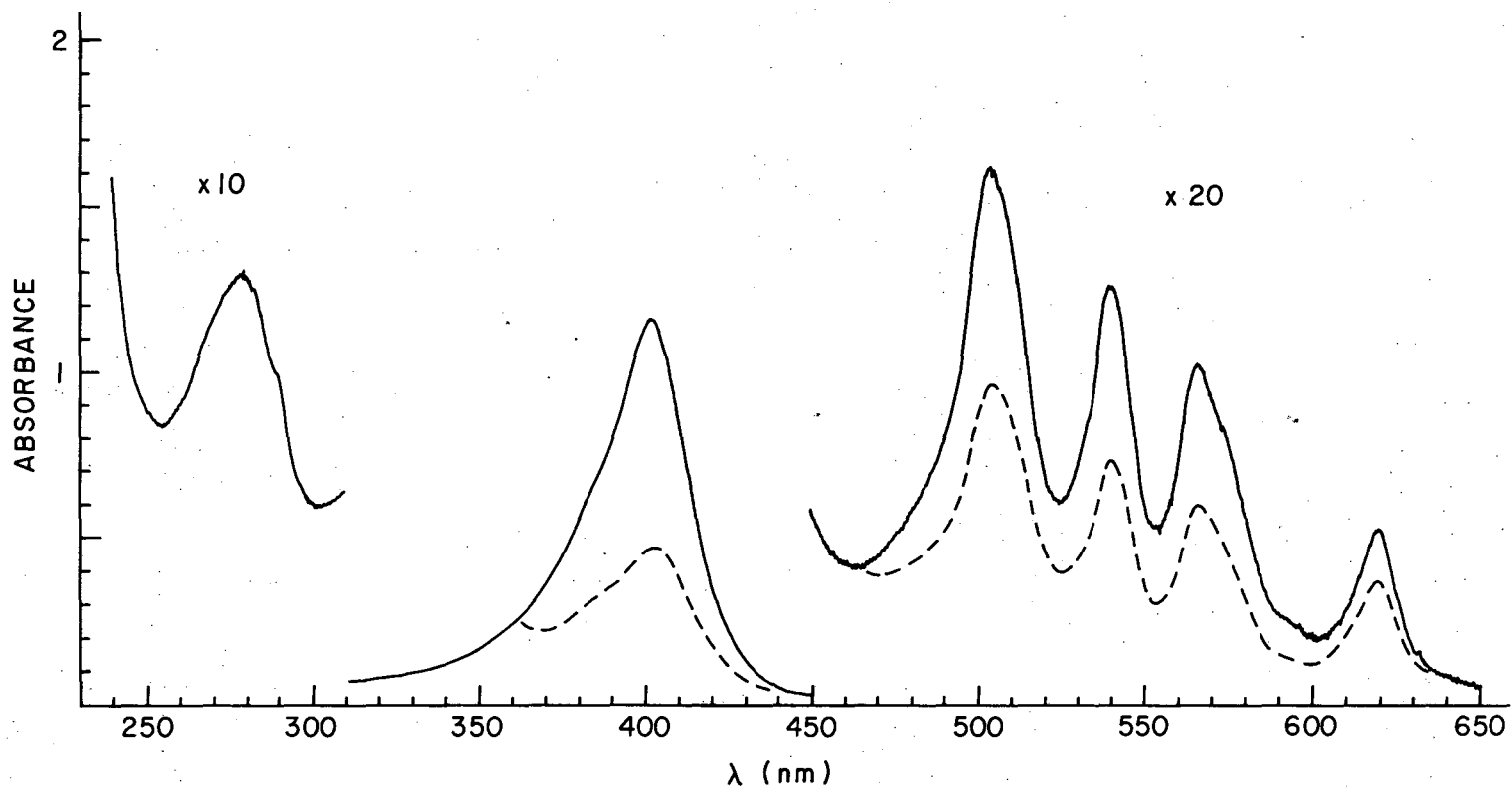


Figure 3. Elution profile of porphyrin cytochrome c from a 2.2×200 cm column of Sephadex G-50 eluted with 0.05 M ammonium acetate/acetic acid buffer, pH 5.0. The ratio of absorbance at 410 nm to 619.5 nm is superimposed over the profile.



XBL755-5258

Figure 4. Optical spectrum of porphyrin cytochrome c (PCC) in solution. The sample is fraction #10 from the elution profile in Fig. 3. Solid line is the spectrum before the addition of dithionite; dashed line, after addition of dithionite. Approximate millimolar extinction coefficients ($160 \text{ cm}^{-1} \text{ mM}^{-1}$ at 404 nm, p. 319, Ref. 24) indicate the concentration is 0.007 mM.

was bubbled through the second sample to displace traces of oxygen. The results for histidine, threonine, proline, 1/2 cystine, and tyrosine were low, just as in most of the other analyses. The asparagine results were not consistent between the two samples. The glutamic acid and glycine results were 10 - 15% higher in the second sample, suggesting some oxidation and degradation reactions.

The most striking result of the analyses was the nearly complete absence of methionine and the corresponding large amounts of methionine sulfoxide.

C. Results and Discussion

Criticism of the HF Procedure for Iron Removal from Cytochrome c

The conditions required for the removal of iron from cytochrome c are somewhat drastic. The protein is subjected to sub-zero temperature, dissolved in anhydrous HF, thawed, lyophilized, and dissolved in guanidine HCl for hours. The effects of these treatments deserve investigation. Robinson²⁴ found that the HF (no guanidine HCl) iron removal technique left the structure of the protein intact. Disc electrophoresis indicated slight deamidation. CD spectra were essentially identical between cytochrome c and PCC. Alpha helix content was calculated to be 30% for PCC and 27% for the native protein. By insertion of iron into PCC, heme cytochrome c could be reconstituted at 5% yield with 80% activity in the succinate oxidase system.

Robinson and Kamen²⁵ stressed the importance of metal-free conditions because copper and zinc were found to incorporate readily into PCC. Copper and zinc impurities found in the preparation described in this work are 2 - 3 times higher than iron.

Fisher et al.²⁶ characterized PCC more thoroughly. Their results generally agreed with Robinson that PCC has the same structure as cytochrome c, but that PCC was more sensitive to thermal denaturation. In comparing PCC and the native protein, Fisher found that: CD measurements suggested similar helical content; viscosity measurements indicated similar compact globular structure; fluorescence showed similar spatial arrangement between the porphyrine ring and tryptophan 59. Fisher also concluded that both proteins refold spontaneously after removal from a solution of guanidine HCl.

A single peak was observed in the Sephadex elution profile in Fig. 3, but Fisher²⁶ and Slama^{46a} both observed a second peak. Fisher did not use a vacuum line; he evaporated the HF in a vigorous stream of nitrogen and dissolved the product in guanidine HCl. Slama evaporated the HF slowly in a vacuum line like Robinson's, but he did not use guanidine HCl. This collective experience suggests that HF treatment and slow evaporation promote aggregation which is counteracted by guanidine HCl. Fisher's rapid evaporation technique seems to cause irreversible denaturation.

The stability of thioether bonds during the HF/guanidine treatment is questionable because: (1) HF can break thioether bonds under certain conditions; (2) amino acid analysis suggests that the HF procedure has

an oxidizing effect on thioether sulfur; (3) oxidized sulfur α to porphyrin seems to be unstable, in fact, almost all the chemical methods for heme cleavage involve some form of oxidation reaction at the sulfur. These three considerations are described below; they indicate that the cystine linkages to porphyrin may be damaged during HF treatment.

Robinson and Kamen²⁵ concluded that HF catalyzed the *formation* of thioether bonds, but they also used HF (with 10% anisole at 20°C for 1 day) to cleave cystine linkages in the preparation of apocytochrome c. The extra peak in the Sephadex G-50 elution profile of Fisher's²⁶ PCC preparation was presumed to contain denatured material in which at least some thioether linkages had been broken. Apparently, the HF/cytochrome system involves an equilibrium between intact and broken thioether bonds.

The amino acid analysis of PCC in this work showed nearly complete conversion of methionine to its sulfoxide, which suggests that the HF/guanidine HCl treatment had an oxidizing effect on thioether sulfur. Nothing definite can be said about the cystine-to-porphyrin bonds because the amino acid analysis of cystine is ambiguous. (Note: Amino acid analysis does not prove the oxidizing effect of HF because the oxidizing effect of amino acid analysis is not defined. Spackman¹⁰ observed oxidation products of methionine in his analyses; Connor claims similar conditions can reduce sulfoxides to methionine. Redox properties of the analysis probably depend on factors such as dissolved air that are difficult to control. One sample in this work was deoxygenated, a

technique which preserved most of the methionine in cytochrome control samples. Therefore, it seems unlikely that all the PCC methionine was oxidized during amino acid analysis. HF/guanidine is suspected as the oxidizing agent.

If the cystine-to-porphyrin thioether bonds are, in fact, oxidized, they are very likely to break. Almost all chemical methods of heme cleavage involve oxidation of the thioether sulfur. These methods include silver²⁹ and mercury³⁰ complexes, performic acid,³¹ iodine plus CNBr,³² and sulfenyl halides.³³ These reactions occur by electron withdrawal from thioether sulfur, i.e., oxidation. (The only known reductive technique involves a sodium amalgam.) Furthermore, Wilson³⁵ found that sulfoxides α to pyrrole were unstable. The only evidence consistent with intact sulfoxides α to porphyrin is Folin's; he claimed to have photo-oxidized the cystine sulfur in cytochrome c with a Xe lamp without breaking the thioether bond.

The presence of intact sulfoxides α to porphyrin might cause a red shift in the peaks of the PCC absorption spectrum, but the sulfoxide's electron withdrawing power is insulated from the conjugated system by the α carbon. Therefore, the red shift may be small, and well characterized controls do not exist.

Broken cystine bonds might be detectable as free -SH groups using p-mercuribenzoate according to Boyer.^{37,38} However, oxidized sulfur may not respond to this test.

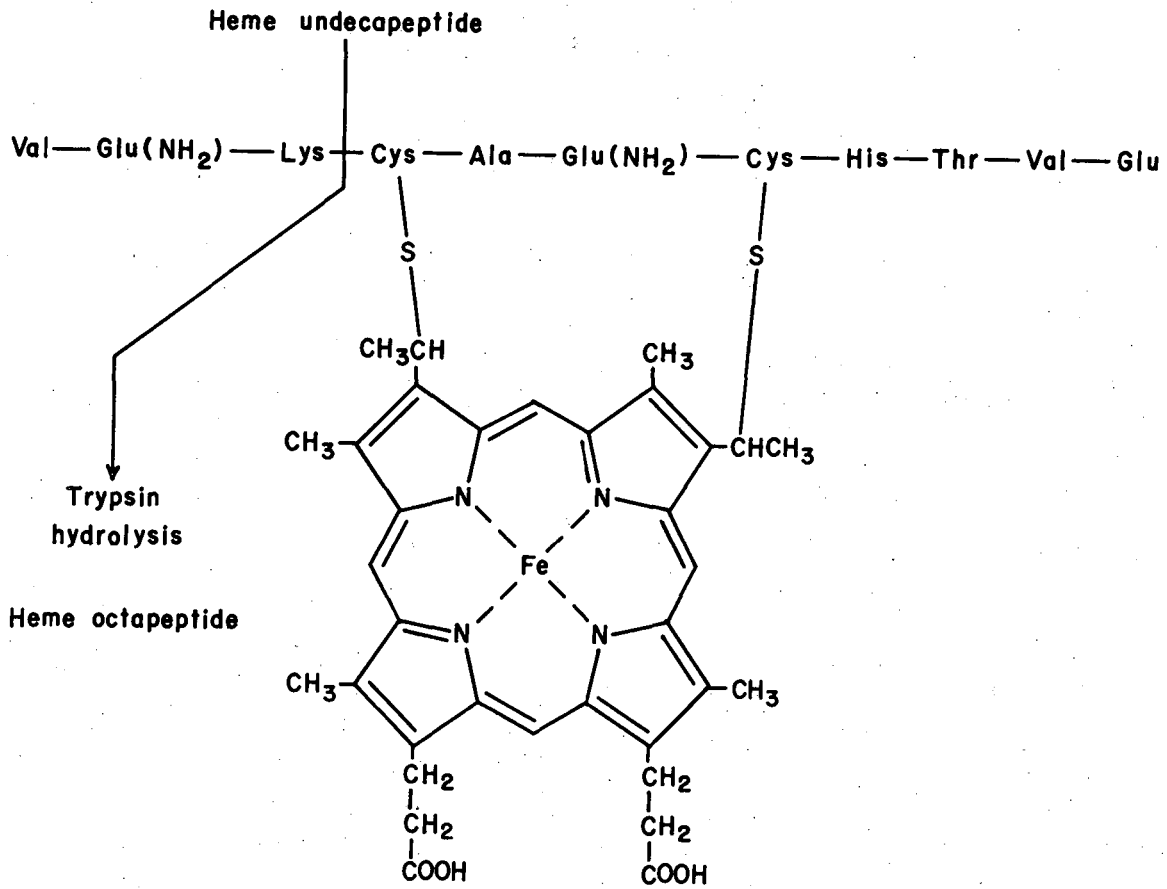
One concludes: (1) that the primary and secondary structures of native cytochrome c are preserved in PCC. (2) The tertiary structure

and spatial arrangements around the heme are probably preserved in PCC. (3) There is some deamidation;²⁴ and (4) substantial oxidation of methionine to its sulfoxide, and perhaps some oxidation of the cystine-to-porphyrin thioether linkages. Whether the cystine sulfoxides α to porphyrin are stable is still undetermined; although the greater amount of evidence favors cleavage.

The Suitability of Microperoxidase as a Model for Cytochrome c

In studies of the iron and sulfur bonding in cytochrome c, it is desirable to have a low molecular weight model that preserves the essential iron and sulfur binding characteristics of the native protein. Microperoxidase⁷ (MP) was selected for this purpose. MP can be called heme undecapeptide, but it is actually a mixture of heme peptides as it comes from the manufacturer (see experimental section). The peptide chain was required to provide a carbon 1s reference signal in the XPS experiments. Variable peptide lengths satisfied this requirement; so, no effort was made to purify the material.

The MP used in this work was prepared by the method of Feder;⁷ although, several other workers have prepared it also.³⁹⁻⁴³ All these methods involve digestion of cytochrome c with pepsin. Heme octapeptide can be obtained by further digestion with trypsin.⁴³ The structures of heme undecapeptide, the major component of MP, and heme octapeptide are shown in Fig. 5. The spectral, magnetic, and redox properties of MP have already been characterized in the early work.



XBL75I-5026

Figure 5. The structure of heme undecapeptide.³⁹⁻⁴³ Heme octapeptide is obtained by digestion of the undecapeptide with trypsin.⁴³

It is generally accepted that between pH 3.4 and 5.8 MP is a pentacoordinate high spin iron complex.^{41,42} The imidazole nitrogen of histidine 18 is believed to bind intramolecularly to the 5 (axial) position on the iron; porphyrin nitrogens occupy the equatorial positions. Above pH 5.8 MP becomes a hexacoordinate low spin complex^{41,42} as the molecules polymerize. The α amino group from valine 11 on a neighboring MP binds intermolecularly to the 6 position of the iron. Total concentration of MP also affects the equilibrium predominance of polymers (1×10^{-5} M) or monomers (1×10^{-7} M).^{43a}

Optical spectra can be used to determine the relative amounts of monomeric, high spin MP and aggregated low spin MP. A spectrum was taken on a 1×10^{-7} M, pH 7.0 solution of MP. As indicated above, this solution could contain monomeric, high spin MP. The Soret peak was at 397 nm; there were visible absorptions at 500 and 622 nm which have been interpreted as charge transfer bands.^{44c} This spectrum is very similar to that of myoglobin,⁴⁴ which also contains pentacoordinate, high spin, heme iron. Monomeric MP would be a better model for myoglobin than cytochrome c.

A 1×10^{-5} M, pH 7.0 MP solution was extensively aggregated in the hexacoordinate, low spin form. Its spectrum resembled that of cytochrome c (Fig. 2), but a small charge transfer absorption at 622 nm and an asymmetric Soret peak (maximum at 400 nm and a shoulder at 407 nm) indicated a significant percentage of high spin monomer.

Nearly complete polymerization was realized when desalted MP solutions were dried into films on quartz plates. Their spectra (Fig. 21)

closely resemble that of ferricytochrome c (Figs. 2 and 19) at neutral pH. A vestigial charge transfer absorption at 622 nm suggests a trace of pentacoordinate high spin monomer. The film is essentially pure hexacoordinate low spin heme iron, like the neutral cytochrome. Previous workers⁴¹ have already established that the paramagnetic susceptibility of neutral to alkaline MP is very close to that of the neutral cytochrome. It has been presumed that this relationship also applies to solid films.

Thus, films of MP reproduce the spectral and spin state properties of native cytochrome c. Therefore, they can serve as a suitable model for the cytochrome in XPS studies. It must be remembered that the MP ligands (imidazole and α amino) differ from the neutral cytochrome (imidazole and methionine); MP more closely resembles the proposed bonding of alkaline cytochrome c (Fig. 1).

MP might be a more effective model of neutral cytochrome c if methionine could be coordinated to the 6 position of the iron. This would require blocking of all carboxyl and α amino groups so that polymerization could not compete with methionine bonding. Harbury and Loach have already done similar experiments in solution,⁴⁵ but they used 10^2 - 10^3 molar excesses of methionine. Techniques must be developed for making films from equimolar solutions. Blocking carboxyl and α amino groups to reduce polymerization also raises the possibility of a completely monomeric film that could model for myoglobin. These experiments are left for the future.

The Carbon 1s Spectrum -- Internal Reference

The aliphatic carbon 1s signal was assigned a BE of 285.0 eV and used as an internal reference in these studies. The cytochrome carbon 1s spectra could be decomposed into three lines that could be assigned approximately to the oxidation states of carbon in the protein. The observed separations between the lines are consistent with the separations observed from the model peptides discussed in Chapter IV. In practice, therefore, any one of the three lines in the C 1s fits could have served as a reference; the aliphatic line was used because it is the dominant line with the least error in position. Since the assignment of the three carbon lines is only approximate, a systematic error (0.5 eV or less) might exist in the BE's derived from this reference technique. However, all the C 1s fits from the different cytochrome samples were consistent with one another; so, shifts and separations may be taken as accurate. The details of these considerations are given below.

Binding energies for C 1s electrons in biologically significant functional groups have already been determined (see Table II, Chapter IV). The carbon atoms of cytochrome c have been grouped according to functional groups in Table III; they have been regrouped into five categories, and finally into three. SUNDER was unable to fit all of the functional groups to the C 1s data; it could not fit the five categories either. It was determined that the resolution of the Berkeley iron-free spectrometer and SUNDER's reliability permitted only a three line fit corresponding to the three categories in Table III.

Table III. The arrangement of carbon atoms in horse heart cytochrome c according to functional groups and rearrangements into five categories and three categories. Five line fits of the C 1s data were unsuccessful. Three line fits of all the cytochrome carbon 1s spectra gave ratios and separations within the limits indicated.

Functional Group		No. of Carbons	No. of Carbons	No. of Carbons	Ratio to Aliphatic Line (Theo./Obs.)	Sep. from Aliphatic Line (eV) (Expected/Obs.)	Binding Energy (eV)
Carboxyl	COOH	14	15	Insignificant	—	—	—
Amino acid carboxyl(ate)	$\begin{array}{c} \text{R}-\overset{*}{\text{C}}\text{H}-\text{COOH} \\ \\ \text{NH}_3 \end{array}$	1					
Unsubstituted amide	$\begin{array}{c} \text{O} \\ \\ \text{R}-\text{C}-\text{NH}_2 \end{array}$	8	112	112	0.37/0.21 ± 0.04	2.9/3.1 ± 0.2	288.0 ± 0.2
Peptide amide	$\begin{array}{c} \text{O} \\ \\ \text{R}-\text{C}-\text{N}-\text{R}' \\ \\ \text{H} \end{array}$	104					
Hydroxyl/ether	R-CH ₂ -OH	14	127	127	0.41/0.45 ± 0.07	1.1/1.1 ± 0.1	286.1 ± 0.1
Peptide α	$\begin{array}{c} \text{O} \\ \\ \text{---N---}\overset{*}{\text{C}}\text{H}_2\text{---}\text{C---N---} \\ \qquad \qquad \\ \text{H} \qquad \qquad \text{H} \end{array}$	113					
Carboxyl α	R- [*] CH ₂ -COOH	14	60	306	1.0/1.0 defn.	0.0/0.0 defn.	285.0
Amino/imino	R-CH ₂ -NH ₂	46					
Thioether	R-CH ₂ -S-R'	8	246				
Aliphatic/aromatic/contaminant		238					

Typical three line fits are shown in Fig. 6. These are the carbon 1s spectra from a film of horse heart cytochrome c dried onto a quartz plate from a solution at pH 6.6. The fits show the data from the first scan, the tenth scan, and the sum of all ten scans. The FWHMs were constrained to be the same for all lines; there were no other restrictions. The dominant line represents aliphatic, aromatic, and contaminant carbon; the middle line represents the peptide α carbons. The contribution from amino/imino and carboxyl α carbon could not be explicitly resolved; it lies between the aliphatic and peptide α lines, and its area is shared by these two lines. The smallest line in the fit represents peptide amide carbon. The contribution from carboxyl(ate) carbon was too small to fit; it was considered insignificant. (The terminology in this paragraph is implicitly defined in Table II and Fig. 4 in Chapter 4 and Table III of this chapter.)

In the fit of all ten scans, the observed separations are 1.1 ± 0.1 eV and 3.1 ± 0.1 eV (cf. 1.1 eV and 2.9 eV observed with model peptides, Table II, Chapter 4). The slightly increased peptide amide separation probably reflects the effect of the carboxyl(ate) contribution, which was not explicitly fitted to the spectrum. Otherwise, the separations are in good agreement with the model peptides in Chapter 4.

The area ratios are difficult to interpret because contaminant carbon, amino/imino carbon, and carboxyl(ate) carbon are not explicitly represented in the fits. Ratios were calculated from the three categories in Table III; amino/imino carbon was arbitrarily assigned to

-191-

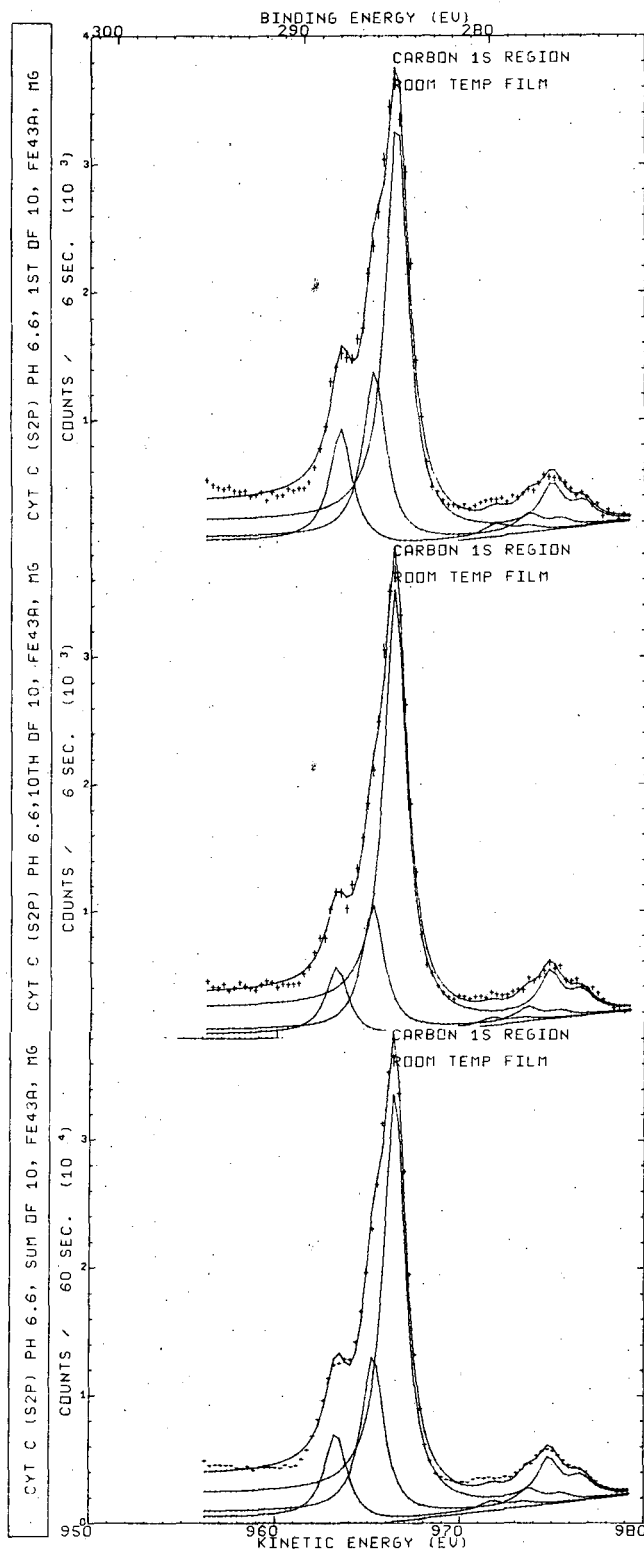


Figure 6. Carbon 1s spectra ($MgK\alpha$) of a film of horse heart cytochrome c dried onto a quartz plate from a solution of pH 6.6. Figure (6a) shows the first scan, (6b) the tenth scan, and (6c) the sum of all ten scans. The calculated lineshapes have FWHM of 1.47, 1.45 and 1.45 ± 0.05 eV, respectively.

the aliphatic line, and contaminant carbon was not considered. These calculated ratios (with respect to the aliphatic line) are 1:0.41:0.39. The observed ratios are 1:0.39:0.21. If the observed ratios are taken literally, they indicate that the amino/imino contribution is included under the middle line and that contaminant carbon has doubled the aliphatic line. This interpretation of the spectrum is very reasonable.

It is apparent that a detailed interpretation of the C 1s fits is not possible, but the three line fits account for the major features in the carbon composition of the cytochrome. The absolute accuracy of the fits can be questioned, but the different cytochrome samples had C 1s spectra very consistent with one another. Therefore, the C 1s spectra could still be used as an internal reference within some undefined systematic error which was probably less than 0.5 eV.

Similar considerations were used to interpret the C 1s spectra of PCC, MP, and mesoporphyrin, which are shown in Figs. 7, 8, and 9.

For purposes of comparison, the C 1s spectra of pH 6 cytochrome c and pH 7 MP, which were taken on a Hewlett Packard 5950A spectrometer, are shown in Figs. 10 and 11. The carbon 1s spectra from the 5950A are complex; up to 21 inflection points and peaks can be observed in the smoothed⁴⁷ carbon 1s spectra of films of pH 7.0 MP and pH 5 - 6 horse heart cytochrome c. It is difficult to distinguish real data from noise, but 15 of these peaks and inflections are reproducible in two films of MP and one film of cytochrome. A specific assignment

-193-

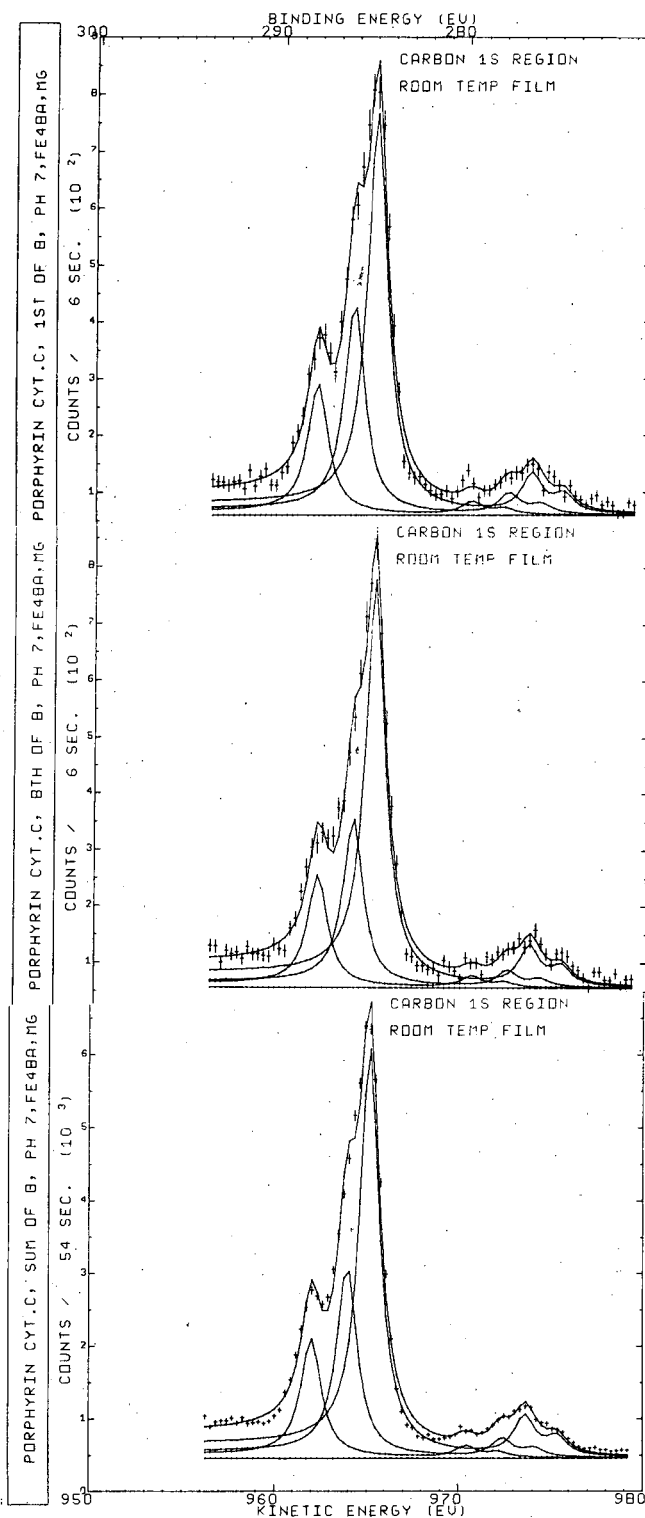


Figure 7. Carbon 1s spectra ($MgK\alpha$) of porphyrin cytochrome c (PCC) dried onto a quartz plate from a solution of pH 7.3. Figure (7a) shows the first scan, (7b) the eighth scan, and (7c) the sum of all eight scans. The calculated lineshapes have FWHM of 1.32, 1.29, and 1.32 ± 0.05 eV, respectively.

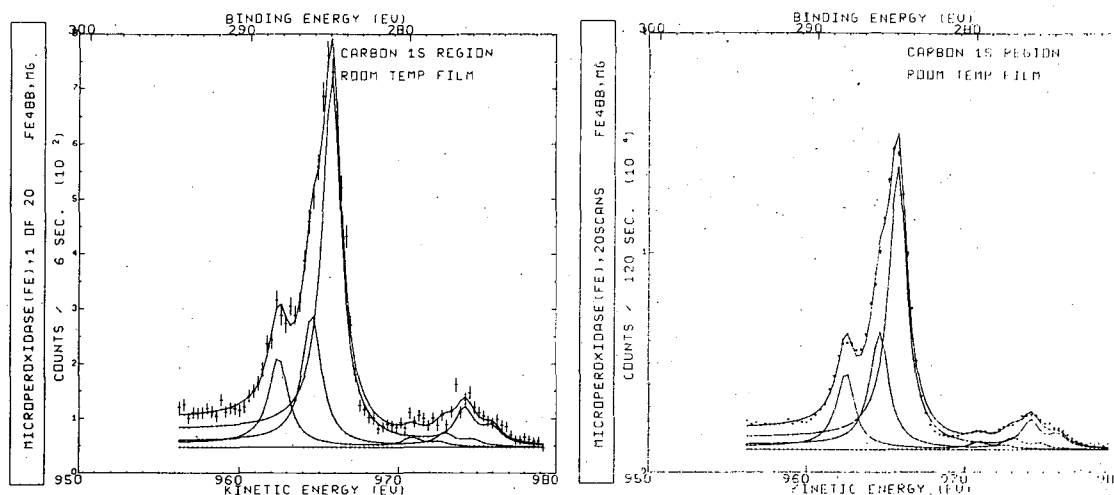


Figure 8. Carbon 1s spectra ($MgK\alpha$) of desalted (Sephadex G-10) microperoxidase (MP) dried onto a quartz plate from a solution of pH 5.9. Figure (8a) shows the first scan, and (8b) the sum of twenty scans. The calculated lineshapes have FWHM of 1.44 and 1.37 ± 0.05 eV, respectively.

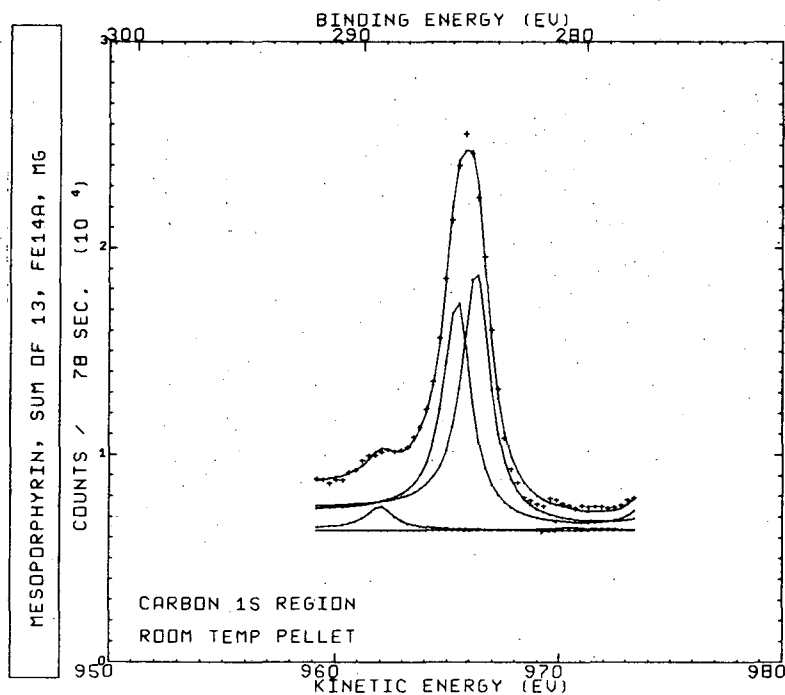


Figure 9. Carbon 1s spectrum ($MgK\alpha$, sum of thirteen scans) of mesoporphyrin in the form of a pellet at room temperature. The calculated lineshapes have FWHM of 1.49 ± 0.06 eV.

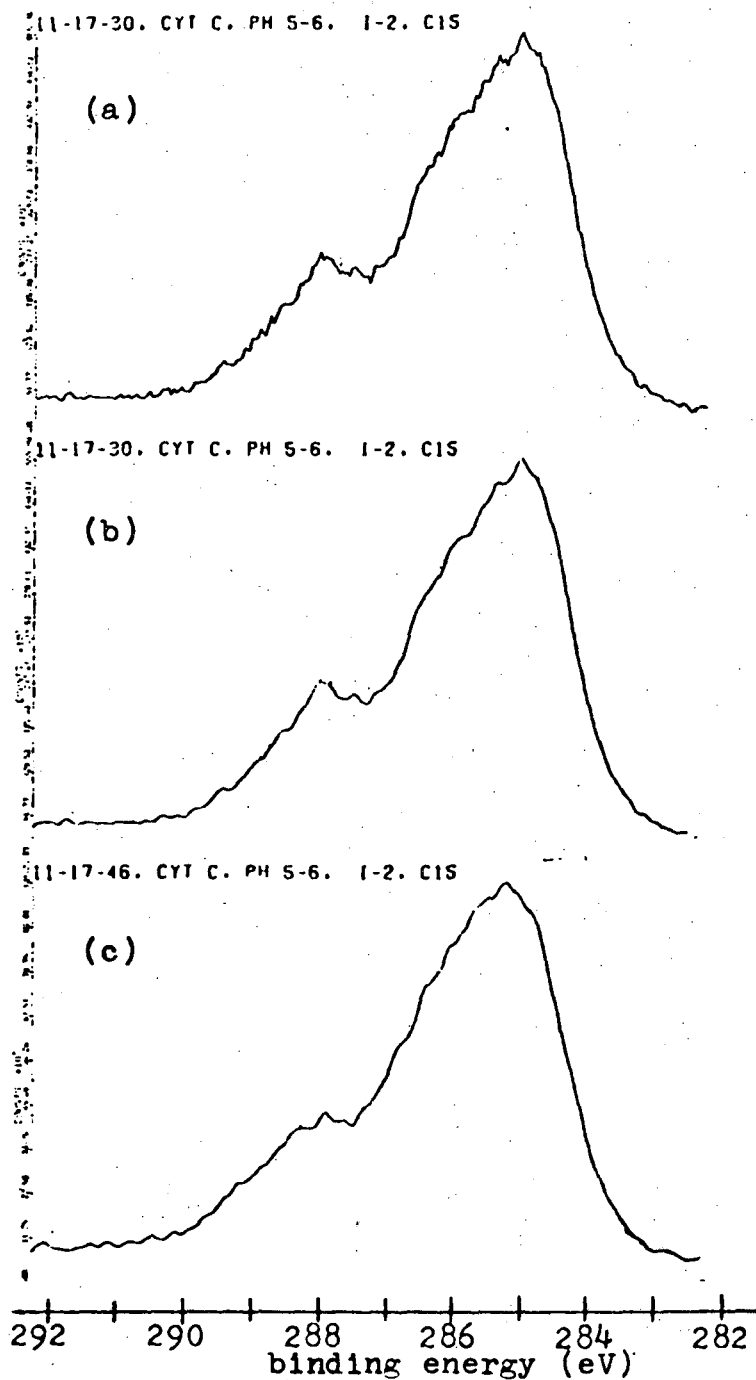


Figure 10: Carbon 1s spectra of dialyzed cytochrome c (HP 5950A spectrometer) dried onto gold platens from a solution of pH 5-6. Fig. 10(a) raw data after 0-4 min. exposure to x-rays (800 watts), (b) same data smoothed according to ref. 47, and (c) smoothed spectrum after 400 min. exposure.

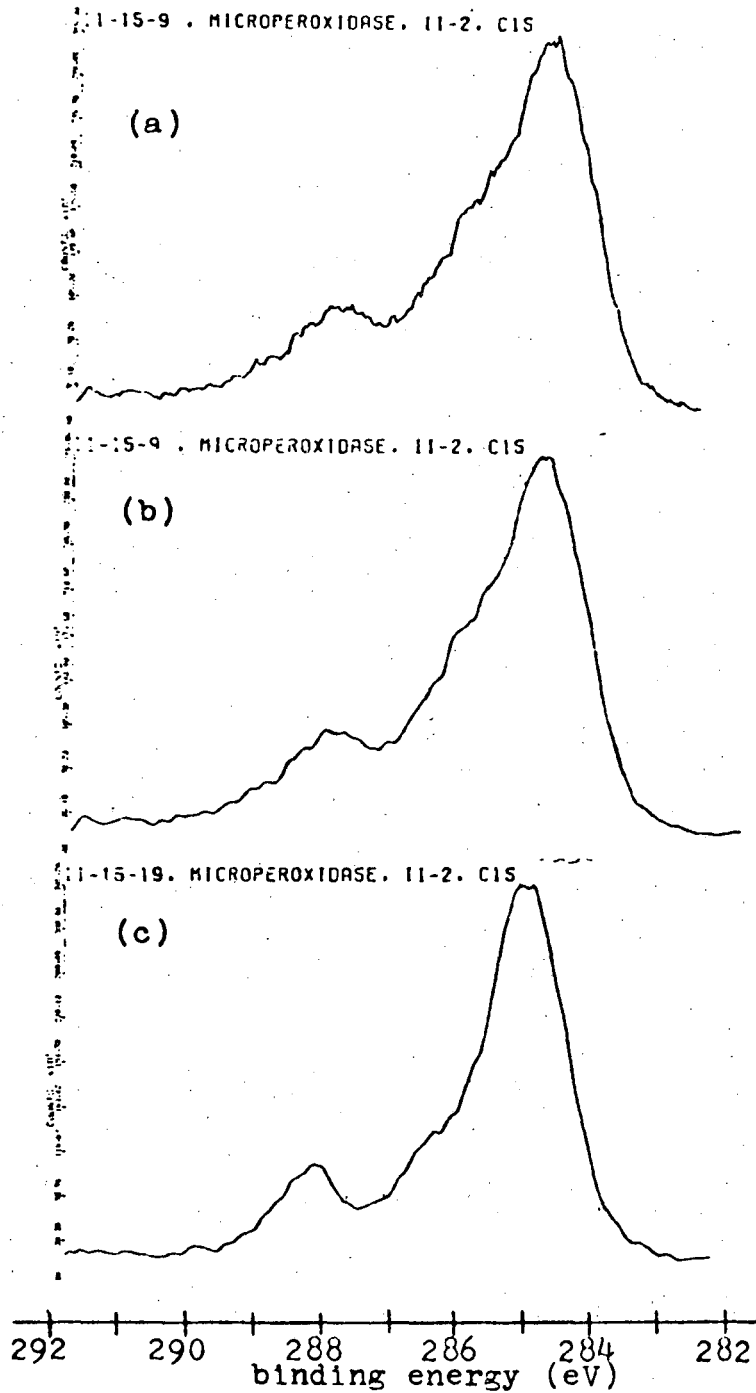


Figure 11: Carbon 1s spectra of microperoxidase (HP 5950A spectrometer) dried onto gold platens from a solution of pH 7. Fig. 11(a) raw data after 0-2 min. exposure to x-rays (800 watts), (b) same data smoothed according to ref. 47, and (c) smoothed spectrum after 114 min. exposure.

of these 15 signals is not possible without similar data on simpler control compounds. A general assignment could be made on the basis of the categories in Table III.

Nitrogen 1s Results

The nitrogen 1s spectra are shown in Figs. 12 - 17. The protein spectra show little structure, which could be expected from the nitrogen results in Chapter 4. The cytochrome c spectrum in Fig. 12 is typical. The data could be fitted satisfactorily with a single line having a FWHM of 1.7 ± 0.1 eV and a BE of 400.2 eV referred to the C 1s spectrum as previously described.

Cytochrome c contains 19 lysine and 2 arginine residues whose amino and guanidyl groups are protonated below pH 9. Model peptides (Chapter 4, Table V) indicate that these protonated groups have a N 1s signal shifted 0 - 1.7 eV from the main N 1s peak. These protonated groups account for 17% of the nitrogen in the protein; therefore, the data were refitted with two lines. The calculated lines had approximately the same intensity and were separated by about 0.7 eV. The separation was approximately consistent with model peptides, but the area ratio did not correspond to the amino acid composition. These results were not reproducible, and the fitting requirements developed in Chapter 3 indicated that this two line fit was unreliable. Therefore, no significance could be attached to fits like Fig. 12b.

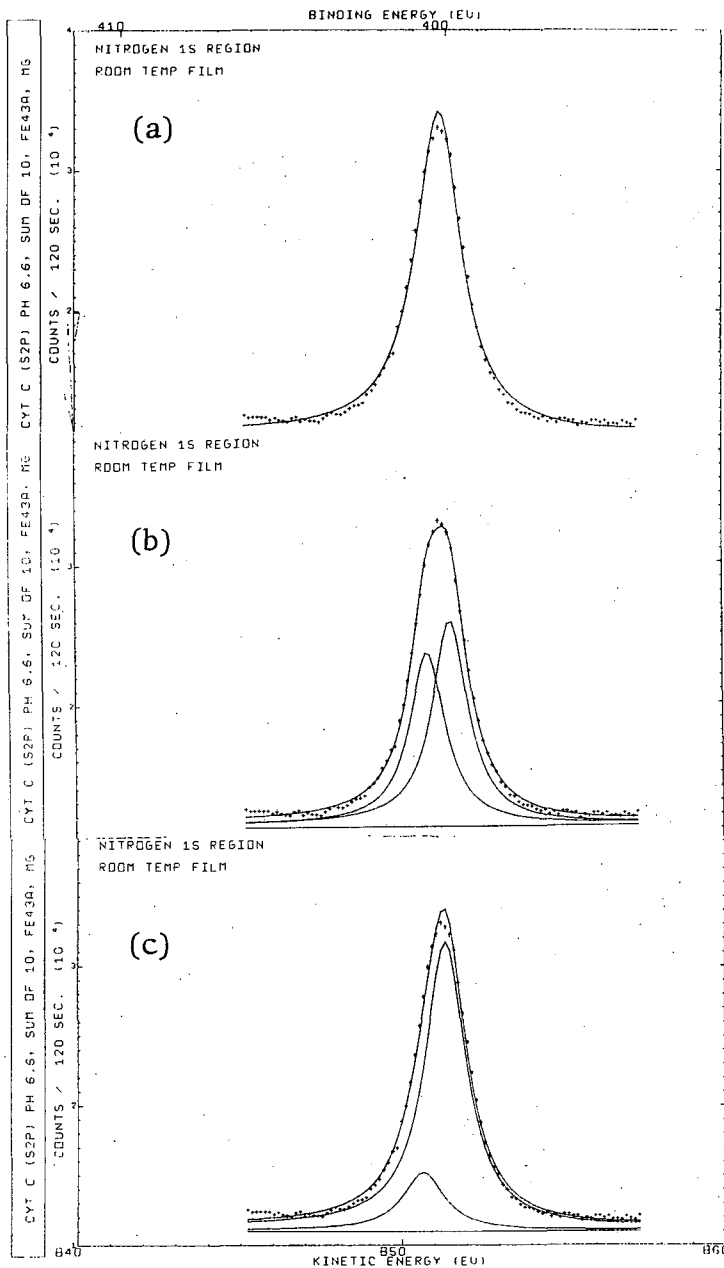


Figure 12. Nitrogen 1s spectrum ($MgK\alpha$) of horse heart cytochrome c dried onto a quartz plate from a solution of pH 6.6. The plots show three fits of the same data from the sum of ten scans: (a) one line (FWHM 1.69 ± 0.05 eV), (b) two lines, ratio (0.8:1) and separation (0.7 ± 0.2 eV) free, FWHM (1.33 ± 0.06 eV) same for both lines, (c) ratio fixed at 0.203:1 to separate the contribution from protonated amino groups, separation (0.7 ± 0.2 eV) left free, FWHM (1.44 ± 0.06 eV) same for both lines.

-199-

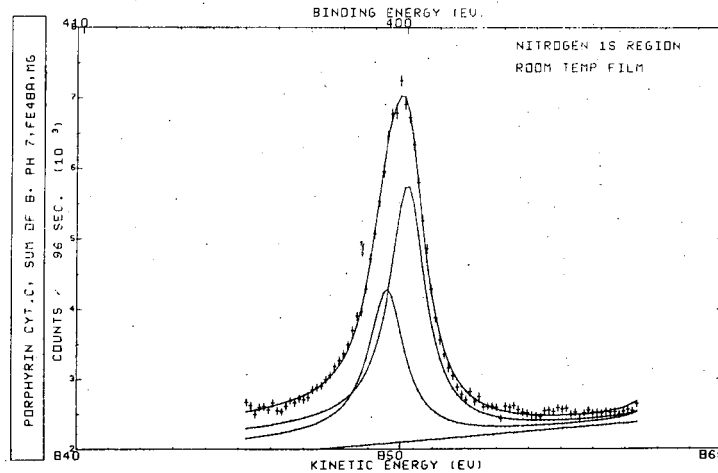


Figure 13. Nitrogen 1s spectrum ($MgK\alpha$) of porphyrin cytochrome c (PCC) dried onto a quartz plate from a solution of pH 7.3: two lines FWHM (1.34 ± 0.04 eV) same for both lines, ratio (0.6:1) and separation (0.6 ± 0.2 eV) left free to vary.

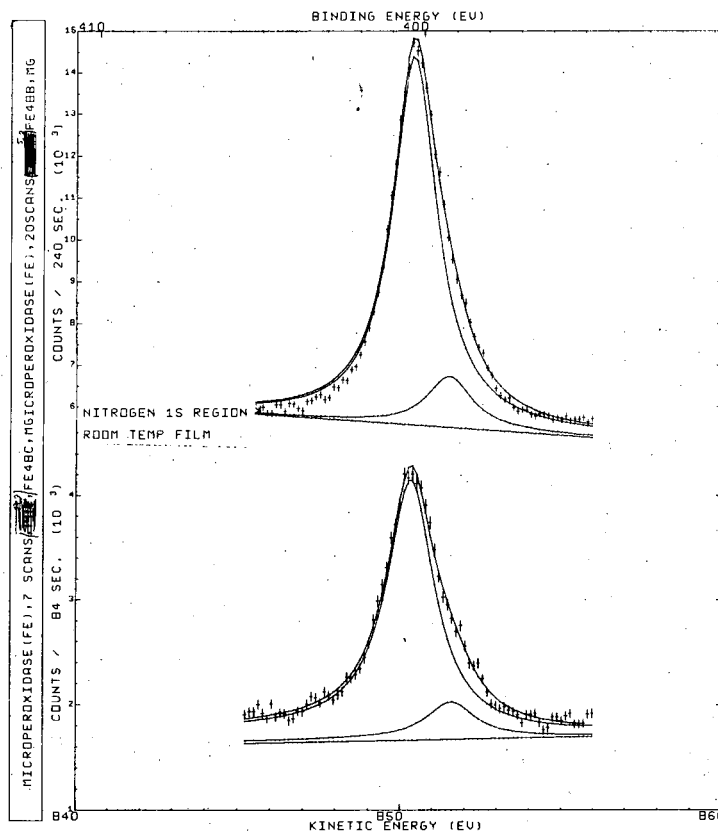


Figure 14. Nitrogen 1s spectra ($MgK\alpha$) from two different samples of de-salted microperoxidase (MP) dried onto quartz plates from solutions of pH 5.9. In each spectrum, FWHM (1.7 and 1.8 eV) same for both lines, ratio (7:1 and 7:1) and separation (1.1 and 1.3 eV) were free to vary.

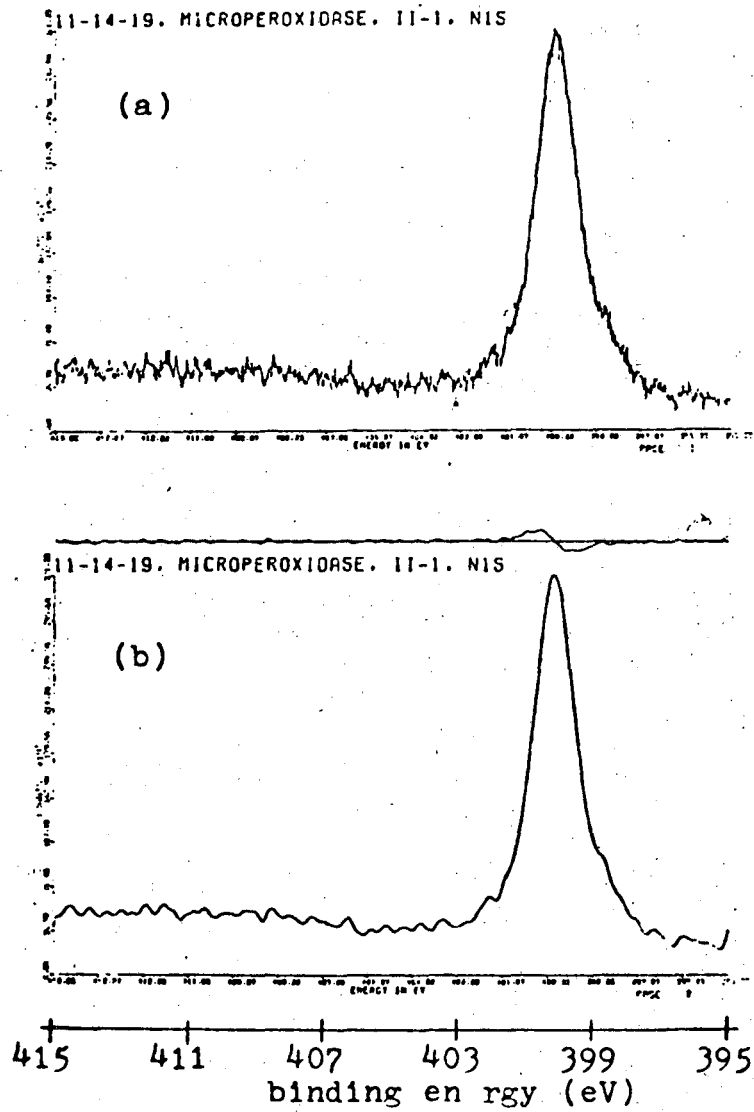


Figure 15: Nitrogen 1s spectrum of microperoxidase (Al K α , HP 5950A spectrometer, 1024 channels in 20 eV) dried onto a gold platen from a solution of pH 7: (a) raw data, (b) same data smoothed according to ref. 47.

-201-

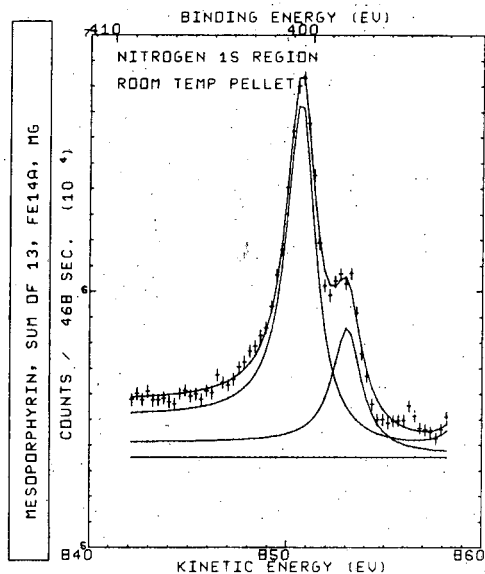


Figure 16. Nitrogen 1s spectrum ($MgK\alpha$, sum of 13 scans) of mesoporphyrin run as a pellet at room temperature; FWHM (1.80 ± 0.05 eV) same for both lines, ratio (3:1) and separation (2.4 ± 0.2 eV) were left free.

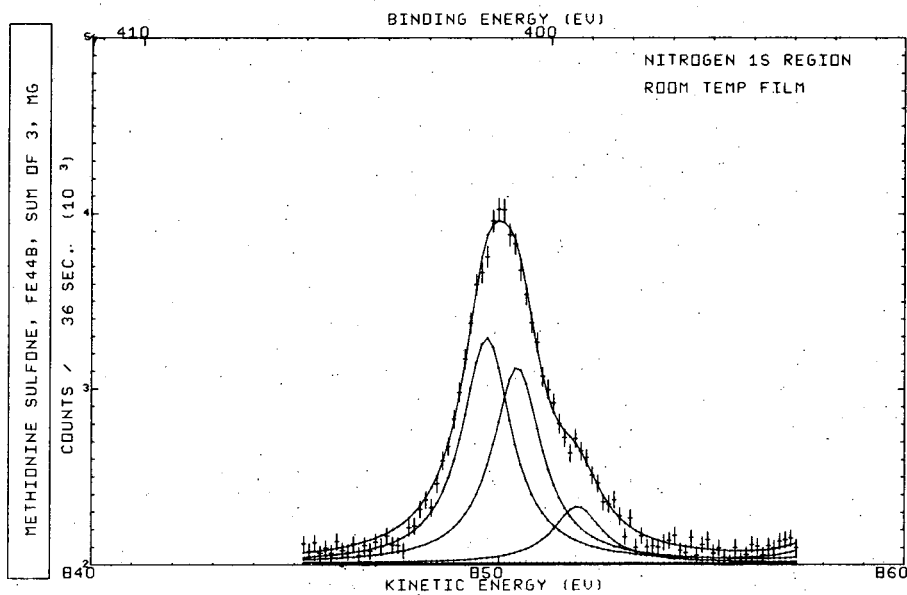


Figure 17. Nitrogen 1s spectrum ($MgK\alpha$, sum of three scans) of methionine sulfone dried onto a quartz plate.

SUNDER could be forced to fit the protonated nitrogen contribution by fixing the two line ratio at 0.203:1, which corresponds to the proportion of lysine and arginine nitrogen. The resulting fit (Fig. 12c) gave a reasonable reproduction of the data. The lines were separated by 0.5 - 0.8 eV, which is approximately consistent with the separation observed in neutral and alkaline peptides (Table V, Chapter 4).

All the cytochrome, PCC, and MP nitrogen had BE's of 400.2 or 400.3 eV when fitted as a single line. This reproducibility is reassuring evidence of the self consistency built into the internal referencing system used in this study.

The N 1s spectrum of mesoporphyrin (Fig. 16) shows two well resolved peaks with BE's of 400.6 and 398.2 eV. The double peak structure is well known from previous studies of porphyrin and related compounds.^{48,49,50} These workers observed separations of 1.9 eV⁴⁸ and 2.0 eV⁵⁰ compared to 2.4 eV observed here. The BE of 398.2 eV agrees with Niwa, et al.,⁵⁰ who also used an internal carbon reference. The two peaks represent protonated and unprotonated nitrogen at the center of the mesoporphyrin ring. The 3:1 ratio suggests an equilibrium mixture of doubly protonated and fully protonated mesoporphyrin molecules in approximately equal proportions. The satellite peak observed by Niwa⁵⁰ could not account for the larger peak in this work.

All of the previous porphyrin studies⁴⁸⁻⁵⁰ have shown that the two peak structure merges into a single peak when a metal is added to the center of the ring. The BE of this peak is midway between the

two original peaks. The data in this work are consistent with this observation; although, the spectra are obscured by the presence of the peptide nitrogens.

Two independently prepared samples of desalted MP had N 1s spectra that could be fitted reproducibly with two lines, as shown in Fig. 14. The dominant line at 400.3 eV represents the nitrogen atoms in the peptide chain. The smaller line at 399.2 eV represents the nitrogen atoms in the heme ring bound to the iron, which is midway between the two mesoporphyrin peaks. The calculated separations in Fig. 14 are 1.1 and 1.3 eV. The calculated area ratios (7.2:1 and 7.0:1) do not correspond to the ratio of peptide to heme nitrogen. This disparity has no significance because the area ratio is the least reliable parameter in a SUNDER fit. In fact, the sitting standards in Chapter 3 indicate that these fits are unreliable. Their reproducibility and agreement with the literature show that these fits are exceptions to the general rules in Chapter 3.

Similar peak structures were resolved in the HP 5950A spectrum in Fig. 15, which shows the N 1s region of MP that contains buffer salts. The separation observed in this spectrum is 1.5 eV, which is slightly greater than those in Fig. 14.

The native sulfur amino acids had simple N 1s spectra with BE's of 401.1 to 401.4 eV and FWHM of 1.5 ± 0.1 eV. The oxidized sulfur amino acids had structure in their N 1s spectra. The most complex is shown in Fig. 17. The numerous lines are unexplained; the sulfur 2p spectrum showed no apparent evidence of reduced impurities.

The Stability of Reference Signals and Optical Spectra

With the source arrangement in the Berkeley spectrometer, an organic sample absorbs photon energy at the rate of 10^6 rad/sec. It is also exposed to an electron flux from the window of the x-ray tube, and an infra-red heat flux from the body of the tube which warms up during operation. The effects of these energy inputs on model peptides have been detailed in Chapter IV. These effects will now be considered in relation to the samples in this section.

Changes in the carbon 1s reference spectra are shown in Figs. 6 - 11. In Figs. 6a and 6b, the peptide amide and peptide α lines have diminished with respect to the aliphatic line over the course of the experiment. The loss is due to the combined effects of decarboxylation and the accumulation of contaminant carbon. The effects are less pronounced in Figs. 7 and 8.

The HP 5950A spectrometer was more sensitive to subtle changes. The MP spectra in Figs. 11b and 11c are simpler to analyze than the corresponding cytochrome spectra in Fig. 10. The structure of the MP carbon 1s signal changes noticeably in the vicinity of 286 eV and in the minimum between 287 - 288 eV. These are approximately the regions where peptide α carbon (286.1 eV) and peptide amide carbon (287.9 eV) are found. It suggests that the peptide chain is being altered during the experiment. A definitive analysis of these differences is not possible without the spectra of simpler models, but my current speculation is that the peptide linkages are being reduced.

There are also subtle losses of intensity between 284.5 - 285 eV, since C 1s BE's of gaseous aromatic molecules are slightly lower than those of gaseous aliphatic molecules.⁵⁶ This structure may be associated with solid phase aromatic carbon that cannot be resolved on the Berkeley spectrometer. (The gas/solid comparison is reasonable because C 1s chemical shifts are about equal in both phases. See Ref. 19 in Chapter 4.) The loss of this structure can be interpreted in conjunction with the optical spectra described later as the loss of conjugation in the heme ring and other aromatic side chains.

Figure 18 shows the stability of the N 1s spectrum. N 1s data from a film of horse heart cytochrome c dried onto a quartz plate from a solution of pH 6.6 were fitted with two lines as in Fig. 12b. The total N 1s area from each of eight scans is plotted against x-ray exposure time in Fig. 18. It can be seen that the total N 1s area diminished only slightly with time. The area ratios were approximately constant at $(0.9 \pm 0.1):1$ over all scans except the first $(0.6:1)$. The FWHM of the individual lines was 1.37 ± 0.05 eV for all scans, and the separation was constant at 0.7 eV. With the possible exception of the first scan, the shape of the N 1s spectrum was constant. The stable shape of the N 1s spectrum does not necessarily imply chemical stability in the photon-electron-IR flux. Table V in Chapter 4 shows that the biologically relevant forms of nitrogen (except protonated amino groups) are indistinguishable in the Berkeley spectrometer. Therefore, chemical changes may not be reflected in the spectrum. On

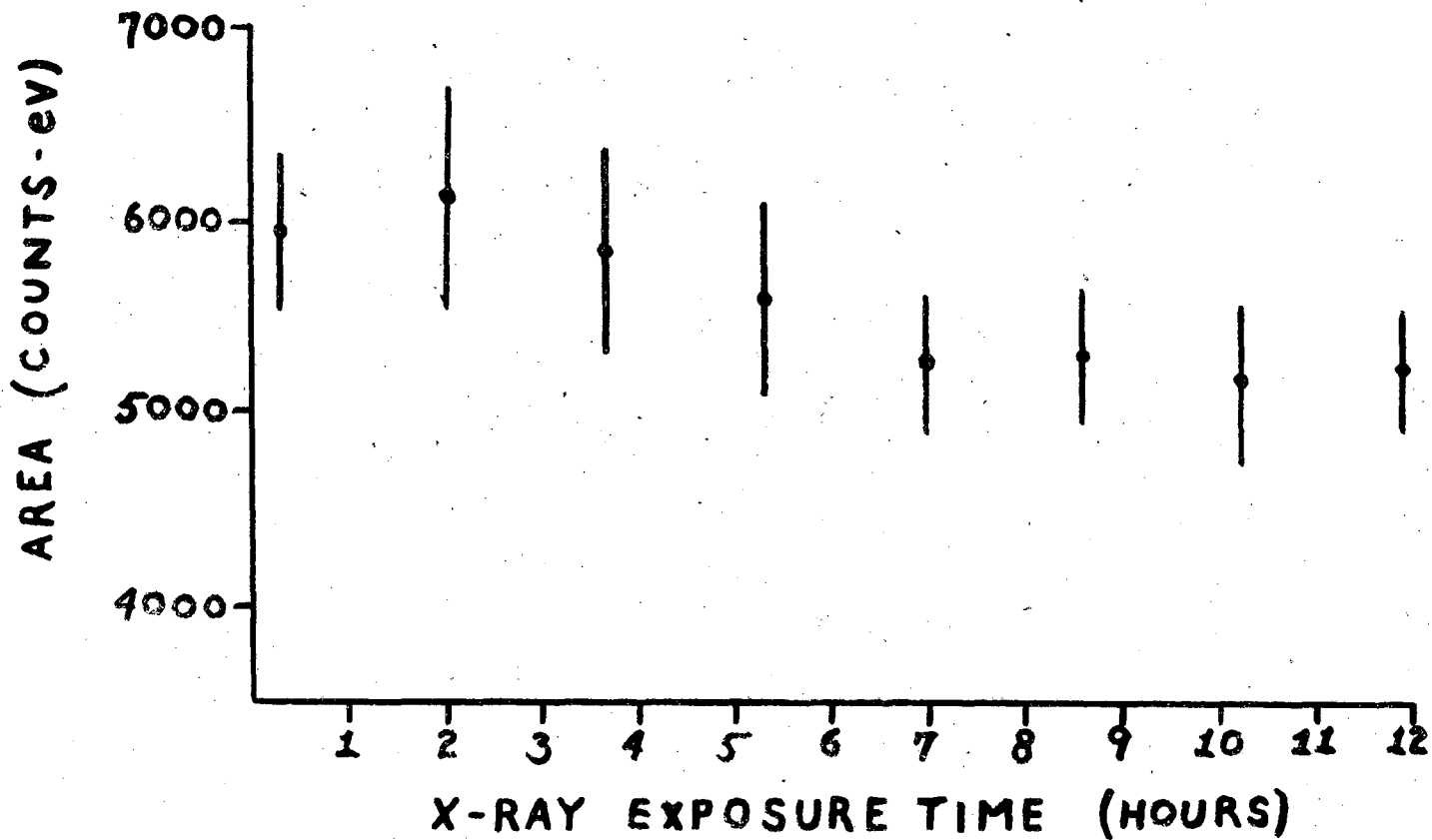


Figure 18. Nitrogen 1s peak area vs. x-ray exposure time (10^6 rad/sec). Sample is horse heart cytochrome c dried onto a quartz plate from a solution of pH 6.6.

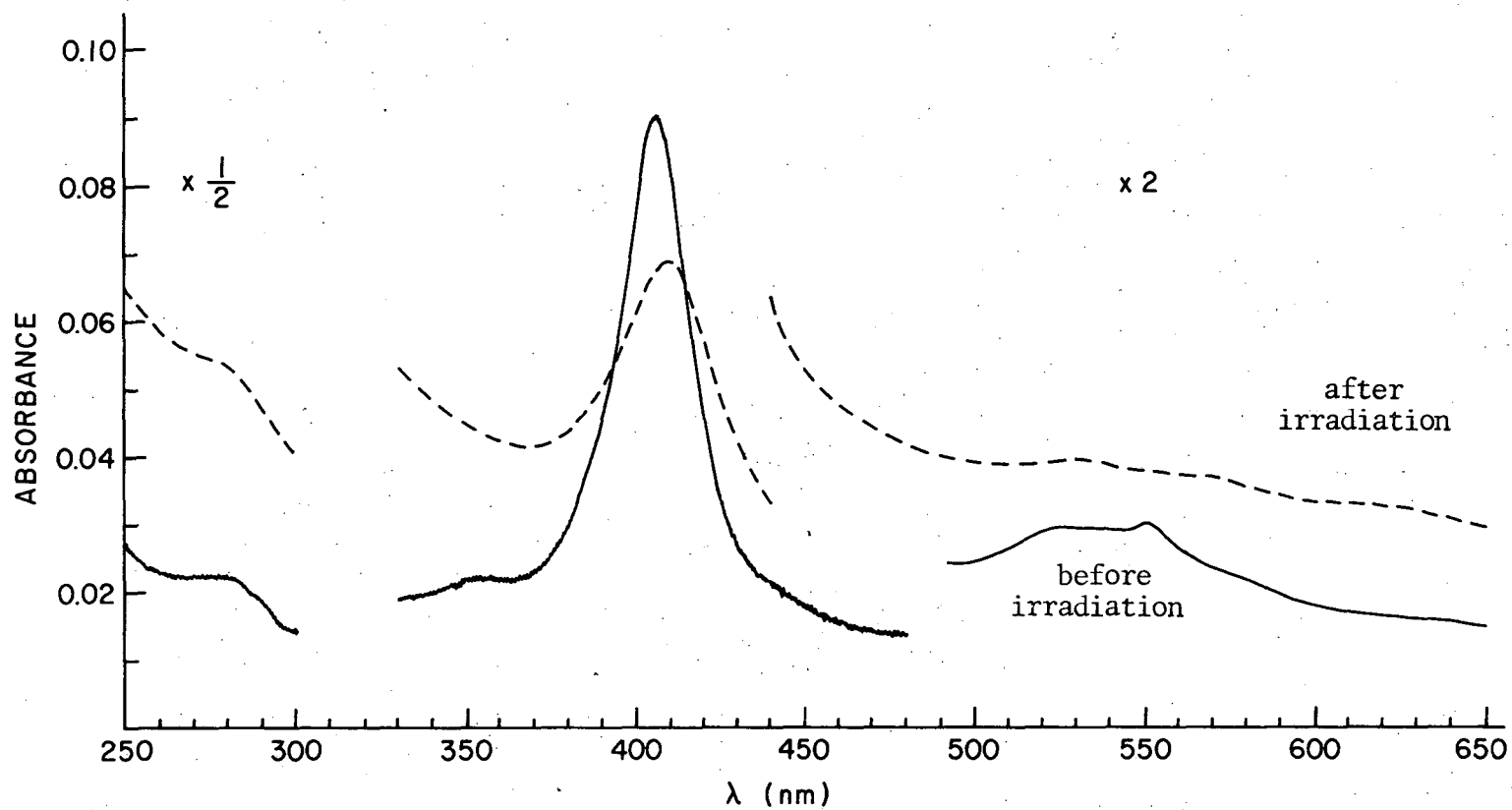
the basis of Fig. 18, it can be said that minimal amounts of nitrogen volatilize as ammonia, methyl amine, etc.

The estimated (see Chapter 2) rate at which the sample absorbs photon energy (10^6 rads/sec) is high enough to saturate the sample with free radicals in a second. The experiments, however, last more than 10 hours. The results summarized above show that the reference signals in the Berkeley spectrometer are not sensitive to damage done by these massive photon doses. Damage still cannot be taken for granted, and it will be considered further.

The optical spectra of a pH 11.0 film of horse heart cytochrome c before and after exposure to radiation are shown in Fig. 19. There are several difficulties associated with taking optical spectra through solid films on a quartz plate even when a similar quartz plate is placed in the reference beam:

1. unequal reflection off the sample film and reference plate;
2. scattering due to inhomogenieties in the film, such as hair-line cracks;
3. absorption flattening on thick, heavily cracked films.

These problems were generally not serious in the unirradiated films. Fig. 19 shows the worst case. The ratios of the Soret peak to the other major absorptions show different ratios from solution work¹³ by 0 - 40%. Ratios in other films were within 10% of the literature values. In such cases, it was assumed that the extinction coefficients from solution¹³ were applicable to the solid films.



XBL755-5259

Figure 19. Optical absorption spectra (Cary 118) of a film (thickness of order 10^{-1} microns) of horse heart cytochrome c dried onto a quartz plate from a solution of pH 11.0. Solid line is the film spectrum before irradiation. Dashed line is the spectrum after 17 hr exposure to the x-ray tube.

The 550 nm absorption indicates that about 15% of the protein is reduced. The solution from which the film was prepared contained 8% reduced impurity. The technique of preparing the film, therefore, tended to reduce the sample.

The optical spectra taken after irradiation show an increase in scattering across the entire spectral range and a reduction or elimination of the π - π^* absorptions. The increased scattering is probably due to denaturation. This interpretation has been reinforced by the insolubility of irradiated films in water. Unirradiated films are readily soluble.

The loss of the π - π^* transitions in the visible region and the reduction of the Soret intensity can be interpreted as the loss of conjugation in the heme ring. The Soret peak is not observed in porphyrinogens and bile pigments where the conjugation around the porphyrin ring has been interrupted. It is, however, present in some Zn complexes of bile pigments where conjugation is preserved through the metal.^{14c} The formation of bile pigments by exposure of iron heme proteins to β and x-irradiation has already been documented in solution (Ref. 14c, pp. 21, 22). It is reasonable to extend these observations to the solid films if one anticipates results to be discussed soon, viz., the electron flux from the x-ray tube window reduces the samples.

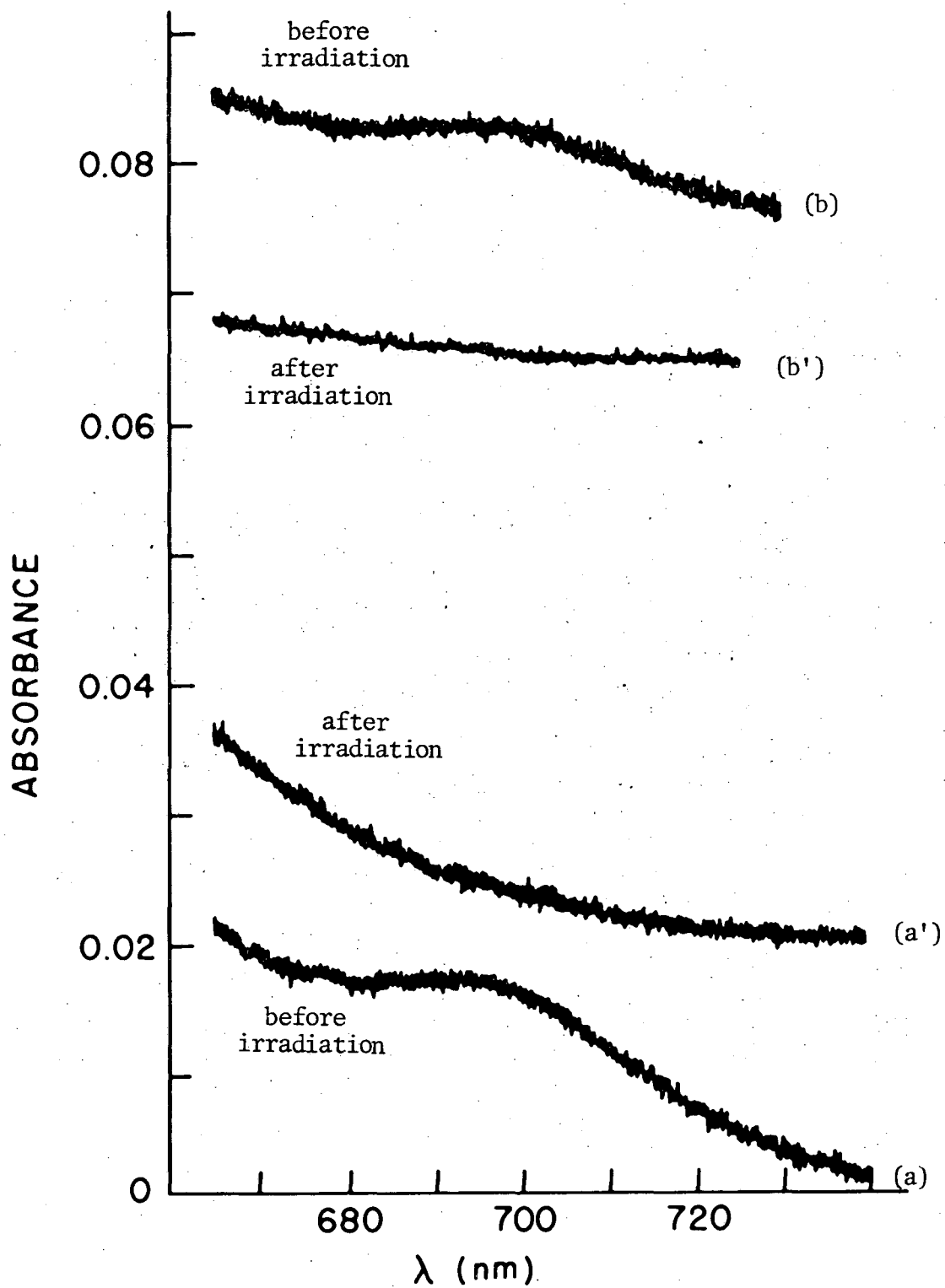
It is interesting to note that the solution spectrum of PCC also lost intensity upon addition of dithionite (see Fig. 4). Any comparison between the reducing effect of dithionite in solution and the reducing effect of electrons in solid film would, of course, be tentative in

the absence of supporting evidence. However, it may serve as a starting point in suggesting possible mechanisms for the loss of intensity in the solid film.

Figure 20 shows an absorption at 695 nm. In solution at neutral pH, this absorption is indicative of histidine-iron-sulfur bonding^{12, 16,17,18} as shown in Fig. 1. The existence of this absorption in the solid film shows that at least some of the iron-sulfur bonds have been preserved in the preparation of the film. The absorption was reproducible in at least two films, but its interpretation can only be qualitative. When the samples were prepared (see experimental section) the central portion dried into a smooth, thin film, but a thick, heavily cracked crust tended to form on the outer rim of the film. Fig. 19 was taken through the thin film in the center of the sample, but the weak 695 nm band could not be observed in these spectra because it was hidden within the noise level. The 695 nm band had to be taken through the thick, cracked crust. Scattering artifacts and absorption flattening were the main factors governing absorbance readings through the crust; absorbance ratios and literature extinction coefficients could not be used to determine the percentage of intact iron-sulfur bonds.

Various attempts to locate the 695 nm band after irradiation failed. This absorption is due to charge transfer^{12,16-18} from either ligand to iron or porphyrin to iron. If the transfer is from ligand to iron, the loss of the 695 nm band implies that the iron-sulfur bonds have been broken. If the transfer is porphyrin to iron, the loss at 695 nm

Figure 20. 695 nm region observed through the crust around two neutral films of horse heart cytochrome c. Spectrum (a) shows a crust dried from a solution of pH 7.2. The reference beam has been attenuated to maximize the quality of the signal; therefore, the absorbance is artificially low. Beam attenuation did not significantly improve the signal; the unattenuated absorbance at 695 nm is 0.085. Spectrum (a') shows the same crust after 20 hr exposure to the x-ray tube. The reference beam has also been attenuated in this spectrum. Spectrum (b) shows a crust dried onto quartz from a solution of pH 6.6. Spectrum (b') shows the same crust after 14 hr exposure to the x-ray tube. The reference beam has not been attenuated in spectra (b) and (b'). The overall level of absorption in (a') is greater than in (a); the reverse is true of (b) and (b'). These baseline differences between spectra recorded before and after irradiation may be due to: scattering induced by denaturation of the protein in the x-rays, inability to reproduce the position of the sample in the optical spectrometer, differences in reference beam attenuation.



XBL755-5261

Figure 20. See legend on previous page.

means the heme ring has been broken, but that the iron-sulfur bonds may still be intact. It is also possible that the 695 nm absorption is still present, but indistinguishable because of the increased scattering in the spectrum.

Figure 21 shows the visible spectra of a film of desalted MP dried onto a quartz plate from a solution of pH 5.9 both before and after irradiation. The spectrum before irradiation very closely resembles that of the cytochrome film. This similarity has already been discussed; it means that the MP film is a reasonable model of heme iron in the cytochrome. It must be emphasized that the MP contains no methionine. The MP iron is bound axially by histidine 18 and the α amino group on valine 11 from a neighboring MP molecule. Therefore, this MP film most closely resembles the proposed bonding arrangement for cytochrome at high pH (Fig. 1).

The spectrum after irradiation shows less damage than the corresponding cytochrome spectra. Increased scattering is not a problem. Presumably, the short peptide chain, the rigid heme, and intermolecular bonding minimize denaturation. There is, however, a general decrease in intensity across the entire spectral region which is consistent with the cytochrome spectra.

Sulfur 2p Results

One of the goals of this series of experiments was to observe the chemical shift of sulfur bound to iron in cytochrome c at neutral pH as shown in Fig. 1. Horse cytochrome c contains two

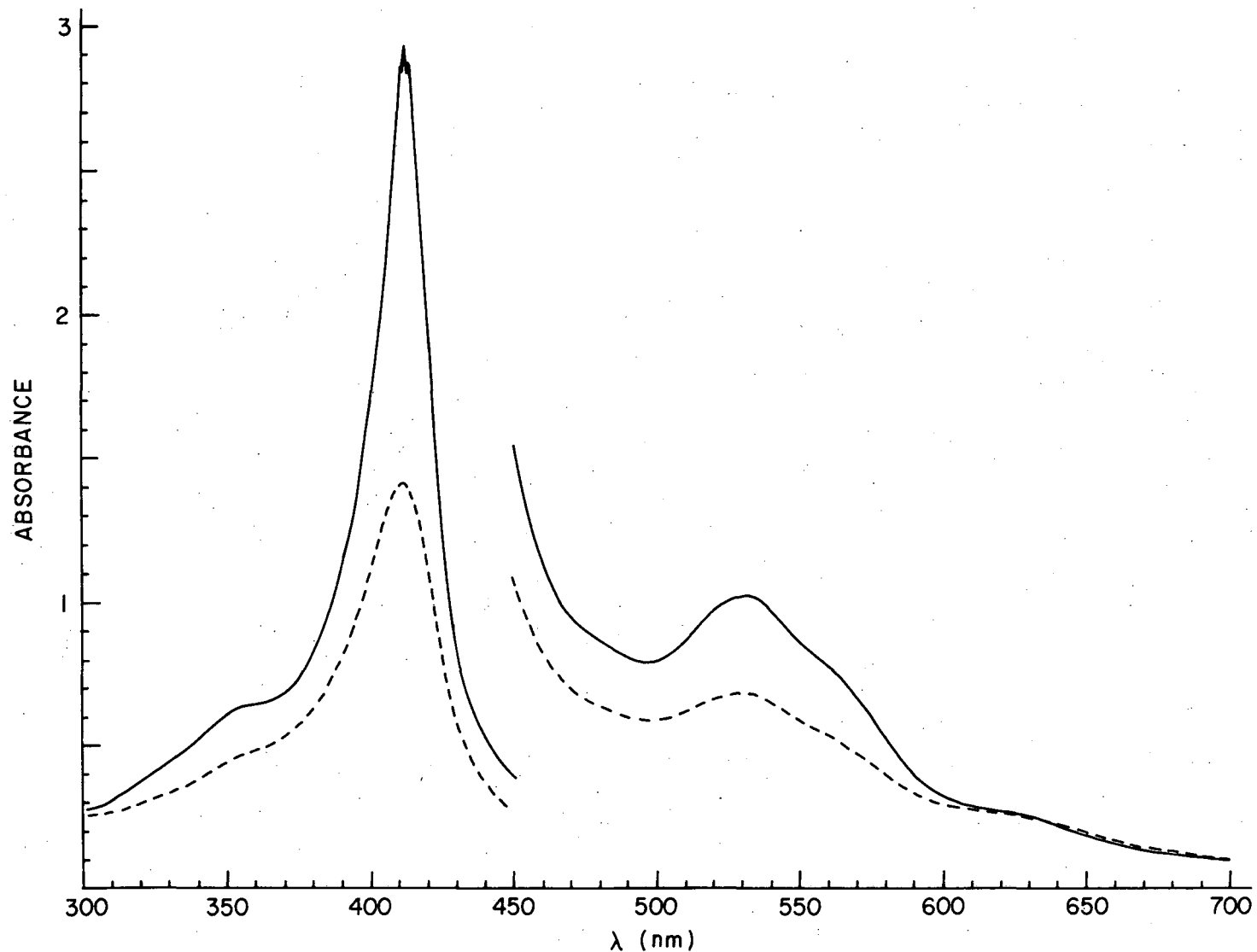


Figure 21. Optical absorption spectra (Cary 118) of a 0.3 micron film of desalted microperoxidase (MP) dried onto a quartz plate from a solution of pH 5.9. Solid line is the film spectrum before irradiation. Dashed line is the spectrum after 15 hr exposure to the x-ray tube.

XBL 755-5260

methionine residues and two cystine residues.² The heme ring is bound to the cystine sulfur in the form of thioether bridges;² so, the molecule contains four sulfur atoms all in the form of thioether. Referring to Fig. 1, a single S 2p peak corresponding to thioether sulfur is expected from samples of cytochrome c at acid and alkaline pH. At neutral pH, a second contribution is expected at higher binding energy (BE) that represents the sulfur bound to the iron. The ratio of shifted peak to the thioether peak is expected to be 1:3.

The sulfur spectra that were actually observed are shown in Figs. 22 - 33. Spectra of cytochrome c at pH 1.5, 3.0, 6.6, and 11.2 are shown in Figs. 26 - 31; they are more complicated than expected. Each spectrum shows at least three peaks at 153 eV, 163 eV, and 167 eV. The assignment of many of the observed peaks remains in doubt. The observed binding energies are summarized in Table IV.

A pure thioether sulfur 2p signal is given by the α -methionine spectrum in Fig. 22. Its BE is 163.3 eV. SUNDER was used to fit 1/2, 3/2 components to this peak; the calculated parameters are given in Fig. 22. Cysteine HCl, cystine, and reduced glutathione were found to have S 2p signals that were similar to methionine in BE and shape. The characteristics of a S 2p signal in a single chemical environment were determined from the average of these four signals. For the whole 2p doublet, BE = 163.6 ± 0.3 eV, FWHM = 2.2 ± 0.1 eV. For the individual 1/2, 3/2 components, BE(3/2) = 163.3 ± 0.2 eV, separation = 1.03 ± 0.03 eV, FWHM = 1.1 ± 0.1 eV. Thus, the sulfur amino acids in their native form had S 2p spectra that were essentially indistinguishable in the Berkeley spectrometer.

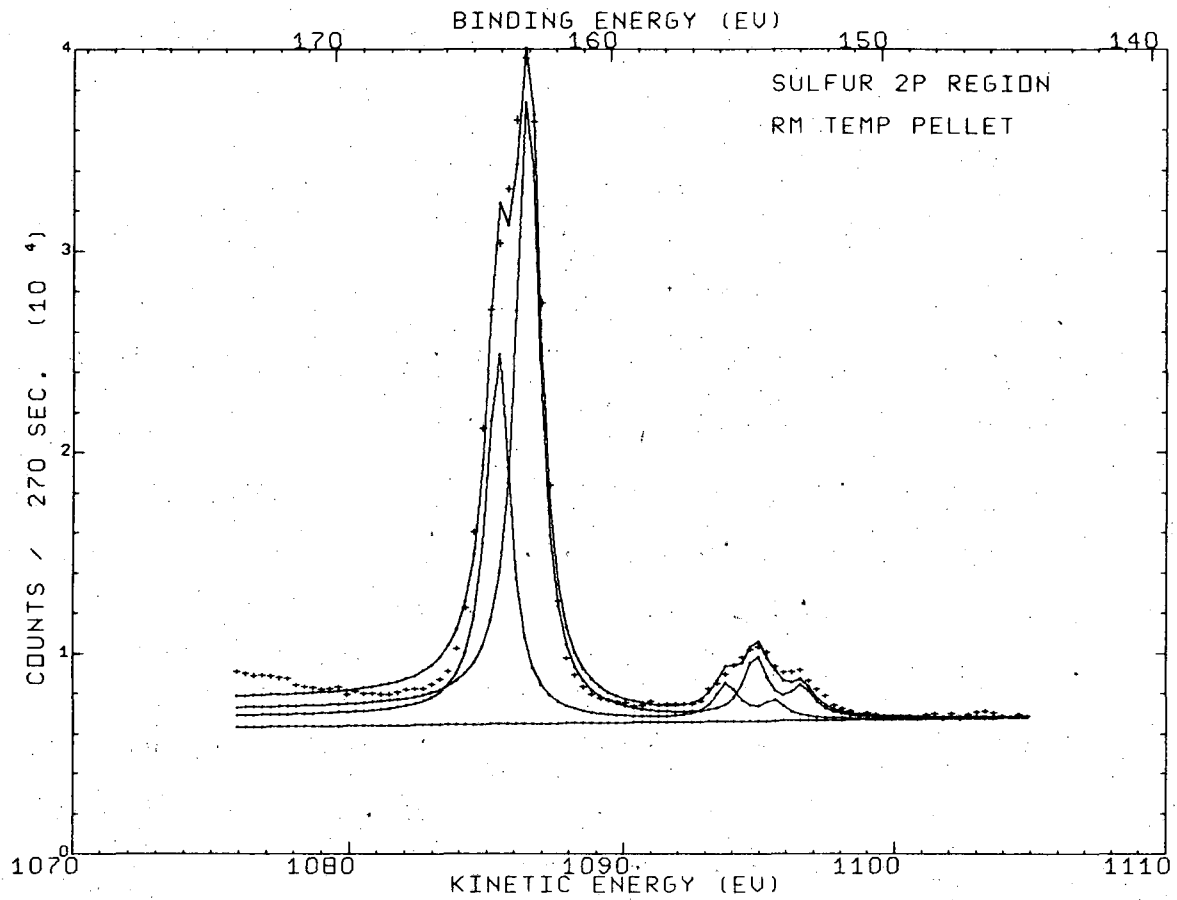


Figure 22. Sulfur 2p spectrum (MgK α) of methionine. Calculated parameters: FWHM = 1.06 ± 0.04 eV, separation = 1.06 eV, ratio = 1:1.7. Total signal has FWHM 2.1 eV and BE 163.3 eV. Spectra of cysteine HCl, cystine, and reduced glutathione are very similar to this one.

-217-

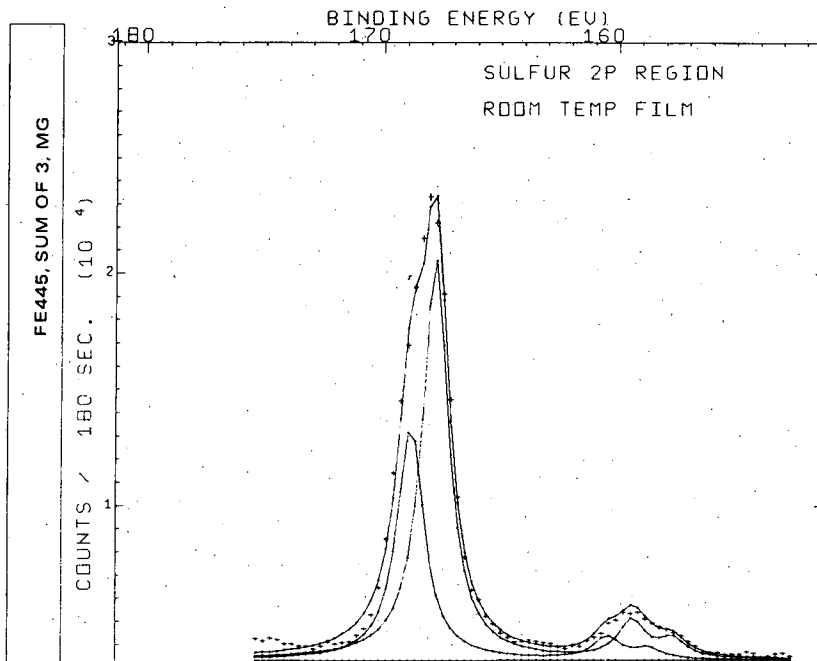


Figure 23. Sulfur 2p spectrum ($MgK\alpha$) of methionine sulfone. The two fitted lines (FWHM = 1.37 ± 0.05 eV, separation = 1.1 eV) represent 1/2, 3/2 components. Total signal FWHM 2.2 eV, BE 168.1 eV.

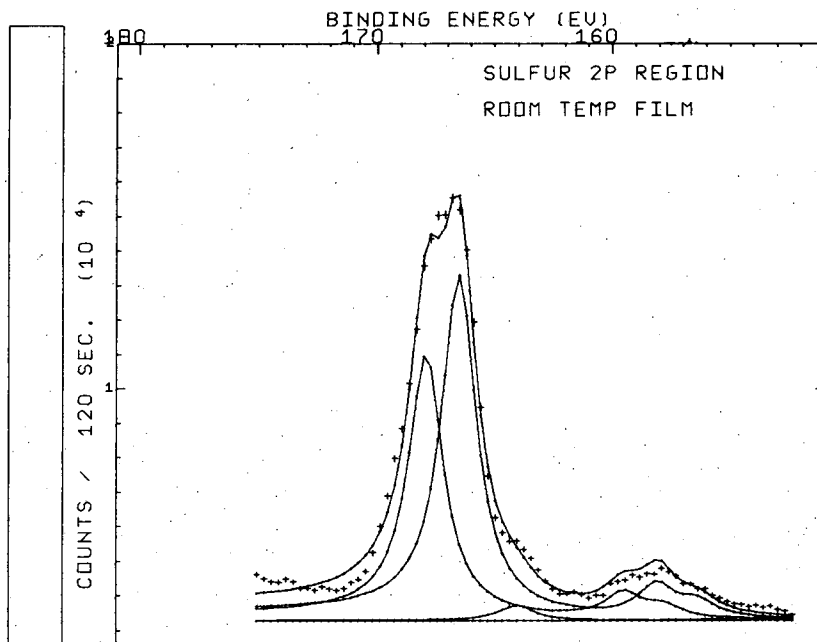


Figure 24. Sulfur 2p spectrum ($MgK\alpha$) of cysteine sulfinic acid. Fitted lines represent S 2p doublets in various oxidation states. There is a small signal near 164 eV that corresponds to native cysteine which was probably formed during the experiment.

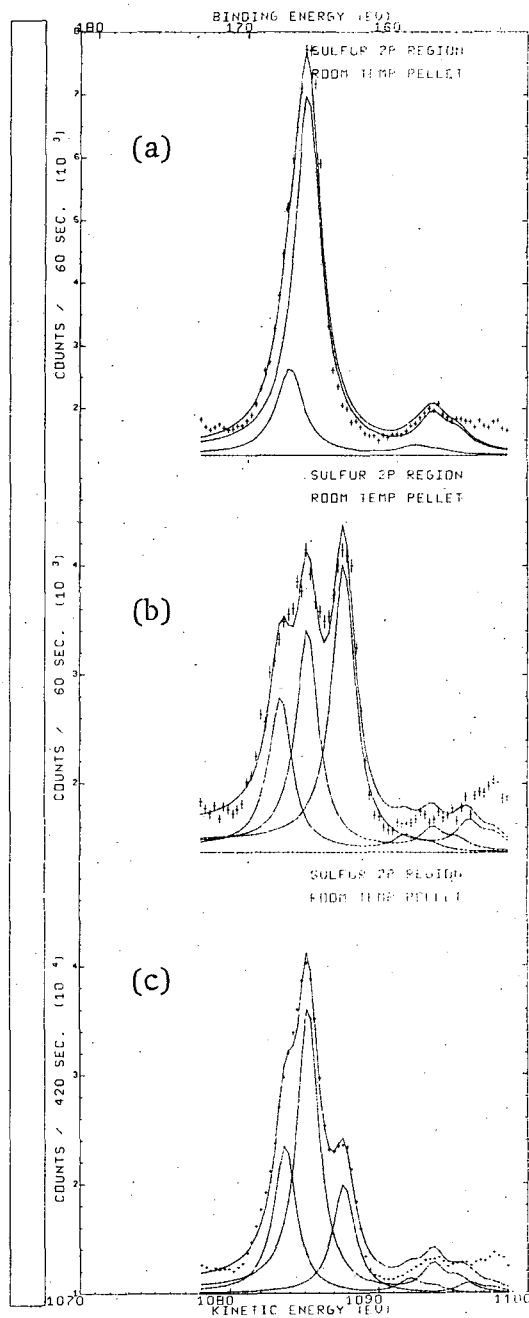


Figure 25. Sulfur 2p spectra ($MgK\alpha$) of methionine sulfoxide. Fitted lines represent S 2p doublets in various oxidation states. Figure (25a) shows the first scan, (25b) the seventh scan, and (25c) the sum of all seven scans. Reduction of the sulfoxide to a specie with the same BE as methionine is evident in this sequence.

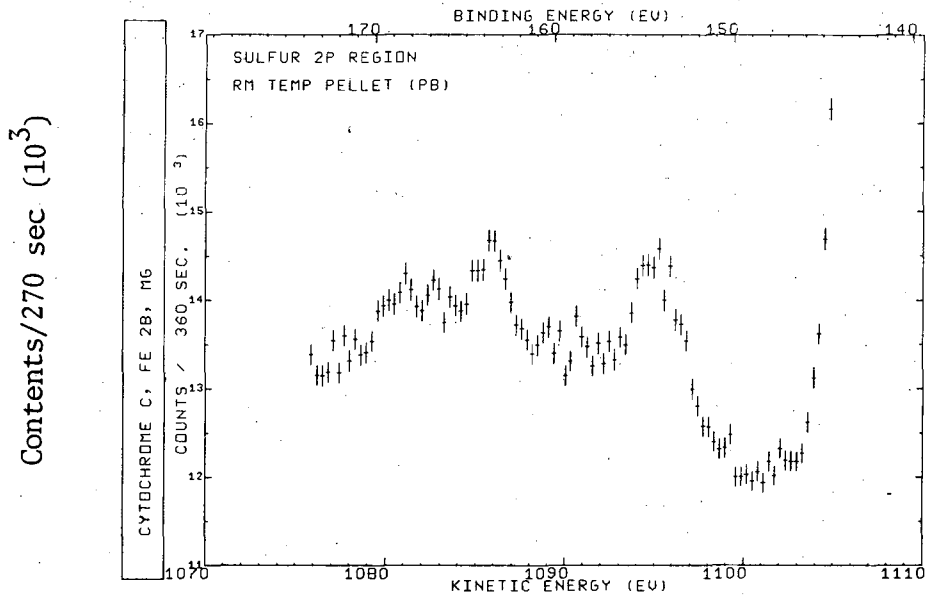


Figure 26. Sulfur 2p spectrum ($MgK\alpha$) of horse heart cytochrome c lyophilized from pH 1.8, pressed into a pellet, and run at room temperature on a Pb backing.

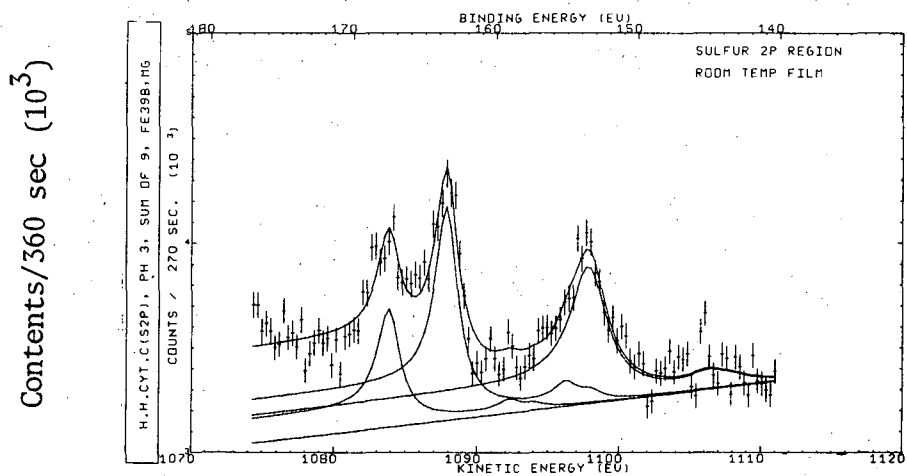


Figure 27. Sulfur 2p spectrum ($MgK\alpha$) of horse heart cytochrome c dried in a film on a quartz plate from a solution of pH 3.0.

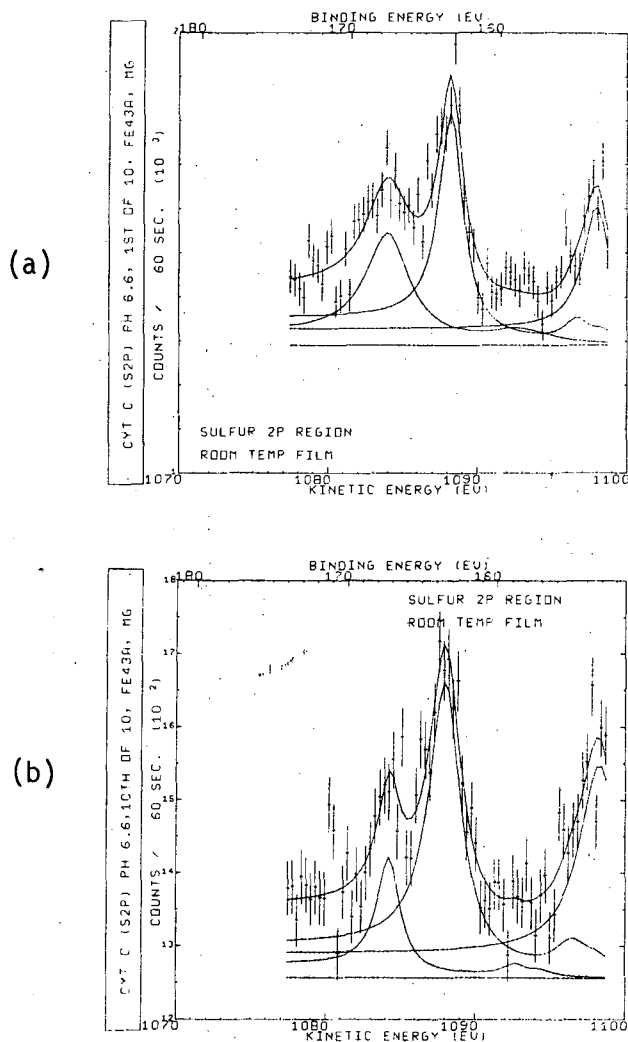
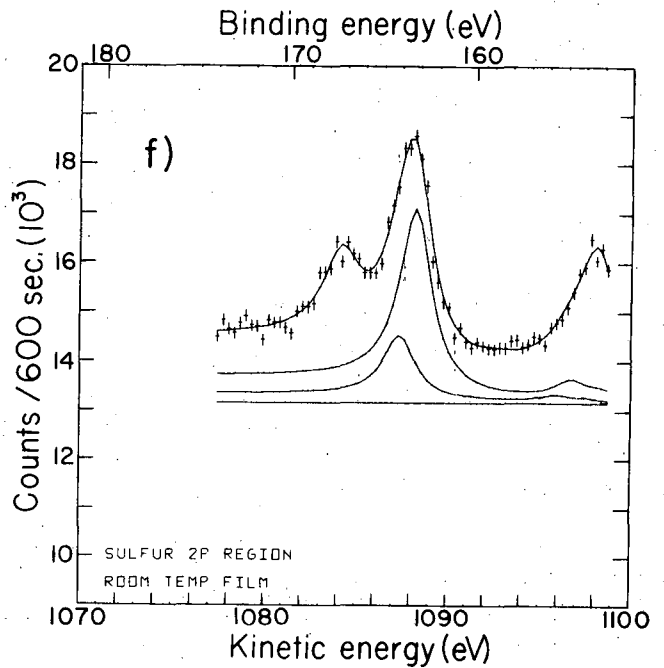
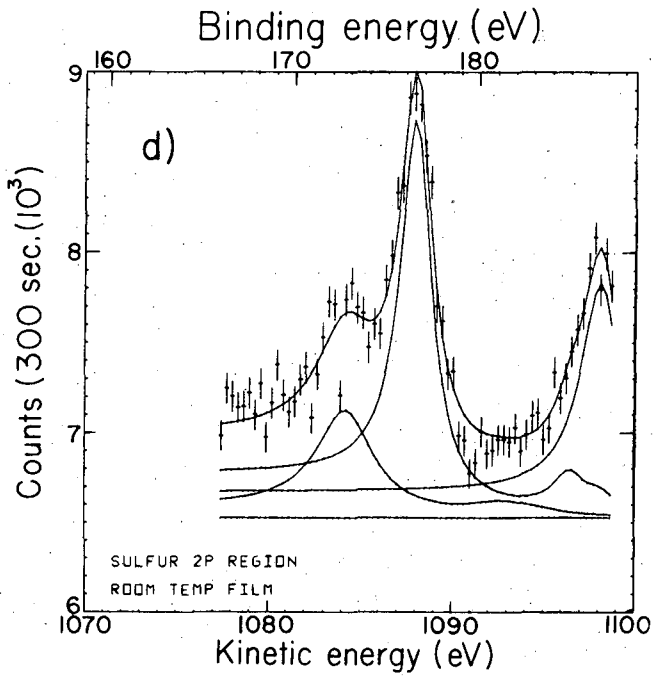
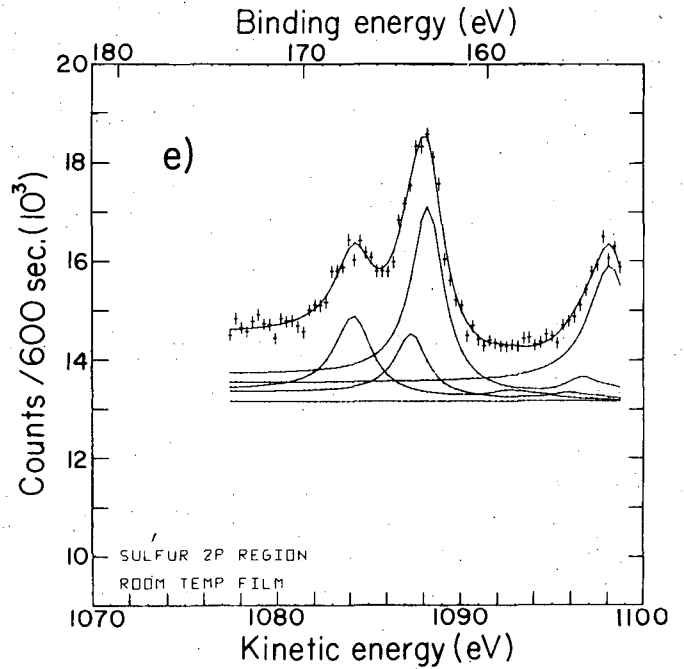
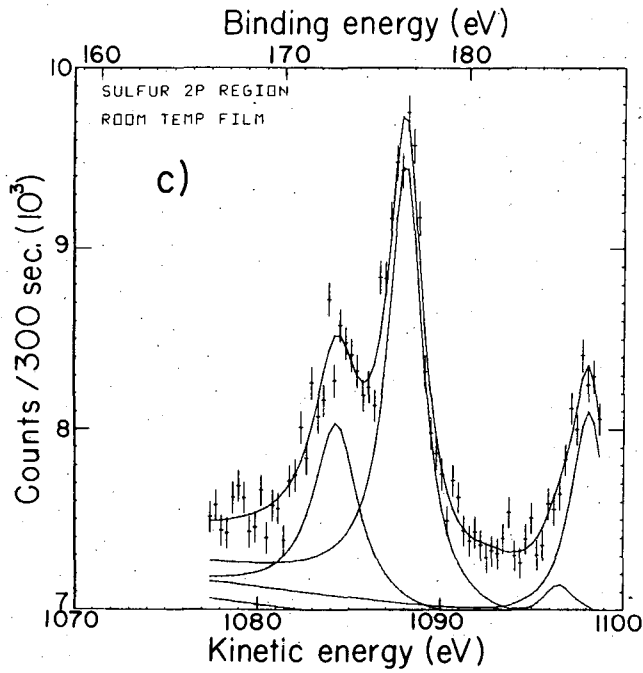


Figure 28. Sulfur 2p spectra (MgK α) of horse heart cytochrome c dried in a film onto a quartz plate from a solution of pH 6.6. Fig. 28a shows the first scan; 28b shows the tenth scan. SUNDER calculated (FWHM free for all three lines) an apparent decrease of the 167 eV line with respect to the thioether line between (a) [ratio = 1:1] and (b) [ratio = 1:4], but the noise is too high to calculate a reliable ratio. The signal is more clear in (c) [sum of scans 1 - 5, FWHM free for all three lines] and (d) [scans 6 - 10, FWHM free, tails fixed to be the same as (c)]. The ratio is constant at 1:2 in both spectra, but the 167 eV line in (d) can be made smaller by choosing the appropriate tail parameter.

Figure 28e shows the sum of all ten scans with two lines (FWHM fixed at 2.2 eV) under the thioether peak. Figure 28f is the same fit with extraneous lines deleted for clarity. The smaller line is shifted to 164.1 eV; the calculated ratio is 1:3.



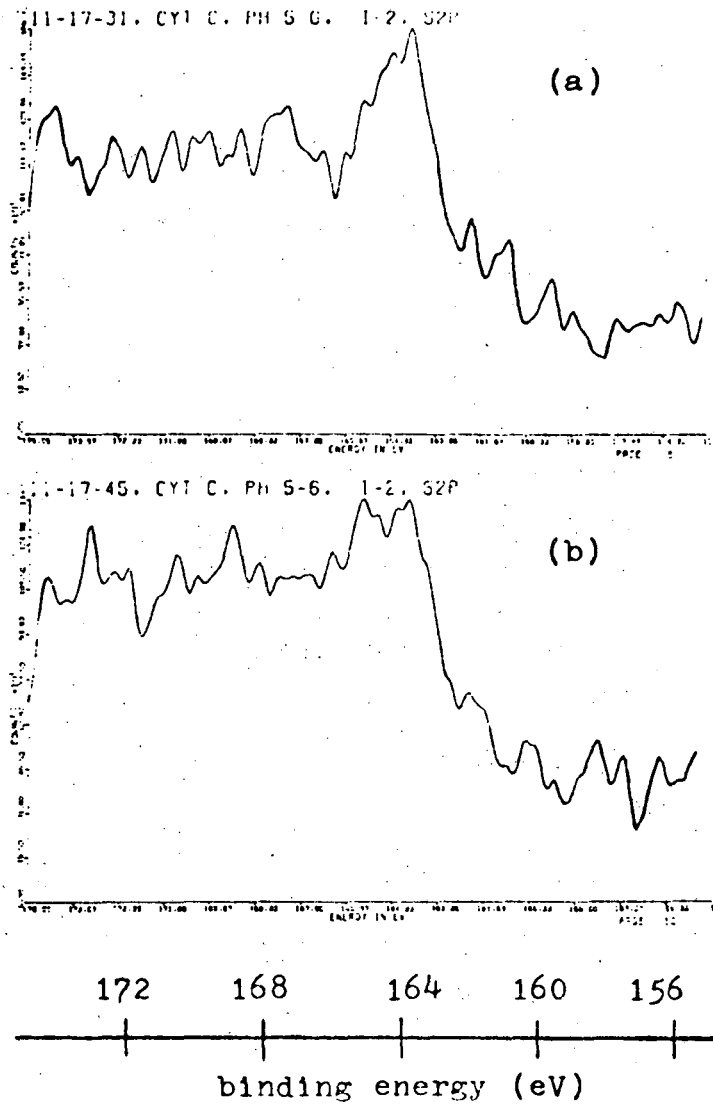


Figure 29. Sulfur 2p spectra of horse heart cytochrome c (HP5950A spectrometer) dried in a film onto a gold platen from a solution of pH 5-6. (a) 262 min. exposure to x-rays, (b) 661 min. exposure to x-rays.

-223-

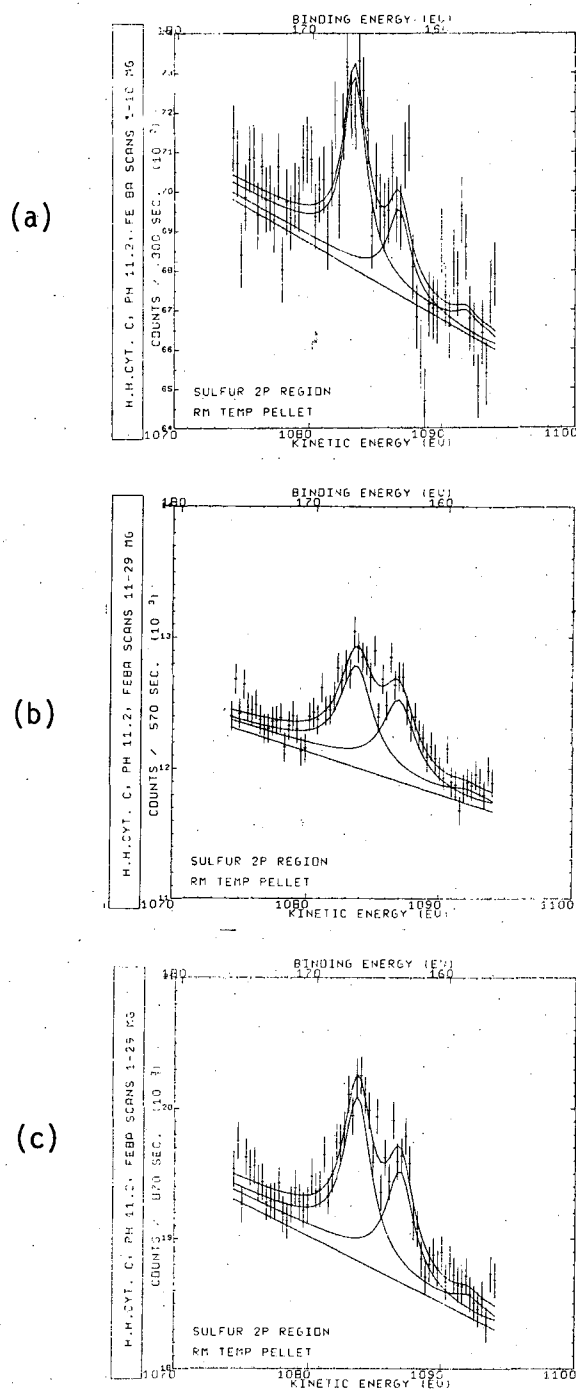


Figure 30. Sulfur 2p spectra ($MgK\alpha$) of horse heart cytochrome c lyophilized from pH 11.2, pressed into a pellet, and run at room temperature. Figure 30a shows the sum of scans 1 - 10; 30b shows the sum of scans 11 - 29; and 30c shows the sum of all 29 scans. There appears to be a decrease of the 167 eV line with respect to the thioether line. Statistics make this claim tentative; a ratio of 1.5:1 in both (a) and (b) would be within the computational error.

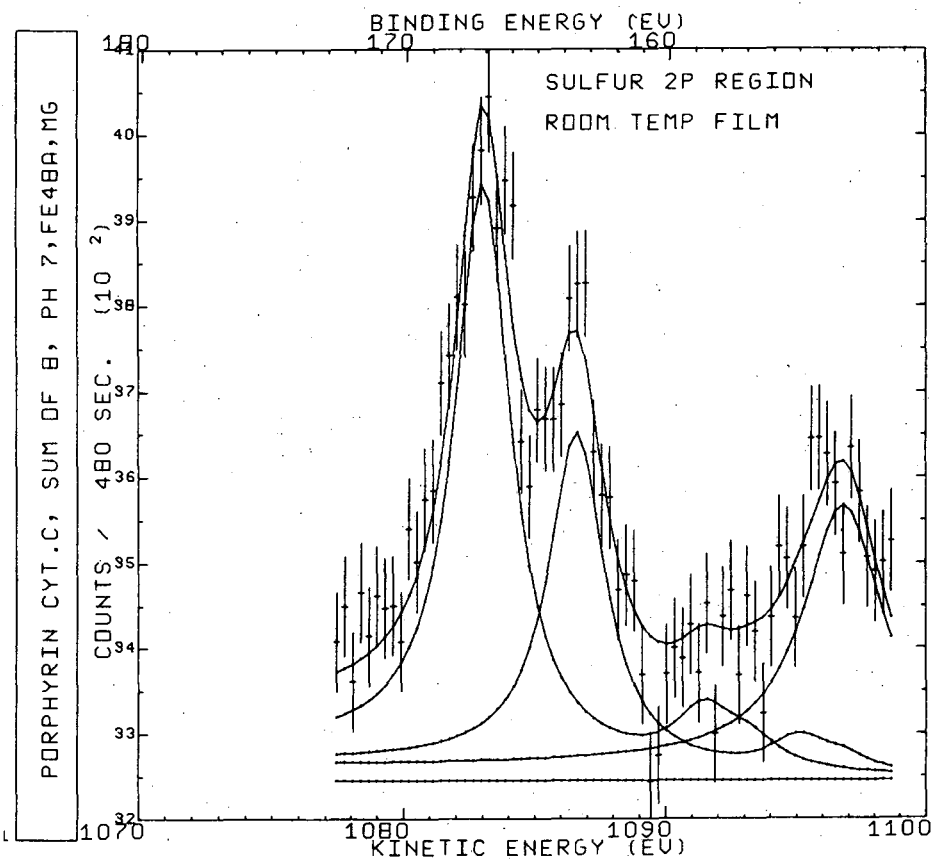


Figure 31. Sulfur 2p spectrum of porphyrin cytochrome c (PCC) dried in a film onto a quartz plate from a solution of pH 7.3.

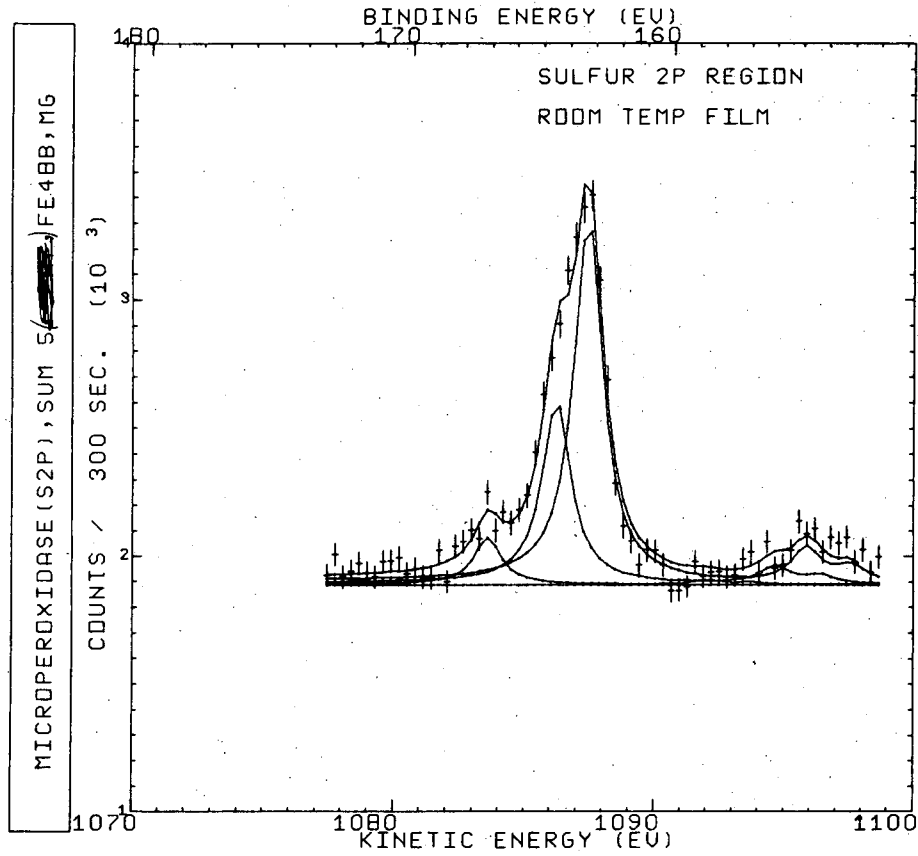


Figure 32. Sulfur 2p spectrum ($MgK\alpha$) of desalted microperoxidase (MP) dried in a film onto a quartz plate from a solution of pH 5.9.

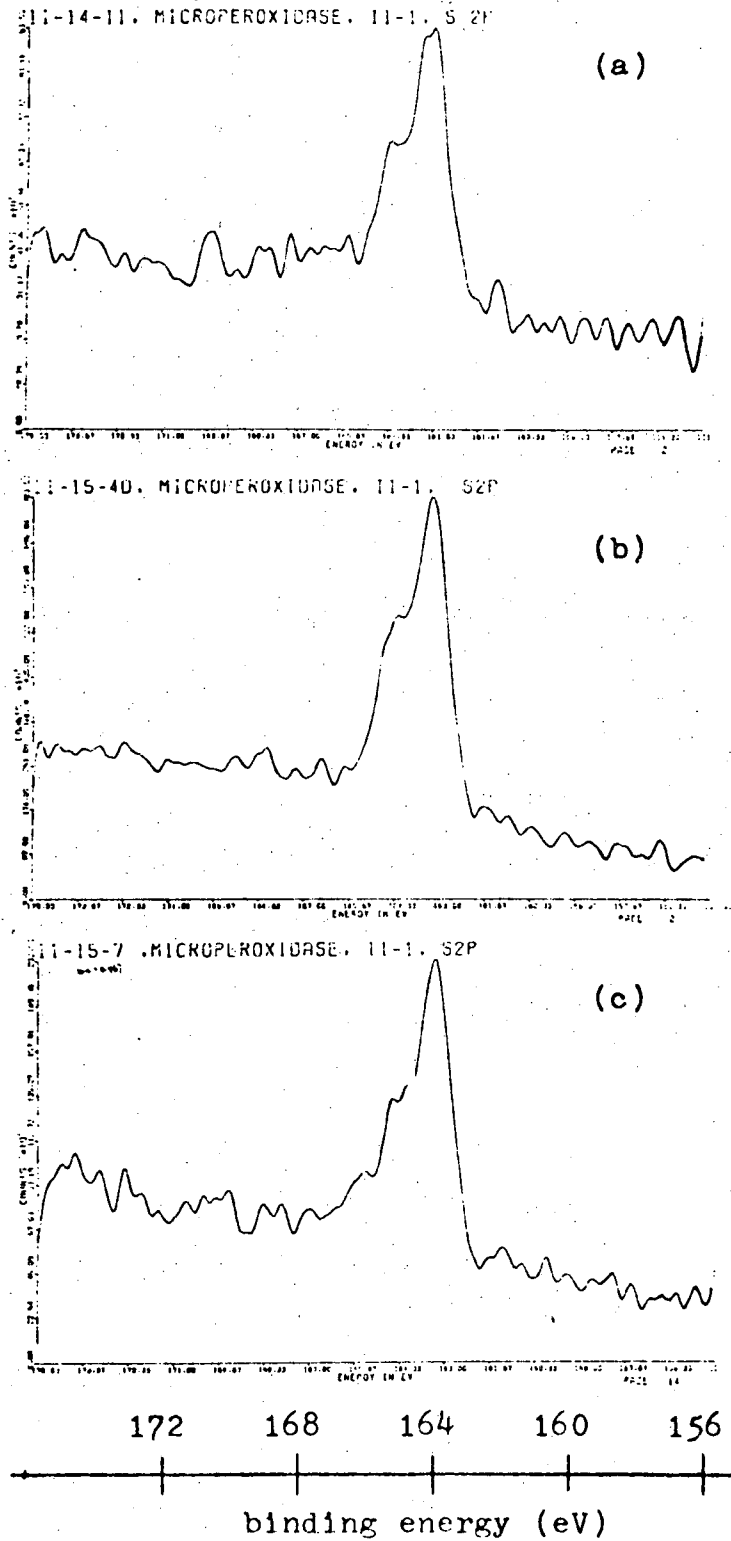


Figure 33. Sulfur 2p spectra (HP5950A spectrometer) of microperoxidase dried in a film on a gold platen from a solution of pH 7 containing buffer salts. (a) 20 min. in x-rays, (b) 370 min. in x-rays, (c) 474 min. in x-rays, 44 min. exposure to low energy electron flood gun (0.25 ma., 0 volts).

Table IV. Sulfur 2p BE's observed in the cytochrome experiments. BE referred to aliphatic C 1s at 285.0 eV as described previously. Sample forms are indicated as F for films and P for pellets. [Ratios are indicated in brackets.] (FMM are indicated in parentheses.) The four techniques used for the preparation of cytochrome samples were described in the experimental section. A signal was observed in the S 2p region which was due to the sample plate. Its position is given in the last column.

Horse Heart Cytochrome c Samples											
Expt. No.	Cyt. Prep. Tech. No.	pH/ Sample Form	Scans	Sulfur 2p BE (eV)						Ratio	Sample Plate Sulfur Line
				168.0	167.0	166.0	165.0	164.0	163.0		
2B	2	1.8/P	7	168.4	166.7				163.6 (2.3)	[1:1:2]	154
3D	2	1.5/P	9		167.5				163.2 (2.5)	[1:2]	152.3
41B	2	1.5/P	10	168.5		165.7			163.4 (2.5)	[1:1:2]	153.6
39B	3	3.0/F	9		167.5				163.5 (1.9)	[1:1.8]	153.5
1B	1	7/P	6		166.8				163.5 (2.5)	[1:2]	153.5
42B	3	7.2/F	10		166.9				163.4 (2.4)	[1:3.5]	153.9
43A	4	6.6/F	1st		167.5 (3.5)				163.3 (1.9)	[1:1.1]	153.6
"	"	"	1-5		167.2 (3.0)				163.5 (2.3)	[1:1.9]	153.4
"	"	"	6-10		167.2 (3.6)				163.4 (2.0)	[1:2.1]	153.3
"	"	"	10th		167.2 (1.9)				163.4 (2.5)	[1:4]	153.2
"	"	"	1-10		167.3 (2.4)				163.4 (2.3)	[1:3]	153.3
"	"	"	"		167.3			164.1	163.2		
8A	2	11.2/P	1-10		166.8 (2.0)				163.5 (2.0)	[1:0.44]	
"	"	"	11-29		166.9 (3.0)				163.7 (3.0)	[1:0.8]	
"	"	"	1-29		166.9 (2.5)				163.7 (2.5)	[1:0.68]	
40B	3	11.3/F	9		167.5				163.6 (2.5)	[1:2]	153.6
43B	4	11.0/F	10		167.1				163.5 (2.3)	[1:1.5]	153.3

(Continued)

Table IV. (Continued)

Control Samples									
Name, pH/Form	Scans	Sulfur 2p BE (eV)						Ratio	Sample Plate Sulfur Line
		168.0	167.0	166.0	165.0	164.0	163.0		
PCC, pH 7.3/F	8		167.1				163.6 (2.6)	[1:0.6]	153.4
Desalted MP, pH 6/F	5		167.2 (1.3)			164.5 (1.3)	163.3 (1.3)	[0.15:0.5:1]	
Cysteine HCl/P	2					164.3	163.3		
Cystine/P	3					164.3	163.3		
Methionine/P	9					164.1	163.0		
Reduced Gluthathione	15					164.4	163.4		
Cys. Sulfinic Acid	2		167.9 (1.8)	166.5 (1.8)		164.1		[0.77:1:0.04]	
Cysteic Acid/F	2	168.8	167.8 (1.3)					[0.6:1]	
Met. Sulfone/F	3	168.8	167.8 (1.4)					[0.6:1]	
Met Sulfoxide/P	1st		167.2	166.0 (2.2 fixed)				[0.25:1]	
"	7th		167.9	166.0 (1.9)			163.6	[0.7:1:1.3]	
"	1-7		167.6	166.0 (1.8)			163.6	[0.5:1:0.4]	

On the basis of these results, it is reasonable to assign the peak at 163.5 ± 0.3 eV in the cytochrome, PCC, and MP spectra to thioether sulfur in its native form.

A definite assignment of the peak at 153 eV has not been made. It has several characteristics:

- (1) it appears in the blank runs on both aluminum and quartz sample plates;
- (2) its position corresponds closely to the silicon 2s signal;
- (3) its position bears no relationship to any major photoelectron or Auger signals in aluminum;
- (4) it appears with both aluminum and magnesium x-ray anodes;
- (5) it appears in all the cytochrome (including PCC) spectra from both pellets on aluminum and on quartz plates;
- (6) its position does not correspond to any major photoelectron or Auger lines in the cytochrome c samples, including reagents used for pH adjustment;
- (7) it appears in the spectra of cysteic acid and methionine sulfoxides, which were the poorest quality films in the series of experiments.

(1), (2), and (7) indicate that when this signal appears, it originates from the sample plate or some other factor in the experimental geometry. (3), (5), and (6) suggest the possibility that it may be characteristic of the cytochrome; although, this possibility

seems unlikely in view of (7). This peak has, therefore, been assigned to the sample plate, but its origin is ambiguous.

There is also a peak at 167 eV which appears consistently in the cytochrome spectra with the following characteristics:

- (i) it has the same BE as SO_3^- (Ref. 1);
- (ii) it occurs among the BE's for the various forms of oxidized sulfur amino acids;
- (iii) it appears in all the cytochrome spectra;
- (iv) it is very intense in the spectrum of PCC;
- (v) it appears with additional peaks in the region of oxidized sulfur amino acids in the spectra of cytochrome prepared at pH 1.5;
- (vi) it appears with only minimal intensity in the spectrum of MP;
- (vii) it does not appear at all in the spectra of the sulfur amino acids in their native form.

Since sulfate salts are commonly used to precipitate proteins, observation (i) immediately raised the suspicion that tightly bound sulfate remained with the protein even after dialysis. This possibility could be eliminated on the basis of the total sulfur analysis given in Table II. It was found that the maximum sulfate impurity was one SO_4^- per three cytochrome molecules after dialysis. Therefore, sulfate impurities cannot possibly account for the size of the 167 eV peak.

There are several pieces of evidence that are consistent with assigning the 167 eV peak to partially oxidized sulfur amino acids, particularly methionine sulfoxide, of yet undetermined origin. Foremost is the fact that the second largest 167 eV peak is observed in the spectrum of PCC (Fig. 31) which is at least 99% iron free. The immediate conclusion is that iron-sulfur binding cannot be the only possible source of this 167 eV peak; there must be at least one more. It is essential to note that the amino acid analysis of PCC (Table I) showed only traces of methionine, but correspondingly large amounts of methionine sulfoxide, even in the deoxygenated sample.

The oxidized sulfur amino acids have S 2p BE's above and below 167.2 eV (observation ii). The only form with a peak right at 167.2 is methionine sulfoxide (Fig. 25a).

Finally, there are some cytochrome samples that show additional structure beyond 167 eV (observation v, Fig. 26). This structure was evident in two of the three pH 1 - 2 samples; it was not observed in samples from pH 3 or higher. The additional structure appears to coincide with the BE's observed for the higher oxidation states of the sulfur amino acids, but the noise level prevents a specific identification. The heme iron oxidizes spontaneously to Fe(III) under aerobic conditions at this extreme pH (see cytochrome preparation #2 in the experimental section); the implication here is that the sulfur amino acids are oxidized also.

Therefore, the existence of an intense 167 eV peak in the iron-free PCC and the correspondence of the 167 eV peak plus additional

structure to the BE's of oxidized sulfur amino acids suggest that this signal is due to oxidized sulfur. In particular, sulfoxides are suspected.

If, in fact, sulfoxides are responsible for the 167 eV peak, then the 167 eV signal should behave like the methionine sulfoxide signal. It can be seen from Fig. 25 that the methionine sulfoxide signal shows evidence of chemical reduction during an experiment. The first scan, Fig. 25a shows only two lines at 166.0 and 167.2 eV (FWHM's fixed at 2.2 eV). In the seventh scan, Fig. 25b, another peak has evolved at 163.6 eV which corresponds to the area lost by the 166.0 eV line. The methionine sulfoxide was evidently reduced to a specie resembling methionine, probably because of the electron flux impinging on the sample from the x-ray tube window.

It is not clear whether or not the cytochrome c spectra show the same reduction that was observed in Fig. 25. Fig. 30 shows the S 2p spectrum of a pellet of cytochrome c lyophilized from pH 11.2. Fig. 30a shows the sum of scans 1 - 10; 30b shows scans 11 - 29. SUNDER was used to fit two lines to both sets of data. The calculated ratio of the 167 eV line to the thioether line was found to be $(2.2 \pm 0.8):1$ in the first two scans, but in scans 11 - 29 the ratio dropped to $(1.3 \pm 0.2):1$. The 167 eV line diminished with respect to the thioether line over the course of the experiment. However, the spectral noise and resulting computational errors are so large that the ratio may be constant within experimental error at about 1.5:1.

A similar situation was observed with the film of pH 6.6 cytochrome c. The 167 eV line seems to decrease with respect to the thioether line between the first and tenth scans (Fig. 28a,b), but the noise prevents a quantitative determination. In fact, the ratio of the 167 eV line to the thioether line is constant at $(0.50 \pm 0.03):1$ in Fig. 28c,d where scans 1 - 5 and 6 - 10 of the same pH 6.6 film are shown. (The comparison of these area ratios is actually somewhat artificial. These ratios can be adjusted up or down by an appropriate choice of the tail parameters in SUNDER. For consistency, the tail parameters in Fig. 28d were fixed to be the same as in 28c.)

Fig. 29a,b show the first and eighth scans from the HP 5950A spectrometer of a pH 5 - 6 film of cytochrome c. There is some structure in the first scan (29a) between 167 - 168 eV which appears flattened in the eighth scan (29b), but the structure is essentially indistinguishable from the noise.

If it is to be claimed that methionine sulfoxide contributes to the peak at 167 eV, then this peak should behave like methionine sulfoxide during an experiment. In fact, there is no cytochrome spectrum with a 167 eV peak that clearly shows reduction like Fig. 25. Therefore, the assignment of methionine sulfoxide to the 167 eV peak must remain tentative.

There are two minor points regarding Fig. 25. First, the two lines in 25a have not been assigned. The larger line at 166.0 eV presumably represents sulfoxide. Therefore, the 167 eV line must

represent some higher oxidation state which is present as an impurity. When the term "sulfoxide" is applied to the 167 eV signal in cytochrome c, it must be understood to include all the intermediate sulfur oxidation states between sulfide and sulfone. Second, the 166 eV line position is stable, but the 167.2 eV line shifts to 167.9 eV in the seventh scan, this shift may be a spurious result of a SUNDER fit, or it may indicate that disproportionation is taking place instead of simple reduction.

There are also reasons to believe that iron-sulfur bonding contributes to the 167 eV peak. At neutral pH, the sulfur of methionine 80 is supposed to be bound to the iron (Fig. 1). Films of pH 6.6 cytochrome c showed an optical absorption at 695 nm; therefore, it is known that at least some of the iron-sulfur bonds in the film are intact, and an appropriate chemical shift is expected. If the sulfur bound to the iron is assigned to the 167 eV peak, a 4 eV shift from the thioether peak is implied. However, 4 - 5 eV shifts have already been observed in the binding of sulfur to copper in plastocyanine;⁵⁴ so a 4 eV shift for sulfur bound to iron is not unreasonable. Finally, a peak ratio of 1:3 is expected if one methionine out of four sulfur amino acids binds to the iron. A ratio of 1:2 was observed in the spectra of pH 6.6 cytochrome c in Fig. 28c,d. This ratio is reasonably close to the expected ratio, and unlike methionine sulfoxide, the ratio is apparently stable. So, some sulfur is known to be bound to iron (Fig. 20), and the 167 eV peak has a ratio and separation

with respect to the thioether peak that can be rationalized in terms of iron-sulfur bonding.

There are, however, some arguments against the assignment of the 167 eV peak to the iron-methionine binding. The first, of course, is that the 167 eV peak is large in the PCC sample which is 99% iron-free. Second, the 167 eV peak, also appears in acid and alkaline pH samples where, according to Fig. 1, the methionine is not bound to the iron. Fig. 1 is based on work in solution, while the XPS is done on films or lyophilized pellets. To rationalize the XPS results with the solution work, it is necessary to postulate that the protein denatures in condensed phases such that the methionine is always bound to the iron regardless of pH. Finally, with isolated exceptions, iron-sulfur model compounds have S 2p BE's in the range of 162 - 165 eV (see Ref. 47, p. 179 ff); therefore, a BE of 167 eV seems somewhat large.

Still, the 695 nm optical absorption in the pH 6.6 cytochrome films shows that some sulfur is definitely bound to the iron, and a measurable shift is expected. An alternative to the 167 eV peak can be found in the HP 5950A spectra of pH 5 - 6 cytochrome c. Eight scans were taken in the S 2p region, the first and eighth scans are shown in Fig. 29. There are numerous peaks throughout the spectra, but all eight scans had a feature at $BE = 165.2 \pm 0.2$ eV. That the signal is observed in all eight scans strongly suggests that it is real in spite of the high noise level. It would obviously be premature

to assign this signal to the sulfur bound to heme iron, but it is consistent with the S 2p BE's of iron-sulfur model compounds. Therefore, this signal can be rationalized about as well as the 167 eV peak in terms of iron-sulfur bonding.

SUNDER made a similar fit to the S 2p spectrum of pH 6.6 cytochrome c in the Berkeley spectrometer (Fig. 28e,f). Fig. 28e shows the sum of ten scans with two lines fitted under the thioether peak. (The FWHM's were fixed at 2.1 eV, the width of a standard S 2p doublet.) Fig. 28f is the same fit as 28e with extraneous lines deleted for clarity. The larger line stands at 163.2 eV, in agreement with the thioether peak position the smaller line was shifted to 164.1 eV. The calculated ratio was 1:3 in agreement with the model of binding one sulfur out of four to heme iron. Again, it would be premature to assign the 164.1 eV line to sulfur bound to iron because this fit is not reliable. This result is to be regarded only as an indicator of another possible alternative to the 167 eV peak as the S 2p signal shifted by iron binding.

Lastly, the 167 eV peak could be a product of radiation damage. This has been considered, and a mechanism was proposed in which the cystine thioether bridges to the heme could be oxidized as an indirect result of photon absorption by the heme iron. There are four steps.

- (1) Iron absorbs a photon which creates a 2p photohole.
- (2) The iron relaxes by an Auger cascade, which leaves the iron multiply ionized. Theoretically, the iron 2p hole state could

acquire a charge of up to +8;⁵¹ the available Auger spectra of iron⁵³ suggest that a charge of +2 or +3 over the initial atomic charge is more reasonable.

- (3) The multiply ionized iron fills its Auger holes by drawing electrons from the porphyrin ring. This process has already been suggested;⁵² there is some experimental support for it.⁵²
- (4) The positive holes in the porphyrin migrate by mutual repulsion to the periphery of the ring where they find a thioether bridge and oxidize it.

PCC was prepared to test this mechanism. Without heme iron, the process could not be initiated, and the 167 eV peak should be absent. Instead, PCC shows a large 167 eV peak. According to this mechanism, MP should have a large 167 eV peak; it does not. Furthermore, only 1% of the atoms in the measured layer of an organic sample absorb a photon during a 10 hour experiment. The mechanism may be realistic, but the results would be unobservably small.

Although the mechanism fails to account for the 167 eV peak, each step has experimental justification. It is probably one of several mechanisms by which proteins may degrade upon high energy photon absorption.

In conclusion, from the data presented here, it is possible to interpret the 167 eV peak as: (1) the sum of contributions from

oxidized sulfur amino acids and sulfur bound to iron; or (2) as oxidized sulfur amino acids with sulfur bound to iron appearing at a lower BE, perhaps between 164 - 165 eV. It is not possible to assign the 167 eV peak exclusively to sulfur bound to iron because the second largest 167 eV peak was observed in the 99% iron-free PCC sample, and the PCC amino acid analysis showed nearly complete conversion of methionine to its sulfoxide.

The question of the BE of sulfur bound to heme iron in cytochrome c might be resolved by the use of appropriate models. A film of specially modified heme undecapeptide and methionine has already been suggested. Another interesting possibility involves attaching methionine and histidine to the propionic acid side chains of mesoporphyrin according to Warne and Hagar.⁵⁵ Sulfur and imidazole ligands would then be available to bind the axial positions of the iron.

The final question involves the origin of the proposed oxidized sulfur amino acids. The amino acid analysis of dialyzed cytochrome c (Table I) showed about 20% conversion of methionine to its sulfoxide. It is, therefore, unlikely that the oxidized sulfur was in the protein from the manufacturer. (This conclusion is tentative. Recall that amino acid analysis can oxidize or reduce methionine depending on specific conditions. See experimental section.)

The oxidized sulfur is probably produced at acid pH during the preparation of the samples. All of the samples showing large 167 eV peaks were exposed to low pH. PCC (Fig. 31) was exposed to acid during

the HF iron removal process; a pH 11 cytochrome pellet (Fig. 30) was brought to pH 1.8 with HCl and then to pH 11 with KOH. The samples with extended structure beyond 167 eV (Fig. 26) were pellets lyophilized from pH 1 - 2. Cytochrome c that was extensively dialyzed, but never exposed to strong acid, showed only a medium size 167 eV peak (Fig. 28). MP was in a neutral solution only long enough to pass through Sephadex G-10 for desalting; it showed a small 167 eV signal (Fig. 32). No oxidized sulfur was observed in the spectra of the native amino acids (Fig. 22), which were pressed into pellets directly from the bottle without any exposure to water. The collected results suggest that the sulfur oxidizes in minutes at pH 1 and over hours or days at neutral pH.

Iron 3p Results

It was hoped that the heme iron core orbitals would show a chemical shift reflecting the different ligands shown in Fig. 1. The Fe 3p level of cytochrome c at various pH values and of desalted microperoxidase (MP) were measured on the Berkeley spectrometer. The Fe 3p and Fe 2p levels of MP (containing buffer salts) were measured on a HP 5950A spectrometer.⁶ Fe 3p and Fe 2p BE's have already been measured in non-heme iron proteins,^{1,47,57} iron-sulfur model compounds,^{1,47,57} and porphyrin complexes.^{1,48,57} Metal BE's for complexes of porphyrin with several other metals have also been reported.^{48,49}

Iron BE's measured in this series of experiments are shown in Table Va,b along with BE's reported by other workers. A typical Fe 3p signal was found to have a FWHM of 2.8 ± 0.3 eV in the Berkeley spectrometer. A typical Fe 2p signal was found to have a FWHM of about 0.8 eV on the HP 5950A spectrometer. The spectra are shown in Figs. 34 - 39.

The iron spectra have several characteristics:

- (1) The spectra from both the Berkeley and HP 5950A spectrometers show evidence of reduction during the course of an experiment.
- (2) The oxidized Fe 3p BE's in cytochrome c and MP, measured on the Berkeley spectrometer, fall within the range of 52.0 ± 0.2 eV, which is remarkably low.
- (3) The oxidized Fe 3p and Fe 2p BE's in MP, measured on the HP 5950A spectrometer are normal; they agree with corresponding BE's for non-heme iron proteins, iron-sulfur models, and porphyrin complexes.
- (4) The Fe 3p signals in cytochrome c and MP, measured on the Berkeley spectrometer, show evidence of a contribution at 54 - 55 eV. Whenever SUNDER could fit a lineshape to this contribution, the ratio in all cases was within (0.2 - 0.3):1.
- (5) The Fe 3p BE of cytochrome c samples prepared at various pH values showed no measurable shift. XPS failed to distinguish the different ligand arrangements in Fig. 1.

Table Va. Fe 3p BE's observed in this work and the work of others. (Where possible, BE's have been adjusted from the original work to be consistent with the C 1s reference system used in this work.) Sample forms are indicated as F for films and P for pellets. [Ratios are indicated in brackets.] (FWHM are indicated in parentheses.) The four techniques used for the preparation of cytochrome samples were described in the experimental section.

Horse Heart Cytochrome c Samples (This Work)										
Expt. No.	Cyt. Prep. Tech. No.	pH/ Sample Form	Scans or X-Ray Exposure Time	Iron 3p Be (eV)						Ratio
				55.0	54.0	53.0	52.0	51.0	50.0	
3E	2	1.5/P	12		54.3 (2-1/2 - 3)		51.8			[1:3]
39B	3	3.0/F	7	68.2	54.8		52.0 (2.8 ± 0.4)			[1:5]
1A	1	7/P	6-13	56.5?			51.1 (3.2)			
"	"	"	13	56.5?			51.3 (2.7)			
6A	2	6.7/P	15		54.8?		52.1 (2.2)			
42C	3	7.2/F	10				51.8 (3.2 ± 1.1)			
43A	4	6.6/F	8		54.8		52.0 (3.0)			[1:5]
43B	4	11.0/F	8		54.6		51.8 (3.0 fixed)			[1:4]
Desalted Microperoxidase (This Work)										
48B	-	5.9/F	12 1/2 hr.		55.5			50.8 (1.9 ± 0.1)	49.0	[0.18:0.7:1]
48B	-	5.9/F	7		55.4 (2.2)		51.5 (2.8)		49.2	[0.25:0.96:1]
Microperoxidase (This Work, Buffer Salts, HP 5950A)										
45B	-	7/F	14 hr.	56.2	55.4	54.9	54.0	52.9	51.5	49.3

(Continued)

Table Va. (Continued)

Compound	Ref.	55.0	54.0	53.0	52.0	51.0	50.0	49.0
Hemin Cl	1,57	55.2						
Fe(III)Cl phthalocyanin	"	55.4						
Ferrichrome A	"	55.9						
Oxidized rubredoxin	"	55.6						
Reduced HIPIP	"		54.0					
Oxidized clostridial ferredoxin	"		54.4					
Oxidized spinach ferredoxin	"		54.6					
K_3FeF_6	"	58.7						
$Fe(CO)_5$	"	55.0						
$Fe(C_5H_5)_2$	"		54.7					
FeS_2	"		54.0					
Fe (metal)	"			53.4				

Table Vb.

Compound	Ref.	Iron 2p BE's (*marks main peak)													
		716	715	714	713	712	711	710	709	708	707	706	705	704	703
Microperoxidase (buffer salts, HP 5950A)															
33 min exposure to x-rays	(This Work)	716.7	715.3			712.9	711.3	710.4*	709.0		707.4		705.6	704.4	
324 min exposure	"	716.3	715.4		713.5			710.9*	709.2	708.2*			705.7		
640 min exposure (300 min flood gun)	"	716.3	715.7				711.9	710.5*	709.1*		707.0				703.6
Holm's compound	47						711.9	710.6*							
(n-Bu ₄ N) ₂ (Fe ₂ (SCH ₂ CH ₂ S) ₄)	47						711.3			708.6*					
Fe(SP ₂ NP ₂ S) ₂	47					712.7			709.4*						
Fe(SP ₂ NP ₂ O) ₃	47	716.7						711.8*							
Fe(SP ₂ NC(C ₄ H ₈)S) ₃	47					712.9	711.2*								
Spinach ferredoxin	47			714.2					710.7*						
HIPIP	47			714.3				711.8*	709.7						
K ₃ Fe(CN) ₆	48									708.5					
K ₄ Fe(CN) ₆ ·3H ₂ O	48										707.2				
Fe(III)Cltetra phenylporphin	48							711.9							
Fe(II)(pip) ₂ tetra phenylporphin	48										707.5				
Fe(II)Cl protoporphyrin	48								710.5						
Fe(II)(pip) ₂ protoporphyrin	48											706.1 ?			

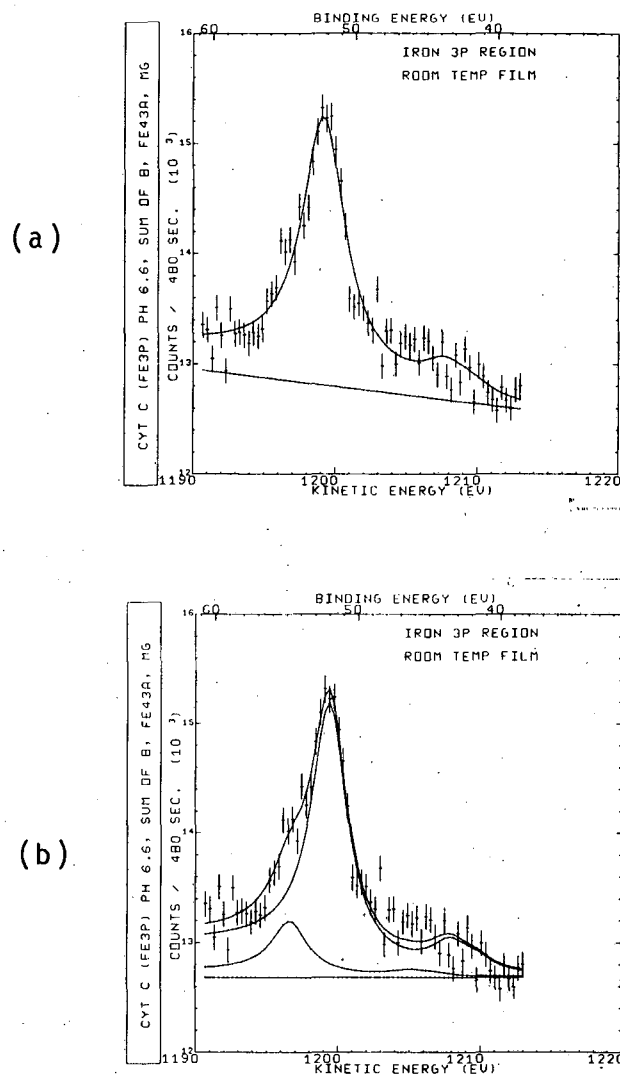


Figure 34. Two fits of the same data. Iron 3p spectrum of horse heart cytochrome c dried in a film onto a quartz plate from a solution of pH 6.6. Sum of 8 scans accumulated over 13 hr.

- (a) Single line, BE = 53.2 eV, FWHM = 3.7 ± 0.3 eV.
- (b) Two lines, BE = 54.8 and 52.0 eV, FWHM constrained to be same for both lines = 3.0 ± 0.3 eV, ratio free to vary = 1:5.

-245-

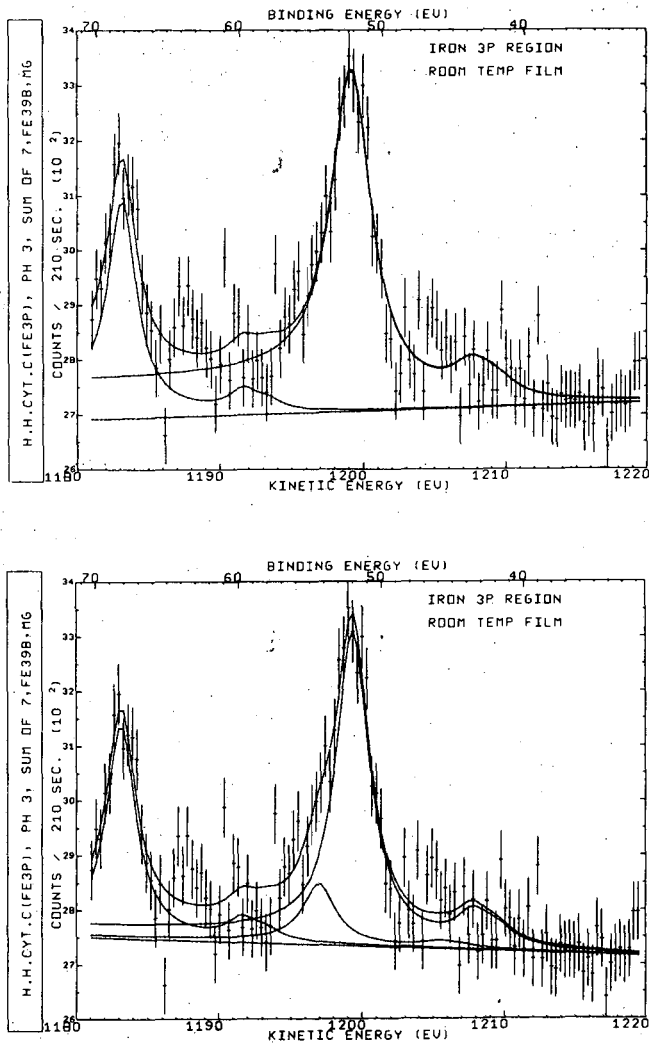


Figure 35. Two fits of the same data. Iron 3p spectrum of horse heart cytochrome c dried in a film onto a quartz plate from a solution of pH 3.0. Sum of seven scans accumulated over 3 hours.

- (a) Main peak fitted with a single line, BE = 52.2 eV, FWHM = 3.4 ± 0.3 eV.
- (b) Main peak fitted with two lines, BE = 54.4 eV and 52.0 eV, FWHM constrained to be the same for both lines = 2.8 ± 0.4 eV, ratio free to vary = 1:5.

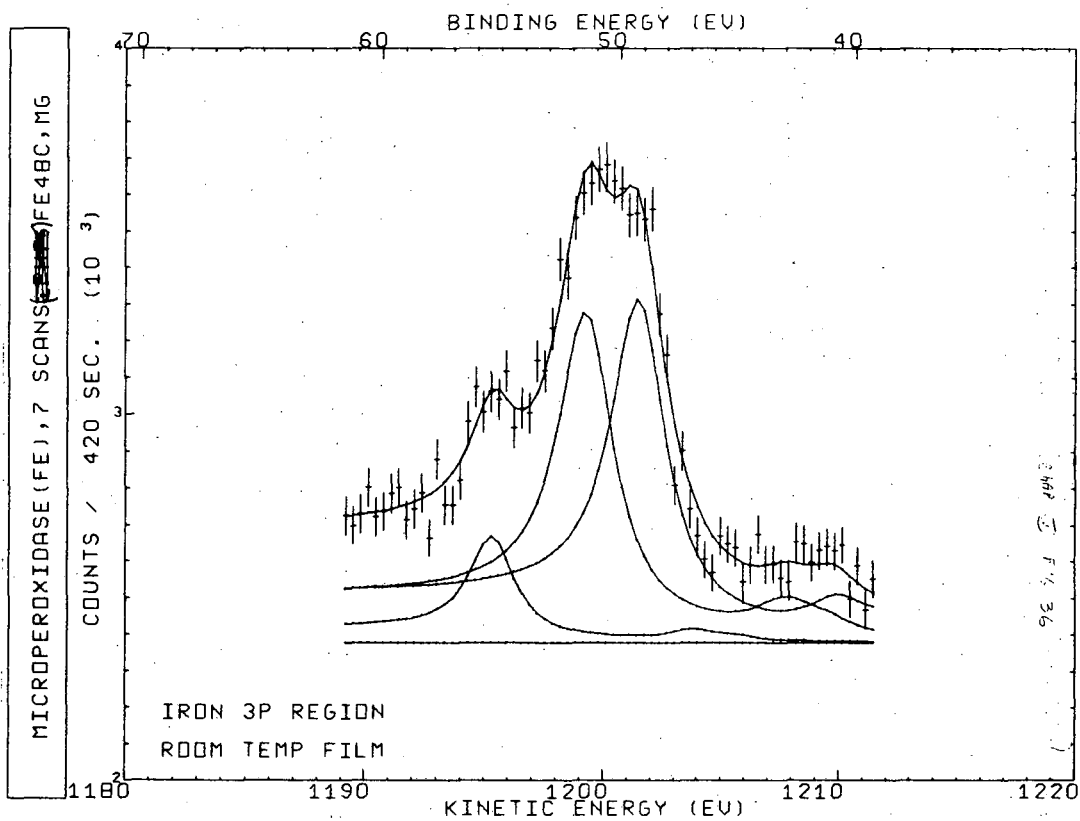


Figure 36. Iron 3p spectrum of desalted microperoxidase (Fig. 5) dried in a film onto a quartz plate from a solution of pH 5.9. This spectrum shows the sum of 7 scans accumulated over 11 hours; therefore, these data represent an average signal from fresh and damaged sample.

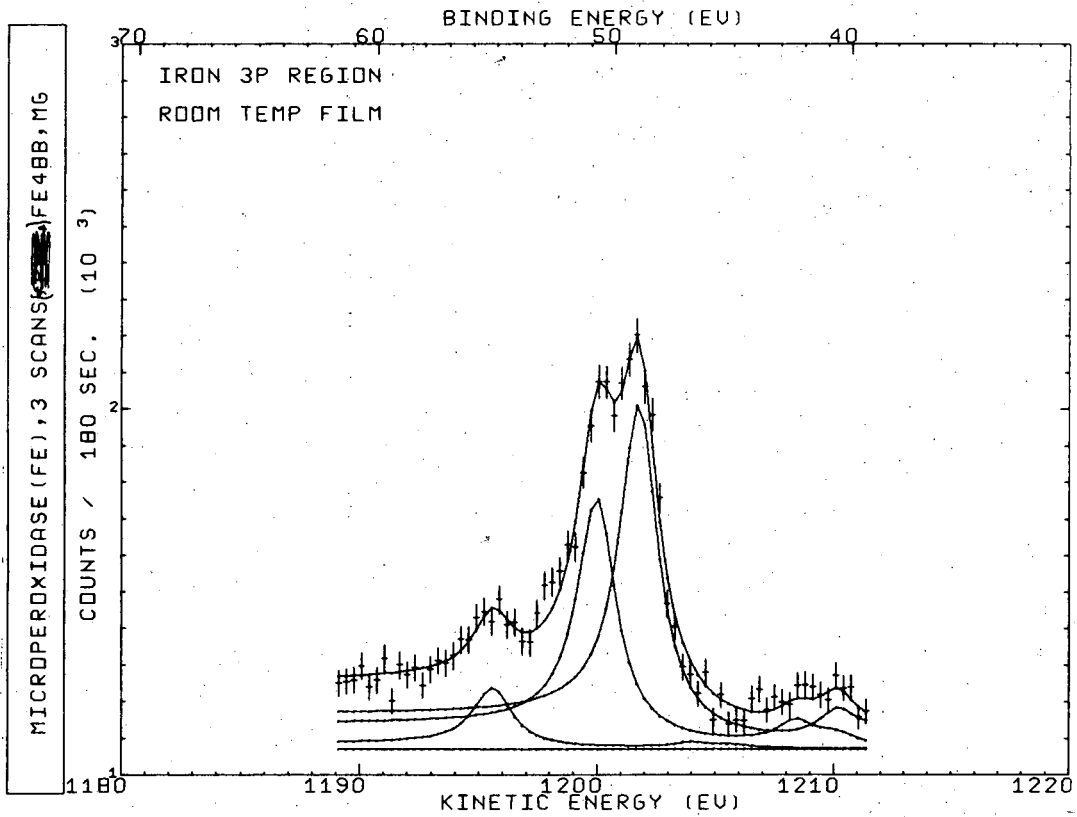


Figure 37. Iron 3p spectrum of desalted microperoxidase (Fig. 5) dried in a film onto a quartz plate from a solution of pH 5.9. The sample was exposed to x-rays for 9 hours before this spectrum was accumulated over 4 additional hours; therefore, these data emphasize the signal from a damaged sample. The reduced iron line at 49 eV is proportionally larger in this spectrum than in Fig. 36.

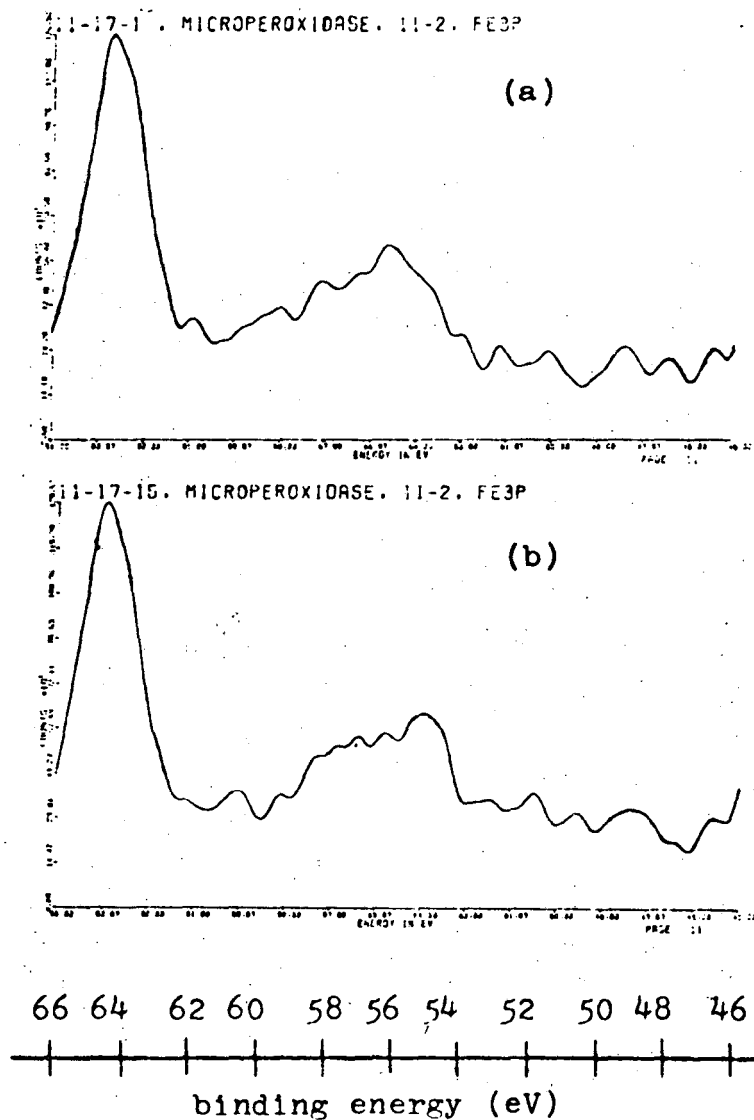


Figure 38. Iron 3p spectra (HP5950A spectrometer) of microperoxidase (Fig. 5) dried in a film onto a gold platen from a solution of pH 7 containing buffer salts. (a) After 850 min. exposure to x-rays and 350 min. exposure to a low energy electron flood gun. (b) After 1350 min. exposure to x-rays and 350 min. exposure to the flood gun. The sample has apparently been reduced because the main peak shifted to lower BE. The flood gun was not on during these measurements. The large peak at 64 eV is the Na 2s signal from the buffer salts.

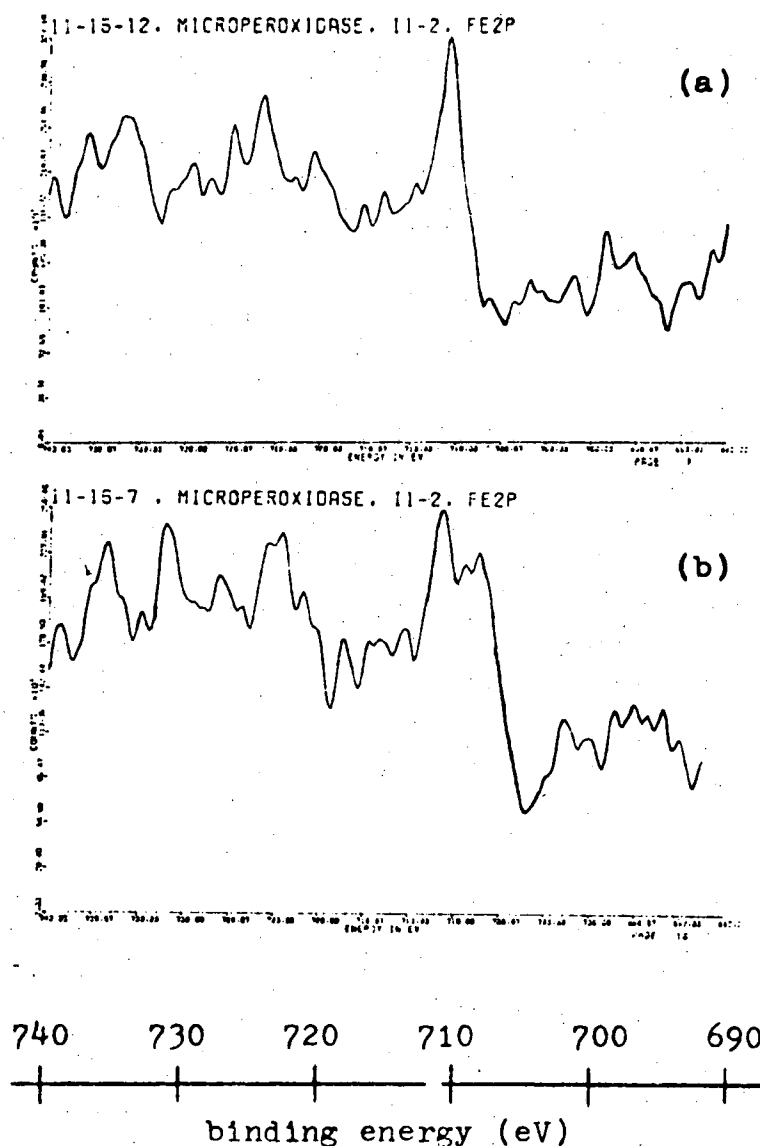
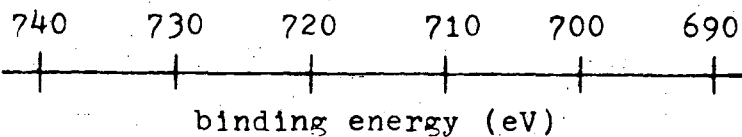
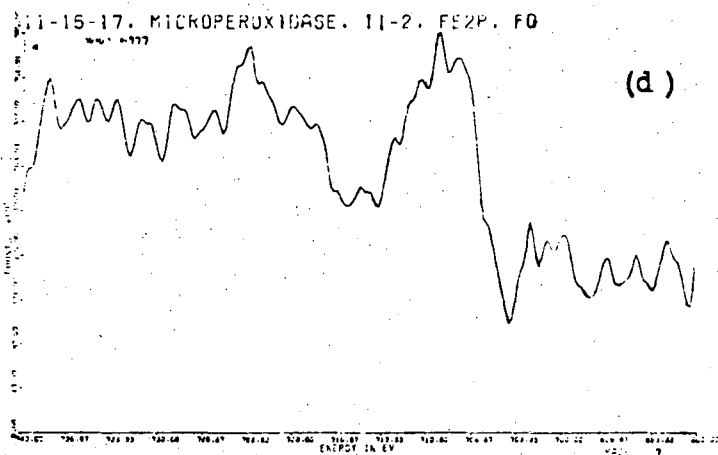
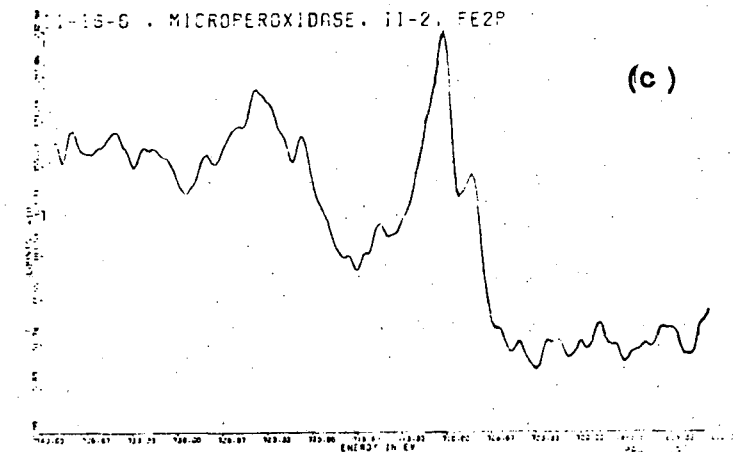


Figure 39. Iron 2p spectra (HP5950A spectrometer) of microperoxidase (Fig. 5) dried in a film onto a gold platen from a solution of pH 7 containing buffer salts. (a) First scan of 24 min. taken after 8 min. exposure to x-rays. (b) Last 24 min. scan taken after 290 min. exposure to x-rays. (c) and (d) shown on next page. (c) Sum of twelve 24 min. scans. Total of 315 min. exposure to x-rays. (d) 90 min. scan with the flood gun on (1 ma., 0 volts) after 550 min. previous exposure to x-rays and 210 min. previous exposure to flood gun.



- (c) Sum of twelve 24 min scans. Total of 315 min exposure to x-rays.
- (d) 90 min scan with the flood gun on (1 mA, 0 volts) after 550 min previous exposure to x-rays and 210 min previous exposure to flood gun.

The growth of a reduced specie is evident in Figs. 36, 37, and 39. The main peak in the Fe 3p spectrum of desalted MP (Fig. 5) can be decomposed into two lines (Figs. 36, 37) with BE's of 51.5 and 49 eV. A comparison of Figs. 36 and 37 shows that the 49 eV line grows at the expense of the 51.5 eV line during an experiment. The Fe 3p spectrum of desalted MP is shown in Fig. 36. These data were accumulated over 11-1/2 hr of exposure to the photon and electron fluxes from the x-ray tube; they represent an average of the signal from fresh and photon/electron damaged sample. Fig. 37 shows similar data accumulated over the last 4 hr of a 12-1/2 hr experiment; these data emphasize the signal from a long exposure time. The 49 eV line is proportionally larger in this spectrum than in Fig. 36. The 49 eV line is interpreted as an experimental artifact that grows from the 51.5 eV line during exposure to the x-ray tube. The parent line at 51.5 eV is interpreted as ferric iron because the sample films are known to contain low spin ferric iron at the beginning of an experiment. (See discussion of optical spectra.) The 49 eV line is most probably iron reduced to the ferrous state by the electrons incident on the sample from the x-ray tube window. Similar behavior has already been discussed with the sulfur spectra (Fig. 25).

The evolution of a reduced specie is more evident in Fig. 39. These data show the first scan (39a), last scan (39b), and sum of twelve scans (39c) of the Fe 2p region of an MP film taken on the HP 5950A spectrometer. The growth of a peak at 708.2 eV is easily observable. The separation from the parent peak at 710.4 eV peak is consistent with the separations observed in Figs. 36 and 37 (2.2 and 1.8 eV, respectively).

I propose that the unusually low Fe(III) 3p BE is an indication of heme iron that lies in the plane of the porphyrin ring; the normal BE indicates heme iron displaced above the plane of the ring. Heme iron partially displaced from the plane of the ring probably shows an intermediate BE, but the BE need not be linear with the displacement. Displacement of the iron from the plane of the porphyrin has been identified with high spin iron-porphyrin complexes,^{59,60} the iron atoms of low spin complexes lie in the plane of the ring.^{59,60} Therefore, my proposal is equivalent to stating that the Fe 3p BE in heme complexes is sensitive to the spin state of the iron. This interpretation also implies that, under XPS experimental conditions, it is easier to transfer electrons from porphyrin to iron in a heme complex when the iron lies in the plane of the ring rather than when the iron is displaced.

This interpretation assumes that the unusually low BE can be explained by extra-atomic relaxation.⁵⁸ This phenomenon refers to delocalizing a photohole by filling it with electrons from neighboring atoms and molecules. The effect on BE can be described in terms of Eq. (1):

$$BE = E_f - E_i \quad (1)$$

where E_f = energy of the final state of the photoionization process, i.e., the total energy of an atom or molecule containing a photohole.

E_i = energy of the initial state, i.e., the total energy of an atom or molecule before photoionization.

BE = binding energy of the photoejected electron.

The delocalization of the photohole's positive charge over neighboring atoms leads to a reduction of E_f , and therefore, a reduction of BE.

It is important to emphasize that extra-atomic relaxation reduces BE by lowering the final state energy of the photohole. If BE is lowered by this effect, it does not imply an unusually low energy for the orbital from which the photoelectron was ejected. Orbital energies are characteristic of E_i , the initial state, and they are not affected by extra-atomic relaxation.

The iron in cytochrome c is particularly susceptible to the effects of extra-atomic relaxation because it is in the low spin state and it lies in the plane of the porphyrin ring.³ A photohole in the iron can be stabilized considerably by transferring an electron from the porphyrin to fill the hole. Thus, the hole can be delocalized over the conjugated system of the porphyrin. The optical spectra of the cytochrome and de-salted MP films measured in this work show that these samples contained low spin ferric iron in the porphyrin plane. Fe 2p and 3p photoholes could disperse over the porphyrin ring, thereby lowering the "hole" state energy and, therefore, the Fe 2p and 3p BE.

An analogous electron transfer and hole migration model was discussed earlier in connection with oxidation of sulfur by photon absorption at the iron.

The higher Fe 3p BE of non-heme iron proteins relative to cytochrome c can now be understood. There is no conjugated porphyrin ring available to delocalize photoholes and reduce the BE.

However, Table V shows that many iron-porphyrin complexes also have BE's that are high compared to cytochrome c. These complexes -- hemin

chloride, chlorotetraphenylporphinatoiron(III), and chloroproporphyrinatoiron(II) -- all contain high spin iron. Numerous crystal structure determinations^{59,60} have shown that, in heme complexes, high spin iron is displaced from the plane of the porphyrin. The average displacement is 0.48 \AA above the plane.⁵⁹ I claim that the displacement of the iron hinders the electron transfer that allows delocalization of photoholes over the porphyrin. Therefore, the photohole is not stabilized, and the observed BE is not lowered.

The lowest Fe 2p BE's observed in Table Vb are those of bis(piperidine)tetraphenylporphinatoiron(II) and bis(piperidine)protoporphyrinatoiron(II). The structure of the former compound is known;⁶² it is a low spin iron complex with the iron in the plane of the porphyrin. It is assumed that the same is true of the latter compound. These complexes can stabilize Fe 2p photoholes by delocalization over their conjugated rings; their Fe 2p BE's are 2 - 5 eV lower than those of the high spin iron porphyrin complexes that contain iron atoms displaced from their rings. Zeller and Hayes⁴⁸ expressed doubt about the validity of the Fe 2p BE for bis(pip)protoporphyrinatoiron(II); 706.1 eV was reported as an upper limit.

The collected results from the Fe 3p measurements on the Berkeley spectrometer (Table Va) and Fe 2p measurements from the literature (Table Vb) are completely consistent with the proposal that the effect of extra-atomic relaxation on BE allows one to distinguish the spin state of iron in heme complexes, or equivalently, to determine whether the iron is in or out of the porphyrin plane.

In apparent contradiction to the proposal developed above, it was found that Fe 2p and 3p BE's of MP measured on the HP 5950A spectrometer were high. Desalted MP samples measured on the Berkeley spectrometer were found to contain low spin (in plane) iron; the BE's measured on the HP 5950A spectrometer are consistent with high spin (out of plane) iron and non-heme iron proteins.

In fact, there may be no disagreement at all. The following essential facts were detailed in previous sections.

- (a) In a film, MP polymerizes such that the sixth (axial) position of iron is occupied by the α amino group of a neighboring MP molecule. The iron is bound octahedrally; it is low spin; it lies in the porphyrin plane.
- (b) Optical spectra proved that the desalted MP films prepared for the Berkeley instrument contained low spin (in plane) ferric iron. No optical spectra could be taken through the sample plates used in the HP 5950A instrument.
- (c) The MP films measured on the HP 5950A spectrometer were prepared with material taken directly from the bottle. This MP contained buffer salts.
- (d) During the preparation of a film, salts migrate to the center while protein forms a crust around the perimeter.

The salt concentration in the measured region of the MP films run on the HP 5950A spectrometer was very high. The count rate for iron in the MP film was about equal to that of a dialyzed cytochrome c film;

it should have been six times higher. The sodium 2s peak from the buffer salts dominates the FE 3p spectra in Fig. 38.

I suggest that the iron in the MP measured on the HP 5950A spectrometer is high spin and displaced from the porphyrin plane. The small amount of MP in the center of the sample plate did not polymerize in the presence of the high salt concentration. I believe the MP in these films was predominantly monomeric containing pentacoordinate, high spin iron with a buffer salt anion occupying the axial position. Therefore, it is reasonable that such films would be consistent with other high spin complexes.

The spectra in Fig. 38 and the data in Table Va support this hypothesis. The main peak is broad (FWHM = 4 eV) and shows considerable structure. It seems to reflect iron in several different environments adsorbed on the salt crystals. Some minor peaks in Fig. 38a have BE's (51.5 and 49.3 eV) that correspond very closely to the BE's of low spin (in plane) iron observed in desalted MP on the Berkeley spectrometer. (See Table Va.) This result suggests that only a small portion of the MP in the HP 5950A spectrometer precipitated in the low spin form. (Of course, the minor peaks in 38a may be spectral noise, and the correspondence of BE's may be fortuitous.)

It has been shown that all of the cytochrome and MP data can be interpreted in terms of a proposed extra-atomic relaxation model. The model remains a proposal and not a proof. More work is necessary. If the low spin (in plane) heme iron BE's are, in fact, being lowered by

the dispersion of photoholes over the conjugated porphyrin ring, then the effect should be mitigated by breaking the conjugation of the ring. A complex of iron in the plane of a bile pigment should have a higher BE than low spin iron in heme. Also, a series of iron porphyrin complexes with known crystal structures^{59,60} must be measured to establish the relationship between the BE shift and the displacement of iron from the porphyrin.

If the proposed interpretation is correct, then one concludes that under XPS experimental conditions, there can be electron transfer from porphyrin to iron in heme complexes. The transfer is favored when the iron is in the porphyrin plane more so than when the iron is displaced. On the basis of this conclusion, one might speculate about the mechanism of electron transport in cytochrome c. However, the extreme conditions of an XPS experiment (vacuum, condensed protein film, radiation, core holes) make an extrapolation to biological conditions tenuous.

In addition to the main FE 3p peak at 52 eV, there is a shoulder in the cytochrome spectra at 54 - 55 eV; a similar signal appears as a distinct peak in the MP spectra at 55.5 eV. A lineshape was fitted to this signal whenever possible (Figs. 34 - 37). In all cases, the calculated ratio of the 55 eV line to the 52 eV line was observed to be (0.2 - 0.3):1. Within the error of the calculation, this ratio could be constant through all the spectra.

It is most likely that this signal is the result of multiplet splitting⁶¹ or two electron excitations.⁶¹ The constant ratio of the 55 eV line to the 52 eV line strongly suggests this. (The calculated

ratios are not reliable according to the standards developed in Chapter III. The apparently constant ratio observed here may be a coincidence.)

This signal can also be interpreted as a product of radiation damage. Optical spectra of the cytochrome and MP sample films after irradiation indicated loss of conjugation in the porphyrin, and perhaps actual fragmentation of the ring. A signal from an iron atom complexed to such reduced or fragmented species will resemble that from a non-heme iron protein which has no conjugated system over which it can disperse a photohole. Indeed, the BE of the 55 eV line is consistent with the non-heme iron proteins.

The peak may also reflect an equilibrium of high spin (out of plane) iron and low spin (in plane) iron. This situation is not evident in the optical spectra of the films (no large absorptions at 620 nm).

Finally, we recall that ferric iron was reduced to ferrous iron during an experiment (Figs. 36, 37). It might be postulated that the 55 eV signal was the dominant peak at the beginning of the experiment, and that it degraded into the 52 and 49 eV peaks with exposure to the x-ray tube. This scenario is not consistent with the constant ratio between the 55 and 52 eV lines in Figs. 36 and 37.

In conclusion, five characteristics of the iron spectra were listed at the beginning of this discussion. From these observations, it has been learned that chemical reduction of iron takes place during a measurement. Roughly 10 hours are required to degrade 50% of a ferric sample into some uncharacterized reduced specie, probably the ferrous analogue

of the original sample. The reducing agent is most likely the flux of electrons from the x-ray tube window. Similar behavior was observed in the sulfur spectra.

These experiments showed that XPS cannot distinguish ligand changes about the iron of low spin heme compounds.

It is proposed that XPS can clearly distinguish iron that is in or out of the porphyrin plane of heme compounds. Iron displaced from the porphyrin plane is identified with the high spin state, and iron in the plane is identified with the low spin state.^{59,60} Therefore, it is also proposed that XPS can distinguish the spin state of iron in heme complexes. The basis of the determination is a large shift in BE which is attributed to extra-atomic relaxation.

REFERENCES, CHAPTER V.

1. L.N. Kramer, Ph.D. dissertation, University of California, Berkeley, 1971, Lawrence Berkeley Laboratory Report #LBL-306.
2. E. Margoliash and A. Schejter, Adv. Protein Chem. 21, 173 (1966).
3. R.E. Dickerson, et al., J. Biol. Chem. 246, 1511 (1971).
4. H. Theorell and A. Akesson, J. Am. Chem. Soc. 63, 1812 (1941).
- 5a. B. Chance and G.R. Williams in Advances in Enzymology F. Nord (Ed.), Vol. 17, pp. 65 - 134 (1956).
- 5b. A.L. Lehninger, The Mitochondrion (W.A. Benjamin, New York, 1965), pp. 54 ff.
- 5c. E. Margoliash in Encyclopedia of Biochemistry, R. Williams and E. Lansford (Eds.) (Reinhold, New York, 1967), p. 274.
6. The co-operation of Dr. F.J. Grunthamer and Prof. H.B. Gray in permitting me to use this apparatus is gratefully acknowledged.
7. N. Feder, J. Histochem. and Cytochem. 18 (12), 911 (1970).
8. Prof. H. Rapoport, private communication.
9. The analysis was performed by V. Tashinian, Department of Chemistry, University of California, Berkeley.
10. D. Spackman, W. Stein, S. Moore, Analyt. Chem. 30 (7), 1190 (1958).

11. The steps in the procedure were provided by V. Tashinian (see Ref. 9).
12. J.C. Sutherland, M.P. Klein, J. Chem. Phys. 57, 76 (1972).
13. E. Margoliash and N. Frohwirt, Biochem. J. 71, 570 (1959).
14. Gouterman et al., have written 25 papers dealing with the theoretical interpretation of porphyrin spectra and structures. Those most applicable to iron complexes are:
 - a. M. Zerner and M. Gouterman, Theor. Chim. Acta 4, 44 (1965); and 8, 26 (1967).
 - b. M. Zerner, M. Gouterman, H. Kobayashi, Theor. Chim. Acta 6, 363 (1966).A more empirical treatment of porphyrin spectra is given by Falk:
 - c. J.E. Falk, Porphyrins and Metalloporphyrins (Elsevier, New York, 1964), Chap. 6.
15. Ref. 14c, p. 82.
16. E. Schechter and P. Saludjian, Biopolymers 5, 788 (1967).
17. B. Sreenathan and C. Taylor, Biochem. Biophys. Res. Commun. 42, 1122 (1971).
18. W. Eaton and R. Hochstrasser, J. Chem. Phys. 46, 2533 (1967).
19. S. Moore, J. Biol. Chem. 238, 235 (1963).

20. J.B. Nielands in Haematin Enzymes, J.E. Falk, R. Zemberg, and R.K. Morton (Eds), Vol. 19, part 1, p. 211 (1959) (Symposium of International Union of Biochemistry, Canberra).
21. Schlesinger and Martin, J. Am. Chem. Soc. 36, 1589 (1914).
22. M.S. Jones and O.T.G. Jones, Biochem. J. 119, 453 (1970).
23. A.B. Robinson, Ph.D. dissertation, University of California, San Diego, 1967. (Available through University Microfilms, #68-9719, Ann Arbor, Michigan.)
24. T. Flatmark, A. Robinson, Structure and Function of Cytochromes, K. Okunuki, M. Kamen, J. Sekuzu (Eds.), (University Park Press, Baltimore, 1968), p. 318.
25. A. Robinson, M.S. Kamen, Ibid., p. 383.
26. W.R. Fisher, H. Taniuchi, C.B. Anfinsen, J. Biol. Chem. 248 (#9), 3188 (1973).
27. L.C. Dickinson and J.C.W. Chien, Biochem. Biophys. Res. Comm. 58, 236 (1974).
28. Analysis performed by Dr. Robert Giauque of the Lawrence Berkeley Laboratory.
29. K.G. Paul, Acta Chem. Scand. 5, 389 (1951).
30. S. Sano, K. Tanaka, J. Biol. Chem., 239, PC3109 (1964).
31. E. Margoliash, N. Frohwirt, E. Wiener, Biochem. J. 71, 559 (1959).

32. F. Lederer, J. Tarin, European J. Biochem. 20 482 (1971).
33. A. Fontana, F. Veronese, E. Boccu, FEBS Letters 32, 135 (1973).
34. M. Folin, A. Azzi, A. Tamburro, G. Jori, FEBS Letters 20, 215 (1972).
35. Grant Wilson, Ph.D. Dissertation, University of California, Berkeley, 1974, pp. 108 -112.
36. J. Falk, D. Perrin, in Haematin Enzymes, part 1, Falk, Lemberg, & Morton (Eds.), (Pergamon Press, New York, 1961), p. 56.
37. P.D. Boyer, H.L. Segal in The Mechanism of Enzyme Action, McElroy and Glass (Eds.) (Johns Hopkins Press, Baltimore, 1953).
38. P.D. Boyer, J. Am. Chem. Soc. 76, 4331 (1954).
39. C. Tsou, Biochem. J. 49, 367 (1951).
40. H. Tuppy and S. Paleus, Acta Chem. Scand. 9, 353 (1955).
41. S. Paleus, A. Ehrenberg, H. Tuppy, Acta Chem. Scand. 9, 365 (1955).
42. a. A. Ehrenberg, H. Theorell, Nature 176, 158 (1955).
b. A. Ehrenberg, H. Theorell, Acta Chem. Scand. 9, 1193 (1955).
43. a. H. Harbury, P. Loach, Proc. Nat. Acad. Sci. USA 45, 1344 (1959).
b. H. Harbury, P. Loach, J. Biol. Chem. 235, 3640 (1960).
c. Ibid, p. 3646.

44. There is a voluminous literature on myoglobin, see, for example:
 - a. E. Antonini, M. Brunori, Frontiers of Biology, Vol. 21, Neuberger and Tatum (Eds.), (North-Holland, Amsterdam, 1971), Chap. 3 (deals with general properties).
 - b. T. Hzuka, T. Yonetani, Adv. Biophys. 1, 157 (1970). (Spin changes)
 - c. Smith and Williams in Structure and Bonding, Vol. 7, P. Hemmerich, et al. (Eds), (Springer-Verlag, New York, 1970), pp. 1 - 45 (ferric heme spectra).
45. A. Harbury et al., Proc. Nat. Acad. Sci. USA 54, 1658 (1965).
46. a. Dr. James Slama, private communication.
 - b. R. Connor in Organic Chemistry: An Advanced Treatise, H.H. Gilman (Ed.) (John Wiley, New York, 1943), pp. 870 ff.
47. A complete description of the Fourier transform smoothing routine used on the HP 5950A data in this work is given in: F.J. Grunthaner, Ph.D. dissertation, California Institute of Technology, 1974.
48. M. Zeller, R. Hayes, J. Am. Chem. Soc. 95, 3855 (1973).
49. D. Karweik, N. Winograd, D. Davis, K. Kadish, J. Am. Chem. Soc. 96, 591 (1974).
50. Y. Niwa, H. Kobayashi, T. Tsuchiya, J. Chem. Phys. 60, 799 (1974).
51. E. Clementi, C. Roetti, Atomic Data and Nuclear Data Tables, Vol. 14 (#3 & 4) (Academic Press, New York, Sept. - Oct., 1974).

52. A. Nath, M. Klein, W. Kundig, S. Lichtenstein, Mössbauer Effect Technology, Vol. 5 (Plenum Press, 1969), p. 163.
53. L. Yin, E. Yellin, I. Adler, J. Appl. Phys. 42 (9), 3595 (1971).
54. F.J. Grunthaner, to be published.
55. P. Warne, L. Hager, Biochemistry 9 (7), 1599 (1970).
56. D.W. Davis, Ph.D. dissertation, University of California, Berkeley, 1973, See Table V.
57. L.N. Kramer and M.P. Klein in Electron Spectroscopy, D.A. Shirley (Ed.) (North-Holland Publ. Co., Amsterdam, 1972), p. 733.
58. D.A. Shirley, Chem. Phys. Lett. 16 (2), 220 (1972).
59. J.L. Hoard in Structural Chemistry and Molecular Biology, Rich and Davidson (Eds.) (W.H. Freeman Co., San Francisco, 1968), pp. 573 ff.
60. J.L. Hoard, Science 174, 1295 (1971).
61. C.S. Fadley, Theoretical Aspects of X-Ray Photoelectron Spectroscopy, NATO Advanced Study Institute on Electron Emission Spectroscopy, Ghent University, Ghent, Belgium, Aug. 28 - Sept. 8, 1972.
62. L. Radonovich, A. Bloom, J. Hoard, J. Amer. Chem. Soc. 94 (6), 2073 (1972).

VI. XPS STUDY OF THE BINDING OF RARE EARTH IONS TO ATP

A. Introduction

It has been proposed that rare earth ions can act as substitutes for calcium ion in biological systems.¹⁻⁴ Spectroscopic data regarding the binding of Ca^{++} to proteins is scarce due to the lack of electronic transitions in convenient spectral regions.^{1,2} Lanthanide ions, however, show sharp visible and ultraviolet absorptions, characteristic fluorescence, and are paramagnetic. When rare earths have been substituted for calcium, they may thus be able to act as spectroscopic probes of calcium binding sites in proteins.

It has already been shown that, like Ca^{++} , Nd^{3+} accelerates the activation of trypsinogen to trypsin.² Lu^{3+} restores the activity of calcium-free Bacillus subtilis α -amylase.⁴ The apparent ability of lanthanides to substitute for calcium has been attributed to the fact that both calcium and rare earth ions form predominantly electrostatic complexes.^{1,2}

Dr. Raymond Chang (a visiting professor from Williams College, Williamstown, Massachusetts) used phosphorus NMR to study complexes of rare earth ions and ATP.¹³ The goal was to characterize rare earth binding to biological molecules that were less complicated than enzymes. In support of Dr. Chang's work, a project was initiated to study lanthanide-ATP complexes by XPS.

B. Experimental

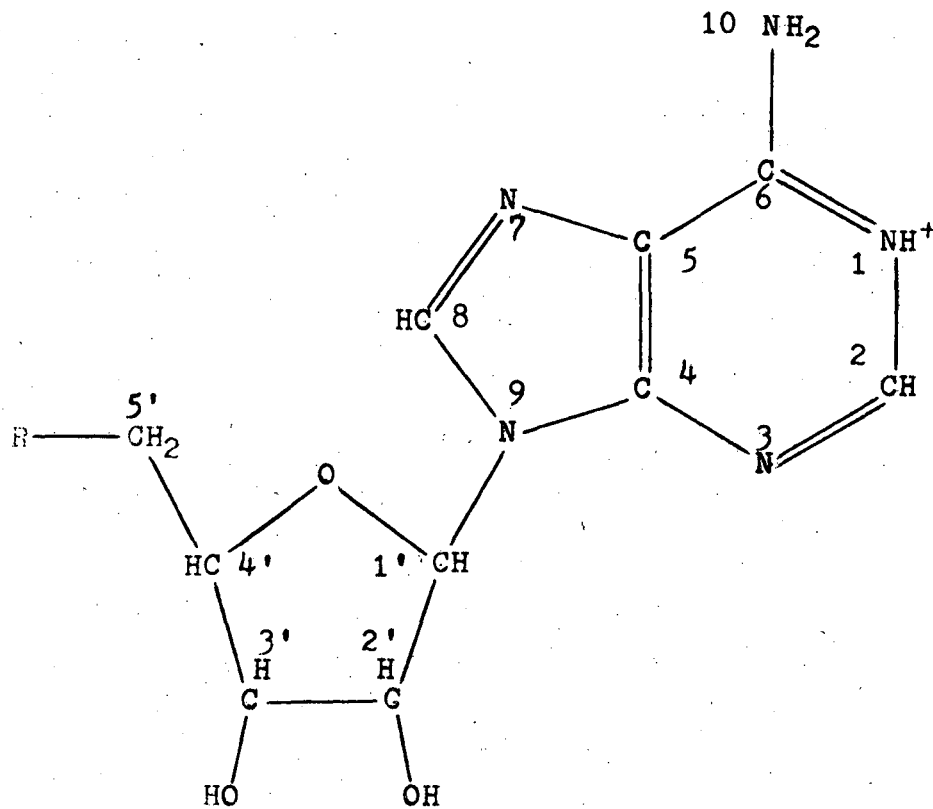
ATP (Sigma, lot #110C-7410, and National Biochemicals) was obtained from commercial sources as the disodium salt and used without further purification. AMP, adenosine-5'-monophosphate (Sigma, type III, lot #22C-7770), $\text{NdCl}_3 \cdot 6\text{H}_2\text{O}$ (Alfa, lot #022272), EuCl_3 , and TTP, triphosphate ($\text{Na}_5\text{P}_3\text{O}_{10}$, Sigma, lot #80C-5240) were also used without further purification.

An attempt was made to slowly precipitate AMP under conditions similar to those that yielded single crystals for the x-ray structure determination of AMP.²⁵ 110 mg of AMP (Sigma, sodium salt) were dissolved in 3 ml of glass distilled water, adjusted to pH 2.9 with 1 M HCl, and allowed to stand in a refrigerator overnight. The resulting precipitate was filtered, washed, and dried on a lyophilizer. Helena Ruben obtained an x-ray powder pattern⁵ on a sample of this material using copper $K\alpha$ radiation (35 kV, 20 mA, 8 hr exposure). For comparison, a theoretical powder pattern was calculated⁵ from the crystal structure of AMP published by Kraut and Jensen.²⁵

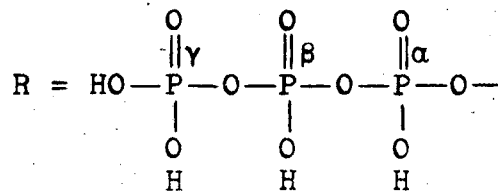
Other samples of AMP were lyophilized from solutions of pH 5.0 (HCl) and 11.3 (NaOH).

Analyses for neodymium were performed gravimetrically by precipitation of the oxalate and ignition to Nd_2O_3 according to the method of Kolthoff and Elving.⁶ $\text{NdCl}_3 \cdot 6\text{H}_2\text{O}$ was analyzed in the form of crystals directly from the bottle and as a stock solution (10.8313 g dissolved in 500 ml water). Crystals of $\text{NdCl}_3 \cdot 6\text{H}_2\text{O}$ adsorb water and CO_2 during

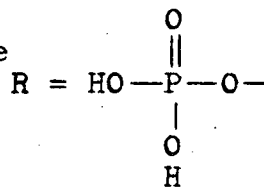
Figure 1. The molecular structures of ATP, AMP, and TPP.



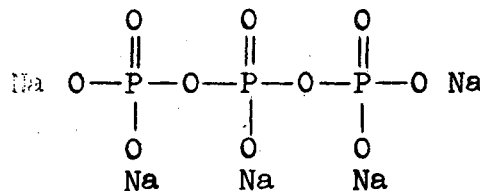
(a) ATP
adenosine-5'-triphosphate
(free acid form)



(b) AMP
adenosine-5'-monophosphate
(free acid form)



(c) TPP
tripolyphosphate
 $\text{Na}_5\text{P}_3\text{O}_{10}$



the weighing procedure; it was necessary to extrapolate the sample weights to zero time of atmospheric exposure.

The chloride concentration of the NdCl_3 stock solution was determined⁷ by titration with dichlorofluorescein⁸ and Ag^+ . The lavender color of Nd^{3+} interfered with the end point; therefore, it was necessary to remove the Nd^{3+} by precipitation with oxalate and analyze the supernatant for Cl^- .

The neodymium complex of ATP was prepared as follows. 0.9 mg of $\text{NdCl}_3 \cdot 6\text{H}_2\text{O}$ crystals and 1.5 g of ATP (approximately equimolar quantities) were each dissolved in 15 ml of 0.3 M acetic acid, acetate buffer, pH 5.0, packed in ice. The Nd^{3+} solution was added dropwise to the ATP solution with constant stirring; the complex precipitated immediately. Without the buffer, an undesirable globular precipitate was obtained. The precipitate suspension was stirred for two minutes while packed in ice. The precipitate was centrifuged and washed twice with cold water to remove excess buffer. In some preparations, the precipitate was washed a third time with cold water; in others, it was washed with ethanol to remove water immediately and minimize hydrolysis of the complex. The precipitate cake was then frozen and then dried on a lyophilizer. A typical yield was 1.5 g of product.

The complex was analyzed⁹ for neodymium by adding 20 ml of 1:3 HNO_3 to 0.12 g of complex and boiling for a few minutes to dispel oxides of nitrogen. One gram of $(\text{NH}_4)_2\text{S}_2\text{O}_8$ was added, and the solution was boiled for 15 minutes to oxidize all organic material and destroy excess

persulfate. The solution was allowed to cool and was diluted to 25 ml with distilled water. Nd^{3+} was then determined spectrophotometrically.¹⁰ A spectrophotometric calibration curve was prepared from several aliquots of the NdCl_3 stock solution described above. ATP controls showed no interference in the neodymium determination.

Phosphate was analyzed by the method of Lowry and Lopez.^{11,12} 0.5 g of NdATP complex were dissolved in 20 ml of water and 2 ml of concentrated HClO_4 , boiled for 8 minutes, and diluted to 250 ml with distilled water. A 1.00 ml aliquot was mixed with 18 ml of pH 4 buffer (0.1 M acetic acid, 0.025 M sodium acetate) and 2.5 ml of 1% ascorbic acid solution. 2.5 ml of ammonium molybdate solution (1 g in 100 ml of 0.05 N H_2SO_4) were added; the solution was mixed immediately and brought to a total volume of 25 ml with pH 4 buffer. The absorbance was measured at 700 nm five and ten minutes after the molybdate addition. Simultaneous readings were made on standard solutions of K_2HPO_4 and ATP, and on control samples containing known amounts of Nd^{3+} and ATP and known amounts of Nd^{3+} and adenosine.

Elemental analyses for carbon, hydrogen, nitrogen, and phosphorus were performed by a professional analytical chemist.⁷

Dr. Chang prepared complexes of Eu^{3+} with ATP and Nd^{3+} with tri-polyphosphate (TPP) by mixing equimolar solutions of the respective reagents.

XPS samples were pressed into pellets at 500, 1000, and 1500 p.s.i. The measurements were made with $\text{MgK}\alpha$ radiation in the Berkeley iron-free spectrometer.

C. Results and Discussion

Powder Pattern

The powder pattern of AMP (pH 3, fully protonated) was obtained to determine the applicability of the published crystal structure²⁵ to the samples used in the XPS experiments. For each of the most intense lines in the calculated⁵ powder pattern, it was possible to locate a corresponding line of medium or strong intensity in the observed pattern. However, the observed pattern showed many other intense lines. The observed pattern also had several lines in common with the powder patterns of anhydrous and monohydrated AMP (Powder Diffraction Files, #7-702 and #16-993). It seems that the powder pattern observed in this work represents AMP that has precipitated in several crystalline forms. It is evident that the structure published by Kraut and Jensen²⁵ cannot be used as a "blueprint" of the AMP samples in this work, but it remains useful as a source of qualitative ideas to aid the interpretation of the XPS spectra. The bond distances and angles are, of course, still useful. Finally, it is not surprising that the observed powder pattern failed to reproduce the pattern calculated from the structure of Kraut and Jensen²⁵ because even these workers report that they were unable to reproduce this crystal form at a later date.²⁵

Similar caution must be applied to the use of the published ATP structure²⁶ to interpret XPS spectra because this compound was also difficult to crystallize.

Sample Purity

The results of the chloride, neodymium, phosphate, and elemental analyses are given as weight per cents in Table I. The gravimetric neodymium analyses of $\text{NdCl}_3 \cdot 6\text{H}_2\text{O}$ crystals show erratic results; these data reflect contamination of the crystals by atmospheric water and CO_2 . The analyses of the NdCl_3 stock solution were satisfactorily reproducible. It can also be seen that the phosphorus results obtained by the professional analytical chemist⁷ agreed with the phosphate analysis by the method of Lowry and Lopez.^{11,12} The comparison is shown in sample #1 of the Nd and ATP complexes.

The data in Table I have been converted into molar ratios which are shown in Table II. The Nd^{3+} and Cl^- concentrations in the NdCl_3 stock solution were found to be self consistent to a high degree of accuracy. The low C/H ratio is probably due to the presence of water of hydration.

The results from the Nd and ATP complexes show the expected 3:1 ratio for P/Nd and the expected 2:1 ratio for C/N. It would seem that the preparations contain one Nd per ATP molecule. However, the C/Nd and C/P ratios indicate a deficiency of carbon. There appears to be one Nd per triphosphate chain, but it seems that some of the Nd-triphosphate complexes separated from their parent ATP molecules. The Nd-triphosphate complex precipitated out of the solution; the adenosine residue was left in solution and discarded with the water washings.

Table I. Weight percentages observed for the various analyses described in the experimental section.

Sample	Observed Weight Per Cent					
	Cl	Nd	P	C	H	N
NdCl ₃ ·6H ₂ O crystals						
Sample #1		41.17 ± 0.03				
#2		41.56 ± 0.02				
#3		41.25 ± 0.04				
Average		41.00 ± 0.02				
NdCl ₃ stock soln. ^a						
Sample #1		41.16 ± 0.05				
#2		41.20 ± 0.06				
#3		41.12 ± 0.05				
Average		41.16 ± 0.03				
Sample #4	30.60 ± 0.05					
#5	30.61 ± 0.05					
Nd and ATP complexes						
Sample #1		20.1 ± 0.5	12.84 ± 0.06 12.9 ± 0.3 ^b	14.55 ± 0.07	2.63 ± 0.02	
#2		20.0 ± 0.5	13.2 ± 0.3	17.2 ± 0.3	2.5 ± 0.1	9.8 ± 0.2
#3		19.5 ± 0.5	12.86 ± 0.06	14.52 ± 0.07	2.81 ± 0.02	8.64 ± 0.04

^a%Nd × 0.01 = g Nd per 50 ml stock solution.

^bAverage of two values: 13.2 and 12.5 obtained by the method of Lowry and Lopez.^{11,12} Other P, C, H, N results obtained by Tashinian (Ref. 7).

Table II. Molar ratios derived from the analyses described in the experimental section.

		NdCl ₃ Stock Soln.	Nd and ATP Complexes		
			Sample #1	Sample #2	Sample #3
$\frac{Cl}{Nd}$	Theo	3.00			
	Obs	3.02 ± 0.01			
$\frac{P}{Nd}$	Theo		3.00	3.00	3.00
	Obs		2.97 ± 0.08	3.07 ± 0.10	3.07 ± 0.08
$\frac{C}{Nd}$	Theo		10.00	10.00	10.00
	Obs		8.69 ± 0.22	10.3 ± 0.3	8.94 ± 0.23
$\frac{C}{P}$	Theo		3.33	3.33	3.33
	Obs		2.92 ± 0.02	3.36 ± 0.10	2.91 ± 0.02
$\frac{C}{H}$	Theo ^a		0.71	0.71	0.71
	Obs		0.46 ± 0.01	0.58 ± 0.01	0.43 ± 0.01
$\frac{C}{N}$	Theo		2.00	2.00	2.00
	Obs		—	2.05 ± 0.05	1.96 ± 0.01

^aThe theoretical C/H ratio assumes one proton on the phosphate chain and one proton at N(1) and no water of hydration.

Assuming this model to be correct, the maximum Nd-triphosphate impurity is 7%. This is a low level impurity in the Berkeley iron-free spectrometer.

The structure of the Nd and ATP complex is not determined by these data. It can only be said that the sample is 93 - 100% pure as a 1:1 complex of Nd and ATP, based on atomic ratios.

The rare earth complexes of ATP were soluble at alkaline pH. Dr. Chang made phosphorus NMR measurements on the dissolved complexes. His results¹³ indicated that the rare earth coordinated to the α and γ phosphate groups of ATP. In these solutions, a chloride or hydroxy counterion was required to balance the charge on the formally tripositive metal.

By analogy to the solution results, the Nd and ATP complexes precipitated from pH 5 in this work are written as Nd(ATP)Cl; although, the presence of chloride was never confirmed by analysis. Chloride was assumed in this case because the complex was prepared with NdCl₃. Similarly, complexes of Eu and ATP are written as Eu(ATP)Cl.

Carbon 1s and Nitrogen 1s Results

The interpretation of carbon 1s and nitrogen 1s binding energies in nuclei acid bases has been controversial since 1970. CNDO calculations on these molecules have been possible for several years. Their biological significance has made them the subject of intense computational effort.¹⁴⁻²⁰ Barber and Clark¹⁵ reported a linear relationship between calculated orbital energies and measured C 1s and N 1s BE's in

adenine, cytosine, and thymine. A linear relationship between measured BE and calculated atomic charge was reported to be valid for C 1s BE's, but not for N 1s BE's; van der Avoird¹⁶ reported that a linear relationship between charge and N 1s BE was possible if Madelung potentials were considered. Brundle²¹ has suggested that the poor resolution in C 1s spectra of nucleic acid bases cannot support the detailed interpretations of Barber and Clark. Further calculations^{18,20} have emphasized that final state effects, such as charge redistribution, have as much effect on C 1s and N 1s BE as initial state effects, such as atomic charge.

The data obtained here have not been able to resolve the ambiguous interpretation of C 1s and N 1s spectra. The C 1s spectrum of ATP (Fig. 1) is shown in Fig. 2a. There are only two resolved peaks; all the other ATP, AMP, and metal(ATP)Cl C 1s spectra show the same general characteristics as Fig. 2a.

There are organic vapors in the spectrometer vacuum that condense on the surface of the sample. The C 1s BE of this contaminant layer corresponds to aliphatic and aromatic carbon (see Chap. 4, especially Fig. 3), which has the lowest BE of all biologically relevant forms of carbon. All the carbon atoms in ATP are bound to one or two electronegative atoms. All these carbons should have 1s BE's greater than that of aliphatic/aromatic carbon.^{22,23,24} Therefore, the higher BE peak in Fig. 2a has been assigned to the carbon in ATP while the lower BE peak has been assigned to the contaminant layer and any low BE C 1s signals from the ATP.

The C 1s spectrum of AMP (Fig. 2b) generally reproduces the shape of the ATP spectrum (Fig. 2a). The C 1s spectrum of Nd(ATP)Cl (Fig. 2c)

-277-

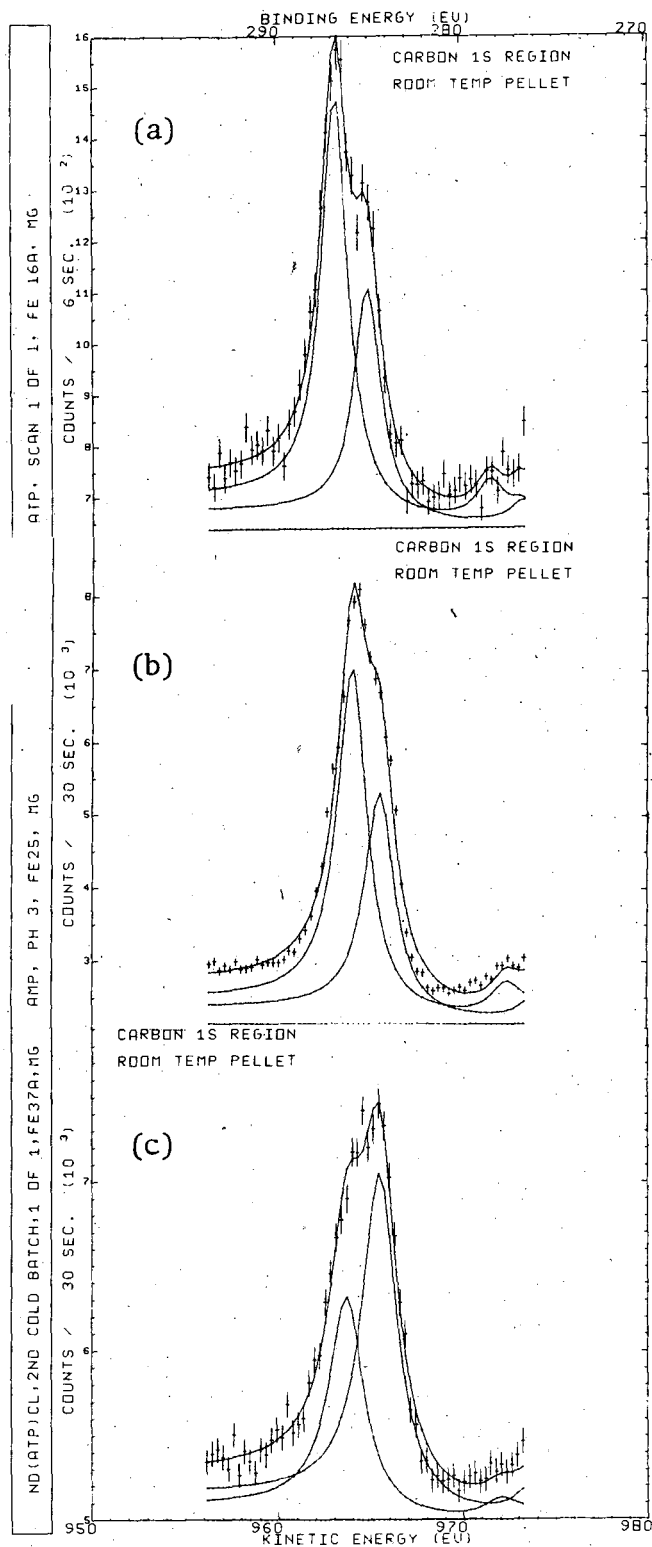


Figure 2. Carbon 1s spectra of: (a) ATP in the free acid form, (b) AMP lyophilized from a solution of pH 3, (c) Nd(ATP)Cl.

shows a reversal in the ratio of the two C 1s peaks relative to ATP. It is possible that this is due to the Nd^{3+} ion upsetting the hydrogen bonding in the tightly packed²⁶ ATP lattice. It is more likely that this ratio represents the variable amounts of organic vapors that condense on the sample surface.

There are basically three kinds of carbon in ATP: carbon singly bound to oxygen (all five carbons in the ribose ring), and carbon bound to one or two nitrogens (the five carbons in the adenine system). Data on hydroxyl and ether carbons,^{22,24} pyrrole,²³ and 1,2,4-triazole²⁴ indicate that these carbons should have 1s BE's 1.1 to 1.5 eV higher than aliphatic carbon. Ten C 1s signals so closely spaced could not possibly be distinguished on the Berkeley iron-free spectrometer; they would appear as a single, broadened peak as observed in the form of the higher BE peak in Fig. 2a.

Barber and Clark¹⁵ reported five C 1s BE's for adenine ranging from 284.7 eV to 287.8 eV as measured on a prototype AEI ES100 spectrometer. It is not obvious from the published report how these workers were able to discern five peaks under a signal which probably resembled Fig. 2a; they did not show any spectra or describe any curve fitting procedure. Since organic vapors probably also contaminate the vacuum of the AEI ES100, their assignment of the 284.7 eV signal deserves more careful study. The 287.8 eV assignment might correspond to a slight shoulder in Fig. 2a. Generally, Brundle's criticisms²¹ of Ref. 15 seem well founded.

The lack of specific assignments for the C 1s signal diminishes its utility as an internal reference standard. The lower BE C 1s peak

has been identified with aliphatic carbon. This peak is assigned a BE of 285.0 eV, and it is used as the reference signal. This choice is equivalent to using the contaminant C 1s signal as an external reference. It was shown in Chapter 4 that, in general, this procedure is not valid. However, it should be self-consistent at least within this series of similar compounds. (O 1s and N 1s cannot serve as alternative internal references because their spectra are different among ATP, AMP, and the metal complexes.)

It is also difficult to make a specific assignment of the N 1s data because several authors^{15,20} maintain that there is no direct relationship between calculated atomic charges and N 1s BE's. However, these objections rely, at least partially, on the conclusions of Barber and Clark,¹⁵ who show no spectra or curve fitting procedure.

Admittedly, calculated charges are, at best, a qualitative guide to the assignment of N 1s BE's in ATP and related compounds. Crystal structures of AMP²⁵ and ATP²⁶ show extensive hydrogen bonding,^{25,26} close packing,²⁶ and a salt bridge²⁵ between the proton at N(1) and a phosphate oxygen. No calculation accounted for the salt bridge; Jordan and Sostman¹⁹ considered intermolecular hydrogen bonding.

Nevertheless, an assignment of the N 1s spectrum of ATP (free acid form) is proposed on the basis that positive atomic charge yields higher N 1s BE. The data are shown in Fig. 3. Two lines were fitted to the data; the BE's are 401.0 eV and 399.8 eV.

The proposed assignment is based on the following considerations. The structures of AMP²⁵ and ATP²⁶ are protonated at N(1). (The proton

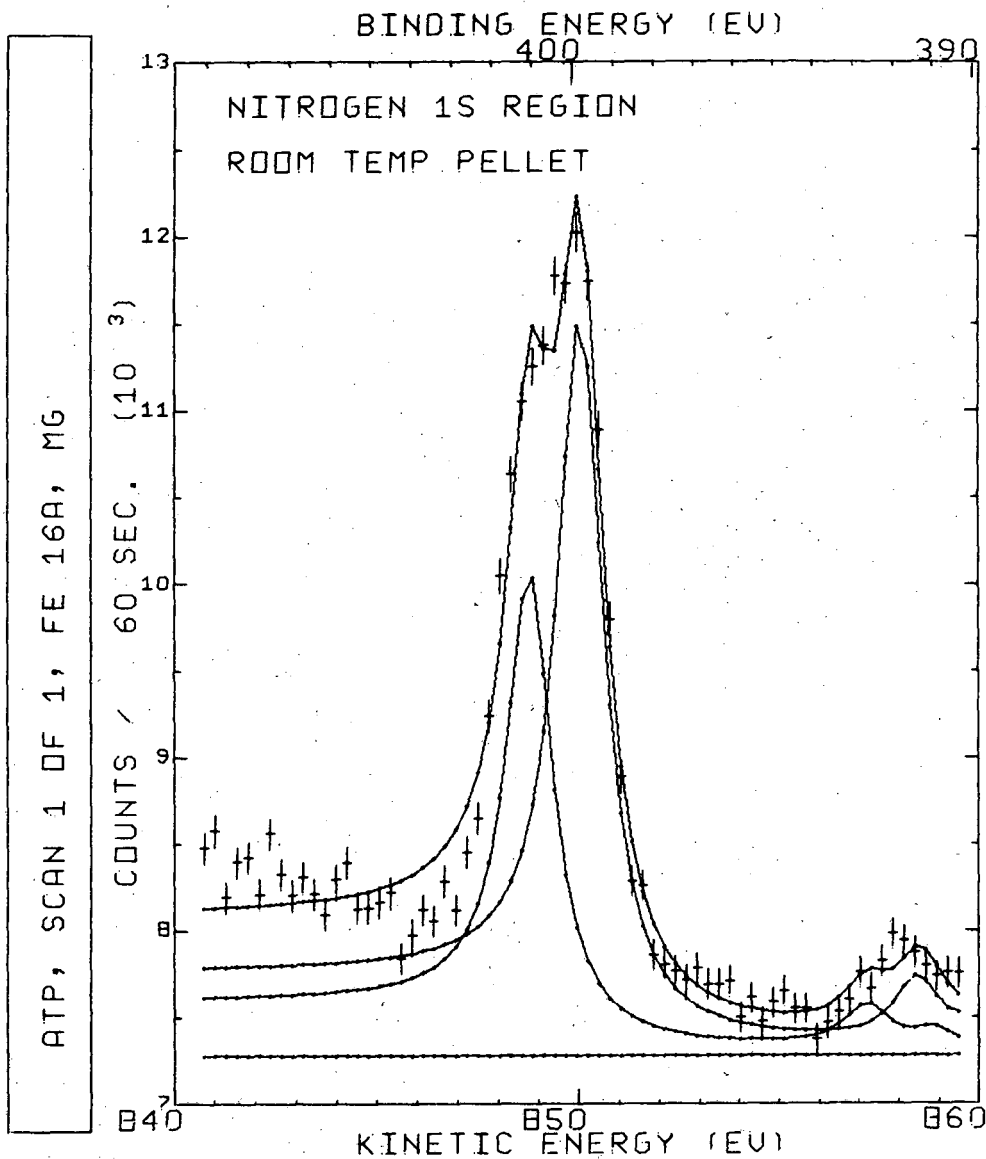


Figure 3. Nitrogen 1s spectrum of ATP in the free acid form. The BE's are (401.0 ± 0.2) eV and (399.8 ± 0.2) eV. The FWHM of each line is (1.37 ± 0.08) eV, which is consistent with the narrowest N 1s peaks observed in peptides and amino acids. The ratio is $2.0:(3.0 \pm 0.3)$. Three lines fitted to these data had FWHM's of (1.04 ± 0.06) eV, which were unrealistically narrow. The proposed assignment of the spectrum is given above each line. (See Fig. 1.) The assignment is tentative; a definitive assignment requires data from a series of substituted purines.

could not actually be resolved in the structure of ATP.²⁶) N(9) is expected to resemble a pyrrole nitrogen; its unshared pair of electrons should be delocalized, leaving it with a positive charge. Therefore, protonated N(1) and positive N(9) have been associated with the 401 eV line in Fig. 3. The structures of AMP²⁵ and ATP²⁶ show that the amino group at N(10) is unprotonated. Unprotonated amino groups have a BE of 400 eV (Chap. 4, Table V). Therefore, N(10) has been associated with the 399.8 eV line, along with N(3) and N(7). This assignment is consistent with the observed 2:3 ratio.

A CNDO²⁷ program was used to calculate charges on the nitrogen atoms. For simplicity, the ribose ring on N(9) was substituted by a methyl group. The proton at N(1) was retained. The results are given in Table III along with the results from similar calculations by Jordan and Sostman.¹⁹ The CNDO charges can be divided roughly into one group containing N(1) and N(9), and a second group containing N(3), N(7), and N(10). The N(1),(9) group, which was associated with the 401 eV line in Fig. 3, has a less negative charge than the N(3),(7),(10) group associated with the 399.8 eV line. Therefore, the proposed assignments for Fig. 3 imply a correlation between N 1s BE and the net charge on a given nitrogen within this particular molecule.

A definitive assignment of adenosine N 1s spectra requires data from a characterized set of substituted purines.

A three line fit of the data in Fig. 3 yielded lines with a FWHM of 1.0 eV. The fit seems unrealistic because the narrowest N 1s peak observed in model systems had a FWHM of 1.4 eV (Chap. 4, Table V). The FWHM of each line in Fig. 3 was 1.4 eV.

Table III. Calculated charges on nitrogen atoms in N(9)-methyl adenine·H⁺. (See Fig. 1 for atomic positions.)

	<u>N(1)</u>	<u>N(3)</u>	<u>N(7)</u>	<u>N(9)</u>	<u>N(10)</u>
This work, (CNDO) ^a	-0.10	-0.15	-0.15	-0.06	-0.19
Ref. 19, (CNDO) ^a	-0.13	-0.16	-0.12	-0.09	-0.21
Ref. 19, (MINDO) ^a	-0.74	-0.52	-0.43	-0.62	-0.71

^aCNDO (Complete Neglect of Differential Overlap) and MINDO (Intermediate Neglect of Differential Overlap) refer to techniques of semi-empirical molecular orbital calculations.

The data from the disodium salt of ATP are shown in Fig. 4. The BE's and area ratio in Fig. 4a agree with the fit of the free acid in Fig. 3. However, the lines in Fig. 4a (FWHM = 1.7 eV) are wider than in Fig. 3 (FWHM = 1.4 eV). A reasonable three line fit of the $\text{Na}_2\text{H}_2\text{ATP}$ data was possible with the FWHM of each line fixed at 1.40 eV; it is shown in Fig. 4b. The crystal structure of $\text{Na}_2\text{H}_2\text{ATP}^{26}$ shows that each sodium ion coordinates to three phosphate oxygens and to N(7). Presumably, the Na-N(7) coordination gives rise to the third line in the $\text{Na}_2\text{H}_2\text{ATP}$ data which could not be fitted to the free acid ATP data. It is not possible to determine which of the three lines is associated with the Na-N(7) bonding.

Typical N 1s spectra of Nd(ATP)Cl are shown in Fig. 5. The results from all the Nd(ATP)Cl experiments are summarized in Table IV. The spectra closely resemble those of $\text{Na}_2\text{H}_2\text{ATP}$. With some exceptions, the two line fits (Fig. 5a) preserve the 2:3 ratio observed in the ATP samples, but the FWHM's are slightly wider. The three line fits fell into two classes resembling Figs. 5b and 5c. Fig. 5c is very similar to the N 1s spectrum of $\text{Na}_2\text{H}_2\text{ATP}$ (Fig. 4b). Little significance can be associated with the different area ratios between the two classes of three line fits. They may reflect two classes of neodymium to nitrogen coordination arrangements, but it is more likely that they reflect numerical instability in the SUNDER fitting program. In fact, it was possible to obtain the fit in Fig. 5c from the data points in Fig. 5b by an appropriate choice of the tail parameter in the SUNDER program. The average N 1s BE's for all the three line fits in the Nd(ATP)Cl and

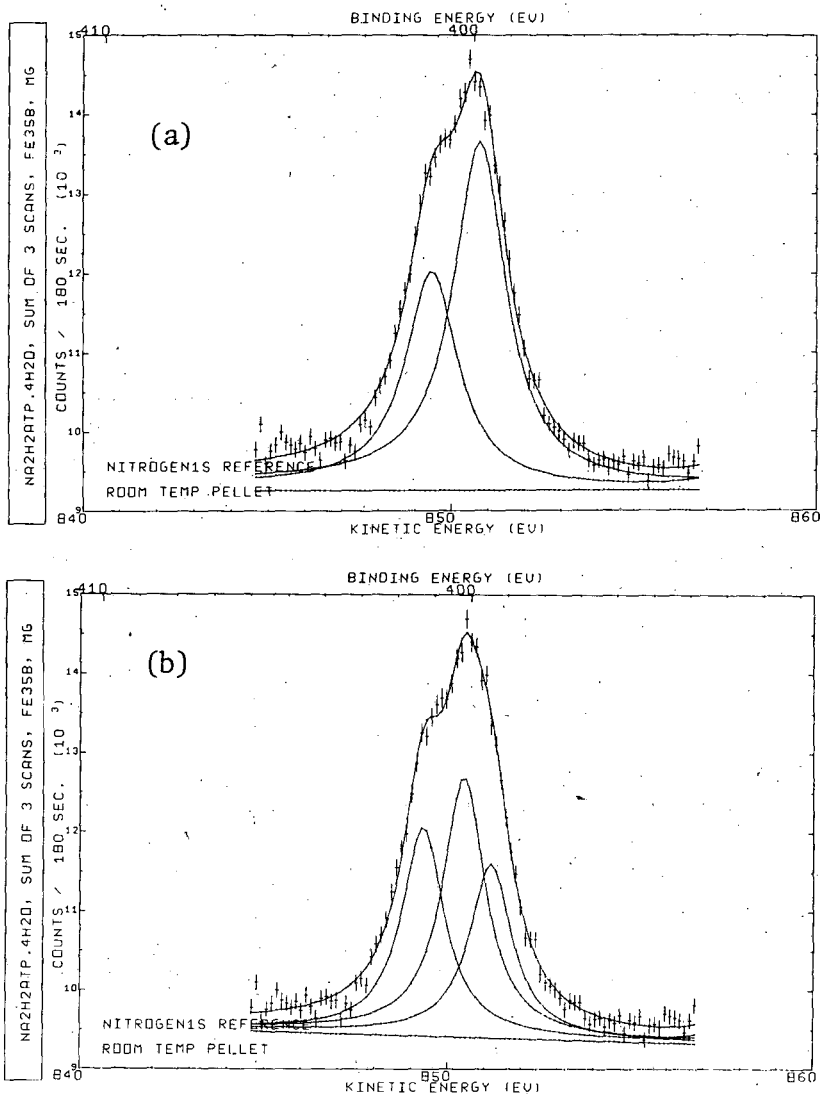


Figure 4. Nitrogen 1s spectra of the disodium salt of ATP, N_2H_2ATP . Two fits of the same data.

- (a) Two line fit with the ratio and separation left free to vary. BE's (± 0.2 eV) are 401.2 eV and 399.8 eV. Calculated ratio is 2.0:(3.2 ± 0.2). The agreement with Fig. 3 is acceptable.
- (b) Three line fit with FWHM's fixed at 1.40 eV. BE's (± 0.2 eV) are 401.3 eV, 400.2 eV, and 399.4 eV. A reasonable three line fit of the free acid ATP data in Fig. 3 was not possible. It is likely that a three line fit was possible in these data because of Na-N(7) coordination. (See text and Ref. 26.)

-285-

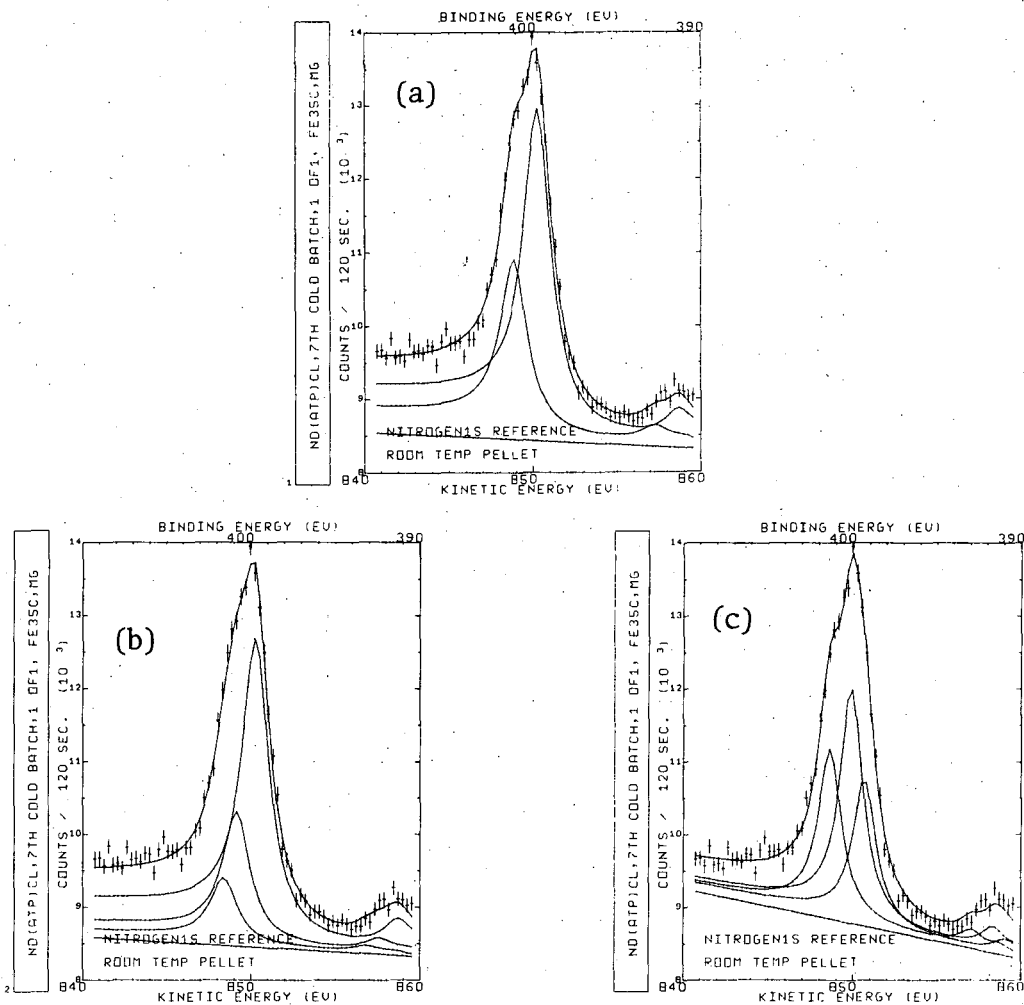


Figure 5. Nitrogen 1s spectra of Nd(ATP)Cl. Three fits of the same data.

- (a) Two line fit with all fitting parameters left free to vary. BE's (± 0.2 eV) are 401.0 and 399.7 eV. FWHM's are (1.96 ± 0.07) eV. Calculated ratio is 2.0: (3.7 ± 0.3) .
- (b) Three line fit with all parameters free.
- (c) Three line fit with the tail parameters fixed at 0.05. (See Chap. 3 for definition of tail parameter.)

Table IV. Observed nitrogen 1s binding energies^d for ATP and related compounds. See Figure 1 for abbreviations and structures. In most cases, the data were fitted once with two lines and again with three lines. The results of both fits are given in the table.

Expt. No.	Compound	Nitrogen 1s Binding Energies (eV)			FWHM (eV)	Ratios
		401.0	400.0	399.0		
25	AMP, pH3	400.7		399.5	1.52 ± 0.08	2.0:(2.7 ± 0.2)
		400.9		399.9 399.1	1.23 ± 0.08	(1.2 ± 0.2):(1.5 ± 0.3):1.0
23A	AMP, pH 5 ^a	400.4		398.8	1.53 ± 0.08	1.0:(2.6 ± 0.3) ^a
26	AMP, pH 11 ^a	400.7		399.2	1.41 ± 0.07	1.0:(3.2 ± 0.3) ^a
22A	AMP directly from bottle ^a	400.6		399.2	1.42 ± 0.07	1.0:(2.3 ± 0.2) ^a
16A	ATP directly from bottle	401.0		399.8	1.37 ± 0.08	2.0:(3.0 ± 0.3)
		401.4	400.5	399.6	1.04 ± 0.06	(0.7 ± 0.1):(0.8 ± 0.1):1.0
35B	Na ₂ H ₂ ATP from bottle	401.2		399.8	1.73 ± 0.06	2.0:(3.2 ± 0.2)
		401.3	400.2	399.4	1.40 fixed	(1.2 ± 0.2):(1.5 ± 0.1):1.0
19B	Nd(ATP)Cl ^b	400.9		399.4	2.02 ± 0.14	2.0:(3.8 ± 0.9)
		401.5	400.3	399.2	1.62 ± 0.15	(0.4 ± 0.1):(0.7 ± 0.2):1.0
35C	Nd(ATP)Cl	401.0		399.7	1.96 ± 0.07	2.0:(3.7 ± 0.3)
		401.6	400.85	399.7	1.93 ± 0.10	0.2:0.4:1.0
		401.4 ^c	400.1 ^c	399.3 ^c	1.63 ± 0.09 ^c	(1.2 ± 0.3):(1.6 ± 0.4):1.0 ^c
36A	Nd(ATP)Cl	401.0		399.6	1.92 ± 0.09	2.0:(3.0 ± 0.2)
		401.5	400.5	399.4	1.64 ± 0.10	(0.4 ± 0.1):(0.8 ± 0.1):1.0
		401.6 ^c	400.5 ^c	399.5 ^c	1.59 ± 0.09 ^c	(0.4 ± 0.1):(0.8 ± 0.1):1.0 ^c
37A	Nd(ATP)Cl	400.2			2.98 ± 0.10	
		401.1		399.7	2.01 ± 0.07	2.0:(2.8 ± 0.2)
		401.4	400.3	399.3	1.61 ± 0.07	(0.8 ± 0.1):(1.2 ± 0.1):1.0
		401.2	400.1	399.2	1.78 ± 0.08	(1.0 ± 0.1):(1.4 ± 0.2):1.0
37B	Nd(ATP)Cl	400.7		399.4	2.04 ± 0.09	(0.9 ± 0.1):1.0
		401.2	400.1	399.1	1.58 ± 0.10	(0.7 ± 0.1):(1.2 ± 0.2):1.0
Eu1B	Eu(ATP)Cl ^b	400.7		399.4	2.02 ± 0.12	2.0:(3.3 ± 0.4)
		401.3	400.6	399.4	1.85 ± 0.06	(0.19 ± 0.04):(0.57 ± 0.04):1.0

^aA high binding energy N 1s peak was observed in these spectra which is not included in the BE scale or ratios.

^bThese samples were prepared with unbuffered solutions of MCl₃ and ATP. It is likely that ATP coprecipitated with the metal complexes.

^cThe tail parameter in these spectra was fixed to 0.05 (see Chapter 3).

^dExperimental error in the tabulated binding energies is ± 0.2 eV.

Eu(ATP)Cl spectra are: (401.4 ± 0.2) eV, (400.4 ± 0.2) eV, and (399.3) eV. These positions agree with those observed for $\text{Na}_2\text{H}_2\text{ATP}$. (Recall that the three line fit for the free acid of ATP was unrealistic.) As in the two line fits, the three line fits have FWHM's (1.7 eV) that are wider than the FWHM's in the three line fit of $\text{Na}_2\text{H}_2\text{ATP}$ (FWHM 1.4 eV). Apparently, broadening is the only detectable difference between the N 1s spectra of the sodium and neodymium (or europium) compounds of ATP.

The N 1s spectra of AMP lyophilized from solutions of pH 3, 5, and 11 are shown in Fig. 6. In the pH 3 sample (Fig. 6a), the 2:3 ratio characteristic of the ATP samples has been preserved within computational error. The ratio may be slightly lower than 2:3 because of deamination at N(10) after 12 hours of exposure to the x-ray tube. The ratio increases in the higher pH samples (Figs. 6b and 6c), presumably because a decreasing proportion of molecules are protonated at N(1).

A N 1s peak at high binding energy is clearly visible in Figs. 6b and 6c, and in the N 1s spectrum of AMP directly from the bottle, which is not shown. This peak was discussed in detail in Chap. 4. Its origin is not known, but it appears to be enhanced by alkaline pH conditions. (See Fig. 8c, Chapt. 4.)

The N 1s spectrum of the free acid form of ATP was scanned 15 times for 23 hours to determine its stability in the energy flux from the x-ray tube. The data from the 15 individual scans and the sum of all 15 scans were fitted with two lines. The data were remarkably stable. The area of each line fell by about 25%, probably because of deterioration of the x-ray anode. The area ratio (average, 2:3.1; range, 2:3.3 to 2:3.8)

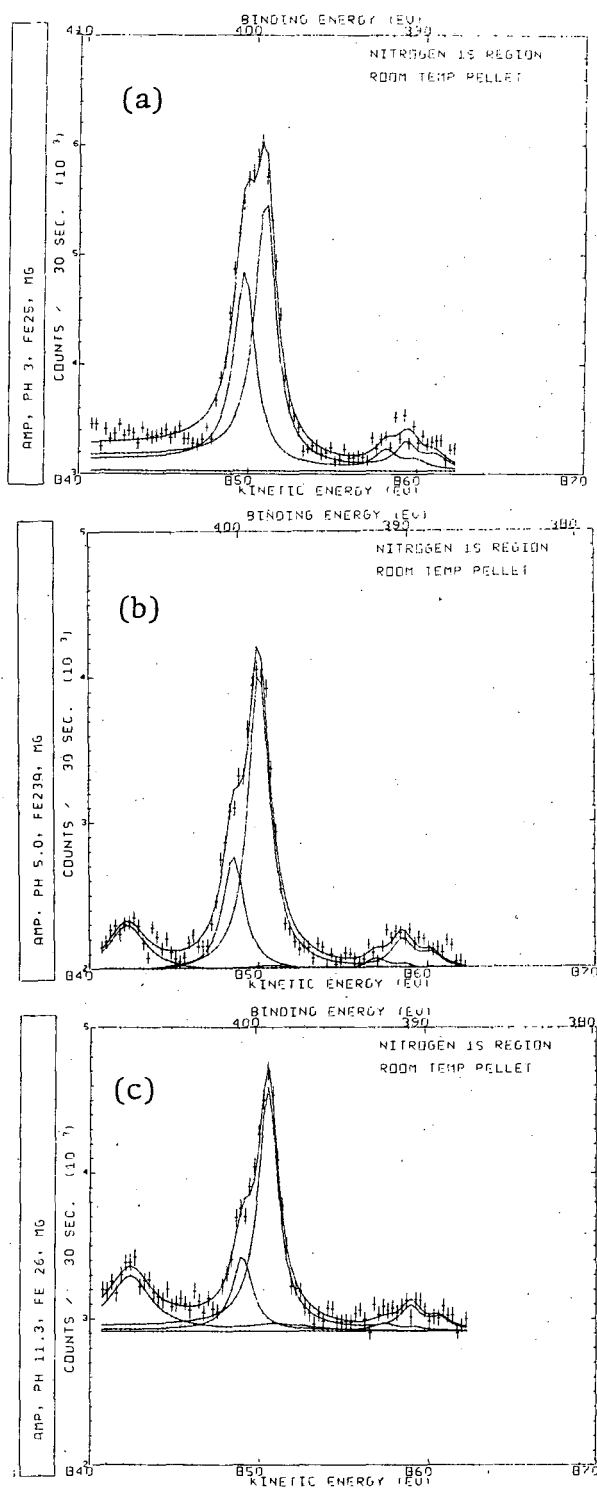


Figure 6. Nitrogen 1s spectra of AMP lyophilized from solutions of pH 3, 5, and 11. See Table IV for BE's, FWHM's, and ratios. The peak at 407 eV was discussed in Chapt. 4. Its origin is not known.

was preserved through the entire series of spectra. The FWHM (average, 1.4 eV; range, 1.89 - 1.34 eV) and separation (average, 1.26 eV; range, 1.35 - 1.24 eV) were also stable.

Phosphorus 2p Results

A series of AMP samples were lyophilized from solutions of pH 3, 5, and 11 to characterize the BE and FWHM of an adenosine phosphate group in the fully protonated, monosodium, and disodium forms, respectively.²⁸ The P 2p signals from these samples were fitted with one line to approximate the shape of the total P 2p doublet, and with two lines to approximate P 2p_{1/2,3/2} components. The results are summarized in Table V, typical spectra are shown in Fig. 7. The BE's show no obvious pattern that could be related to protonation. The BE of the pH 5 sample is abnormally low. It is unlikely that this BE reflects an unusual bonding arrangement in the monosodium salt because the N 1s BE's of this compound are similarly low; instead, instability in the C 1s referencing system used in these experiments probably causes the irregular behavior of the pH 5 AMP BE's. In any case, the P 2p shift from the fully protonated form to the disodium salt is 0.4 - 0.8 eV, which is less than half a typical P 2p FWHM. This shift is not significant.

The ATP spectra (Fig. 8) show P 2p BE's slightly higher than the AMP group, but again, the shift is small. The P 2p peaks of ATP show FWHM's that are equal to or less than those of the AMP group.

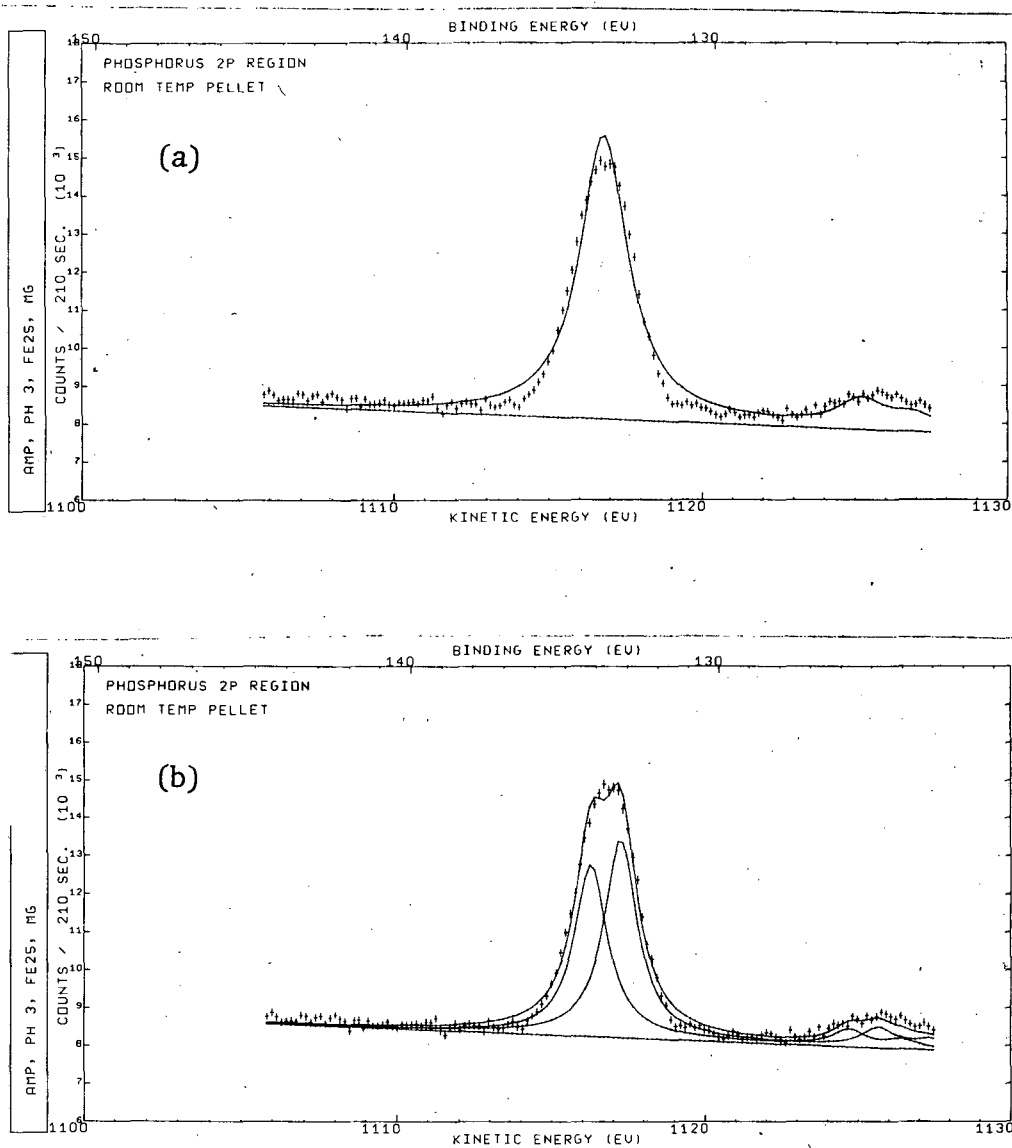


Figure 7. Phosphorus 2p spectra of AMP lyophilized from a solution of pH 3. Two fits of the same data.

(a) BE is (133.6 ± 0.2) eV; FWHM is (1.88 ± 0.2) eV.

(b) BE's (± 0.2 eV) are 134.1 and 133.2 eV; FWHM's are (1.29 ± 0.04) eV; ratio is 1.0:(1.1 ± 0.1).

Table V. Observed phosphorus 2p binding energies^a for ATP and related compounds. See Figure 1 for abbreviations and structures. The data were fitted with one line and two lines; the results of both fits are given in the table.

Expt. No.	Compound	Phosphorus 2p Binding Energies (eV)			FWHM (eV)	Ratios	
		134.0	133.0	132.0			
25	AMP, pH 3	133.6			1.88 ± 0.06	1.0:(1.1 ± 0.1)	
		134.1	133.2		1.29 ± 0.04		
23A	AMP, pH 5	133.0			1.70 ± 0.06	1.0:(1.3 ± 0.1)	
		133.5	132.6		1.21 ± 0.05		
26	AMP, pH 11	133.2			1.81 ± 0.08	1.0:(1.2 ± 0.2)	
		133.8	133.0		1.30 ± 0.08		
22A	AMP directly from bottle	133.5			1.72 ± 0.09	(1.7 ± 0.3):1.0	
		133.8	132.9		1.28 ± 0.05		
16A	ATP directly from bottle	133.9			1.65 ± 0.12	1.0:(1.5 ± 0.3)	
		134.4	133.6		1.20 ± 0.11		
35B	Na ₂ H ₂ ATP from bottle	133.7			1.82 ± 0.07	1:2 fixed	
		134.2	133.4		1.44 ± 0.07		
19B	Nd(ATP)Cl	134.0			1.92 ± 0.09	(1.3 ± 0.2):1.0	
		134.4	133.5		1.42 ± 0.10		
35C	Nd(ATP)Cl	133.8			2.1 ± 0.2	(1.3 ± 0.2):1.0	
		134.2	133.3		1.64 ± 0.10		
36A	Nd(ATP)Cl	133.7			1.74 ± 0.12	1.0:(1.1 ± 0.6)	
		134.1	133.2		1.30 ± 0.08		
37B	Nd(ATP)Cl	133.7			2.01 ± 0.11	(0.95 ± 0.08):1.00	
		134.2	133.2		1.38 ± 0.10		
22A	TPP	133.6			1.89 ± 0.07	1.0:(1.2 ± 0.1)	
		134.2	133.2		1.33 ± 0.06		
		134.3	133.6	132.9	1.08 ± 0.06		1:1:1 fixed
22C	NdTPP	133.6			2.09 ± 0.09	1.0:(1.0 ± 0.2)	
		134.1	133.2		1.50 ± 0.10		
			133.8	132.8	1.68 ± 0.09		2:1 fixed
		134.2	133.5	132.8	1.41 ± 0.10		1:1:1 fixed
Eu1B	Eu(ATP)Cl	133.9			2.06 ± 0.11		

^aExperimental error in the tabulated binding energies is ±0.2 eV.

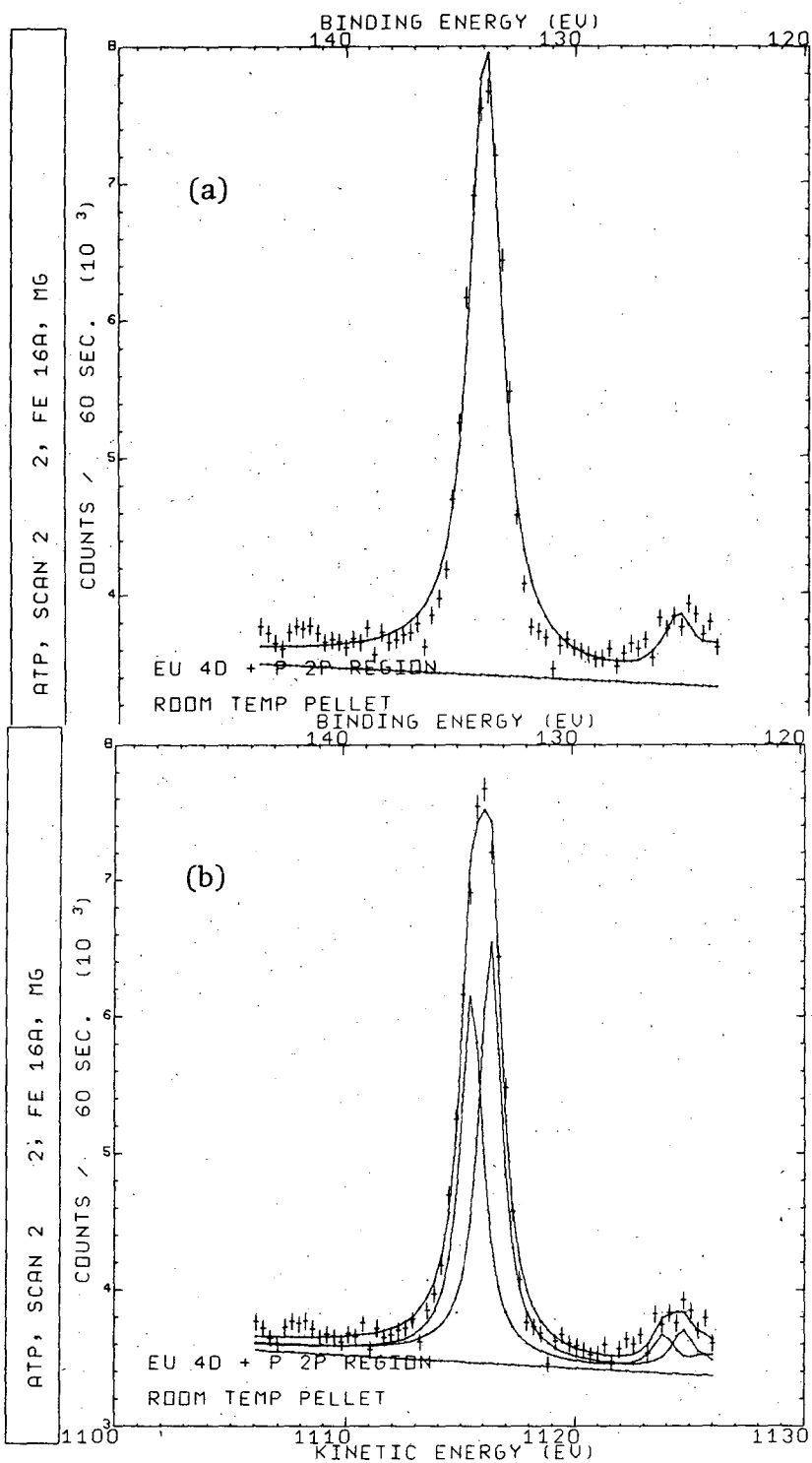


Figure 8. Phosphorus 2p spectra of ATP (free acid form). Two fits of the same data.

(a) BE (133.9 ± 0.2) eV; FWHM (1.65 ± 0.12) eV.

(b) BE's (± 0.2 eV) are 134.4 and 133.6 eV; FWHM's are (1.20 ± 0.11) eV.

The data from the AMP and ATP samples were averaged to yield the shape of a P 2p peak from an adenosine phosphate group. The total P 2p signal was found to have an average FWHM of (1.76 ± 0.08) eV. The narrowest reasonable P 2p FWHM appears to be 1.6 eV. The two line fits indicate that the P $2p_{1/2,3/2}$ components have an average FWHM of (1.29 ± 0.08) eV and a separation of (0.9 ± 0.1) eV. The calculated ratio of the P $2p_{1/2,3/2}$ components was never 1:2 unless this ratio was fixed in a particular fit, such as in $\text{Na}_2\text{H}_2\text{ATP}$.

It can be seen from Table V that the P 2p BE's of Nd(ATP)Cl (Fig. 9), Eu(ATP)Cl , $\text{Na}_5\text{P}_3\text{O}_{10}$ (tripolyphosphate, TPP, Fig. 1), and NdTPP are all similar to those of free acid and disodium ATP. Where similar compounds were measured, the P 2p BE's observed here are consistent with literature values.^{29-32,34}

Apparently, the P 2p BE of ATP is not sensitive to the exchange of protons for sodium ions or neodymium ions.

Assuming that P 2p BE shifts were produced, but not resolved in the spectra, SUNDER was used to fit the P 2p data of all compounds according to various bonding schemes. The results of these fits were unrealistic or ambiguous. Three line fits consistent with three observably non-equivalent phosphate groups were unrealistic because the calculated linewidths were too narrow. It was often possible to make two line fits with the area ratio fixed at 2:1; this scheme is consistent with Chang's¹³ interpretation that Nd^{3+} binds to the α and γ phosphate groups of ATP and TPP, leaving the β phosphate group unperturbed. However, two line

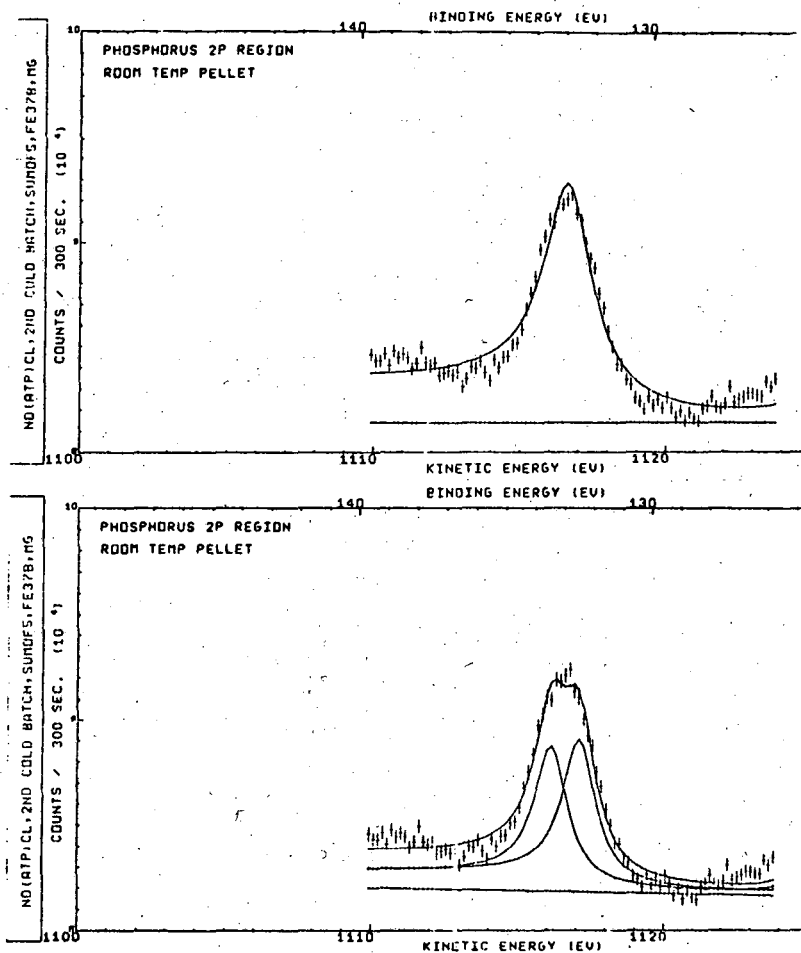


Figure 9. Phosphorus 2p spectra of Nd(ATP)Cl. Two fits of the same data.

- (a) BE is (133.7 ± 0.2) eV; FWHM is (2.01 ± 0.11) eV.
- (b) BE's (± 0.2 eV) are 134.2 and 133.2 eV; FWHM's are (1.38 ± 0.10) eV; ratio is 1.0:(1.0 ± 0.1).

fits with the ratio left free to vary yielded ratios of 1:1. Both kinds of fits were statistically equivalent. Results of such fits are given in Table V with TPP and NdTPP.

Negligible P 2p BE shifts accompanying heavy metal binding are well documented. Blackburn *et al.*³⁰ found no shift in complexes of Ni, Pd, and Cd to $(C_6H_5)_3P$; they interpreted this result in terms of metal to phosphorus π backbonding. Morgan *et al.*³¹ observed no P 2p shift when mercury was bound to the phosphoryl oxygen of $(C_6H_5)_3P=O$; this result was attributed to the low polarizability of oxygen.

The oxygen 1s spectra of ATP and its complexes were obscured by water of hydration and atmospheric adsorption. An O 1s shift corresponding to Nd binding could not be observed.

It is unlikely that π backbonding could explain the small P 2p shift in this work because lanthanide bonding to oxygen donor ligands is considered to be electrostatic rather than covalent.² Furthermore, phosphate represents the maximum oxidation state of phosphorus. There are four oxygen atoms bound to each phosphorus. Any P 2p shift to higher BE, representing additional electron withdrawal from phosphorus, is expected to be small.

Finally, if the Nd-phosphate binding is similar to the sodium-phosphate binding, then a P 2p BE shift is not expected. Darnall and Birnbaum² have already pointed out that the chemical complexes of calcium and the lanthanides have similar bonding structures. These complexes often involve oxygen donor ligands, and the bonding is electrostatic

rather than covalent. (See Ref. 2 and references therein.) The +3 lanthanide oxidation state stabilizes these complexes, but it does not alter the bonding structure. Thus, they claim that the substitution of lanthanide ions for calcium (or magnesium) in protein complexes has little effect on the protein. It is possible that these similarities extend to the substitution of H^+ or Na^+ in ATP with Nd^{3+} and one or two Cl^- counterions; the result would be an insignificant P 2p BE shift.

Since the analysis of $Nd(ATP)Cl$ showed one Nd per ATP molecule, the replacement of two Na^+ ions in Na_2H_2ATP by one Nd^{3+} is expected to be accompanied by some conformational change.³³ XPS does not seem to be sensitive to any such change.

D. Conclusions

The controversy regarding the assignment of the C 1s and N 1s spectra has not been resolved in this work. The assignments proposed here are tentative; a definitive assignment requires corroborative data from a characterized series of substituted purines.

An anomalous N 1s peak at high binding energy is clearly evident in the AMP samples lyophilized from pH 5 and 11. More details on this peak have been given in Chapt. 4.

The N 1s signal was unusually stable during 23 hours of exposure to the unfavorable environment of the x-ray tube.

Finally, the substitution of Na^+ in Na_2H_2ATP with Nd^{3+} is accompanied by almost no change in the N 1s and P 2p spectra, except for some

slight broadening. There are reasons to expect a small P 2p shift, but the same is not true of N 1s. It is suggested that the principles which govern the substitution of lanthanides for calcium in proteins can be extended to the substitution of Nd^{3+} for Na^+ in the $\text{Na}_2\text{H}_2\text{ATP}$ system. In these spectra, there is no evidence contrary to this interpretation. However, the data cannot distinguish whether one Na^+ has been replaced by one Nd^{3+} and two Cl^- counterions, or whether both Na^+ have been replaced by Nd^{3+} . In this latter case, a conformational change is likely.

The relevant metal BE's are summarized in Table VI. Their spectra are generally broad and difficult to interpret.

Table VI. Observed metal binding energies for complexes of ATP. See Figure 1 for abbreviations and structures.

<u>Compound</u>	<u>Level</u>	<u>Binding Energy (eV)</u>
Nd(ATP)Cl	Nd 4p _{1/2}	240 ± 1
Nd(ATP)Cl	Nd 4p _{3/2}	229.4 ± 0.6
	"	228.9 ± 0.6
Nd(ATP)Cl	Nd 4d	≈ 122
Eu(ATP)Cl	Eu 4p _{3/2}	262 ± 1
Eu(ATP)Cl	Eu 4d _{3/2}	142.3 ± 0.2
Eu(ATP)Cl	Eu 4d _{5/2}	136.3 ± 0.4

REFERENCES, CHAPTER VI

1. Birnbaum, E.R., Gomez, J.E., Darnall, D.W., J. Am. Chem. Soc. 92, 5287 (1970).
2. Darnall, D.W., Birnbaum, E.R., J. Biol. Chem. 245, 6484 (1970).
3. Luk, C.K., Biochemistry 10, 2838 (1971).
4. Smolka, G.E., Birnbaum, E.R., Darnall, D.W., Biochemistry 10, 4556 (1971).
5. The original pattern is on file with Dr. A. Zalkin, Lawrence Berkeley Laboratory, Bldg. 70A, Room 4405-C, Berkeley, CA 94720. The file no. is 7813; a theoretical powder pattern for AMP was calculated by Helena Ruben and Donald Ward, who are Dr. Zalkin's assistants.
6. Kolthoff, I.M. and Elving, P.J. Treatise on Analytical Chemistry, Part II, Vol. 8 (Interscience, New York, 1963), pp. 26-53, esp. p. 34.
7. The analysis was performed by V. Tashinian, Department of Chemistry, University of California, Berkeley, CA 94720.
8. Walton, H.F., Principles and Methods of Chemical Analysis, 2nd Edition (Prentice Hall, Englewood Cliffs, N.J., 1964), pp. 379 ff.
9. Vogel, A.I., A Textbook of Quantitative Inorganic Analysis Including Elementary Instrumental Analysis, 3rd Edition (Longman, London, 1961), pp. 787-788.
10. Ref. 6, pp. 97 ff. See exp. Table XIV, p. 102.
11. Lowry and Lopez, J. Bio. Chem. 162, 421 (1946).

12. Leloir, L. and Cardini, C., in Methods in Enzymology, Vol. III, (S. Colowick and M. Kaplan, Eds.) (Academic Press, New York, 1957), pp. 840 ff, esp. p. 845.
13. Chang, R., private communication.
14. Mely, B., and Pullman, A., Theor. Chim. Acta 13, 278 (1969).
15. Barber, M. and Clark, D.T., Chem. Commun. (1970), pp. 23, 24.
16. van der Avoird, A., Chem. Commun. (1970), p. 727.
17. Clementi, E., Mehl, J., and von Niessen, W., J. Chem. Phys. 54, 508 (1971).
18. Rein, R., Hartman, A., and Nir, S., Isr. J. Chem. 10, 93 (1972).
19. Jordan, F., and Sostman, H.D., J. Am. Chem. Soc. 94, 7898 (1972), and references therein.
20. Bossa, M., Gianturco, F. and Maraschini, F., J. Electron. Spectrosc. and Relat. Phenom. 6, 27 (1975).
21. Brundle, C.R., Appl. Spectrosc. 25, 8 (1971).
22. Table II in Chapter 4 of this dissertation.
23. Gelius, U., et al., Phys. Scr. 2, 70 (1970).
24. Gelius, U., et al., Phys. Scr. 3, 237 (1971).
25. Kraut, J., and Jensen, L., Acta Crystallogr. 16, 79 (1963).

26. Kennard, O., et al., Proc. R. Soc. London A 325, 401 (1971).
27. Davis, D.W., Ph.D. dissertation, University of California, Berkeley, 1974.
28. Handbook of Biochemistry, Selected Data for Molecular Biology, 2nd Edition (Sober, Ed.), Chemical Rubber Co. Press, Cleveland, 1970, p. J-67.
29. Pelavin, M., Hendrickson, D., Hollander, J., and Jolly, W., J. Phys. Chem. 74, 1116 (1970).
30. Blackburn, J., Nordberg, R., Stevie, F., Albridge, R., and Jones, M., Inorg. Chem. 9, 2375 (1970).
31. Morgan, W., Stec, W., Albridge, R., and van Wazer, J., Inorg. Chem. 10, 926 (1971).
32. Swartz, W., Hercules, D., Anal. Chem. 43, 1066 (1971).
33. Bayley, P. and Debenham, P., Eur. J. Biochem. 43, 561 (1974).
34. J. Hedman, M. Klasson, J. Lindberg, C. Nordling, in Electron Spectroscopy, D.A. Shirley (Ed) (North Holland, Amsterdam, 1972), pp. 681 ff.

VII. CONCLUSIONS

Some of the technical difficulties that faced XPS studies of biological systems have been mitigated, or at least, they are more clearly characterized. An internal carbon 1s reference system has been developed which gives highly reproducible results in protein samples.

The radiation dose absorbed by the sample was calculated to be large, 10^6 rad/sec. It was reported (Chapt. IV) that solid amino acid samples saturate with free radicals when 10^6 rads have been absorbed; therefore, the saturation time in the Berkeley spectrometer is a second. At this dose rate, radiation damage was found to be a problem. Iron and sulfur spectra (Chapt. V) both showed photoreduction in the photons, electrons, and heat emitted by the x-ray tube. However, several hours were required to reduce 50% of the observed atoms. This half-life is long compared to the one second saturation time. Protein carbon 1s and nitrogen 1s spectra generally preserved their shape throughout extended experiments; the nitrogen 1s spectrum of ATP was essentially unchanged after 23 hours of exposure to the x-ray tube.

Given that the x-ray sources in the best commercial instruments are 10^2 - 10^3 times less intense than that of the Berkeley spectrometer; and given the long half-life of XPS signals, it seems possible that radiation effects can be minimized by adding the data from several samples that have been exposed for a short time.

It has been possible to make a biologically significant interpretation of the data in this dissertation only in the case where a large BE shift was observed. In the cytochrome studies (Chapt. V) a systematic 4 eV difference was found between the Fe 3p BE's of high and low spin heme complexes. This shift could be interpreted in terms of charge redistribution in the "hole" state following photoejection. Apparently, iron atoms in the porphyrin plane (low spin) could delocalize the "hole" state charge more effectively than iron atoms out of the porphyrin plane. Therefore, this 4 eV shift could be attributed to the effect of the final state on BE.

In contrast, initial state effects, such as the oxidation state of the parent atom, did not seem to cause large shifts. The extent to which these smaller shifts will yield information in the future depends on improved spectrometer resolution and the accumulation of a pool of data on characterized systems.

This report was done with support from the Department of Energy. Any conclusions or opinions expressed in this report represent solely those of the author(s) and not necessarily those of The Regents of the University of California, the Lawrence Berkeley Laboratory or the Department of Energy.

TECHNICAL INFORMATION DEPARTMENT
LAWRENCE BERKELEY LABORATORY
UNIVERSITY OF CALIFORNIA
BERKELEY, CALIFORNIA 94720